THÈSE DE DOCTORAT

UNIVERSITÉ PIERRE ET MARIE CURIE

École Doctorale de Sciences Mécaniques, Acoustique, Electronique et Robotique de Paris (ED 391)

Présentée par :

Paul Grandgeorge

Pour obtenir le grade de

DOCTEUR DE L'UNIVERSITÉ PIERRE ET MARIE CURIE

Le flambage élasto-capillaire de fibres et de membranes fibreuses fines pour la conception de matériaux étirables

---

Surface-tension induced buckling of thin fibers and fibrous membranes: a novel strategy to design stretchable materials

---

Dirigée par
Arnaud Antkowiak et Sébastien Neukirch
à l'Institut Jean le Rond ∂'Alembert

Soutenance prévue à l'UPMC le 9 Février 2018 devant le jury composé de :

Dominic VELLA	Rapporteur
José BICO	Rapporteur
Jean-Jacques MARIGO	Examinateur
Davide BIGONI	Examinateur
Régis WUNENBURGER	Examinateur
Yves BRECHET	Examinateur
Natacha KRINS	Invitée
Sébastien NEUKIRCH	Co-directeur de thèse
Arnaud ANTKOWIAK	Co-directeur de thèse

Remerciements

Un immense merci à Arnaud Antkowiak et à Sébastien Neukirch d'avoir été les directeurs de thèse qu'ils ont été durant ces trois années. Merci de m'avoir tant écouté, tant conseillé, et tant appris.

Merci infiniment à Natacha Krins de m'avoir accueilli dans son labo et dans ce monde aussi mystérieux que fascinant qu'est celui de la chimie.

Merci aux grand-e-s chercheur-e-s comme Régis Wunenburger, Arnaud Lazarus, Thomas Séon, Benoît Roman où Stéphanie Deboeuf pour toutes les belles discussions qu'ils m'ont offertes.

Merci à mes collègues pour tous les si bons moments partagés. Je pense notamment à Aurélie Hourlier-Fargette, qui a été un soutien intelligent tout au long de ma thèse (et qui l'est encore !), à Hervé Elettro, qui m'a légué un beau sujet d'étude et qui continue à me régaler de sa bonne humeur, à Raphaël Leiba, véritable vecteur de vie au labo et à Benjamin Bugeat, avec qui j'ai pris cafés, bières, et un malins plaisirs à me jouer de la langue française.

Merci aux étudiants en stage avec lesquels j'ai eu la chance de travailler en salle Savart; Manon Lestimé, Julien Froustey, Anton Mladenov et Florian Poydenot.

Merci à mes rapporteurs pour la lecture consciencieuse de mon manuscrit, José Bico et Dominic Vella, et à mes examinateurs de m'avoir écouté avec bienveillance lors de ma soutenance, Davide Bigoni, Régis Wunenburger et Yves Bréchet.

Merci finalement aux gestionnaires en or de ∂'Alembert, dont l'aide et le soutien se sont étendus bien au-delà des tâches administratives, Simona Otarasanu, Olivier Labbey et Catherine Dejancourt.

Juliana, merci d'avoir été à mes côtés tout au long de ce doctorat.

Abstract

This PhD thesis focuses on the mechanical interactions between liquids and thin elastic structures. First, we study the mechanics of a liquid drop sitting on an undeformable horizontal fiber. We numerically and analytically investigate how capillarity and gravity affect the shape of the drop and the forces it develops on the fiber. This understanding allows us to introduce a precise fiber-radius measurement technique, experimentally validated on micronic fibers.

Capillary forces developed by drops are sometimes strong enough to deform thin elastic fibers. For example, upon compression of its ends, a spider capture silk fiber spontaneously buckles and spools inside water droplets naturally sitting on it. This elasto-capillary coiling provides the composite system with an apparent extreme extensibility as excess fiber (coiled inside the liquid drop) is continuously spooled in or out of the liquid drop, thus ensuring tension throughout large deformations. This mechanical behavior could potentially be of interest for stretchable electronic connectors but the large bending stiffness of metallic fibers jeopardizes the elasto-capillary in-drop coiling. We overcome this limitation by attaching a beam of soft elastomer to the functional stiff fiber. This soft auxiliary beam strategy favors coiling by enhancing capillary forces without significantly increasing the overall elastic bending rigidity of the new composite fiber. We also study the coiling and uncoiling dynamics of the drop-on-a-single-fiber compound, presenting a novel experiment for the study of contact line dynamics.

Elasto-capillarity with thin elastic fibers provides one-dimensional stretchability. This strategy is generalized to two-dimensional structures by infusing, or *wicking*, a thin free-standing fibrous membrane with a wetting liquid. When the boundaries of this wicked membrane are brought closer, the solid membrane wrinkles and folds inside the liquid film, and the system therefore remains globally flat. We experimentally and theoretically study the mechanical response of this novel hybrid material whose main feature lies in a mixed liquid-solid behavior: the liquid provides surface tension while the solid fibrous membrane ensures inextensibility. Finally, we analyze the buckling pattern displayed by the wicked membrane upon compression and propose a theoretical model recovering the main experimental observations.

Keywords: surface tension, elasto-capillarity, elastic instabilities, buckling, wetting dynamics, stretchable electronics

Résumé

Dans cette thèse, nous étudions les interactions mécaniques entre de structures élastiques fines et des liquides. Dans un premier temps, nous nous intéressons à une goutte liquide posée sur une fibre horizontale indéformable. L'influence de la tension de surface et du poids de la goutte sur la forme qu'elle adopte sont quantifiées à travers une étude numérique et théorique de ce système. Cette compréhension nous permet d'introduire un nouvel outil de précision pour la mesure de fibres fines, validé expérimentalement pour des fibres microniques.

Dans certains cas, les forces capillaires développées par la goutte peuvent être suffisantes pour déformer la fine fibre sur laquelle elle est posée. Par exemple, lorsqu'elle est comprimée, une fibre de soie de capture d'araignée flambe et s'embobine spontanément au sein des gouttes d'eau qui la décorent naturellement. Cet enroulement élasto-capillaire confère une extensibilité apparente remarquable à la fibre hybride qui s'embobine et se débobine au gré des déformations imposées, tout en restant globalement tendue. Ce comportement mécanique pourrait revêtir un intérêt particulier pour les connecteurs électroniques étirables. Mais la rigidité à la flexion de fibres métalliques conductrices compromet l'enroulement élasto-capillaire. Cet obstacle est ici surmonté en apposant une fibre d'élastomère souple à la fibre fonctionnelle dure. Cette stratégie de la fibre auxiliaire souple facilite l'enroulement en renforçant les forces capillaires sans pour autant augmenter significativement la rigidité à la flexion globale de la nouvelle fibre composite. Par ailleurs, la dynamique d'enroulement et de déroulement est étudiée pour une goutte sur fibre simple, et permet d'introduire une expérience originale pour l'étude de la dynamique de la ligne de contact.

L'élasto-capillarité assure l'étirabilité unidimensionnelle de fibres élastiques fines. Nous étendons cette stratégie aux structures bidimensionnelles en imbibant une fine membrane fibreuse d'un liquide mouillant. Lorsque les bords de cette membrane imbibée sont rapprochés, la membrane se plisse au sein du film liquide et reste ainsi globalement plate malgré la déformation imposée. L'étude expérimentale et théorique de ce nouveau matériau hybride révèle un comportement à la fois liquide et solide : le liquide infusé confère une tension de surface tandis que la membrane fibreuse solide assure l'inextensibilité. Finalement, le motif de flambage dessiné par la membrane au sein de la couche liquide lorsqu'elle est comprimée est analysé et interprété par un modèle théorique.

Mots clés : tension de surface, élasto-capillarité, instabilités élastiques, flambage, dynamique de mouillage, électronique étirable

Contents

Introduction

Material science, throughout history, searches for materials exhibiting the best properties to fulfill human-defined functions (Ashby and Johnson 2013). For example, in the civil engineering area, materials such as stone or steel ensure mechanical robustness for the construction of edifices or bridges and withstand large stresses while undergoing little deformation. But the function of a material is also conditioned by the geometry it is given. For construction, the typical 'I' shaped cross-section of beams endows them with a higher bending rigidity than a circular-shaped cross-section of equivalent surface area and therefore allows them to resist larger loads without buckling.

Over the last decades, the interplay between material properties and geometry has evolved and novel properties have been brought forward by new materials. For example, buckling, historically associated with structural failure (Gordon 1991), is now put to contribution in the erection of buildings such as the 300 m² tent presented in Figure 1. Here, a carefully designed 2-dimensional grid of beams is laid down on the ground and then buckled and anchored at its periphery to give rise to a functional 3-dimensional structure; this temporary edifice housed the forum during the Solidays festival in 2011 in France (du Peloux et al. 2013).

Figure 1 – 300 m² gridshell structure hosting the forum during the Solidays festival (2011) in Paris (France). Here, buckled beams shape a roof and provide mechanical robustness to the structure. Reproduced from du Peloux et al. (2013).

The out-of-plane buckling of 2-dimensional structures also allows us to rethink the design of complex 3-dimensional architectures at much smaller scales, as presented in Xu et al. (2015) where microscopic 3-dimensional objects are effortlessly manufactured. And at these small scales, pre-buckled metallic connectors on stretchable polymers can even buffer large deformations of electronic circuits (Rogers et al. 2010): controlled buckling then provides stretchability to materials *a priori* hardly deformable. Another compelling example of stretchability through geometry and buckling is presented in Rafsanjani and Bertoldi (2017) where buckling-induced kirigami provides apparent stretchability to relatively stiff materials. Again, stretchability is here not achieved by stretching the material at its microscopic level, but by allowing it to rearrange spontaneously throughout an imposed extension.

Controlled buckling and geometrical re-organization are not the only candidates for material stretchability. Recent advances in polymer science have allowed the engineering highly deformable, yet extremely tough, materials such as the hydrogels presented in
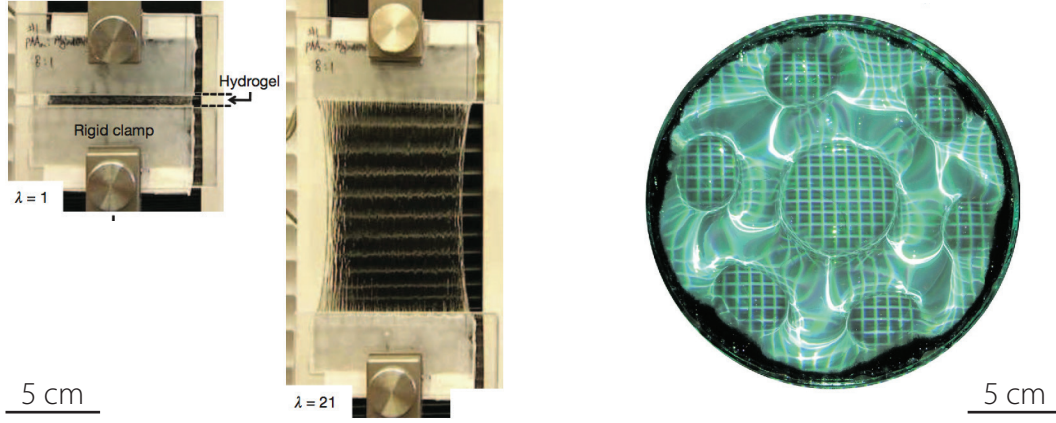
Figure 2 – **Left** – Tens of kPa-modulus hydrogel undergoing a 21-fold extension without rupturing. Reproduced from Sun et al. (2012). **Right** – Hundreds of Pa-modulus polyacrylamide gel in a circular recipient. Here, the recipient faces downwards, leading to the capillary Rayleigh-Taylor instability at the gel surface. Reproduced from Mora and Pomeau (2017).

Sun et al. (2012). These polymers, of Young's moduli of few tens of kPa, can undergo extreme deformations and such a polymeric sheet undergoing a 21-fold extension without rupturing is presented in Figure 2-left. An even softer polyacrylamide gel is presented in Figure 2-right, reproduced from Mora and Pomeau (2017). It has a Young's modulus of only a few hundreds Pa and although it is solid, it undergoes the surface-tension induced Rayleigh-Taylor instability when its recipient is turned upside-down. Capillarity, usually attributed to liquids, is here strong enough to compete with the elastic resistance of this jelly-like material.
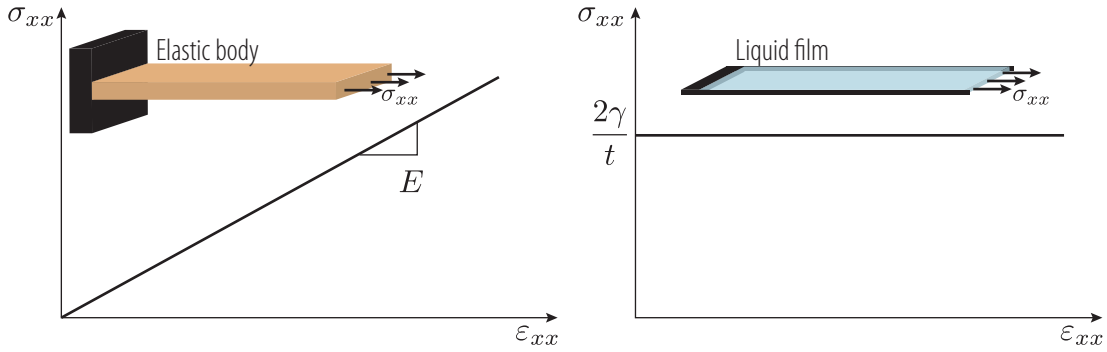
Figure 3 – **Mechanical behavior of elastic solid and liquid film. Left** – As an elastic body is extended, its tensional stress increases linearly with deformation. **Right** – A liquid film of surface tension γ is now extended. Provided the thickness t of this film remains constant, its equivalent inner stress does not depend on deformation.

Before further discussing how capillarity can shape elastic solids, we present a simple experiment to apprehend the difference between elastic and liquid mechanical behavior in Figure 3. An ideal elastic sample is subjected to an uni-axial deformation ε_{xx}, its stress state is then described by σ_{xx} as:

$$\sigma_{xx} = E\,\varepsilon_{xx} \tag{1}$$

where E is the sample Young's modulus. In this case, as deformation gets larger, stress increases. A similar geometry is now considered, but instead of probing a solid elastic sample, a liquid film of surface tension γ on a frame is mechanically tested; deformation is imposed by quasi-statically displacing one of the straight edges of the frame. Averaging the

stresses over the liquid film thickness t then provides this liquid film's stress-deformation relation:

$$\sigma_{xx} = \frac{2\gamma}{t}. \tag{2}$$

For the liquid film, stress does not depend on deformation. The elasticity of a solid object provides mechanical robustness but also limits its deformation span. Liquids, on the other hand, are not known for their mechanical resistance, but can undergo extreme deformations. Taking advantage of the strengths of both these complementary properties could trigger the design of novel stretchable materials.

Spider capture silk was recently found to exhibit both solid and liquid properties. In this case, the capillary forces developed by liquid drops naturally sitting on the fiber are strong enough to make the fiber buckle and coil within them when the fiber ends are brought closer. This mechanism, first described in Vollrath and Edmonds (1989) and later studied in Elettro (2015) is presented in Figure 4. It endows thin fibers with an apparent extreme stretchability, as the spontaneous coiling of fiber within liquid drops upon compression provides 'fiber reserves' which are recruited upon subsequent extension.

50 µm
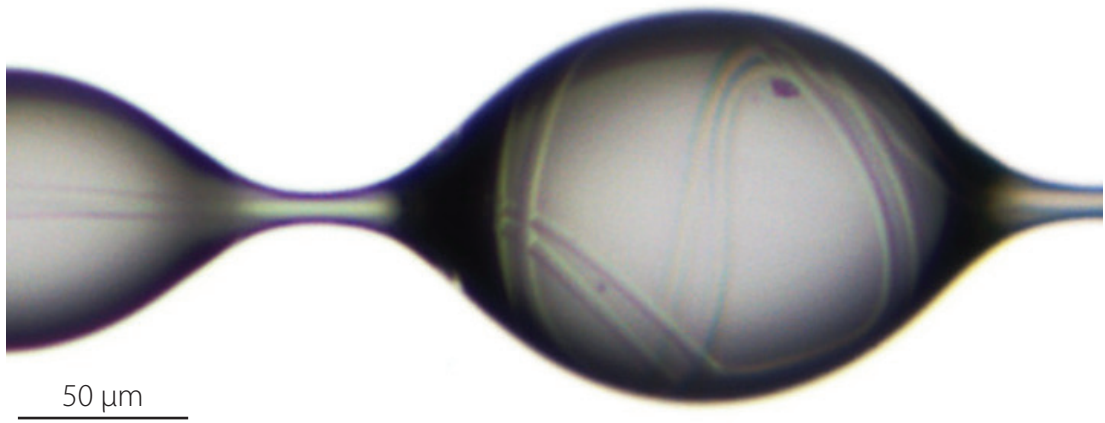
Figure 4 – Nephila capture silk coiling spontaneously inside liquid glue droplets. The surface forces developed by the drops compel the thread to buckle and coil within them. Reproduced from Elettro et al. (2016).

In this PhD thesis, we further study how the alliance of elasticity and capillarity provides a new candidate-strategy for the design of stretchable materials. This work is divided in five chapters. We focus on the mechanics of a liquid drop sitting on a rigid (i.e. undeformable) fiber in the first chapter. The gained expertise allows us to develop a simple tool for the precise fiber-radius measurement of micronic fibers. Then, in the second Chapter, we allow for the fiber to buckle and coil inside the drop to minimize the global (i.e. capillary + elastic) energy of the system, and we revisit this elasto-capillary phenomenon with the aim of creating highly stretchable functional fibers by making them eligible for in-drop coiling. In the third Chapter, we study the coiling and uncoiling dynamics of the drop-on-fiber system and introduce a new setup to experimentally study the liquid triple line dynamics. Fiber loops spontaneously stored inside drops provide one-dimensional stretchability and motivates the extension of this study to two-dimensional stretchability. This challenge is met in Chapter 4, where wicking a thin fibrous membrane with a wetting liquid leads to the spontaneous apparition of elasto-capillary wrinkles and folds, 'membrane reserves', which will be further studied in Chapter 5. These five chapters are finally summarized and perspectives are proposed in the last Chapter.

Please note that for ease of reading, experimental details are provided using this style throughout this manuscript.

Part I

Drop on a thin fiber

1 | Drop on a rigid fiber

Contents

Liquid drops surround us every day and their somewhat surprising behavior never fails to awaken our curiosity. For example, we take a plate and deposit a small water droplet on it. The drop now sits on top of the plate and nothing spectacular happens: the drop's weight pulls it downwards, but this force is balanced by the reaction force provided by the solid plate. We now flip the plate upside down and naively expect for the drop to fall, as there no longer is a solid support under it to prevent it from falling. We look under the plate and surprise! the drop is still under the plate, as if 'sticking' to it. This unexpected sticking behavior actually finds its root in the surface tension of the drop: it develops capillary forces strong enough to balance it own weight.

If a drop sits on a flexible substrate, these capillary forces are sometimes even strong enough to deform this substrate. The study of the deformation of elastic structures under capillary effects is called elasto-capillarity. For example, Fritz Vollrath and Donald Edmonds discovered that liquid glue droplets naturally sitting on spider capture silk provide sufficient capillary forces as to make the thin silk fiber bend and spool inside the drops (Vollrath and Edmonds 1989). This phenomenon was later studied in Elettro et al. (2016) and this work will provide further contributions concerning this mechanism. But before focusing on the elasto-capillary effects of a drop on a fiber, we make a detour and study the capillary effects of a drop on a fiber, i.e. we first do not consider fiber deformation.

The shape adopted by a drop on a rigid fiber without considering gravity has been extensively studied in literature. For example, an important question in the domains of fiber coating or detergency applications is whether a drop deposited on a fiber wraps around it, thus adopting an axially symmetric shape (barrel configuration) or sits only on a side of the fiber (clam-shell configuration). This chapter first revisits these two configurations using the energy minimization software Surface Evolver and summarizes the advances made

over the last decades. More recently, interesting works such as Eral et al. (2011) or Bintein (2015) have studied the influence of electric fields on the shape adopted by drops on fibers.

On the other hand, gravitational effects on drop-on-fiber systems have been explored only over the past few years and therefore deserve special attention. We develop a model to predict the forces applied by a horizontal cylindrical fiber on a liquid drop sitting on it and how they are related to the hanging height of the drop in the gravity field. This study allows us to introduce a novel precise fiber-radius measurement technique.

We finally propose a new simple model to predict which is the largest drop that can sit on a fiber before falling off.

1.1 Drop

A liquid drop levitating in air is presented in Figure 1.1. It has a surface energy $E = A\gamma$ where A is its total surface area and γ is its interface energy. The difference in pressure between the exterior and the interior of the drop is given by the Laplace pressure jump:

$$\Delta P = P_{\text{in}} - P_{\text{out}}$$
$$= \gamma \left(\frac{1}{R_1} + \frac{1}{R_2} \right) \tag{1.1}$$

where R_1 and R_2 are the principal radii of curvature of the drop. When the drop is perfectly spherical, $R_1 = R_2 = R$ with R the radius of the drop and in this case, the pressure jump reads $\Delta P = 2\gamma/R$.
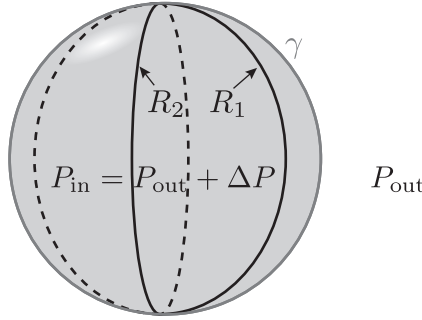
Figure 1.1 – Spherical drop and its two principal radii of curvature R_1 and R_2. Due to its surface tension γ, the inner pressure P_{in} is higher than the outer pressure P_{out} by a constant term ΔP.

If gravity forces cannot be neglected, the capillary pressure jump is not constant anymore as it balances hydrostatic pressure.

1.2 Drop on a planar surface

Liquid drops on planar surfaces are commonly observed in every day life and their industrial applications are numerous (painting, surface protection, detergency etc.). In order to dive into the physics of a this system, we study a simple configuration: a liquid drop is deposited on a solid planar substrate where it adopts its equilibrium shape (see Figure 1.2). Here, we do not take the weight of the droplet into account. The drop shape is determined by its spreading coefficient S,

$$S = \gamma_{\text{SV}} - \gamma_{\text{SL}} - \gamma \tag{1.2}$$

A Partial wetting $S < 0$

B Total wetting $S \geq 0$

Figure 1.2 – A small drop is deposited on a planar surface and depending on the spreading coefficient S, it either adopts a spherical cap shape (as in **A** where $S < 0$) or it completely spreads and covers the surface (as in **B** where $S \geq 0$).

where γ_{SL}, γ_{SV} and γ respectively denote the solid-liquid, solid-vapor and liquid-vapor interface energies.

Partial wetting $S < 0$

In this case, the drop only wets the surface partially and adopts a spherical cap shape on the planar surface (Figure 1.2-A). The angle displayed between the drop and the substrate, called the equilibrium contact angle θ_Y, strongly depends on the physico-chemical properties of both the liquid and the solid and is given by Young-Dupré's relation:

$$\gamma_{SV} - \gamma_{SL} = \gamma \cos \theta_Y \tag{1.3}$$

Total wetting $S \geq 0$

The drop completely covers the solid substrate and loses its spherical 'drop' shape as it becomes flat. This spreading phenomenon can easily be interpreted physically. A given dry area A of the solid planar substrate possesses an energy $E_{dry} = A\gamma_{SV}$, whereas when it is wet (covered by a layer of liquid), its energy is $E_{wet} = A(\gamma_{SL} + \gamma)$. Since $\gamma_{SV} > \gamma + \gamma_{SL}$, the system always has a higher energy when the area A is dry than when it is wet. Therefore, if liquid is available, it always tends to cover the surface in order to lower the global interface energy of the system.

An every day illustration of a positive spreading coefficient S can be found in one's kitchen. Since vegetable oils display a positive spreading coefficient on most surfaces such as glass of PET-plastics, the accidental deposition of a small droplet on such a surface will lead to the complete covering of it. This explains why oil bottles are sometimes covered with a thin oil layer whereas this is not the case for water bottles. Indeed, since water has a negative spreading coefficient on common surfaces, a water drop does not spread on a surface but remains localized.

1.3 Drop on a cylindrical fiber

Liquid droplets sitting on fibers can be encountered on a daily basis. And may it be on a garden spider web in the morning, on the wires of a fence on a rainy day or even on wet hair, the harmonious shapes they adopt never cease to amaze us. But careful attention to these geometries provide more than satisfaction as they can also provide useful information on the physical properties of the drop or the fiber. However, to gain access to these properties with a mere observation, we must first shed light on the mechanics governing the equilibrium shapes adopted by liquid droplets when sitting on fibers. As simple as this system appears, its underlying mechanics are complex and have therefore been the subject of numerous studies in the past.

As an example, Figure 1.3, reproduced from Lorenceau et al. (2004), presents a set of silicone oil drops of different sizes sitting on a thin nylon fiber (12 μm radius). This simple configuration allows us to introduce the key physical parameters of the system:

○ a is the fiber radius. The fibers will here have radii ranging from few microns to few millimeters.

○ R is the effective radius of the droplet given by $R = \left(3\Omega/(4\pi)\right)^{1/3}$ where Ω denotes its volume. Considering the effective radius of a drop instead of its volume may sometimes seem counterintuitive, but it allows to directly appreciate its characteristic size (millimeters are easier to apprehend that microliters). The drops will here have effective radii ranging from tens of microns to few millimeters.

○ ρg is the specific weight of the droplet. The constant earth acceleration g is taken at 9.81 m/s^2. Water and the silicone oil density are respectively $\rho = 1000$ and 960 kg/m^3.

○ γ_{SL}, γ_{SV} and γ respectively denote the solid-liquid, solid-vapor and liquid-vapor interface energies. The equilibrium contact angle θ_{Y} between the liquid drop and the fiber is given by the Young-Dupré relation: $\gamma_{\mathrm{SV}} - \gamma_{\mathrm{SL}} = \gamma \cos\theta_{\mathrm{Y}}$. Water and silicone oil interface energies are respectively $\gamma = 72$ and 21 mJ/m^2 and their respective equilibrium contact angles with substrates strongly depend on the nature of the substrates. However, it should be mentioned silicone oil often exhibits a zero contact angle with usual materials.
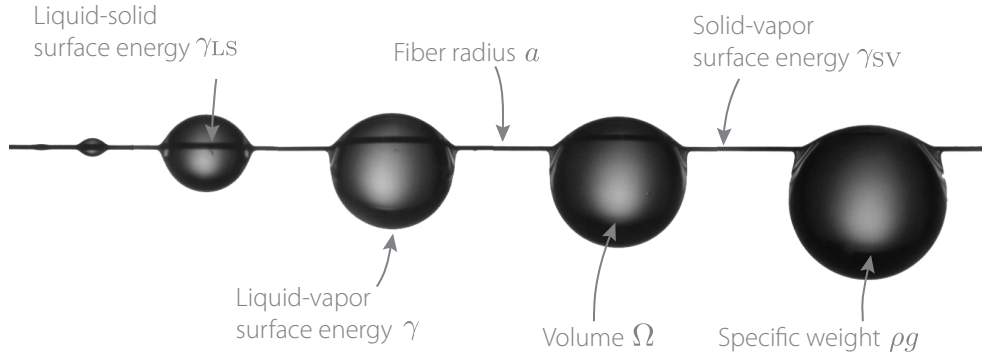
Figure 1.3 – Drops of silicone oil of various volumes ($\Omega = 0.01, 0.10, 0.23, 0.32$ and 0.52 mm^3 from left to right) hanging from a horizontal nylon fiber of radius $a = 12$ μm. Reproduced from Lorenceau et al. (2004).

Now that the principal physical parameters of the drop-on-a-fiber compound have been unraveled, we take a closer look at the droplets sitting on a fiber in Figure 1.3. First of all, interestingly, if the same silicone oil droplets (here deposited on a **cylindrical** fiber) were deposited on a **planar** surface made of the same material as the fiber (nylon), they would spread and rapidly cover the whole surface, thus becoming flat and losing their 'drop' shape. Indeed, silicone oil drops exhibit a zero contact angle with nylon ($\theta_{\mathrm{Y}} = 0$) and therefore spread out on a flat surface (the spreading coefficient S presented in the previous section is positive for silicone oil on nylon). One would expect for the silicone oil drops to behave similarly when deposited on the nylon fiber and spread and cover the whole cylindrical surface of the fiber rapidly. However, this expected scenario where the drop would macroscopically vanish and turn into a liquid 'sleeve' does not take place, the drops remain localized and retain a quasi-spherical shape except locally where the drop surface crosses the fiber (contact line).

Another noteworthy feature of Figure 1.3 is that the shapes adopted by drops strongly depend on their size. Smaller drops have elongated shapes, rather aligned with the fiber's axis, while larger ones are more spherical and shift downwards as they grow (their gravity center lowers as they become larger). Intuitively, this last point makes sense, a drop's weight gains importance as it grows and therefore applies a stronger pulling force, consequently lowering its gravity center. However, little or no intuition explains the fact that smaller drops adopt elongated shapes while larger ones favor sphericity.

And finally, could a sixth, larger drop, be deposited on the fiber? Would it stay, or would it

fall off?

Our observation of five silicone oil droplets sitting on a nylon fiber raises three central questions:

○ What is the equilibrium shape selected by a drop on a fiber?
○ What are the forces acting on the droplet, and how do they affect its shape?
○ What is the size of the largest drop that can sit on a fiber?

The principal past studies addressing these three questions, along with new contributions, will be presented in the following sections.

Throughout this Chapter, the pertinent parameter arrangements used to manipulate the droplets are:

○ $r = R/a$ is the dimensionless effective radius of the drop.
○ $R\kappa$ is the drop radius to capillary length ratio where $\kappa^{-1} = \sqrt{\gamma/\rho g}$ is the gravito-capillary length (also called the capillary length).
○ $w = W/(2\pi a\gamma \cos\theta_Y) = \frac{2}{3}(R\kappa)^3 (a\kappa \cos\theta_Y)^{-1}$ is the dimensionless weight of the drop. The weight of the drop W is given by $W = \rho g\Omega$. It will be shown that the normalizing force $F_{\gamma x} = 2\pi a\gamma \cos\theta_Y$ corresponds to the capillary horizontal force applied by the fiber on the droplet at one meniscus.

Depositing a drop on a fiber is an easy experiment to perform in the laboratory. However, this experiment does not provide some key information about the system. For example, it is complicated (if not impossible) to measure the internal pressure of the drop or the forces applied by the fiber on the drop. In order to fill this gap, we turn to the numerical simulation of liquid droplets on a fiber using the surface-energy minimization software Surface Evolver, which is described in Appendix A.

1.4 Droplet on a fiber in the absence of gravity

We first study the shape that a drop adopts on a fiber without considering the effect of gravity. Although gravity can never be turned off in the lab, this assumption is reasonable for small enough drops for which surface tension forces largely overcome gravity forces. It will further be shown that for this hypothesis to be verified, the effective radius of the drop needs to satisfy $R\kappa \ll (a\kappa \cos\theta_Y)^{1/3}$. We focus on the most common case where the spreading coefficient is negative ($S \leq 0$) and study the behavior of the droplet on fiber depending on its contact angle and its size.

1.4.1 Barrel configuration

The axially symmetric shape adopted by a droplet on a fiber, i.e. when the drop wraps around the fiber, is often referred to as the barrel configuration. Since the pressure inside the drop is uniform, its shape can be calculated using the Laplace pressure jump relation, depicted in Equation (1.1). For a given contact angle θ_Y, the analytical expression of the axially symmetric drop profile was first introduced by B. J. Carroll in Carroll (1976). This result gives access to important physical quantities such as the wet length, the volume, or the pressure inside the drop. Figure 1.4 presents the analytical profile, solution of Equation (1.1) for $\theta_Y = 60º$ and $r = 10$ and the corresponding numerical simulation for the same physical parameters, performed with Surface Evolver.

We briefly introduce the results presented in Carroll (1976) where the aim is to provide a mathematical description of the profile y of the drop along the fiber axis x. The solved

equation corresponds to the Laplace law, ensuring that the pressure is constant inside the drop (constant pressure jump ΔP), Equation (1.1) is written:

$$\frac{1}{R_1} + \frac{1}{R_2} = K. \tag{1.4}$$

A Analytical solution (Carroll 1976)   **B** Numerical solution (Surface Evolver)
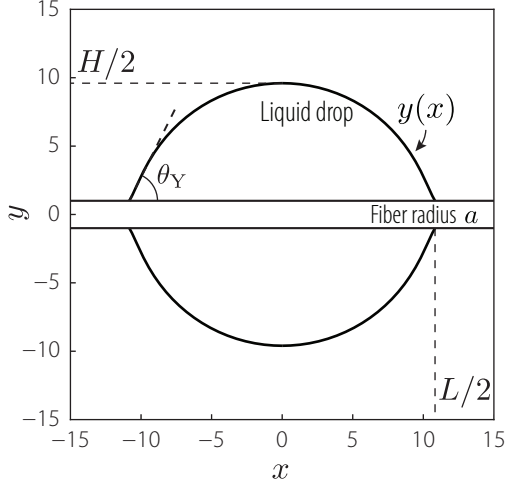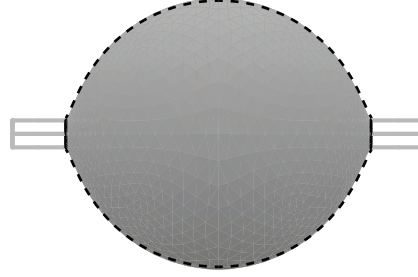
Figure 1.4 – **A** – Solution of Equation (1.1) introduced in Carroll (1976) for $\theta_Y = 60°$ and $r = 10$ (provided in Equation (1.5)). **B** – Under the same conditions, a numerically computed droplet, using Surface Evolver. The dashed lines correspond to the theoretical prediction presented in **A**.

The profile of the drop on the fiber corresponds to an unduloid and is provided implicitly:

$$x(y) = \pm \left[acF\left(\varphi(y), k\right) + hE\left(\varphi(y), k\right) \right] \tag{1.5}$$

where $F(\varphi, k)$ and $E(\varphi, k)$ are respectively the incomplete elliptic integrals of first and second kind. The geometrical parameter c is defined as:

$$c = \frac{H \cos\theta_Y - a}{H - a \cos\theta_Y}. \tag{1.6}$$

k and φ are given respectively by the relations:

$$k^2 = \frac{H^2 - a^2 c^2}{H^2} \qquad \text{and} \qquad y^2 = H^2(1 - k^2 \sin^2\varphi). \tag{1.7}$$

For this simple case (Figure 1.4), the numerically calculated drop shape shows excellent agreement with Carroll's analytical shape prediction. In order to further validate the numerical results provided by Surface Evolver, two key geometrical and physical parameters are compared between theory and numerical simulations for drops of different volumes and exhibiting different contact angles with the fiber in Figure 1.5.

1.4.2 Zero spreading coefficient $S = 0$

As discussed earlier, a drop with zero spreading coefficient (corresponding to a zero contact angle $\theta_Y = 0$) sitting on a fiber behaves counterintuitively; one would expect for it to spread all over the fiber, just as it would on a planar surface. However, a vanishing contact angle between the drop and the fiber is actually not incompatible with a localized drop and is well-captured by Carroll's analytical solution (Equation (1.5)). Indeed, for $\cos\theta_Y = 1$, the parameter c described in Equation (1.6) takes the value $c = 1$ and k and φ remain defined. Although technically possible, manipulating such low contact angles ($\theta_Y < 10°$) when numerically
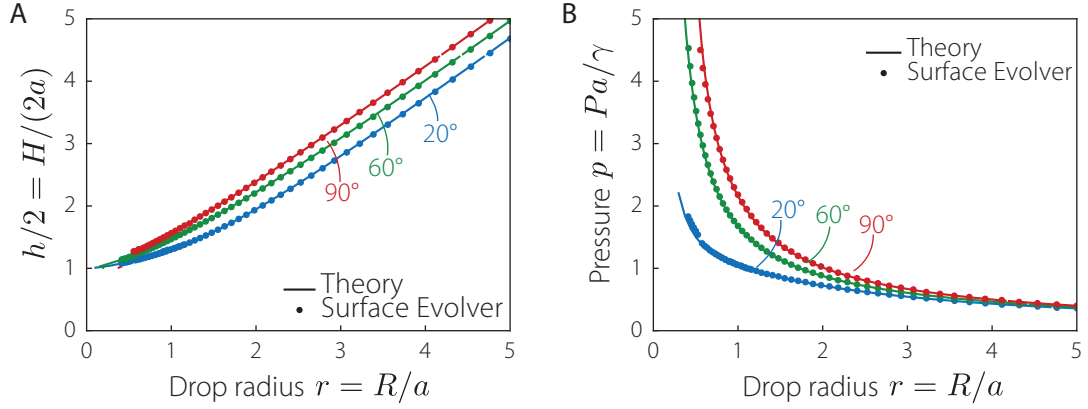
Figure 1.5 – **Analytical and numerical prediction.** **A** – $h/2 = H/2$ vs. dimensionless effective drop radius r for 3 contact angles $\theta_Y = 20°$, $60°$ and $90°$. H corresponds to the drop height, as described in Figure 1.4. **B** – Normalized internal drop pressure vs. dimensionless effective drop radius for the same contact angles. The continuous lines and the dots respectively represent the analytical and numerical solutions.

computing drops on fibers with Surface Evolver is difficult. The menisci of the drop then do not adapt well when the volume of the drop is changed for continuation purposes. Above all, unexpected behaviors are observed when the volume of the drop is decreased, the menisci do no recede as they should. Such an unwanted behavior does not take place when the volume of the drop is increased, the menisci then advance normally, but in order to avoid further doubt concerning the numerical convergence, calculations with Surface Evolver are performed exclusively for contact angles $\theta_Y \geq 20°$.

1.4.3   Barrel to clam-shell transition: the roll-up

In some cases, the archetypal axially symmetrical solution depicted in Carroll (1976) and presented in section 1.4.1, the barrel configuration, is not necessarily the one corresponding to the lowest state of energy. Indeed, if the drop is small or displays a high contact angle with the fiber, it breaks axial symmetry and sits on one side of the fiber. This phenomenon, where the droplet goes from a barrel to a clam-shell configuration is often referred to as the **roll-up** transition and was first observed for detergent applications by N. K. Adam (Adam 1937).
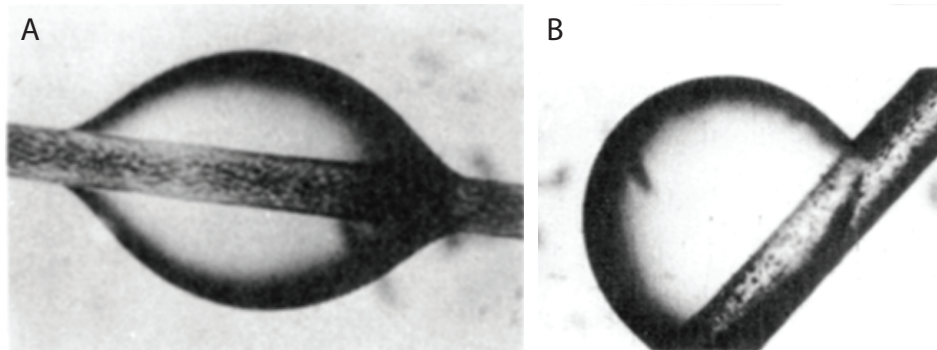
Figure 1.6 – **Barrel-to-clam-shell transition: the roll-up.** **A** – Droplet sitting on a fiber in an axially symmetric barrel configuration. **B** – For a lower contact angle, the axially symmetric equilibrium is no longer stable and the system adopts a clam-shell configuration, where the drop sits on a side of the fiber. Reproduced from Carroll (1986).

The condition for roll-up is not trivial and a stability interpretation was first proposed by Carroll (Carroll 1986) where he considered a small shape perturbation and quantified the difference in pressure it generates. According to this article, a positive pressure change is responsible for the perturbation to grow, and thus attests the instability of the barrel configuration. His calculations led to a criterion depending on the size of the droplet (here represented by $h = H/a$, where H corresponds to the height of the droplet, as described in Figure 1.4) and the contact angle θ_Y between the drop and the fiber. The proposed condition for roll-up reads:

$$2h^3 \cos\theta_Y - 3h^2 + 1 > 0. \tag{1.8}$$

Although it gives insight into the physics at play concerning the roll-up, his prediction matched experimental data poorly; a reproduction of the experimental results compared to the theoretical prediction is presented in Figure 1.7.
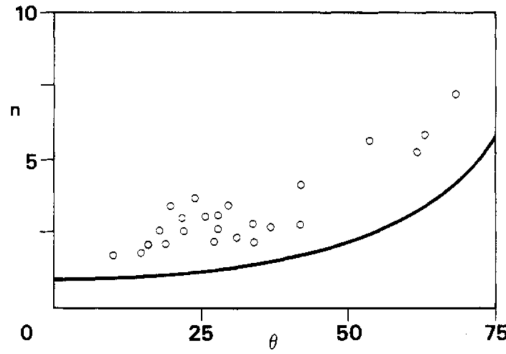
Figure 1.7 – Limit between stable and unstable barrels configurations. Prediction by Caroll (continuous line) and corresponding experimental data. Reproduced from Carroll (1986). In this paper, n corresponds to our h and θ to our θ_Y.

McHale and collaborators proposed another geometrical criterion for roll-up in McHale et al. (1997). In this work, the authors conjectured that whenever the drop exhibits an inflexion point in its profile (in the barrel configuration), it is stable. On the other hand, if no inflexion point is observed, the barrel configuration does not correspond to a local minimum in energy, and it then rolls up to the clam-shell configuration. The limit therefore corresponds to a drop profile for which the inflexion point is on the triple line and they showed that this condition (for roll-up to take place) reads:

$$h < \frac{1 + \sin\theta_Y}{\cos\theta_Y} \tag{1.9}$$

In a subsequent work, using Surface Evolver, McHale and Newton (McHale and Newton 2002) numerically evolved drops sitting on fibers in the clam-shell configuration and calculated their total interface energy. By comparing this energy to the energy of a drop sitting on fiber in the barrel configuration, they were able to add a phase to the (h, θ_Y) diagram where the clam-shell configuration would have a lower energy than the axially symmetric barrel configuration, for a same drop volume. Finally, in 2011, Tung-He Chou and collaborators (Chou et al. 2011) furnished the entire phase diagram by evolving drops on fibers of different volumes $\Omega^{1/3}/a$ in the barrel and clam-shell configuration and probing their stability. This phase diagram is reproduced in Figure 1.8.

In order to assess the stability of the barrel configuration, T. H. Chou and collaborators (see Figure 1.8) evolved drops using the gradient descent tool provided by Surface Evolver. The fact that a drop (initiated in an axially symmetric shape) tends to break this symmetry to end up sitting on the side of the fiber when descending energy gradients clearly shows its instability. However, Surface Evolver also provides another powerful tool to determine the stability of a given conformation: the Hessian (see Appendix A). Indeed, instead of
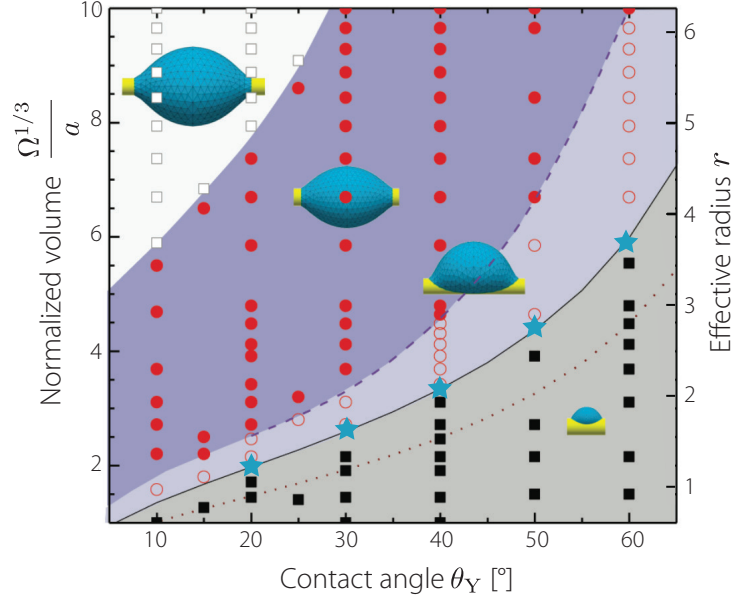
Figure 1.8 – **Barrel and clam-shell configurations' stability in the $(\theta_Y, \Omega^{1/3}/a)$ phase diagram in the absence of gravity**. The full and hollow squares respectively denote clam-shell only and barrel only. The red hollow and full circles show coexistence of both states with lower energy for clam-shell and barrel, respectively. The dotted line describes the roll-up condition proposed by Carroll in 1976 (Carroll 1976), described by Equation (1.8), the continuous line shows the 'inflexion point' condition (McHale et al. 1997) characterized by Equation (1.9) and finally, the dashed line depicts the limit calculated in McHale and Newton (2002) for a clam-shell configuration of lower energy than its barrel-like counterpart. The blue stars were calculated in the present work and correspond to the stability limit of the barrel configuration, using Surface Evolver's powerful Hessian method, in good agreement with T. H. Chou and collaborators. This graph, except for the blue stars, was reproduced from Chou et al. (2011).

descending gradients, this tool seeks for the closest state where the energy gradient's components vanish. In other words, the Hessian method seeks equilibrium states, independent of their stability. The method can give access to the eigenvalues of the corresponding Hessian matrix and is therefore capable of assessing the stability of a solution (if the Hessian matrix has one or more negative eigenvalues, the described state does not correspond to a local energy minimum, and the equilibrium is not stable). This method was validated in the present work by comparing the stability prediction given by Chou et al. (2011) and the ones provided by the Hessian method of Surface Evolver.

1.5 How gravity shapes the drop

When a drop is subjected to gravity, it tends to sag in order to lower its gravity center and the analytical calculation of its shape on a fiber then becomes complicated because the system no longer displays axial symmetry. Using simplified models and Surface Evolver, we propose tools to predict the shape adopted by a drop subjected to its own weight when hanging on a straight horizontal cylindrical fiber.

1.5.1 Wetting drops: the hanging barrel

As shown in the previous section, wetting drops on fiber adopt an axially symmetric undoloid shape in the absence of gravity. This approximation can reasonably be made for small droplets, for which capillary effects dominate on their gravitational counterpart.

Conversely, larger wetting drops, although not necessarily jumping from a barrel to a clam-shell configuration, break symmetry because their weight pulls them downward. Here, making the assumption that the drop is spherical, we study the forces acting on the drop and how they influence the shape it adopts.

First analytical model

Figure 1.9 shows a schematic representation of a liquid spherical drop sitting on a cylindrical fiber. Our aim is to predict at which height the drop naturally hangs, this value is represented by the height of its gravity center C. In the absence of gravity, the point C would be aligned with the fiber axis, corresponding to the axially symmetric configuration discussed in the previous section.
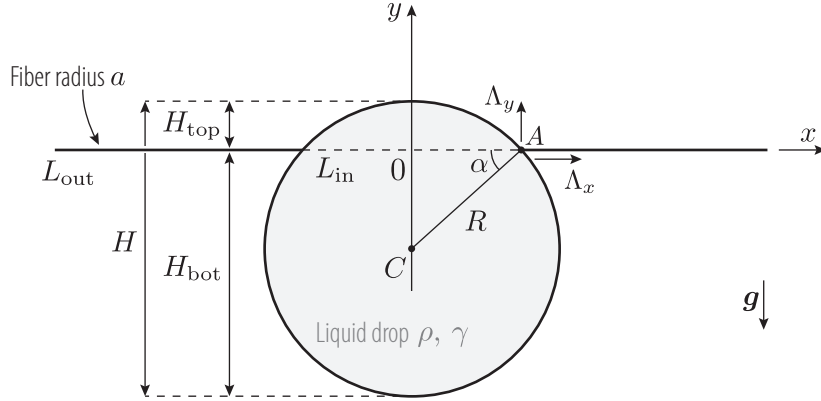
Figure 1.9 – Schematic representation of a spherical drop (radius R) sitting on a cylindrical fiber or radius a.

Now that gravity is no longer neglected, the system favorably decreases its gravitational energy as the drop is lowered. However, lowering the drop also decreases the wet length L_{in} (length between the two menisci) and since we are considering wetting droplets (low contact angle θ_Y), this increases the global interfacial energy of the system. The drop therefore naturally selects a trade-off height in order to **minimize the sum of gravitational and interfacial energies**. To formally characterize this height y_C, we write the total energy of the system:

$$\mathcal{V} = W y_C + 2\pi a \left(L_{out} \gamma_{SV} + L_{in} \gamma_{SL} \right) + 4\pi R^2 \gamma \tag{1.10}$$

where the weight of the drop is $W = \frac{4}{3} \pi \rho g R^3$. Since the fiber has a fixed total length L, we write $L_{out} = L - L_{in}$ and use $L_{in} = 2x_A$ (x_A corresponds to the x-coordinate of the right meniscus, see Figure 1.9):

$$\mathcal{V} = W y_C - 4\pi a x_A \left(\gamma_{SV} - \gamma_{SL} \right) + 2\pi a L \gamma_{SV} + 4\pi R^2 \gamma. \tag{1.11}$$

Moreover, taking advantage of left-right symmetry, we only focus on the right half of the droplet. The constant terms $2\pi a L \gamma_{SV}$ and $4\pi R^2 \gamma$ are discarded as they will not affect energy minimization. The energy of this half droplet then reads:

$$\mathcal{V} = \frac{W}{2} y_C - 2\pi a x_A \gamma \cos \theta_Y \tag{1.12}$$

where Young Dupré's relation $\gamma_{SV} - \gamma_{SL} = \gamma \cos \theta_Y$ was used. As the drop is assumed to be spherical, we write the geometric constraints on the system as follows:

$$x_A = R \cos \alpha \tag{1.13a}$$
$$0 = y_C + R \sin \alpha \tag{1.13b}$$

Introducing the corresponding Lagrange multipliers Λ_x and Λ_y, we consider the Lagrangian

$\mathcal{L} = \mathcal{L}(y_C, x_A, \alpha)$:

$$\mathcal{L} = \frac{W}{2}y_C + 2\pi x_A \gamma \cos\theta_Y - \Lambda_x (R\cos\alpha - x_A) - \Lambda_y(y_C + R\sin\alpha) \tag{1.14}$$

The equilibrium of the system reads $(\partial\mathcal{L}/\partial y_C, \partial\mathcal{L}/\partial x_A, \partial\mathcal{L}/\partial\alpha) = \mathbf{0}$, which leads to:

$$\partial\mathcal{L}/\partial y_C = 0 \quad \Rightarrow \quad \Lambda_y = \frac{W}{2} \tag{1.15}$$

$$\partial\mathcal{L}/\partial x_A = 0 \quad \Rightarrow \quad \Lambda_x = 2\pi a\gamma \cos\theta_Y \tag{1.16}$$

$$\partial\mathcal{L}/\partial\alpha = 0 \quad \Rightarrow \quad \tan\alpha = \frac{\Lambda_y}{\Lambda_x} = \frac{W/2}{2\pi a\gamma\cos\theta_Y} = \frac{w}{2}. \tag{1.17}$$

A similar expression as Equation (1.17) had been presented previously in Lorenceau et al. (2004) for small angles α where the expression $\sin\alpha = \Lambda_y/\Lambda_x$ was proposed. The Lagrange multipliers Λ_x and Λ_y can respectively be interpreted as the horizontal and vertical reaction force applied at the meniscus A. We therefore define $\boldsymbol{F}$ as the force applied by the fiber on the drop at the right meniscus:

$$\boldsymbol{F} = \begin{pmatrix} F_x \\ F_y \end{pmatrix} = \begin{pmatrix} \Lambda_x \\ \Lambda_y \end{pmatrix} \tag{1.18}$$

Interestingly enough, the horizontal reaction force F_x does not depend on the drop size nor on the sagging angle α; whichever the weight of the drop, the fiber applies a force F_x pulling on the drop to the right with:

$$F_x = 2\pi a\gamma \cos\theta_Y. \tag{1.19}$$

The left-right symmetry indicates that a similar force acts on the drop at its left meniscus, pulling the drop with same intensity to the left. On the other hand, the vertical reaction force F_y greatly depends on the weight of the drop. Indeed, each meniscus supports half of the weight of the drop:

$$F_y = \frac{W}{2}. \tag{1.20}$$

In its dimensionless form, $\boldsymbol{F}$ is written:

$$\boldsymbol{f} = \frac{\boldsymbol{F}}{2\pi a\gamma\cos\theta_Y} = \begin{pmatrix} f_x \\ f_y \end{pmatrix} = \begin{pmatrix} 1 \\ w/2 \end{pmatrix}. \tag{1.21}$$

We finally introduce a dimensionless eccentricity parameter

$$e = \frac{H_{\text{bot}} - H_{\text{top}}}{H} \tag{1.22}$$

with $H = (H_{\text{bot}} + H_{\text{top}})$ as described in Figure 1.9. This eccentricity e quantifies the sagging of the droplet due to its own weight and it is positive when the drop hangs downwards. Note that for a perfectly spherical drop, the eccentricity is:

$$e = -y_C/R \tag{1.23}$$

and it takes the value $e = 0$ when the drop displays an axially symmetric configuration and $e = 1$ when the drop's upper boundary is tangent to the fiber. Using Equations (1.13b) and (1.17), we express e as

$$e = \sin\alpha = \sin\left(\arctan\left(\frac{w}{2}\right)\right) \tag{1.24}$$

Note that the eccentricity is very small for a small dimensionless drop weight $w \ll 1$. In this case, the drop's gravity center is almost aligned with the fiber's axis and the drop shape is comparable to the axially symmetric barrel configuration discussed in the previous section.

The condition for a negligible weight of the drop therefore is given by $R\kappa \ll (a\kappa\cos\theta_Y)^{1/3}$ from Equation (1.17). The present model provides physical insight into the geometry and forces at stake in this problem and could be of interest in the field of metrology. Indeed, Equation (1.24) may allow to determine otherwise hard to capture physical and geometrical parameters in micronic systems, such as the surface tension of the liquid or the radius of the fiber. However, strong hypotheses are made, and this model therefore needs to be verified.

Theoretical prediction versus Surface Evolver

The shape adopted by drops subjected to gravity was numerically computed with Surface Evolver. It seems natural to assume that the force $\boldsymbol{F}$ applied by the fiber on the drop at the right meniscus is of capillary origin and in order to test our model, we therefore compare $\boldsymbol{F}$ with the capillary force of the fiber on the drop computed at the right meniscus using Surface Evolver. This numerical force $\boldsymbol{F}_{\gamma,\text{SE}}$ and its dimensionless form $\boldsymbol{f}_{\gamma,\text{SE}}$ are respectively given by:

$$\boldsymbol{F}_{\gamma,\text{SE}} = \begin{pmatrix} F_{\gamma x,\text{SE}} \\ F_{\gamma y,\text{SE}} \end{pmatrix} \quad \text{and} \quad \boldsymbol{f}_{\gamma,\text{SE}} = \boldsymbol{F}_{\gamma,\text{SE}}/\left(2\pi a\gamma\cos\theta_Y\right) = \begin{pmatrix} f_{\gamma x,\text{SE}} \\ f_{\gamma y,\text{SE}} \end{pmatrix}. \tag{1.25}$$

The relations in Equations (1.21) and (1.24) are tested for different conditions and the numerical results are shown in Figure 1.10 for a large drop ($r = 100$) of varying weight (the drop radius is fixed and its density is changed). For this drop size, the predicted forces F_x and F_y as well as the eccentricity e predicted by theory are in excellent agreement with the numerical results provided by Surface Evolver.
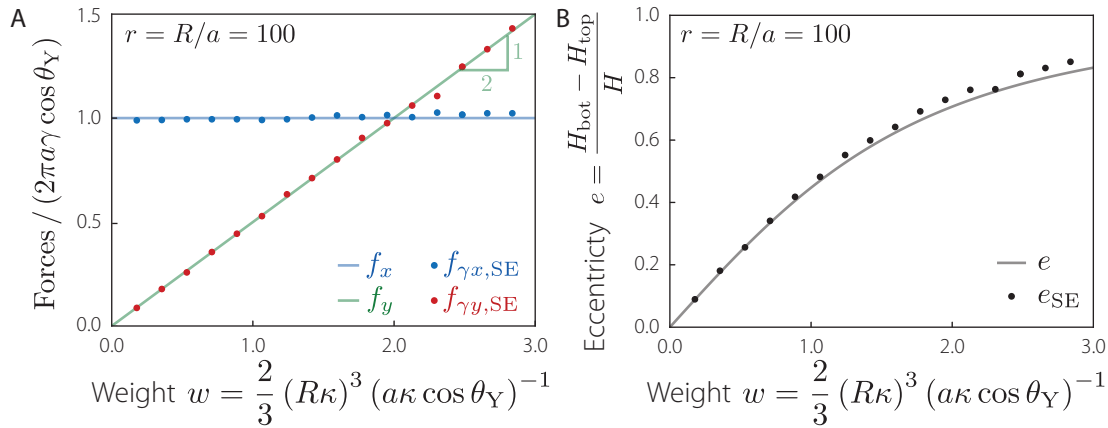
Figure 1.10 – Large drop on a fiber: forces and forms. A – Forces applied by the fiber on the drop at the right meniscus. The blue and red dots respectively correspond to the horizontal and vertical component of the **capillary** force applied by the fiber on the drop at the right meniscus calculated with Surface Evolver. The blue and green continuous lines show the theoretical predictions proposed in Equation (1.21). **B** – Eccentricity e of the drop as a function of the drop's dimensionless weight. The black dots correspond to the numerical Surface Evolver results and the continuous line to the theoretical prediction provided in Equation (1.24). In these numerical experiments, a drop radius was first fixed (here $r = 100$) and κ was then varied to generate different drop weights (the weight w could also be written $w = W/(2\pi a\gamma\cos\theta_Y)$). The numerical results and theory are in good agreement. We use $\theta_Y = 20°$ both for theory and numerical calculations.

1.5.2   Limitations and adaptation of the model for smaller drops

The aforementioned model is in good agreement with the numerical results provided by Surface Evolver for a large drop (*e.g.* of dimensionless radius $r = 100$); the dimensionless

horizontal and vertical forces applied by the fiber on the drop at the right meniscus (respectively f_x and f_y) are well captured by Equation (1.21) and so is the eccentricity e (Equation (1.24)). Our model was also tested for smaller drops ($r = 30$ and $r = 60$) and Figure 1.11 shows the same results as in Figure 1.10 for $r = 30$. Although f_x remains well captured by the model (we find $f_x = f_{\gamma x,\mathrm{SE}} = 1$), the vertical meniscus force $f_{\gamma y,\mathrm{SE}}$ computed with Surface Evolver does not correspond to our theoretical prediction f_y. The eccentricity e_{SE} also presents a difference with the theoretical prediction.

Figure 1.11 – **Smaller drop on a fiber: forms and forces. A** – As in Figure 1.10, the blue and red dots respectively correspond to 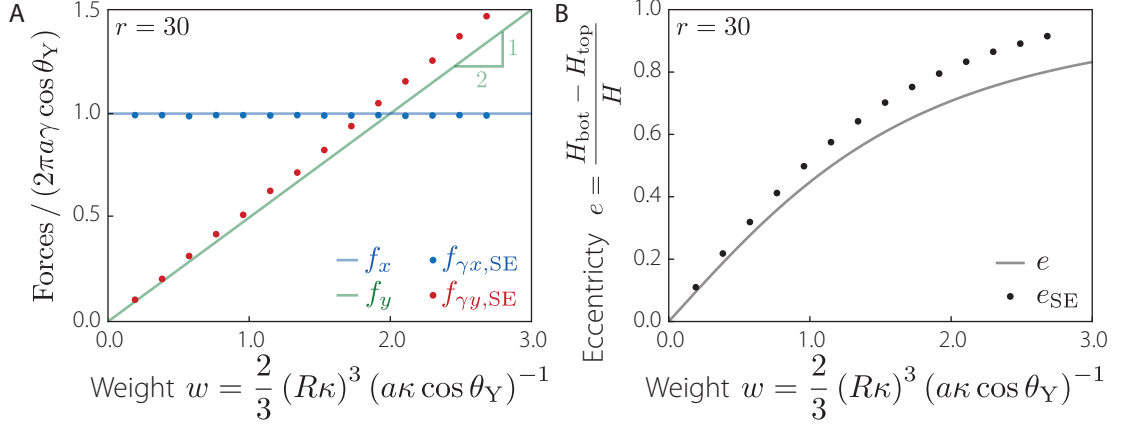the horizontal and vertical component of the capillary force applied by the fiber on the drop at the right meniscus calculated with Surface Evolver. The blue and green continuous lines show the theoretical predictions depicted in Equation (1.21). The theoretical vertical force $f_y = w/2$ is not well captured by only the capillary force $f_{\gamma y,\mathrm{SE}}$ computed with Surface Evolver. **B** – Eccentricity e versus dimensionless weight w. The black dots correspond to the numerical Surface Evolver results and the continuous line to the prediction in Equation (1.24). The eccentricity is not captured well by the model which will therefore be refined in this section. Here, the drop size is $r = 30$ and the contact angle is $\theta_Y = 20^{\mathrm{o}}$.

In order to improve the match between numerical results and theory, we rethink the way the fiber applies a force on the drop and adapt the drop's geometry to predict the eccentricity e correctly.

Pressure force
Only the capillary vertical force $f_{\gamma y,\mathrm{SE}}$ computed with Surface Evolver was previously compared to the theoretical vertical force f_y applied by the fiber in the right meniscus region. However, pressure forces can also act on the drop and f_y therefore may not **only** be of capillary nature. The net pressure force applied by the fiber on the drop is easily computed with Surface Evolver but in order to evaluate this force theoretically, we consider the drop-on-a-fiber system presented in Figure 1.12. First, we approximate the internal drop pressure P as:

$$P = \frac{2\gamma}{R}. \tag{1.26}$$

The geometry of the problem gives (with $\alpha_1 = \alpha + \frac{\delta\alpha}{2}$ and $\alpha_2 = \alpha - \frac{\delta\alpha}{2}$)

$$l_1 = R\cos\left(\alpha + \frac{\delta\alpha}{2}\right); \quad l_2 = R\cos\left(\alpha - \frac{\delta\alpha}{2}\right). \tag{1.27}$$

The angle α is known from Equation (1.17) and in order to determine $\delta\alpha$, we use:

$$2a = R\left(\sin\left(\alpha + \frac{\delta\alpha}{2}\right) - \sin\left(\alpha - \frac{\delta\alpha}{2}\right)\right) \tag{1.28}$$
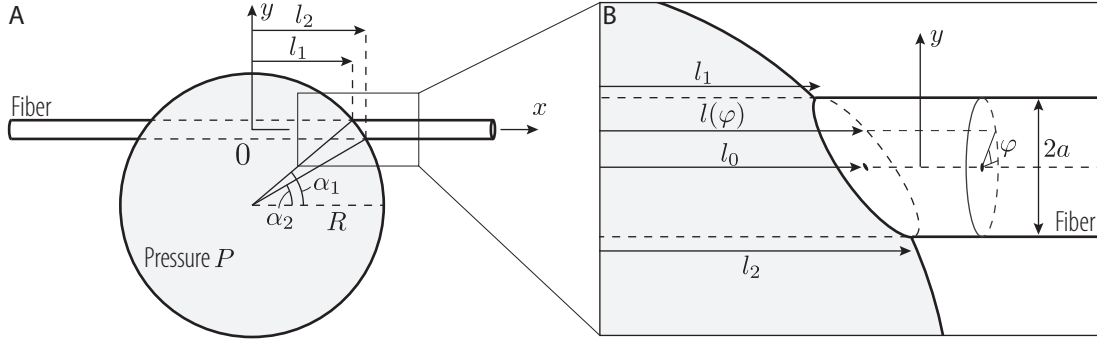
Figure 1.12 – Geometrical characterization of the triple line. A. Global schematic representation of the drop sitting on the fiber. The angles α_1 and α_2 respectively describe the top and bottom limit of the meniscus. **B.** Close-up on the meniscus and its relevant geometrical parameters. Note that the contact angle θ_Y is not taken into account for the determination of the meniscus geometry in this part.

which, for a small $\delta\alpha$, gives

$$\delta\alpha = \frac{2a}{R}\frac{1}{\cos\alpha}. \tag{1.29}$$

Moreover, considering a meniscus profile linear with y, i.e. $l(y) = l_0 + \Delta l\, y/a$ where $\Delta l = l_1 - l_2$, and introducing the variable φ such that $y = a\sin\varphi$, we finally have a meniscus profile given by $l(\varphi) = l_0 + \Delta l\sin\varphi$. The pressure force $\boldsymbol{F}_P$ applied by the fiber on the drop is written

$$\boldsymbol{F}_P = \int_0^{2\pi} P\, l(\varphi)\, a\, \boldsymbol{n}(\varphi)\, \mathrm{d}\varphi = \begin{pmatrix} F_{Px} \\ F_{Py} \\ F_{Pz} \end{pmatrix} \tag{1.30}$$

where $\boldsymbol{n}$ corresponds to the unitary vector normal to the fiber's surface:

$$\boldsymbol{n}(\varphi) = \begin{pmatrix} 0 \\ \sin\varphi \\ \cos\varphi \end{pmatrix}. \tag{1.31}$$

The vertical component of the pressure force F_{Py} is

$$F_{Py} = \int_0^{2\pi} Pl(\varphi)\sin\varphi\, a\, \mathrm{d}\varphi \tag{1.32}$$

which can be integrated and again, considering $\delta\alpha$ is small, we write $\Delta l = R\delta\alpha\sin\alpha$ and finally obtain:

$$F_{Py} = -4\pi\frac{\gamma}{R}a^2\tan\alpha \tag{1.33}$$

which, in dimensionless terms (normalizing forces by $2\pi a\gamma\cos\theta_Y$), reads:

$$f_{Py} = \frac{F_{Py}}{2\pi a\gamma\cos\theta_Y} = -\frac{2\tan\alpha}{r\cos\theta_Y} = -\frac{w}{r\cos\theta_Y}. \tag{1.34}$$

Note that this pressure force f_{Py} is localized near the drop's meniscus because the vertical pressure forces only do not compensate at this location. It is directed in the opposite direction of $f_{\gamma y}$; the drop's own pressure pushes it downwards. The horizontal component of the pressure along the x-axis, f_{Px} is zero because the component of $\boldsymbol{n}$ is zero along x. The other horizontal component of the pressure force, along z, f_{Pz}, is also zero because of the front-rear symmetry of the system. The vertical force applied by the fiber on the drop

f_y is given by the sum of the vertical capillary and pressure forces:

$$f_y = f_{\gamma y} + f_{Py} = \frac{w}{2}. \tag{1.35}$$

We finally write the theoretical vertical capillary force applied by the fiber on the drop:

$$f_{\gamma y} = \frac{w}{2} - f_{Py}. \tag{1.36}$$

The comparison between theory and numerical results, in good agreement, is presented in Figure 1.15-A&B with drop radii $r = 30$ and 60, with $\theta_Y = 20°$. A schematic representation of the forces is presented in Figure 1.13.
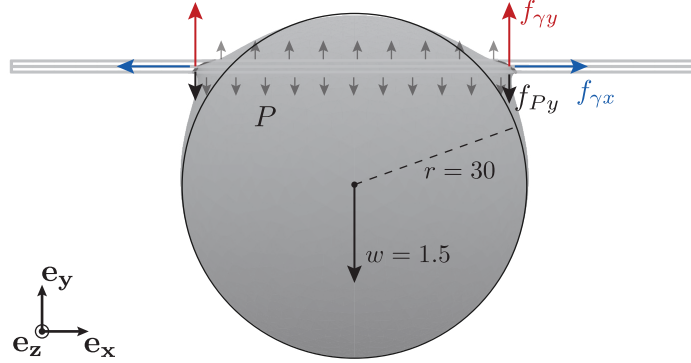

Figure 1.13 – Drop on a fiber numerically calculated with Surface Evolver for $r = 30$, $w = 1.5$ and $\theta_Y = 20°$. The forces $f_{\gamma x}$ and $f_{\gamma y}$ represent the horizontal and vertical **capillary** forces the fiber applies to the drop. Because the triple line is inclined, the fiber-droplet surface area is larger under the fiber than above it, this asymmetry generates a net vertical pressure force f_{Py}, pushing the droplet downwards, as expressed in Equation (1.34). The black circle represents a sphere of radius $r = 30$.

Eccentricity and wet length

The eccentricity e of the drop is also not well captured for the new set of drops. Numerically, it shows to be well above the predicted value (i.e. the drop is lower than expected). Here, we try to understand this behavior in order to refine the model.

Although the drops can generally be considered as spherical in the considered conditions (because $R\kappa < 1$), the interaction of the drop with the fiber alters it sphericity, especially near the menisci. Indeed, because we consider low contact angles θ_Y, the drop has to adapt locally at its menisci to join the fiber a low angle and therefore wets the fiber over a non-negligible fiber length. This is made clear in Figure 1.13, where the menisci extend further than the purely spherical prediction. This is also the case for a drop sitting on a fiber in an axially symmetric configuration (i.e. in the absence of gravity). Indeed, in this case, the wet length L (meniscus to meniscus distance), depends on the fiber radius a and the drop's effective radius R:

$$L = 2\left(R + ad(R/a)\right) \tag{1.37}$$

which in its dimensionless form reads (lengths are normalized by the fiber radius a):

$$\frac{l}{2} = r + d(r) \tag{1.38}$$

where $d(R/a) = d(r)$ corresponds to the dimensionless position shift of the meniscus along the fiber and is presented in Figure 1.14, $d(r)$ also depends on θ_Y. Since a wetting meniscus extends further than predicted by the previously presented model, we adapt it and replace

the eccentricity prediction (Equation (1.24)) by

$$e' = \frac{L \sin \alpha}{2R} = \frac{R + ad(R/a)}{R} \sin \alpha = \left(1 + \frac{d(r)}{r}\right) e$$

$$= \left(1 + \frac{d(r)}{r}\right) \sin \left(\arctan\left(\frac{1}{3}(R\kappa)^3 (a\kappa \cos \theta_Y)^{-1}\right)\right). \tag{1.39}$$

The dimensionless extension $d(r)$ is calculated analytically using $l/2 = x(y = a)$ in Equation (1.5). It should be noted that this approach is not a rigorous demonstration. Indeed, the meniscus geometry is complex and we here restrict this complexity to an increased wet length which we derive from the drop's equilibrium shape in the absence of gravity. However, this model provides satisfying agreement with the numerical simulations (see Figure 1.15) and with the experiments (the translation of this theory to real drops on real fibers will be discussed in the next section).
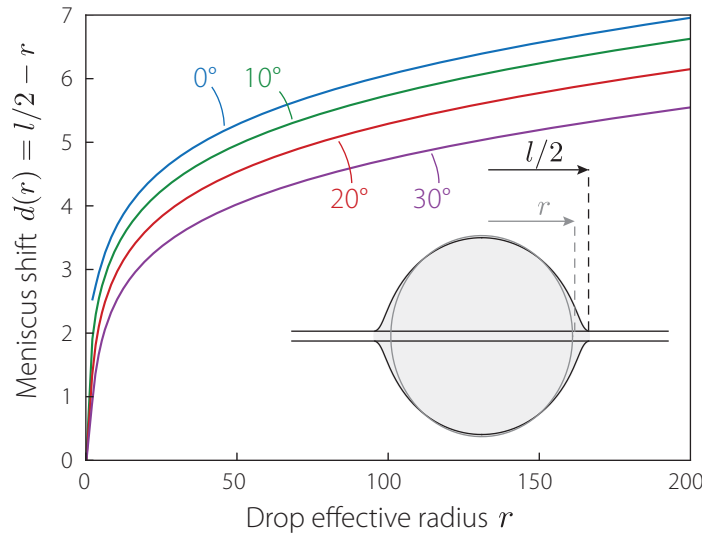
Figure 1.14 – Meniscus axial shift $d(r)$ for different contact angles in the absence of gravity. Because we focus on wetting drops, the results for $\theta_Y = 0°$, $10°$, $20°$ and $30°$ are shown. The inset provides a visualization of an axially symmetrical drop on a fiber for $r = 20$ and $\theta_Y = 20°$. The unduloid shape is obtained from Equation (1.5) and the radius r refers to the dimensionless equivalent radius of this drop.
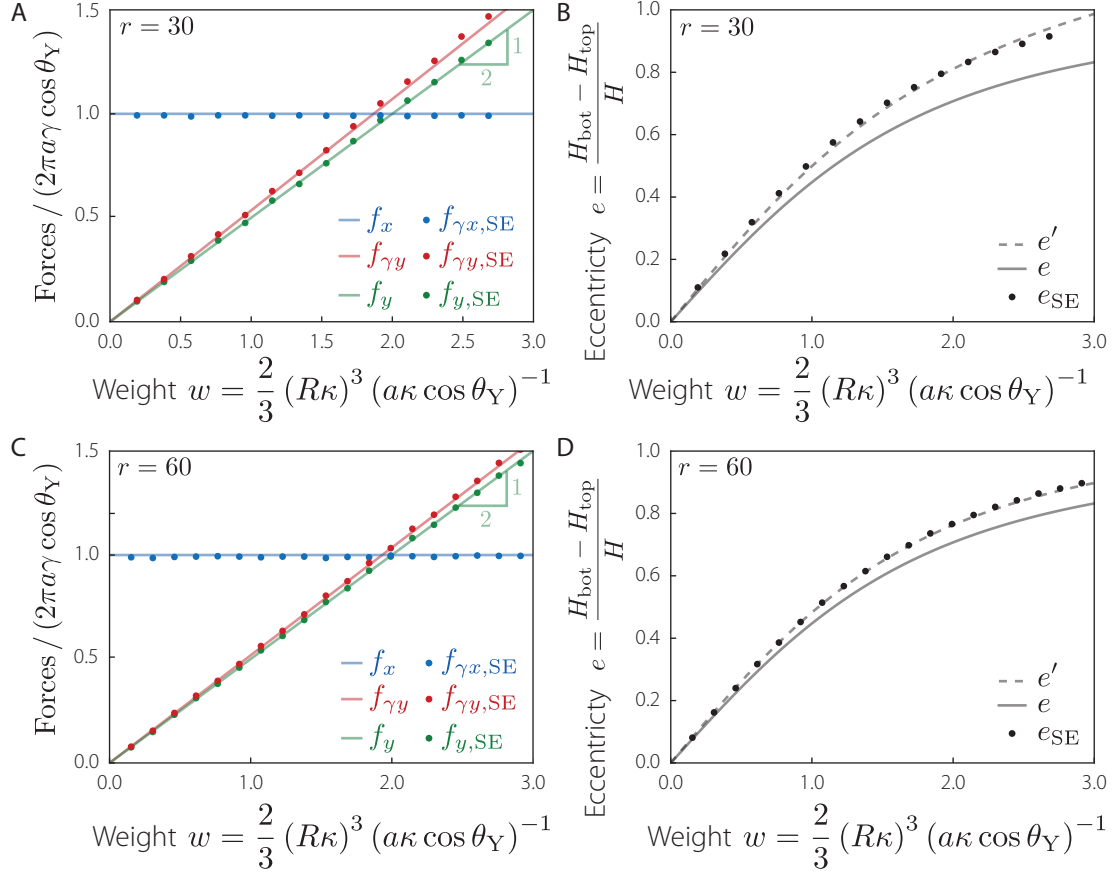
Figure 1.15 – **Smaller drops: forms and forces. A** – Forces applied by the fiber on the drop ($r = 30$) in the right meniscus region. The blue and red dots respectively correspond to the horizontal and vertical component of the **capillary** force applied by the fiber on the drop calculated with Surface Evolver. The green dots, also computed with Surface Evolver, are given by $f_{y,\text{SE}} = f_{\gamma y,\text{SE}} + f_{Py,\text{SE}}$. The blue and green continuous lines show the theoretical predictions proposed in Equation (1.21). The red continuous line presents the theoretical **capillary** force $f_{\gamma y}$ described in Equation (1.36). **B** – Eccentricities e and e' versus dimensionless weight w. The black dots correspond to the numerical Surface Evolver results and the continuous line to Equation (1.24); this poor prediction is improved by taking the geometrical rectification into account as modeled in Equation (1.39) which is represented as a dashed line. The same results are presented in **C** and **D** for $r = 60$. The contact angle is $\theta_Y = 20^\circ$.

1.5.3 Drops to measure thin fibers

The measurement of the radius of thin fibers ($a < 10\,\mu\mathrm{m}$) can be unprecise with usual optical tools such as microscopes since resolution is limited by light wavelength. Other techniques such as laser diffractometry, though elegant (Onofri et al. 2004), are complex to perform and especially tricky for transparent materials because of multiple reflections, leading to constructive and destructive interferences. Here, we propose a novel measurement technique based on the previously described mechanics of heavy drops sitting on thin fibers. The fiber measurement is performed using the following steps. Various droplets of different sizes are deposited on the thin fiber of unknown radius a. The drops' radii R and eccentricity e are optically measured using:

$$e = \frac{H_{\mathrm{bot}} - H_{\mathrm{top}}}{H} \tag{1.40}$$

where H_{top} (H_{bot}) respectively refer to the absolute distance between the highest (lowest) drop's point and the fiber's axis. Since the drops are large ($r > 30$) the effective radius R of the drop can reasonably be taken as $H/2$. The experimental eccentricities e are plotted as a function of the normalized drop radii $R\kappa$ and the free parameter $a\kappa$ of Equation (1.39) is then adjusted to fit the experimental data. The measurements of small eccentricities ($e < 0.2$) are unprecise and are therefore not considered when fitting the fiber radius $a\kappa$. Very large eccentricities ($e > 0.9$), on the other hand, are not well captured by the theoretical model and are also discarded.

A typical example is provided in Figure 1.16 where excellent agreement is obtained between this method and the Scanning Electron Microscopy verification measurement.
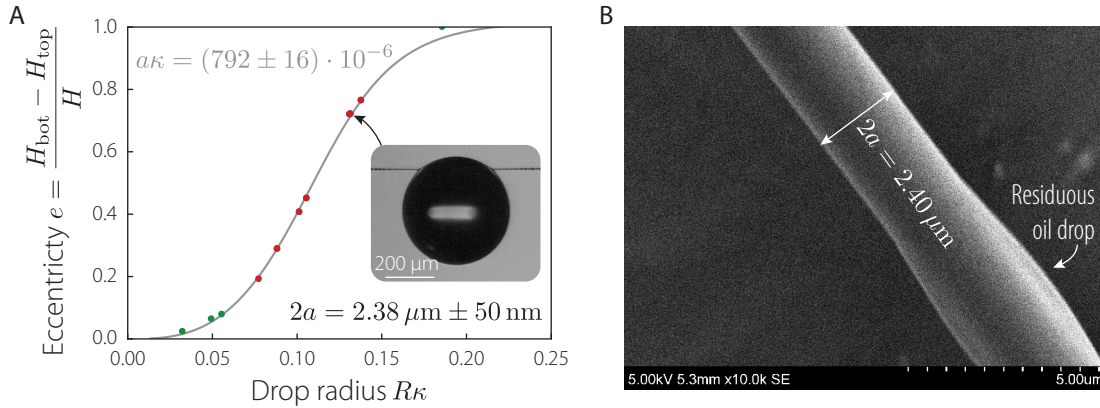
Figure 1.16 – **Measuring thin fibers with drops. A** – Experimental eccentricity of silicone oil droplets sitting on a polyurethane thin fiber versus their dimensionless drop radius $R\kappa$. By fitting the best fiber radius $a\kappa$, one can determine this value, in this example the best fiber radius fit gives $2a = 2.38\,\mu\mathrm{m}$ using Equation (1.39) (gray continuous line). The green and red dots correspond to experimental measurements and in order to enhance the method's precision, the drops considered must have eccentricities in $e \in [0.2, 0.9]$ (indeed, the eccentricity measurement is too unprecise below $e = 0.2$ and the model does not cover extreme eccentricities above $e = 0.9$). Therefore, only the red dots are taken into account to determine $a\kappa$. This method provides great precision as the SEM shot presented in **B** reveals that the fiber has an actual diameter $2a = 2.40\,\mu\mathrm{m}$. The droplets used in this experiment are silicone oil droplets ($\kappa^{-1} = 1.5$ mm) sitting on a polyurethane fiber and the contact angle θ_{Y} is 0°. The effective radius R of the drop is taken as $H/2$.

Figure 1.17 provides two other precise measurements of larger fibers and a measurement verification by independently measuring the fibers' radii with a Leica macroscope (VZ85RC) with a Leica DFC-295 camera.

Figure 1.17 – The fiber measurement technique is applied to two other fibers. By fitting the radius of the fiber using Equation (1.39), the first (left figure) and second (right figure) fiber are respectively found to have radii of 3.98 and 5.71 μm. The corresponding radii are also independently measured with a Leica macroscope, providing 4.11 and 6.0 μm respectively in the left and right figure with an error margin of around 0.5 μm.

1.5.4 Higher contact angles: bifurcation paths

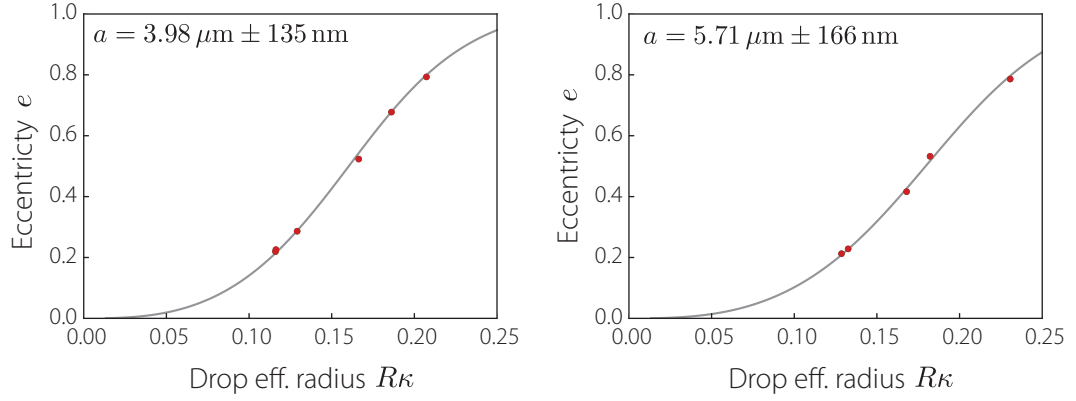Until now, the considered drops had small contact angles with the solid fiber. We now focus on drops exhibiting higher contact angles. Again, we study the effect of gravity on the drops equilibrium shapes. This section will only scratch the surface of this problem and to gain a deeper understanding of its physics, more cases should be studied numerically, and above all, experiments should be performed to validate the numerical simulations.

Figure 1.18 shows the eccentricities corresponding to the equilibria of a drop of radius $r = 7$ and contact angle $\theta_\mathrm{Y} = 70^\mathrm{o}$ depending on its weight w, calculated with Surface Evolver. In order to analyze the stability of the clam-shell configuration, the drop's geometry was initiated as a cube sitting only partly on the fiber (i.e. not wrapped around it), as in Chou et al. (2011) and McHale and Newton (2002). Note that for the clam-shell configuration, the eccentricity conserves the same definition (Equation (1.40)), H_top (H_bot) is defined as the distance between the highest (lowest) point of the drop and the fiber's axis.

The bifurcation diagram presented in Figure 1.18 will be studied in more details in the following two sections. For a good understanding of this diagram, it should be emphasized that a positive weight w corresponds to gravity pointing downwards and conversely, a negative weight corresponds to gravity pointing upwards. For the geometry of the drop, a positive eccentricity e corresponds to a drop hanging downwards whereas an negative eccentricity obviously happens when the drop is mainly above the fiber. Therefore, it should be noted that $e(w)$ is an odd function:

$$e(w) = -e(-w). \tag{1.41}$$

Both the stability of the barrel configuration and the clam-shell configuration are studied in the following sections.

Equilibrium of the barrel configuration
The bifurcation curve corresponding to the barrel configuration in Figure 1.18 shows that for small drop weights, the drop hangs with an eccentricity e well predicted by Equation (1.24) ($e = \sin(\arctan(w/2))$) for w small. At a certain drop weight, around $w = 0.05$, the barrel configuration undergoes a saddle-node bifurcation and therefore no longer exists for $w > 0.05$. It then jumps to the corresponding clam-shell configuration.
Another set of bifurcation paths of the barrel configuration is presented in Figure 1.19, this time for a smaller contact angle $\theta_\mathrm{Y} = 60°$ and smaller effective radii ($r = 3, 3.5, 4$ and 4.4). For large enough effective drop radii ($r = 4$ and 4.4), the behavior of the drop
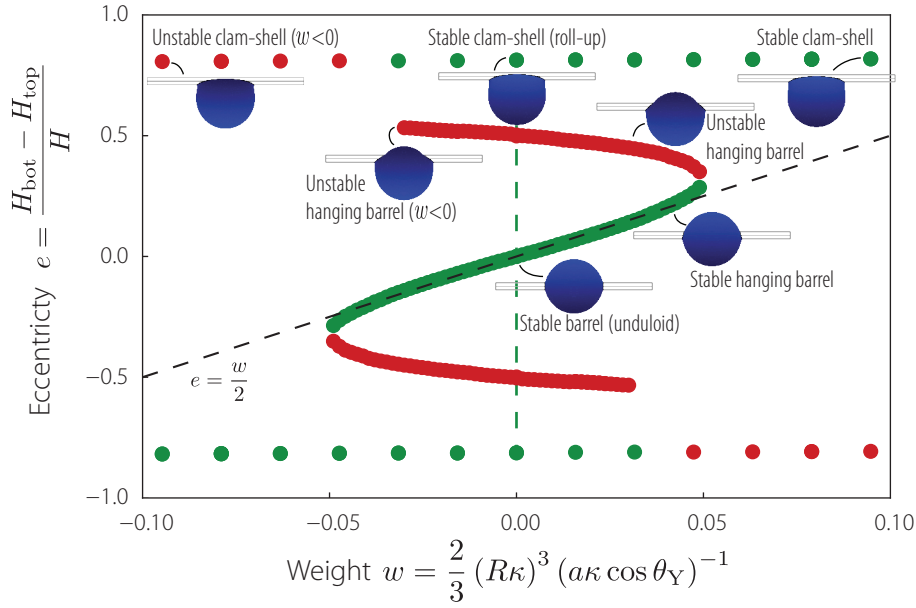
Figure 1.18 – Eccentricity of a drop on a fiber versus its dimensionless weight. The drop has an effective radius $r = 7$ and displays a contact angle $\theta_Y = 70°$) with the fiber. The stability of the barrel and clam-shell configuration are studied. The green and red points respectively correspond to stable and unstable states computed by Surface Evolver. The black dashed line shows the eccentricity prediction of Equation (1.24) for a small hanging angle α. The green dashed line shows the fact that for a zero weight drop, the clam-shell configuration has no preferred orientation (i.e. the drop can sit indistinctively on any side of the fiber). Note that the positive eccentricity clam-shell configuration is predicted as stable by Surface Evolver even for a few values $w < 0$. This inconsistency likely finds its root in the discretization of the drop's surface, leading to a small error in the stability assessment by Surface Evolver. Note that this figure corresponds to a close-up on Figure 1.20.

is conceptually similar to the one described in Figure 1.18: as the weight of the drop is increased, the drop stably displays an increasing eccentricity up until a saddle-node bifurcation where it jumps to the clam-shell configuration. For the two smaller simulated droplets ($r = 3$ and 3.5), the barrel configuration is not stable even for $w = 0$. This is coherent with the stability prediction provided by Chou et al. (2011) in Figure 1.8, for $\theta_Y = 60°$, the limit between stable and unstable barrel configuration lies between $r = 3.5$ and $r = 4$. Departing from this unstable state, the (completely unstable) bifurcation path is easy to obtain with Surface Evolver using the Hessian method. The weight of the drop is gradually increased and the equilibrium shape is calculated at each step.

The unstable branches of the $r = 4$ and 4.4 drops, on the other hand, are more challenging to obtain. The method applied here is to find an easily attainable unstable state (*e.g.* for $r = 3$) for a non-zero drop weight (for example $w = 0.05$). The drop's radius is then gradually increased and its (unstable) equilibrium is found by continuation at each step using the Hessian method. We finally attain the desired unstable branch of a larger drop (*e.g.* $r = 4$).

Equilibrium of the clam-shell configuration
The clam-shell configuration corresponds to the drop sitting only on one side of the fiber and the stability of this configuration will not be studied extensively. Figure 1.20 represents a wider view of Figure 1.18 and therefore allows to study the effect of larger weights. We analyze the upper branch.

The clam-shell configuration, at $w = 0$ hangs lower and lower as its weight is increased.
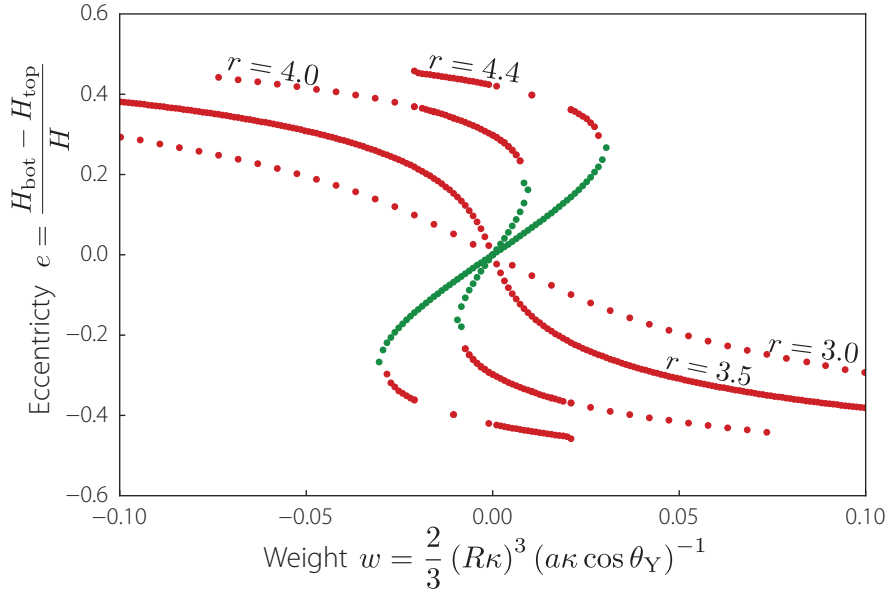
Figure 1.19 – Barrel configuration: e vs. w for $\theta_Y = 60°$ for four different droplet radii $r = 3$, 3.5, 4 and 4.4. Note that for small radii, the barrel configuration is **not** stable even for $w = 0$. Green and red points correspond to respectively stable and unstable states. The stable and unstable clam-shell configurations are not presented in this graph. These bifurcation curves correspond to a cusp bifurcation.

This corresponds to a stable configuration which would experimentally be observed in these conditions. At a certain weight, near $w = 2$, no equilibrium state is found by Surface Evolver anymore. This likely corresponds to a saddle-node bifurcation but the corresponding unstable branch was not found. The fact that no more equilibrium states were found above $w > 2$ probably corresponds to the fact that the drop would have fallen off the fiber.

For negative weights, on the other hand, an unstable equilibrium is found, here corresponding to a drop sitting 'under' the fiber (i.e. on its downside) with gravity pushing it upwards. This configuration is symmetric to the case of a drop sitting on top of the fiber with gravity pushing it downwards. A side view of such a drop is provided in Figure 1.20. This equilibrium shape, although theoretically unstable, could possibly be observed experimentally for a drop on a fiber with enough pinning at the triple line to stabilize it even when it sits on top of the fiber. Surface Evolver allows for the self-penetration of the drop and this is the case for the side view of the numerical simulation presented in Figure 1.20. This extreme configuration is therefore twice unphysical; it is unstable and even if such a state was attained, the triple lines would have merged and the drop would actually wrap the fiber as a barrel.

1.6 The largest drop a fiber can hold

In the previous sections, we theoretically studied droplets of different sizes sitting on a fiber. To better understand the problem's physics, the drop size and its weight were then handled independently. We now turn to the everyday configuration where the drop weight depends on its size and try to answer the question: what is the size of the largest drop that can sit on a fiber before falling off?

The scenario of a falling drop was briefly discussed in the previous section. Although it was not rigorously found, the potential saddle-node bifurcation of the clam-shell equilibrium path (see Figure 1.20) near $w = 2$, $e = 1$ is an example of capillary forces not strong enough
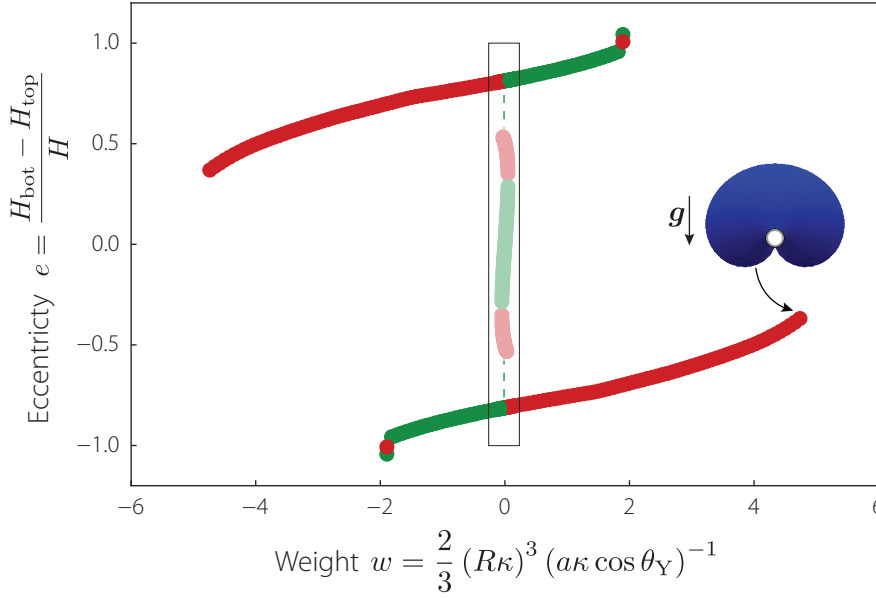
Figure 1.20 – Clam-shell configuration: eccentricity e vs. w for $r = 7$ and $\theta_Y = 70°$. This bifurcation diagram corresponds to the one represented Figure 1.18 with a larger window in order to analyze the behavior of the clam-shell configuration for larger weights. The black rectangle shows the window used Figure 1.18. Near $w = 0$, for the upper branch (near $e = 0.9$) the eccentricity of the drop increases as its weight is intensified, corresponding to a stable hanging clam-shell configuration. Passed a certain weight (here at $w = 2$), Surface Evolver no longer finds equilibrium states, probably attesting the presence of a saddle-node bifurcation there. For negative weights (on the positive eccentricity branch), unstable clam-shell configurations are found, they are equivalent to a drop sitting on top of a fiber in the gravity field.

to hold the heavy drop on the fiber. Here, we will restrict our investigation to wetting drops (small contact angle between the drop and the fiber).

1.6.1 Literature approach: Two capillary menisci securing the drop

The study of the largest drop a fiber can hold was previously carried out in Lorenceau et al. (2004). In this paper, the authors propose that for a drop sitting on a thin fiber, the drop's weight $W = \frac{4}{3}\rho g \pi R^3$ cannot exceed the sum of the maximum forces exerted by the two menisci, each given by $F_{\gamma y, \max} = 2\pi a \gamma$. Figure 1.21 schematically presents this configuration. The drop maximum weight $W^\star_{\mathrm{Lor}}$ just before falling off therefore writes:

$$W^\star_{\mathrm{Lor}} = 2F_{\gamma y, \max} \quad \Rightarrow \quad R^\star_{\mathrm{Lor}} = 3^{1/3} a^{1/3} \kappa^{-2/3} \quad \Rightarrow \quad R^\star_{\mathrm{Lor}}\kappa = 1.44 \left(a\kappa\right)^{1/3} \quad (1.42)$$

where $R^\star_{\mathrm{Lor}}$ corresponds to the equivalent radius of the largest drop and $\kappa^2 = \rho g/\gamma$. The subscript 'Lor' refers to Élise Lorenceau's article (Lorenceau et al. 2004). Their experimental results, shown in Figure 1.22, are in good agreement with this theory as a fit on their data provides:

$$R^\star_{\mathrm{Lor}}\kappa = 1.53 \left(a\kappa\right)^{0.34}. \tag{1.43}$$

Although the agreement between the experiments and the model is satisfying in Lorenceau et al. (2004), the measurement error for small droplet radii (see error bars of Figure 1.22) and the limitation in fiber radius (here $a \geq 10\mu$m) may hide another possible scaling law for thinner fibers.
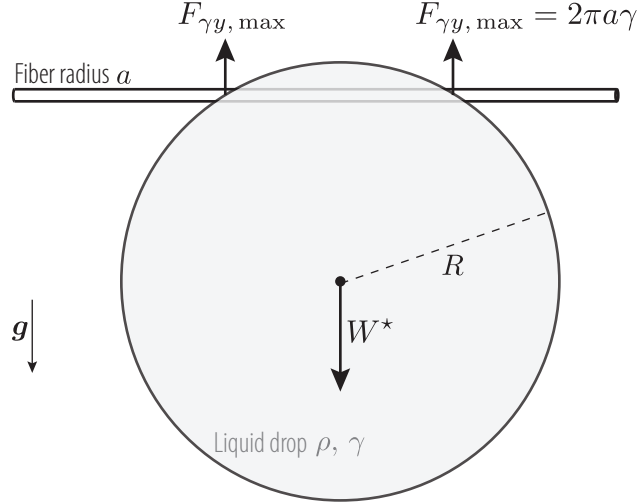
Figure 1.21 – **Large drop on a thin fiber just before falling off.** In Lorenceau et al. (2004), the maximum weight $W^\star$ of the droplet is predicted to be given by $W^\star = 2F_{\gamma y,\,\mathrm{max}}$ where $F_{\gamma y,\,\mathrm{max}}$ represents the maximum vertical force that a capillary meniscus can exert on the drop.
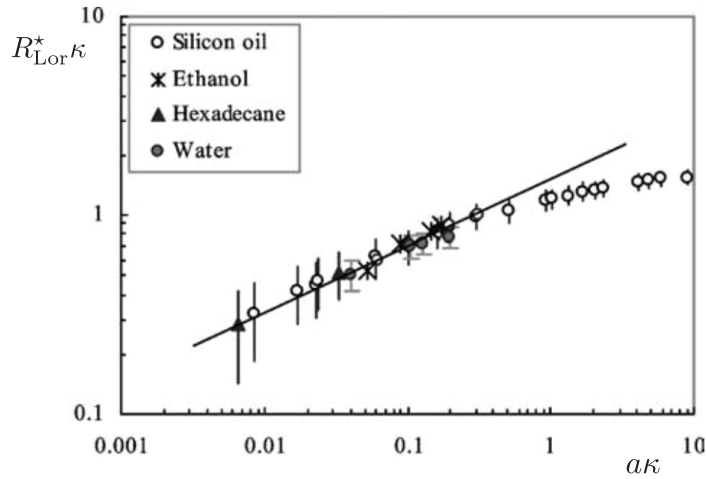
Figure 1.22 – Largest drop (radius $R^\star_{\mathrm{Lor}}$) a fiber of radius a can hold before it falls off. Both $R^\star_{\mathrm{Lor}}$ and a are normalized by the capillary length κ^{-1}. Reproduced from Lorenceau et al. (2004).

1.6.2 Alternative approach: One capillary line securing the drop

Throughout this work, the study of drops on thin fibers led to the fabrication of even thinner fibers than the ones studied in Lorenceau et al. (2004). For example, the fiber presented in Figure 1.16 has a radius $a = 1.2\,\mu\mathrm{m}$. Interestingly, the largest silicone oil drop that can sit on this thin fiber before falling has a significantly larger radius than the one predicted by Lorenceau's theory. We therefore propose an alternative approach to explain this unexpected behavior.

Experimentally, a large droplet on a thin fiber, rather than displaying two menisci as in Figure 1.21, seems to display **one** long triple line of length $2L$ as proposed in Figure 1.23 where L is the wet length. The factor 2 corresponds to the fact that the drops meets the fiber on both the front and the rear side.

We assume the drop remains spherical and that the sphere describing it is tangent to the fiber. We predict the wet length L depending on the hanging angle α as described in
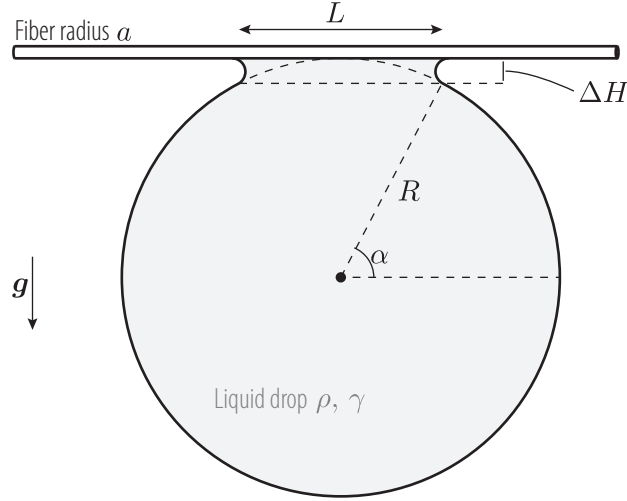
Figure 1.23 – **Large drop on a thin fiber just before falling off.** The droplet is here considered to remain spherical expect near the fiber.

Figure 1.23,

$$L = 2R\cos\alpha = 2R\sin\left(\frac{\pi}{2} - \alpha\right) \tag{1.44}$$

and

$$\Delta H = R\left(1 - \sin\alpha\right) = R\left(1 - \cos\left(\frac{\pi}{2} - \alpha\right)\right) \tag{1.45}$$

We approximate the pressure inside the drop as $P = 2\gamma/R$ and since it is constant everywhere in the drop we have:

$$\frac{2\gamma}{R} = \gamma\left(\frac{1}{R_1} + \frac{1}{R_2}\right) \tag{1.46}$$

anywhere at the drop's surface, with R_1 and R_2 being its principal curvature radii of the drop surface. Near the fiber, since we consider the drop to perfectly wet it, the fiber curvature imposes $R_1 = -a$ and using Equation (1.46):

$$\frac{1}{R_2} = \frac{2}{R} + \frac{1}{a}. \tag{1.47}$$

Since the drop radius is significantly larger than the fiber's ($R \ll a$), we find $R_2 \simeq a$. This long meniscus then has a height $\Delta H = 2R_2 = 2a$. Moreover, considering $\pi/2 - \alpha$ is small, Equations (1.44) and (1.45) are rewritten:

$$L = 2R\left(\frac{\pi}{2} - \alpha\right) \tag{1.48}$$

and

$$2a = \frac{R}{2}\left(\frac{\pi}{2} - \alpha\right)^2 \tag{1.49}$$

which finally leads to:

$$L = 8\,R^{1/2}\,a^{1/2}. \tag{1.50}$$

Considering that the drop falls when the capillary force developed by the long meniscus can no longer support the drop weight, i.e. when $2\gamma L = W^\star$, yields:

$$16\gamma\,R^{\star\,1/2}\,a^{1/2} = \frac{4}{3}\pi\rho g R^{\star\,3} \tag{1.51}$$

or

$$R^\star \kappa = \left(\frac{12}{\pi}\right)^{2/5} (a\kappa)^{1/5} = 1.71\, (a\kappa)^{1/5}\,. \tag{1.52}$$

This new scaling is compared with experiments in Figure 1.24 where a good agreement is found for the power law $R^\star \kappa \sim (a\kappa)^{1/5}$. The prefactor, on the other hand is adjusted to 1 (instead of 1.71).

Note that since the drops are small, their effective radius R is not deduced from their volume but directly measured from a photograph by fitting a circle around the drop as shown in Figure 1.24-left.
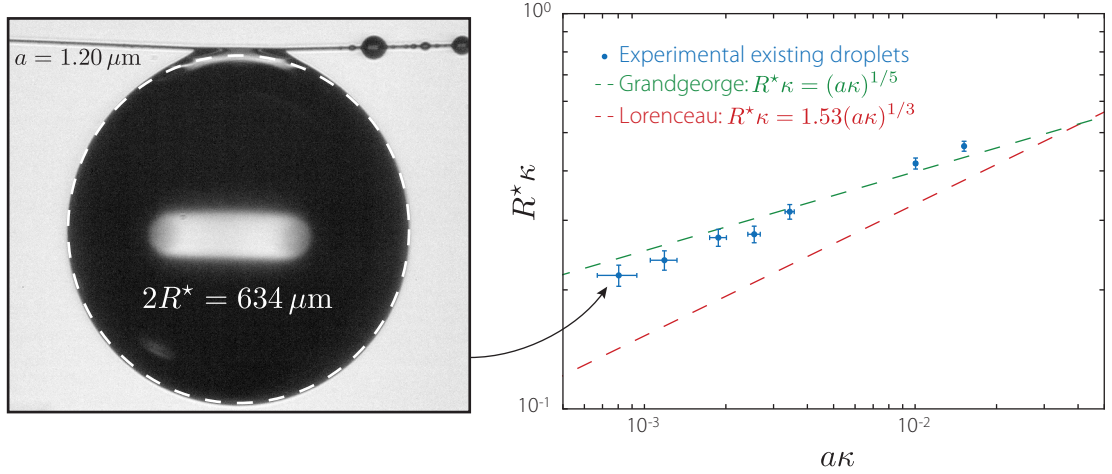
Figure 1.24 – **Left** – Largest v1000 silicone oil drop observed on an $a = 1.20\ \mu$m polyurethane fiber. Its effective radius (here $R^\star = 317\,\mu$m is measured by fitting a circle around it on the photograph (dashed white line). This radius is possibly slightly underestimated as it does not take the volume of the drop near the fiber into account. **Right** – Maximum effective radius droplet $R^\star \kappa$ a fiber of radius $a\kappa$ can hold.

This simple model could probably further be improved with the help of more experimental data. Indeed, although the power law seems satisfying, the predicted prefactor is inaccurate.

2 | Elasto-capillary coiling

Contents

In the previous Chapter, we have shown that when a drop sits on a horizontal fiber in an axially symmetric configuration (barrel configuration), the fiber applies a horizontal force $F_{\gamma x} = 2\pi a \gamma \cos \theta_Y$ on the drop at both its menisci. The force applied at the right meniscus pulls the drop to the right, whereas the one applied on the left meniscus pulls it to the left; the drop is at mechanical equilibrium and usually, the story ends here. However, the action-reaction law indicates the drop applies an equivalent reaction force on the fiber, in the opposite direction, i.e. a compressive load between its two menisci. But what if the fiber is so thin and soft that it cannot withstand this compressive load? In some cases, the compressive force applied by the drop can force the fiber to buckle and coil within it. This surprising phenomenon was first observed in 1989 by Fritz Vollrath and Donald T. Edmonds (Vollrath and Edmonds 1989) on spider capture silk naturally decorated by liquid glue droplets (see Figure 2.1).
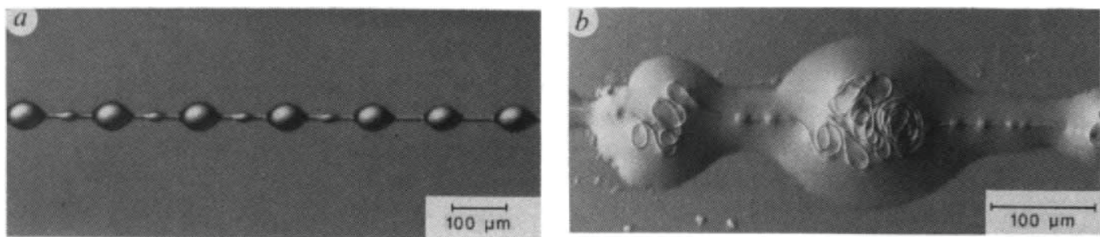
Figure 2.1 – Original observation of the coiling phenomenon of spider capture silk inside liquid glue droplets. Reproduced from Vollrath and Edmonds (1989).

The physics underpinning this in-drop coiling was further studied by Hervé Elettro and collaborators (Elettro et al. 2016, 2015) and Figure 2.2, adapted from Elettro (2015), shows the behavior of a Golden Nephila capture silk thread under compression. The silk thread is compressed starting from its rest length of about 1 cm to less than 1 mm. It should be emphasized that in Figure 2.2-A, the silk thread is not pre-stretched. By keeping the fiber in a humidity-saturated environment, the thread is naturally decorated with liquid glue droplets. When compression starts, i.e. as the ends of the fiber are brought closer as shown in Figure 2.2-B, the fiber does not sag or buckle as one would expect. Instead, it remains straight, as if telescopic throughout compression. The reason behind this unexpected
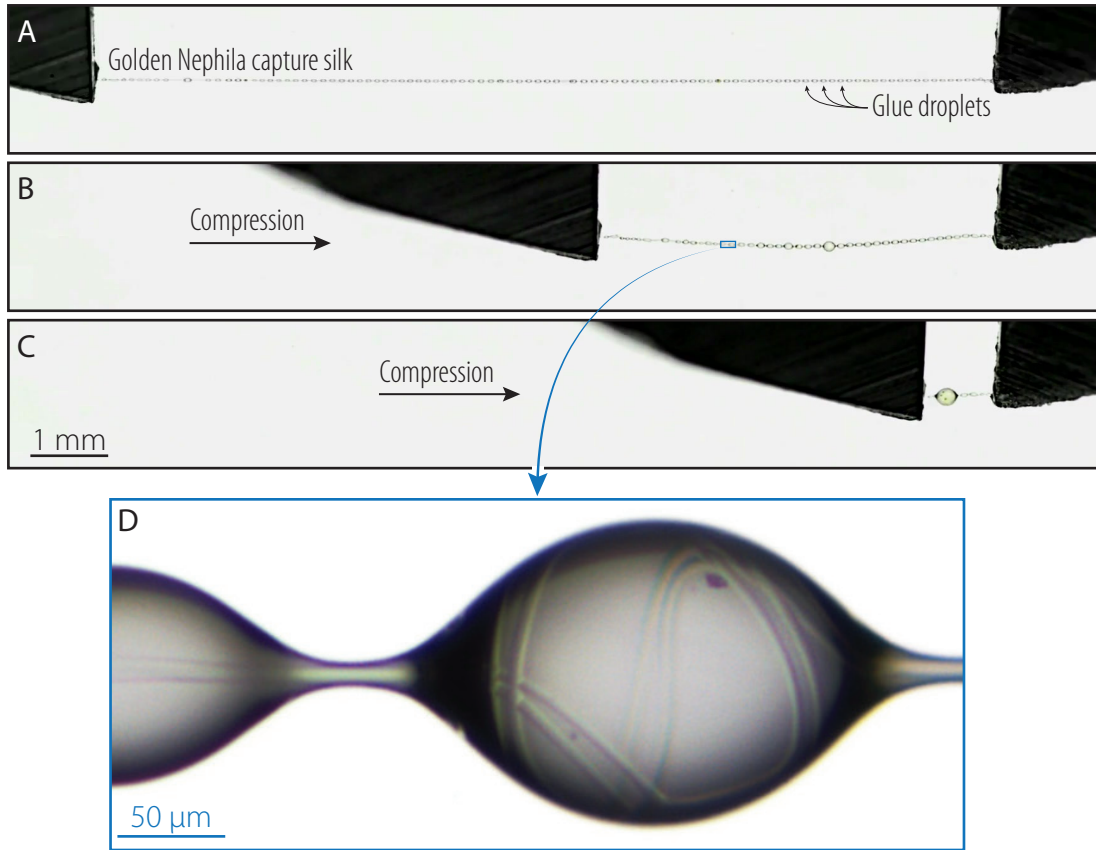
Figure 2.2 – Golden Nephila capture silk thread attached to the jaws of a caliper, liquid glue droplets naturally decorate the thread in a humid environment. In **A**, the fiber is at its rest state (it is not pre-stretched) and its ends are brought closer in **B**. Instead of sagging under its own weight as a usual thread would, it remains straight throughout the compression up to the nearly completely condensed state shown in **C**. The mechanism responsible for this surprising behavior lies in the self-coiling of the fiber inside the droplets during the compression as revealed in **D**. Adapted from Hervé Elettro's PhD thesis (Elettro 2015).

'contractility' lies in the mechanical interaction between the fiber and the liquid droplets. Indeed, as shown in Figure 2.1 and in Figure 2.2-D, the fiber spontaneously coils inside the drop as compression is carried out and fiber excess is therefore 'swallowed' by the drop throughout compression: the capillary compressive force between the drop's menisci is strong enough to make the fiber buckle and coil inside of it.

More generally, the interaction between liquids and elastic flexible structure, elasto-capillarity, has been the subject of many studies throughout the last decades; a quick overview of this discipline is provided in the next section.

2.1 Elasto-capillarity with slender structures: an introduction

Capillary forces developed by a liquid can be sufficient to deform an elastic structure, provided this structure is flexible enough. An example, inspired by Neukirch et al. (2007) is provided in Figure 2.3 where a rigid cylinder of radius R is coated with a liquid of surface tension γ. An elastic plate of thickness t, width W and length L is coated with the same liquid and put in contact with the cylinder. Two scenarios can then take place, the plate can either remain straight as in Figure 2.3-A or bend to adapt to the cylinder surface as shown in Figure 2.3-B.
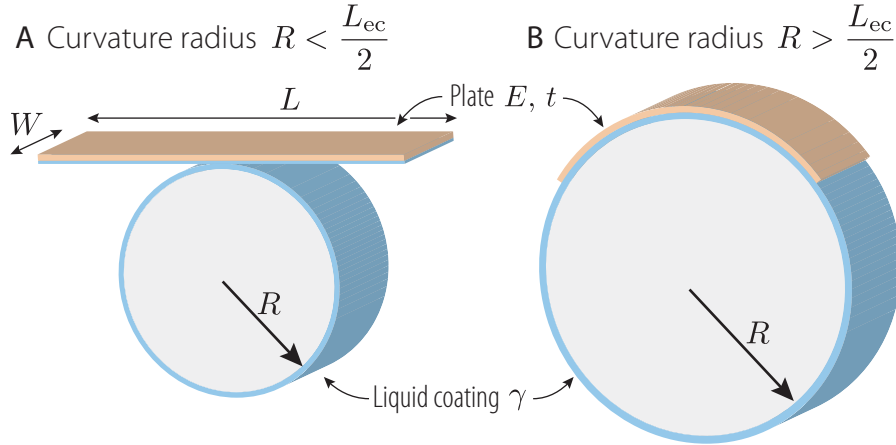
Figure 2.3 – A rigid cylinder is coated with a liquid of surface tension γ and covered by an elastic plate of bending stiffness $EWt^3/12$. If the cylinder has a large enough radius R, the elastic plate spontaneously wraps around it.

To predict the selected shape, we write the total energy of both configurations. If the plate remains straight, the energy is given by the liquid-vapor surface energies:

$$\mathcal{V}_{\text{straight}} = 2\pi RW\gamma + WL\gamma. \tag{2.1}$$

On the other hand, if the plate bends and adopts the cylinder curvature, surface energy is lowered but bending introduces an elastic energy and the total energy then writes:

$$\mathcal{V}_{\text{bent}} = \gamma(2\pi R - L)W + L\frac{EI}{2R^2} \tag{2.2}$$

where E is the Young's modulus of the plate and I its cross-sectional second moment of area with $I = Wt^3/12$. Note that constant terms such as the solid-liquid interface energy of the cylinder-liquid interface $2\pi R\gamma_{\text{SL}}W$ have been discarded in Equations 2.1 and 2.2. We write the energy difference between the bent and straight configurations:

$$\Delta\mathcal{V} = \mathcal{V}_{\text{bent}} - \mathcal{V}_{\text{straight}} = L\frac{EI}{2R^2} - 2\gamma L. \tag{2.3}$$

The bent configuration is selected if it presents a lower total energy than the straight one. This happens when the surface energy gained by the contact of the two wet objects compensates the elastic-bending energetic cost. This condition is given by $\Delta\mathcal{V} < 0$ and yields

$$2R > L_{\text{ec}} = \sqrt{\frac{EI}{\gamma}}. \tag{2.4}$$

In this configuration, the elasto-capillary length L_{ec} provides a threshold for elasto-capillary bending, i.e. it indicates the minimum diameter around which an elastic plate wraps. Figure 2.4 presents other cases where L_{ec} defines the size of elasto-capillary structures. For

example, Figure 2.4-B shows a lamella forming a loop at the interface of a liquid bath. The radius of the loop, studied in Roman and Bico (2010) is given by $L_{ec}/\sqrt{2(1 + \cos\theta_Y)}$.
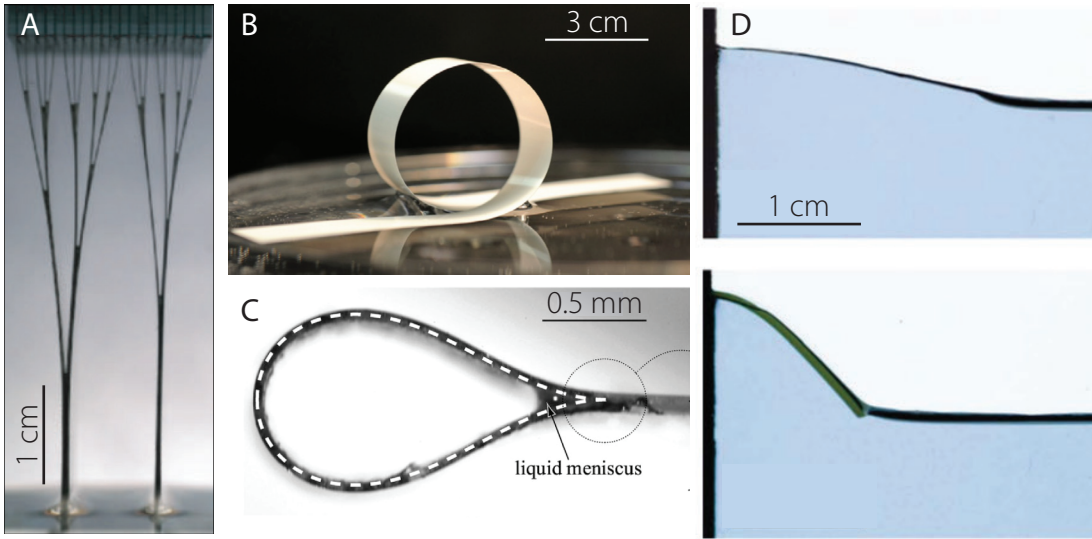
Figure 2.4 – **A** – Elasto-capillary coalescence of flexible lamellae hanging from a brush when it is removed from a bath of wetting liquid. Reproduced from Bico et al. (2004). **B** – Lamella forming a loop at the interface of a liquid bath. Reproduced from Roman and Bico (2010). **C** – PDMS loop held by an ethanol meniscus. Reproduced from Py et al. (2007). **D** – Elasto-capillary meniscus: a polyvinylsiloxane strip is fixed on a side of a narrow box filled with water. Elasto-capillary interactions, along with gravitaty effects, dictate the shape adopted by the strip when water is gradually withdrawn from the box. Reproduced from Rivetti and Antkowiak (2013).

Elasto-capillary interactions can also be harmful for fine structures such as microelectrome-chanical systems (MEMS). Figure 2.5-left, reproduced from Tanaka et al. (1993), presents the surface-tension-induced collapse of micro-pillars of MEMS. Indeed, MEMS usually possess thin beams with low bending rigidities and their fabrication process often requires rinsing with solvents. The attractive capillary forces generated between the pillars by these solvents can be sufficient to make the pillars fold and stick to each other. This stiction phenomenon was studied theoretically for a liquid meniscus between two micro-pillars in Taroni and Vella (2012) (see Figure 2.5-right) and Singh et al. (2014) focuses on the elasto-capillary interactions of an array of pillars.
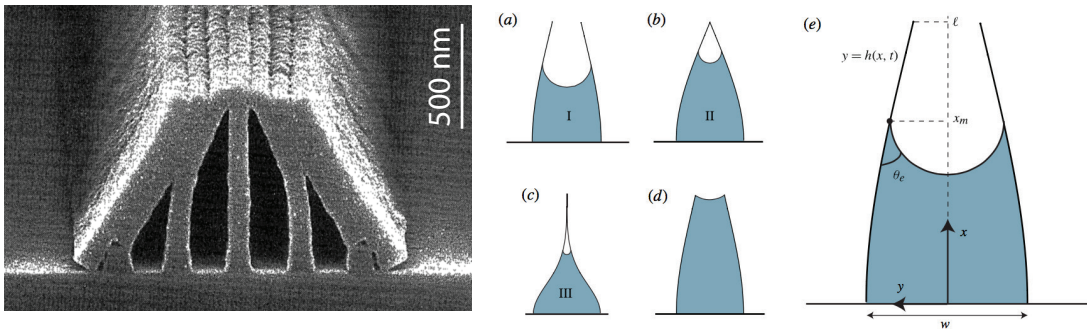
Figure 2.5 – **Left** – A 'tepee' structure is observed as many lamellae stick together due to capillary attractive forces. Reproduced from Tanaka et al. (1993). **Right** – Equilibrium configurations for a volume of liquid confined between two elastic pillars clamped on a rigid base. Reproduced from Taroni and Vella (2012).

Finally, Figure 2.6 presents an advantageous application of elasto-capillarity for the fabrication of MEMS. Here, a hot liquid metal drop is deposited on a 2D pattern and the

capillary forces it develops are strong enough to generate out of plane deformations, thus leading to a 3D structure. When the drop cools down, it solidifies and ensures robustness to the engineered object. Figure 2.6-left shows a scanning electron microscope snapshot of a soldering drop after the elasto-capillary shaping of a 3D fold. Figure 2.6-right shows a micro-fan whose design is made possible with the soldering drops. Depending on their volume, the drops can tune the specific angle of attack of the fan blades.
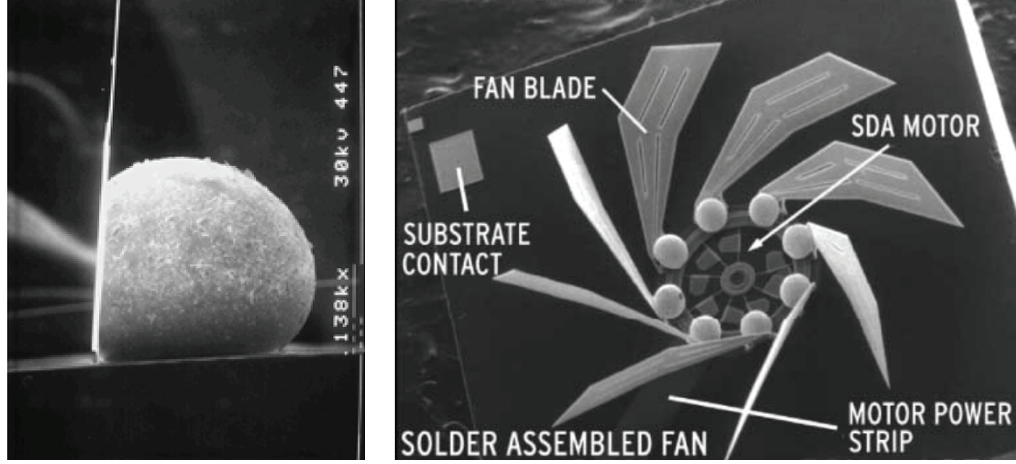
Figure 2.6 – **Left** – Scanning electron microscopy picture of a solder drop. The capillary forces it generates fold a carefully designed 2D pattern. The volume of drop, of the order of 10^{-5} mL can be changed to tune the angle of the fold. Reproduced from Syms et al. (2003). **Right** – This technique is adapted to fabricate a 3D fan from an initially 2D pattern. It allows to obtain the desired blade angle of attack. Reproduced from Linderman et al. (2002).

In the light of these elasto-capillarity examples, we return to the elasto-capillary configuration of a drop deforming a fiber. In order to gain further intuition on the elasto-capillary coiling of capture silk, we turn to a synthetic system displaying the same behavior. Figure 2.7 shows the sequence of a silicone oil drop of radius $R \simeq 1.5$ mm sitting on a silicone polymer fiber of radius $a \simeq 35\,\mu$m (RTV 3535, Young's modulus $E \simeq 1$ MPa). The system is immersed in a water bath in order to provide buoyancy, and therefore cancel gravity. First at its extended state (i.e. ends of the fibers far away from each other), the fiber is straight and the drop adopts an axially symmetric unduloidal shape as discussed in the previous Chapter. The ends of the fiber are now brought closer and the capillary forces applied by the drop on the fiber generate a compressive load $-F_{\gamma x}$ between its two menisci, sufficient to make the fiber buckle inside the drop. As compression is pursued, the fiber further coils inside the drop, thus remaining globally straight except where fiber loops are formed. This self-coiling mechanism is reversible; upon subsequent extension, fiber loops are 'uncoiled' out of the drop and the system comes back to its original state.

Starting from the condensed state, i.e. at a small distance between the fiber ends as in Figure 2.7-D, the self-organized fiber loops inside the drop can be interpreted as 'fiber reserves' which are recruited when the ends of the fiber are pulled apart. This elasto-capillary coiling phenomenon therefore endows a fiber with an apparent extreme extensibility, even up to 50,000 % for a silicone oil drop sitting on a micronic polyurethane (TPU) fiber (see Elettro et al. (2016)). This mechanism could therefore be of interest in the field of stretchable electronics, where extensible connectors are sought. Indeed, as extensibility is here not achieved by stretching the material directly, but by local geometrical rearrangement, it does not rely on the material's intrinsic compliance and is therefore universal in the sense that every material is a potential candidate for in-drop coiling.

With the aim to design functional micro-structures using in-drop coiling, we turn to the use of metallic materials with the drawback that functional materials usually have high Young's moduli (Ashby and Bréchet 2003) (metals for electronics, glass for photonics, for
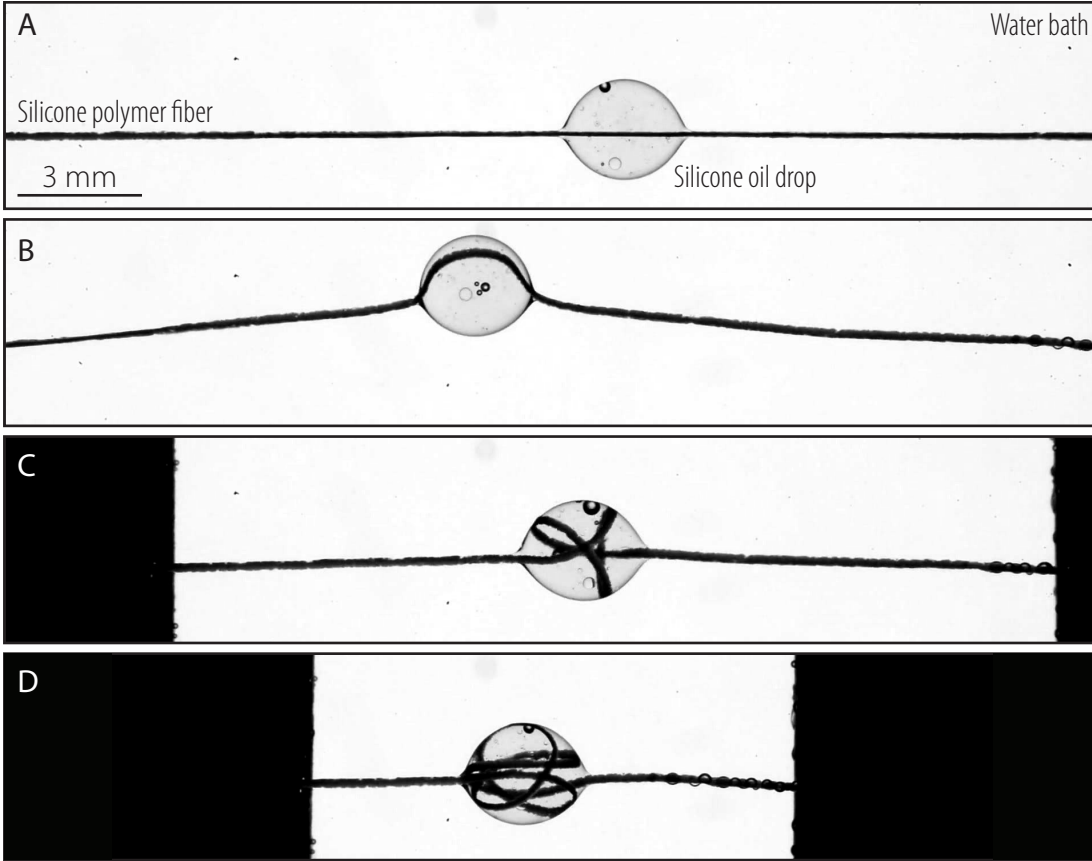
Figure 2.7 – Silicone oil drop ($R \simeq 1.5$ mm) sitting on a silicone polymer fiber of radius $a \simeq 35$ μm and Young's Modulus $E \simeq 1$ MPa. The fiber is first completely straight in **A** and is gradually compressed from **B** to **D**. Throughout this compression, the fiber spontaneously coils inside the silicone oil drop just as the Golden Nephila capture silk coils inside the glue droplets in Figure 2.2. Here, the whole system is immersed in a water bath. This provides buoyancy and therefore allows us to use large drops, which would otherwise fall off the fiber due to their weight.

which $E \sim 50 - 100$ GPa). For these materials, if the bending stiffness is to be kept low, the structure has to be dramatically thin, in the order of nanometers. Yet thin structures are difficult to manufacture (Greiner and Wendorff 2007; Kluge et al. 2008), and lose their functionality (electric resistance of a fiber decreases quadratically with decreasing radius).

In the last decade, interest in flexible electronics has been driven by applications in consumer electronics (*e.g.* flexible laptop or smartphone screens), but also integration in the human body to design sensors that can be implanted on living organs (Rogers et al. 2010). If bending flexibility is achieved by designing thin enough structures, stretching compliance is usually obtained through the use of wavy structures. Some examples where the focus has been on the material side are the use of conductive polymers in the fabrication of conductive elastic materials (Hansen et al. 2007).

With as ultimate goal the design of stretchable connectors, we re-visit the in-drop coiling of fibers in the light of two questions:

○ For a given material (fixed Young's Modulus), what is the thickest fiber (i.e. largest fiber radius a) that can undergo coiling inside a droplet?
○ Once we have identified this limit, can we overcome it?

We answer these two questions by first providing theoretical conditions for in-drop coiling, and then verify them experimentally.

2.2 Drop on a thin elastic fiber: coiling without gravity

Here, we consider a liquid drop sitting on an elastic fiber in the absence of gravity. The fiber has a circular cross-section of radius a, Young's modulus E and total length L. The liquid drop has a total volume $\Omega = \frac{4}{3}\pi R^3$. As long as the drop sits on a straight fiber, it adopts an unduloidal shape (Poincaré 1895; Carroll 1976) as was discussed in the previous Chapter. When $R \gg a$ the unduloid resembles a sphere (of radius R) and we will make this approximation even once the fiber is coiled inside the liquid drop.
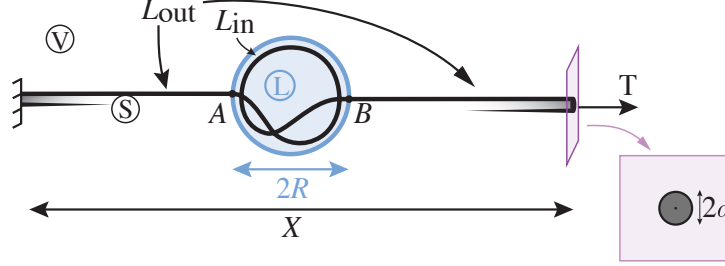

Figure 2.8 – Cylindrical fiber of radius a undergoing coiling inside a liquid drop of radius R in absence of gravity. The fiber is held at a tension T.

The drop-on-fiber system is held under tension T, see Figure 2.8. Furthermore, as we consider small systems (typically $a \sim 10\,\mu\mathrm{m}$, $R \sim 100\,\mu\mathrm{m}$) we need to take surface forces into account. Indeed, due to the stronger affinity of the fiber for the liquid than for the vapor (*i.e.* $\gamma_{\mathrm{SL}} < \gamma_{\mathrm{SV}}$), surface tension forces at the two menisci points A and B tend to compress the fiber inside the drop. Moreover, because the droplet used in the experiments showed to perfectly wet the fibers (i.e. the contact angle between the drop and the fiber is $\theta_{\mathrm{Y}} = 0$), Young Dupré's relation becomes: $\gamma_{\mathrm{SV}} - \gamma_{\mathrm{SL}} = \gamma$.

If the compression between the two menisci is large enough, more fiber can be reeled inside the drop and coiling occurs. To capture the physics of this surprising phenomenon, we now compute the relation between the external tension T, surface tension forces, and other parameters, for the system to be in equilibrium.

Similarly to the energetical approach presented in Section 1.5.1. We list all the contributions to the total potential energy $\mathcal{V}$ of the system once in the coiling regime. The surface energies are $2\pi a\gamma_{\mathrm{SV}}L_{\mathrm{out}}$, $2\pi a\gamma_{\mathrm{SL}}L_{\mathrm{in}}$ where L_{in} is the length of the fiber inside the drop and L_{out} that of the fiber outside the drop. As we do not allow the spherical drop to deform in this model, the surface energy $4\pi R^2\gamma_{\mathrm{LV}}$ of the Liquid-Vapor interface stays constant and is therefore discarded. To compute the bending energy $\frac{1}{2}EI\int_0^{L_{\mathrm{in}}}\kappa^2(s)\,\mathrm{d}s$ of the coiled fiber, where $I = \pi a^4/4$ is the second moment of area of the circular cross-section of the fiber, we perform the simplification where the curvature $\kappa(s)$ of the fiber is uniform and equal to $1/R$, with s the arc length along the fiber. Finally we add the work of the external load $-T\,X$ where X is the end-to-end distance of the system (here, $X \simeq L_{\mathrm{out}}$ because $2R \ll X$). We use $L_{\mathrm{in}} + L_{\mathrm{out}} = L$ to replace L_{in} and find that, up to constant terms, the total potential energy of the system reads

$$\mathcal{V}(L_{\mathrm{out}}) = \left[2\pi a\left(\gamma_{\mathrm{SV}} - \gamma_{\mathrm{SL}}\right) - \frac{1}{2}EI\frac{1}{R^2} - T\right]L_{\mathrm{out}} + \mathrm{const.} \tag{2.5}$$

where we see that the linearity of $\mathcal{V}(L_{\mathrm{out}})$ implies that the load on the system, T, does not depend on its extension X, i.e. we have at equilibrium $\frac{\mathrm{d}\mathcal{V}}{\mathrm{d}L_{\mathrm{out}}} = 0$,

$$T = 2\pi a\gamma - \frac{1}{2}EI\frac{1}{R^2} \tag{2.6}$$

where we write $\gamma = \gamma_{\mathrm{SV}} - \gamma_{\mathrm{SL}}$. At first sight, one could then conclude that coiling inside the drop is always achievable (even when $\gamma_{\mathrm{SV}} < \gamma_{\mathrm{SL}}$) provided the right external load T is applied. Nevertheless if T is negative, that is if a global compression is applied on the

system, then global buckling occurs at $T \propto -\frac{EI}{L^2}$, which is almost zero since L, the total length of the fiber, is large. A necessary condition for coiling to occur in the absence of gravity is then $T > 0$ in Equation (2.6) or

$$2\pi a\gamma > \frac{\pi E a^4}{8R^2} \tag{2.7}$$

which yields a threshold for the fiber radius a as function of E, R, and γ with $a \propto R^{2/3} E^{-1/3}$. Figure 2.9 shows this threshold between coilable and uncoilable systems for silicone oil droplets ($\gamma = 21$ mN/m) sitting on a fiber (for this example we arbitrarly choose the fiber's Young's modulus as $E = 1$ GPa).

Equation (2.7) can be interpreted in terms of forces by saying that coiling is possible whenever the surface tension force of the drop $F_\gamma = 2\pi a\gamma$ is larger than the elastic bending reaction force $F_e = \frac{\pi E a^4}{8R^2}$ of the fiber. We note that in the present case where gravity is absent, it is possible to coil virtually any fiber by choosing a large enough drop: for all (a, E) there exists a R such that Equation (2.7) is satisfied.

In this first approach, gravity is ignored and this angle can sometimes be adopted experimentally for small enough systems, where the major forces involved largely overcome gravitational forces. Figure 2.10 presents two snapshots of a bare polyurethane (TPU) fiber (radius $a = 3.3\,\mu$m) with no droplets sitting on it, the fiber is then compressed by bringing its two ends closer. Since no liquid droplets are present, the fiber buckles globally upon its compression. Note that it moves upwards due to uncontrolled air flows near the setup (the lighting system may heat up the surrounding air locally and thus generate thermal plumes responsible for convection flows).
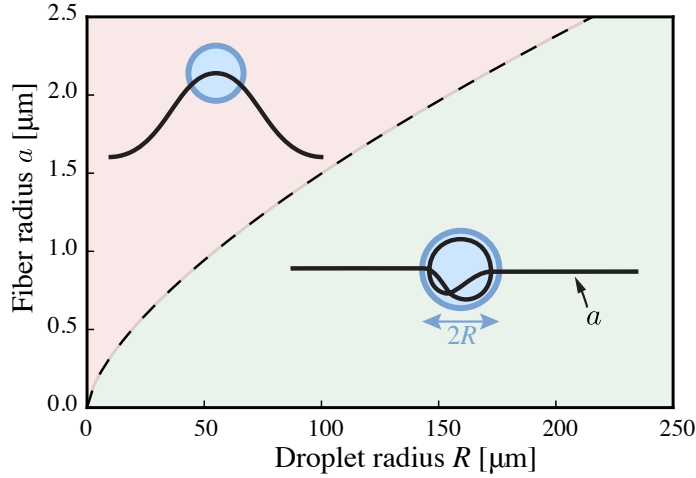
Figure 2.9 – Graphical representation of Equation (2.7) for a silicone oil droplet ($\gamma = 21$ mN/m) sitting on a bare fiber (of Young's modulus $E = 1$ GPa in this example). For a given fiber radius a, in-drop coiling is energetically favorable for a large enough drop. In this case, the compressive capillary force $2\pi a\gamma$ overcomes the elastic bending force $\frac{\pi E a^4}{8R^2}$ and the fiber is coiled inside the drop.

The thermoplastic polyurethane (TPU) fibers are fabricated from pellets (BASF) following a manual melt-spinning process described in Elettro (2015) where a TPU pellet is molten at 225°C on a hot plate and then touched by the tip of needle. Extracting the needle rapidly then draws out a microfiber which immediately solidifies in the air, leaving the operator with a meter-long micro-meter wide fiber. The different TPU's Young's moduli were measured through a force displacement test using the Femto-Tools micro-forces instrument FT-MTA02 (capacitive deflection measurement).

The fiber, in its extended state, is then coated with a thin layer of silicone oil (surface tension $\gamma = 21$ mN/m) which, through the Rayleigh-Plateau instability, rapidly destabilizes in a series of droplets, now decorating the fiber (see Figure 2.11). Upon global compression
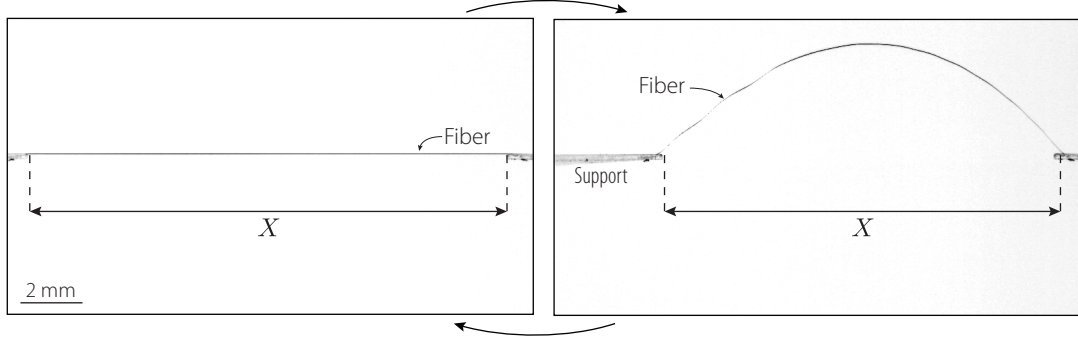
Figure 2.10 – Bare TPU fiber (TPU E1185A, radius $a = 3.3\,\mu$m and Young's modulus $E = 23$ MPa) with no drop sitting on it. Upon compression, the fiber buckles globally and environing air flows lift it.

of the system, a first event of local buckling followed by coiling inside a drop 'swallows' excess fiber. As compression is pursued, more fiber is gradually coiled inside the drop, thus leading to the coalescence of surrounding droplets. One drop of silicone oil (radius $R = 56\,\mu$m) finally remains and compression is entirely absorbed by this self-organized fiber 'reserve': local fiber loops inside the drop. In this case, $F_\gamma = 2\pi a\gamma = 435$ nN and $F_e = \frac{\pi E a^4}{8R^2} = 341$ nN, the condition presented in Equation (2.7) is respected – capillary compressive forces overcome the elastic buckling resistance of the fiber.

> The droplets used for the experiments are silicone oil droplets (viscosity 100 cSt at 25 °C) from Sigma-Aldrich. It is to be mentioned that this silicone oil does not swell TPU, PLA and PEDOT:PSS, but does swell PVS. As a first order approximation, no Young's modulus rectifications were applied to the PVS beams. However, characteristic dimensions of these PVS beams increased by about 20% due to this swelling. Silicone oil was found to perfectly wet all of the used materials (Young-Dupré equilibrium wetting angle $\theta_Y = 0$) which is why we consider $\gamma_{SV} - \gamma_{SL} = \gamma \cos\theta_Y = \gamma$, where γ_{SV}, γ_{SL} and γ are respectively the Solid-Vapor, Solid-Liquid and Liquid-Vapor specific interface energies.

2.3 In-drop coiling of a bare fiber in the gravity field

In the previous section we saw that, if gravity is neglected, coiling can be activated on virutally any fiber provided a large enough liquid drop is used. In the present section we show that once gravity is accounted for, there is an upper limit for the radius of the fiber (of a given material) for which coiling is possible. We consider the system of Figure 2.12, write the total potential energy, and compute its equilibrium. The bending energy is $\frac{1}{2}\,EI\,\frac{1}{R^2}\,L_{\text{in}}$ and, as explained in the previous section, surface energies add up to $2\,\pi\,\gamma\,L_{\text{out}}$ where $\gamma = \gamma_{\text{SV}} - \gamma_{\text{SL}}$. The potential energy for the weight of the drop is $Mg\,y_C$ where C is the center of the spherical drop and $M = \frac{4}{3}\pi\rho R^3$, ρ being the density of the liquid and g the acceleration of gravity. The work of the external load Λ is $-\Lambda X$ where $X \approx L_{\text{out}}\,\cos\beta$. Using $L_{\text{in}} = L - L_{\text{out}}$, the total potential energy is then, up to constant terms

$$\mathcal{V}(\beta, y_C, L_{\text{out}}) = \left(2\pi\gamma - \frac{1}{2}\frac{EI}{R^2} - \Lambda\,\cos\beta\right) L_{\text{out}} + Mg\,y_C \tag{2.8}$$

The three variables of $\mathcal{V}$ are linked by the relation $2y_C + L_{\text{out}}\,\sin\beta = 0$ which expresses the fact that the point D is constrained vertically. We therefore use

$$\mathcal{L} = \mathcal{V} - V\,(2y_C + L_{\text{out}}\,\sin\beta) \tag{2.9}$$
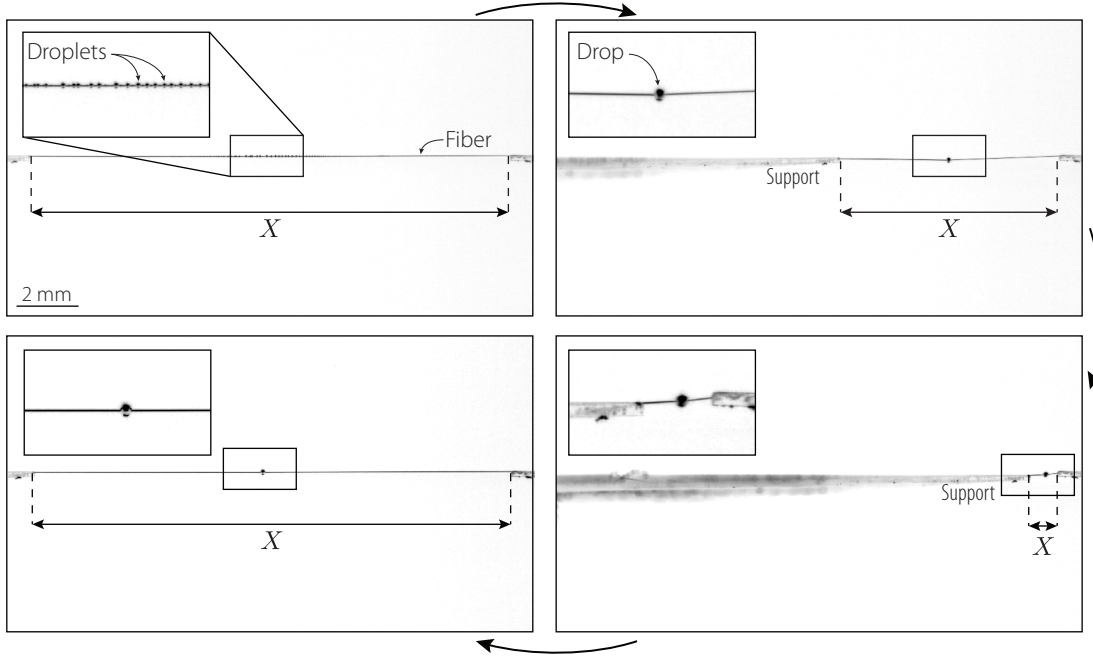
Figure 2.11 – TPU fiber (same as in Figure 2.10, $a = 3.3\,\mu$m and $E = 23$ MPa), now decorated with silicone oil droplets. Upon compression, the fiber undergoes coiling inside the droplets which thereafter coalesce with their neighbors and finally form a single drop ($R = 56\,\mu$m). We here perform a 20-fold compression-extension cycle.

to write the equilibrium of the system as $(\partial\mathcal{L}/\partial L_\mathrm{out}, \partial\mathcal{L}/\partial\beta, \partial\mathcal{L}/\partial y_C) = \mathbf{0}$. Here, V is the Lagrange multiplier associated with the constraint in the vertical position of D and is therefore interpreted as the vertical reaction force from the support at the right end of the fiber. Equilibrium is such that

$$\Lambda\cos\beta + V\sin\beta = 2\pi a\gamma - \frac{1}{2}\frac{EI}{R^2} \tag{2.10a}$$

$$V = \frac{Mg}{2} \tag{2.10b}$$

$$V\cos\beta = \Lambda\sin\beta \tag{2.10c}$$

The last equation shows that the total external force on the system at point D, $\Lambda\mathbf{e_x} + V\mathbf{e_y}$, is along the direction β, that is the fiber outside the drop carries no shear force but a tension $T = \Lambda\cos\beta + V\sin\beta$. The first and second equations in (2.10) are then rewritten
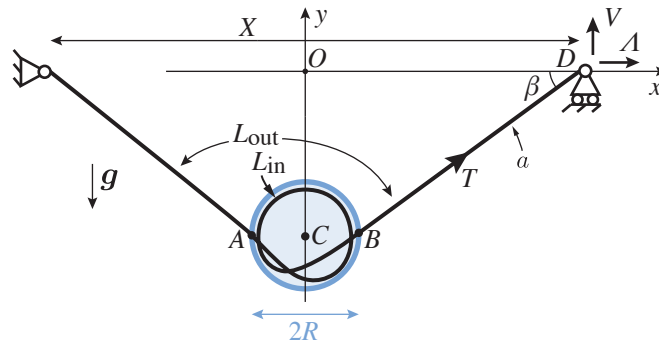
Figure 2.12 – Cylindrical fiber of radius a undergoing coiling inside a liquid drop of radius R in the gravity field. Due to gravity, the coiled state is sagging as the drop's weight pulls it downwards. The equilibrium state displays a sagging angle β which depends on the system parameters, as described in Equations (2.11) and (2.12).

as

$$T = 2\pi a\gamma - \frac{1}{2}\frac{EI}{R^2} \tag{2.11}$$

$$Mg = 2T\sin\beta \tag{2.12}$$

where (2.12) shows that the tension T has to be positive, a limitation already found in the previous Section. Moreover once the parameters Mg, a, γ, EI, R are given, Equations (2.11) and (2.12) yield the angle β at which the system is going to experience coiling, this equilibrium angle β increasing with the weight Mg. As $\beta < \frac{\pi}{2}$, a necessary condition for coiling to occur in the presence of gravity is $T > \frac{Mg}{2}$ which is rewritten as

$$2\pi a\gamma > \frac{\pi E a^4}{8R^2} + \frac{2}{3}\pi\rho g R^3. \tag{2.13}$$

In the force interpretation introduced in the previous Section, this means that for coiling
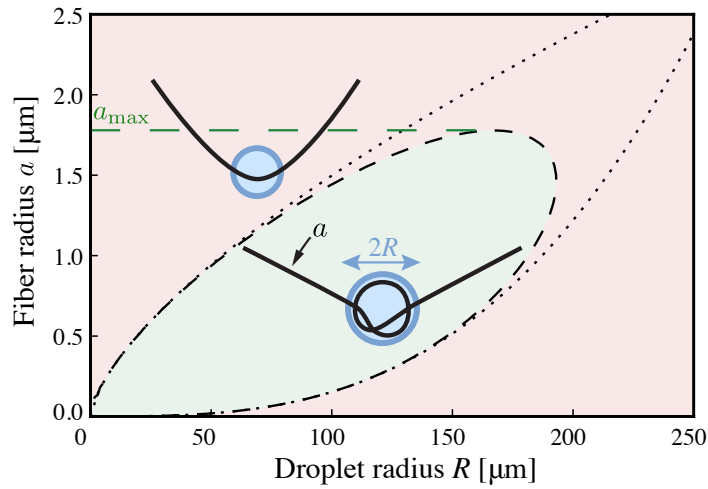
Figure 2.13 – Graphical representation of the inequality (2.13) for a silicone oil drop ($\gamma = 21$ mN/m, $\rho g = 9600$ N/m³) sitting on a fiber (Young's modulus $E = 1$ GPa in this example). For a given fiber of radius a to undergo in-drop coiling, the drop radius R has to be large enough. However, the drop's weight will hinder coiling and eventually prevent it when R exceeds a certain treshold. This generates a coiling region which displays a limit for the fiber radius $a_{\max} = a_{\max}(\gamma, \rho g, E)$ described in Equation (2.14). The upper dotted curve corresponds to the elasto-capillary limit described in section 2.2 (no gravity) and the lower dotted curve shows the gravito-capillary limit $4/3\pi\rho g R^3 < 2 \times 2\pi a\gamma$.

to be possible, surface tension has to overcome the weight of the drop in addition to the bending force of the fiber. Figure 2.13 shows the region, in the plane (a, R), where coiling is possible. We see that in the presence of gravity, once the material parameters ρg, γ, E are given, there is a maximum value $a_{\max}$ to the radius a of the fiber for which coiling is possible. Differentiating (2.13) with respect to R, we compute this maximum radius to be

$$a_{\max} = 2.78 \, \gamma^{5/7} \, (\rho g)^{-2/7} \, E^{-3/7} \tag{2.14}$$

This limitation is due to the fact that capillary forces exerted by an exceedingly large drop are not sufficient to lift it: the weight of the drop prevents it from moving upwards on the fiber. For liquid parameters (used throughout this Chapter) $\rho g = 9600$ N/m³ and $\gamma = 21$ mN/m, we plot in Figure 2.14 the radius $a_{\max}$ as a function of the Young's modulus E of the material of the fiber. In the same figure we report on the experimental coiling character of several fibers and find a good agreement with theory. Moreover the sequence presented in Figure 2.15 provides an example of a heavy silicone oil drop sitting on a TPU fiber. Just as in Figure 2.11, compression of the fiber's ends leads to in-drop coiling of the fiber.

However, in this case, the significant weight of the drop pulls it downwards and the system therefore sags with an angle β defined in Figure 2.12.
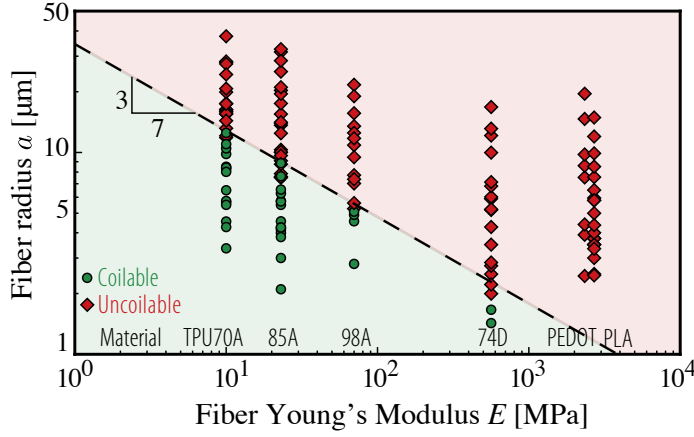

Figure 2.14 – Theoretical and experimental coilable and uncoilable fibers of different materials in the corresponding optimal silicone oil droplet. The theoretical limit between the coilable and uncoilable systems is given in Equation (2.14) and experiments validate theoretical power law $a_{\mathrm{max}} \propto E^{-3/7}$ and the corresponding prefactor. For PEDOT:PSS and PLA fibers, no coiling ever occurred as we were not able to produce thin enough fibers. $\gamma = 21$ mN/m, $\rho g = 9600$ N/m^3.

Polylactic acid (PLA) is commonly used for 3D printing, its Young's modulus was measured using a Shimadzu AG-X Plus electromechanical test frame on a PLA wire of radius 1.5 mm. Just as for the TPU, PLA fibers were fabricated with a melt-spinning technique: a small amount of PLA was molten on a hot plate (290°C) and subsequently pulled out rapidly with the tip of a needle, thus creating the solid microfiber. No active control on the fiber's cross-section radius is possible with this fabrication technique, but it was optically measured after its fabrication for each fiber using a Leica macroscope (VZ85RC) with a Leica DFC-295 camera. The optical resolution of this macroscope is of the order of magnitude of the diameter of the thinnest fibers that were used (around 2 microns). Since the bending stiffness of a cylindrical fiber is proportional to the fourth power of the radius of its cross section, the fibers' radii are a key parameter in the experiments. Therefore an algorithm was written to take into account the blurriness of the image near the fiber edges, and after image post-processing the absolute uncertainty on the fiber's radii was lowered to 0.5 μm.

The materials used throughout these experiments are presented in Table 2.1.

Material	Young's modulus E
PVS shore 8	200 $\pm$ 30 kPa
TPU E1170A	9.50 $\pm$ 2 MPa
TPU E1185A	23.6 $\pm$ 4 MPa
TPU E1198A	66 $\pm$ 10 MPa
TPU E1174D	560 $\pm$ 40 MPa
PEDOT:PSS	2.5 $\pm$ 0.7 GPa
PLA	2.7 $\pm$ 0.7 GPa

Table 2.1 – The materials used for fiber fabrication and their respective Young's modulus E.

In order to determine whether a fiber (with or without auxiliary soft fiber) was 'coilable' in a silicone oil droplet, about 10 droplets of different sizes were put on the fiber, seeking the best droplet size (big enough to allow coiling, but not too big for it not to be too heavy). If the fiber undergoes at least 2 coils inside one of the drops upon compression of its ends, at whichever hanging angle, the fiber is considered 'coilable'. If no droplet leads to this type coiling, the fiber is considered 'uncoilable'. Following this procedure, a fiber would first be tested alone (without auxiliary soft beam), and then would be affixed to the auxiliary soft beam and the composite fiber would be tested. The core fiber and the auxiliary beam stick to each other outside the droplet through the formation of a liquid bridge, but detach from one and other inside the liquid droplet.
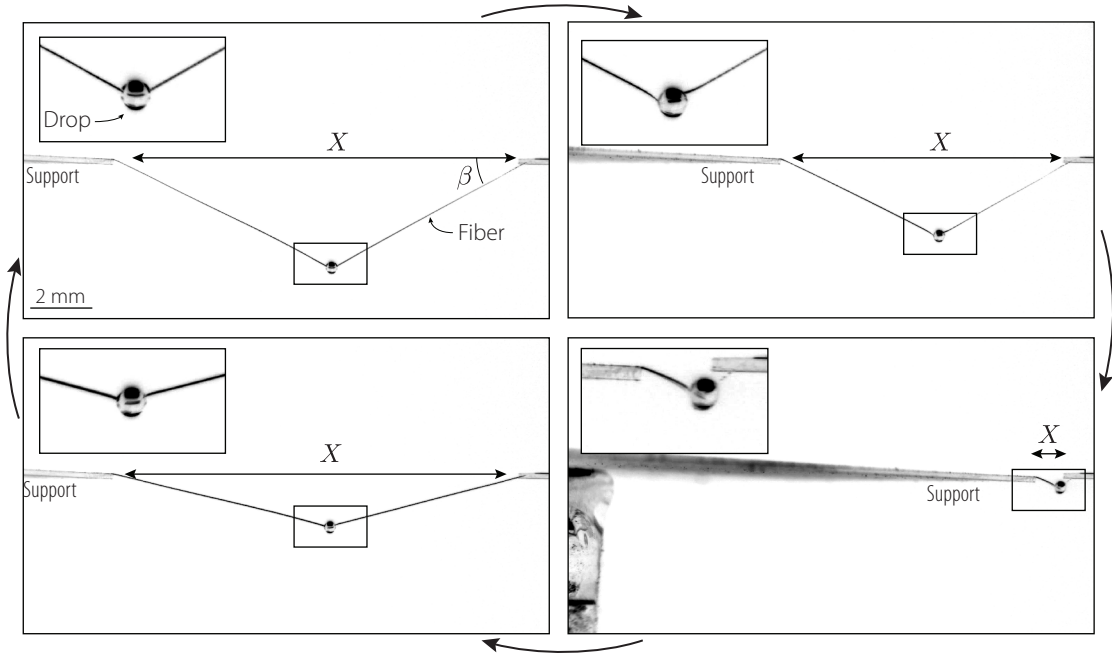
Figure 2.15 – TPU fiber (as in Figure 2.10, $a = 3.3\,\mu$m and $E = 23$ MPa), now decorated with a large silicone oil drop ($R = 215\,\mu$m). When the ends of the fibers are brought closer, the fiber spontaneously coils inside the drop, but with a characteristic hanging angle β caused by the weight of the drop which pulls it downwards. Note that the angle β is not perfectly constant throughout the compression and extension phases.

2.4 Coiling the uncoilable: the auxiliary soft beam

The elasto-capillary coiling mechanism allows to create composite threads that are highly extensible: as a large amount of fiber may be coiled inside a droplet, the total length X of the system may vary by more than a factor ten (Elettro et al. 2016). This extreme mechanical feature could be of interest to design components for stretchable electronics devices. Typical Young's modulus for conducting materials are ~ 100 GPa, which requires the use of sub-micronic fibers, see Figure 2.14 and Equation (2.14). Equation (2.13) shows that for coiling to occur, surface tension has to overcome the sum of the weight of the drop and the bending force of the fiber. A large Young's modulus E implies a large bending force unless we use a drop with a large radius R. Nevertheless we have seen in the previous section that increasing the drop radius is eventually unfavorable to coiling, as it makes the weight too large. Alternatively we can try to increase the surface tension force $2\pi a\gamma$. The span of the possible values for γ being restricted for classical liquids, we are left with the option of increasing the contour length of the triple line, that is the perimeter $2\pi a$ of the fiber. As increasing a rapidly increases the bending force we seem to be in an inextricable situation. Yet the use of a second fiber with low Young's modulus and large perimeter is a way out. We use the system of Figure 2.16 where our fiber of circular cross-section (radius a) is combined to a beam of rectangular cross-section (width w_{soft}, height h_{soft}) and made of soft material (Young's modulus E_{soft}).

Zhermack Shore 8 Polyvinyl-siloxane (PVS), was used to fabricate the soft auxiliary beams. The following technique was used to obtain ~ 2 cm long fibers with $\sim 100\ \mu$m thin cross sections. Before reticulation, the PVS was poured on the 170 μm wide side of a microscope glass slide (VWR,

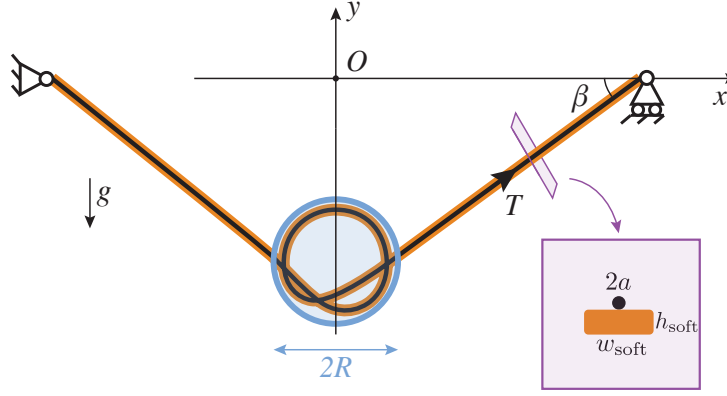**Figure 2.16** – Cylindrical fiber of radius a affixed to a soft beam (rectangular cross section: height h_{soft}, width w_{soft}) undergoing coiling inside a liquid drop of radius R in the gravity field. Due to gravity, the coiled state is sagging and the equilibrium state displays a sagging angle β which depends on the system physical parameters. The composite fiber (core fiber + soft beam) inherits the large beam's perimeter but its bending stiffness mainly depends on that of the core fiber.

22x50 mm, thickness No 1.5). A small part of the PVS then sat on the side when reticulation starts, whereas the surplus ran off the edges. After reticulation ($\approx$ 20 minutes at ambient temperature), a fiber is extracted from the side of the glass slide. Its cross section resembles a circular cap which we will here, for simplification, consider to be rectangular of height and width equal to those observed on the circular cap. These geometric dimensions were observed optically with the Leica macroscope. The aspect ratio $k = \frac{h_{\text{soft}}}{w_{\text{soft}}}$ of the cross-section of the fiber was found to be $k = 0.34$. The perimeter and the quadratic moment of inertia of the cross section were also approximated to be those of a rectangular cross section. Finally, the Young's modulus of our PVS was determined by a force-displacement measurement on a cylindrical fibre of radius 750 μm and length 8.5 cm.

The fiber adheres to the beam when they stand in the air but they separate once they are in the drop. On first approximation we consider the difference $\gamma = \gamma_{\text{SV}} - \gamma_{\text{SL}}$ to have the same value for both the beam and the fiber. Moreover we neglect the area of the fiber compared to that of the beam ($a \ll h_{\text{soft}}, w_{\text{soft}}$). The total potential energy of the system is then written as

$$\mathcal{V} = \left[2\gamma \left(h_{\text{soft}} + w_{\text{soft}} \right) - \Lambda \cos \beta - \frac{1}{2R^2} \left(EI + E_{\text{soft}} I_{\text{soft}} \right) \right] L_{\text{out}} + M g y_C \tag{2.15}$$

which we minimize following the same procedure as in the previous section. The condition for the composite fiber-beam system to coil is then

$$2\gamma \left(h_{\text{soft}} + w_{\text{soft}} \right) > \frac{1}{2R^2} \left(EI + E_{\text{soft}} I_{\text{soft}} \right) + \frac{2}{3} \pi \rho g R^3 \tag{2.16}$$

with $I_{\text{soft}} = \frac{1}{12} w_{\text{soft}} h_{\text{soft}}^3$. The region determined by this inequality is plotted in Figure 2.17 where it is compared to the coiling region for the bare fiber.

We note that the soft beam brings the possibility to use bigger drops and hence coil thicker (*i.e.* larger a) fibers. As in the previous Section, bearing in mind that $EI = \frac{\pi E a^4}{4}$, we calculate from (2.16) the maximum value a_{max} for the radius of the fiber for which coiling occurs in the composite system:

$$a_{\text{max}} = E^{-1/4} \left(1.62 \left(\gamma (h_{\text{soft}} + w_{\text{soft}}) \right)^{5/3} (\rho g)^{-2/3} - 1.27 \, E_{\text{soft}} I_{\text{soft}} \right)^{1/4} \tag{2.17}$$

Fixing ρg and γ, we study how a_{max} varies with the beam parameters for $h_{\text{soft}} = k \, w_{\text{soft}}$. We first optimize the cross-section and find that a_{max} is maximum for

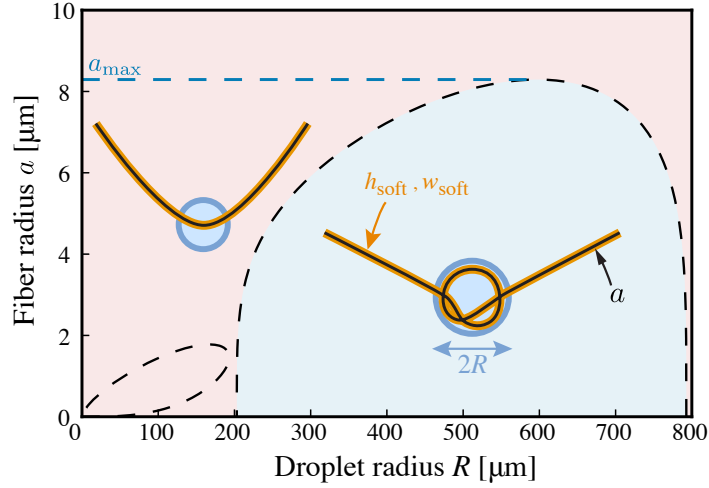$$w_{\text{soft}} = f(k) \, \gamma^{5/7} (\rho g)^{-2/7} E_{\text{soft}}^{-3/7} \tag{2.18}$$

Figure 2.17 – Graphical representation of the inequality (2.16) (blue tongue) for a silicone oil drop ($\gamma = 21$ mN/m, $\rho g = 9600$ N/m^3) sitting on a composite fiber composed of a core fiber of radius a and Young's modulus $E = 1$ GPa in this example, and a soft auxiliary PVS beam ($w_{\mathrm{soft}} = 190$ μm, $h_{\mathrm{soft}} = 65$ μm, $E_{\mathrm{soft}} = 200$ kPa). The small tongue near the origin corresponds to the one shown in figure 2.13, for a silicone oil droplet sitting on a bare fiber. The soft auxiliary artifact allows to achieve coiling for much thicker fibers (larger a). The largest theoretical coilable fiber has a radius a_{max} explicited in Equation (2.17).

see Figure 2.19-left. This optimum value for w_{soft} and the maximum value of a_{max} are plotted in Figure 2.19-right as a function of E_{soft}. We can now inject this optimum value (2.18) in (2.17) to obtain a maximum radius value that only depends on material parameters

$$\max(a_{\mathrm{max}}) = g(k)\, E^{-1/4}\, \gamma^{5/7}\, (\rho g)^{-2/7}\, E_{\mathrm{soft}}^{-5/28} \tag{2.19}$$

In our experiments, the thickness to width ratio $k = \frac{h_{\mathrm{soft}}}{w_{\mathrm{soft}}}$ of the auxiliary beam is $k = 0.34$. For readability, the dependence on k of w_{soft} in Equation (2.18) and $\max(a_{\mathrm{max}})$ in Equation (2.19) is given by two functions $f(k)$ and $g(k)$ who naturally derive from the optimization calculations, they respectively take the values $f(0.34) = 10.9$ and $g(0.34) = 3.0$.

Experimentally we use a beam with $E_{\mathrm{soft}} = 200$ kPa, $h_{\mathrm{soft}} = 65$ μm, and $w_{\mathrm{soft}} = 190$ μm not far from the optimum value, see Figure 2.19-left. We then study how a_{max} varies as the Young's modulus E of the fiber material is varied, see Figure 2.18. For the composite system $a_{\mathrm{max}} \propto E^{-1/4}$, which is favorable compared to the $E^{-3/7}$ behaviour observed in the case of a bare fiber. We find a good agreement for the power law of a_{max} as a function of E, but a factor 2 systematic error on the prefactor between theory and experiments for fibers with moduli in the MPa-GPa interval. The presented model considers that for coiling to happen, the surface tension force has to overcome the weight of the drop plus the elastic bending force of the fiber. This bending force is deduced from the curvature of a spherically coiled elastic fiber. However, at early stage of buckling, the elastic bending force is higher than that of the post-buckled (i.e. coiled) fiber. Moreover, experimentally, we observe that the composite fiber buckles in mode 2 (i.e. with an 'S' shape), therefore increasing the difference between the modeled bending force and the real one. This may explain the constant factor 2 error between theory and experiment.

An example of a fiber too stiff to coil inside a silicone oil drop at its native state (i.e. without auxiliary soft beam) is provided in Figure 2.20. In spite of the presence of a silicone oil drop on the fiber, compression does not lead to in-drop coiling, but to the global buckling of the fiber. In Figure 2.21, we affix an auxiliary PVS soft beam to this
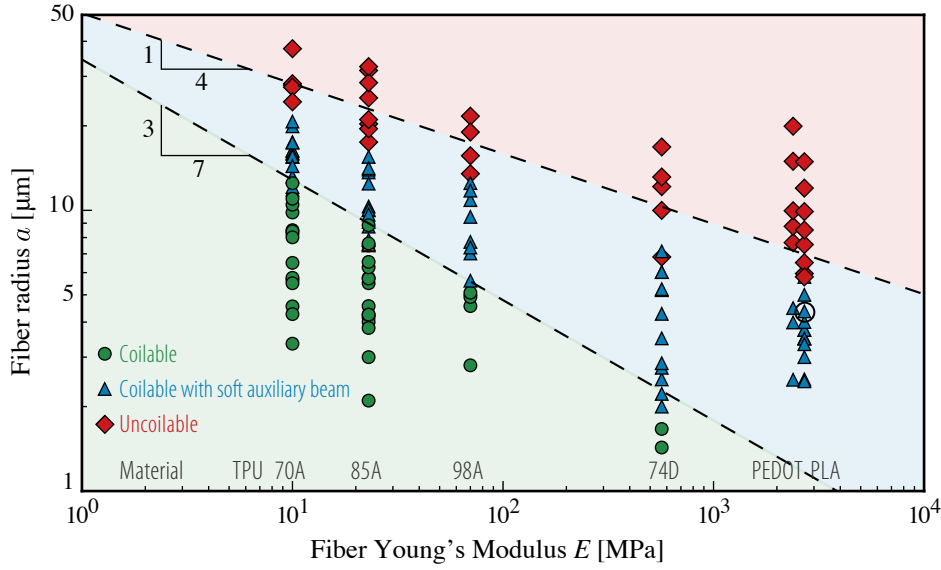
Figure 2.18 – Theoretical and experimental coilable and uncoilable fibers of different materials in the corresponding optimal silicone oil droplet ($\gamma = 21$ mN/m, $\rho g = 9600$ N/m^3). Composite fibers are composed of a core fiber (radius a and Young's modulus E) and an auxiliary PVS beam ($w_{\text{soft}} = 190$ μm, $h_{\text{soft}} = 65$ μm, $E_{\text{soft}} = 200$ kPa). The theoretical limit between the coilable bare fiber and the coilable fiber with auxiliary beam is given by Equation (2.14). The theoretical limit between coilable fibers with auxiliary beam and uncoilable fibers is given by Equation (2.19). For PEDOT:PSS and PLA fibers, no coiling could happen for a bare fiber but thanks to the auxiliary beam strategy, micronic fibers were coiled inside silicone oil droplets. The theoretical power law $a_{\max} \propto E^{-1/4}$ seems appropriate to describe the frontier between the coilable with auxiliary beam and the uncoilable region of this phases diagram. However, a systematic error of about a factor 2 between theory and experiments shows that this simple model could be refined. The circled experimental point will further be analyzed in details.
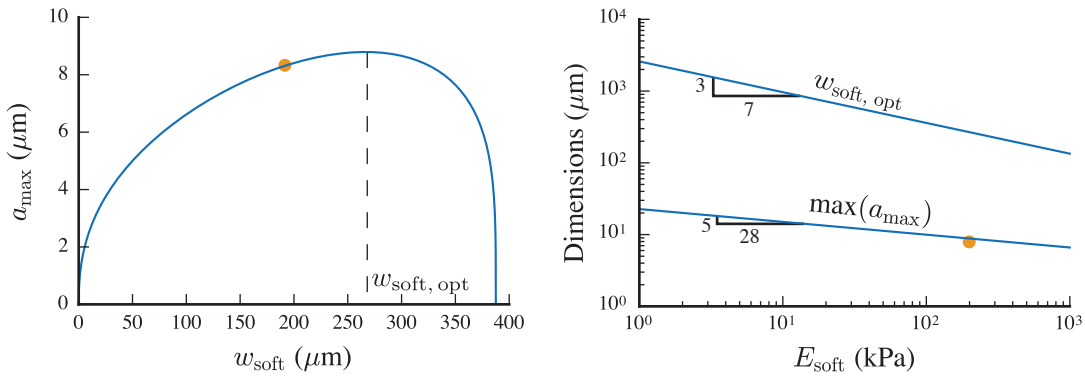
Figure 2.19 – Optimal dimensions for the fiber and the auxiliary beam width. The auxiliary beam has Young's modulus E_{soft} (PVS) and an aspect ratio $k = h_{\text{soft}}/w_{\text{soft}} = 0.34$ (value used experimentally). The silicone oil drop has $\gamma = 21$ mN/m and $\rho g = 9600$ N/m^3. The core fiber in this example has a Young's modulus of $E = 1$ GPa. **Left** – Largest coilable fiber radius $a_{\max}$ as a function of the width w_{soft} of the auxiliary beam of Young's modulus $E_{\text{soft}} = 200$ kPa as given by Equation (2.17). The function has a maximum at $w_{\text{soft}} = w_{\text{soft, opt}}$, see Equation (2.18). The orange dot corresponds to the experimentally-used auxiliary beam, which was not far from being optimal. **Right** – $w_{\text{soft, opt}}$ as a function of the Young's modulus E_{soft} of the auxiliary beam, Equation (2.18), and the corresponding maximum coilable core fiber's radius $\max(a_{\max})$, Equation (2.19). The orange dot shows the value $a_{\max}$, given by Equation (2.17), for the experimentally-used auxiliary beam.
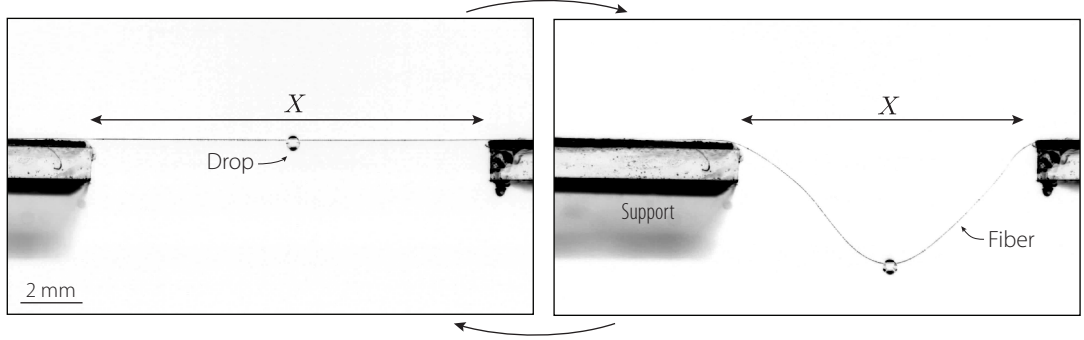
Figure 2.20 – Silicone oil droplet ($R = 240\,\mu$m) sitting on a bare PLA fiber ($a = 4.1\,\mu$m, $E = 2.7$ GPa). This fiber corresponds to the circled experimental point in Figure 2.18, it is too stiff to coil inside any silicone oil drop upon compression (various drop radii were tested, none led to coiling). Indeed, here the capillary compressive force is $F_\gamma = 0.54\,\mu$N is much lower than the elastic resisting force $F_e = 5.2\,\mu$N. The weight of the drop is $Mg = 0.55\,\mu$N.
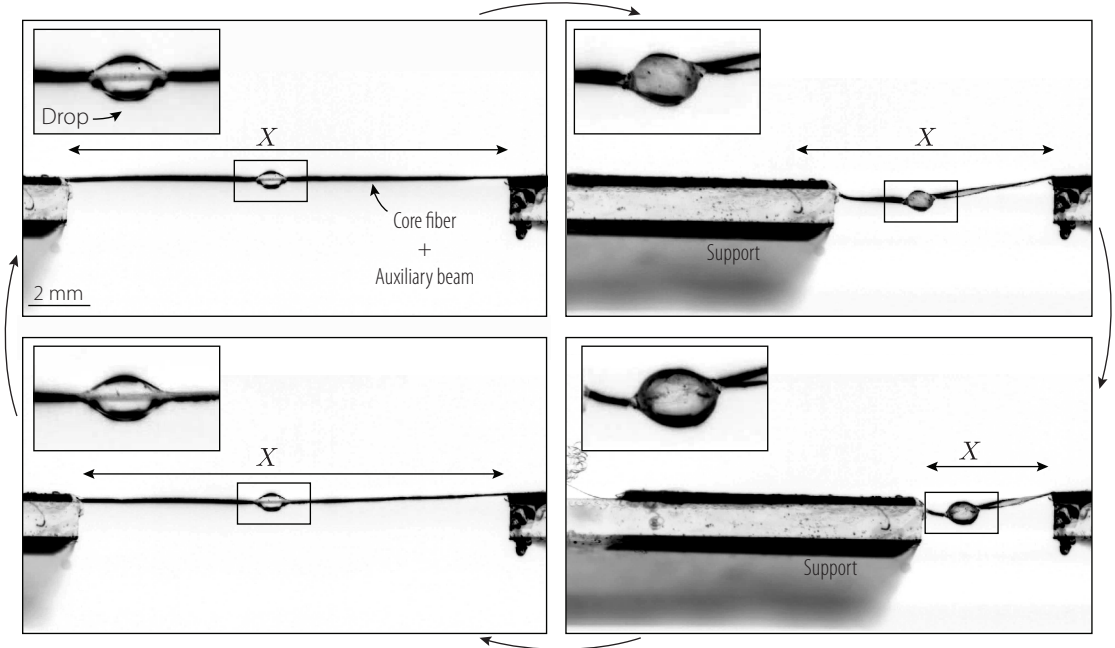
Figure 2.21 – A PVS auxiliary beam ($w_{\text{soft}} = 190\,\mu$m and $h_{\text{soft}} = 65\,\mu$m, $E_{\text{soft}} = 200$ kPa) is now affixed to the PLA fiber shown in Figure 2.20 ($a = 4.1\,\mu$m, $E = 2.7$ GPa) and decorated with a silicone oil drop ($R = 260\,\mu$m). The bare PLA fiber would not coil inside any silicone oil drop because of its high bending stiffness. The presence of the soft auxiliary beam does not increase the bending stiffness of the system significantly, but it highly increases the capillary compressive forces generated by the drop. When this composite fiber is compressed, it therefore spontaneously coils inside the drop.

PLA fiber and again put a drop on this composite fiber. The capillary compressive force between the drop's menisci is increased and in-drop coiling takes place when the ends of the fiber are brought closer.

> The core fiber and auxiliary beam naturally stick to each other outside the drop due to a capillary bridge which extends along the entire length of this composite fiber. Note that when coiling inside the drop, the two fibers no longer remain attached as they are now both immersed in the liquid drop.

2.5   Towards electronic functionalization: coiling conductive PEDOT:PSS fibers

As mentioned earlier, the coiling of a microfiber inside a droplet is a building block for highly extensible threads. Moreover, in-drop coiling stores the fiber surplus and releases it while keeping the system under tension and straight. This feature could be of interest for stretchable electronics where extensible electric connections are sought. As shown in figure 2.18, the auxiliary soft fiber technique allows for micronic fibers to undergo in-drop coiling for materials with Young's moduli up to few GPa, whereas they would have to be sub-micronic in the case of a bare fiber.
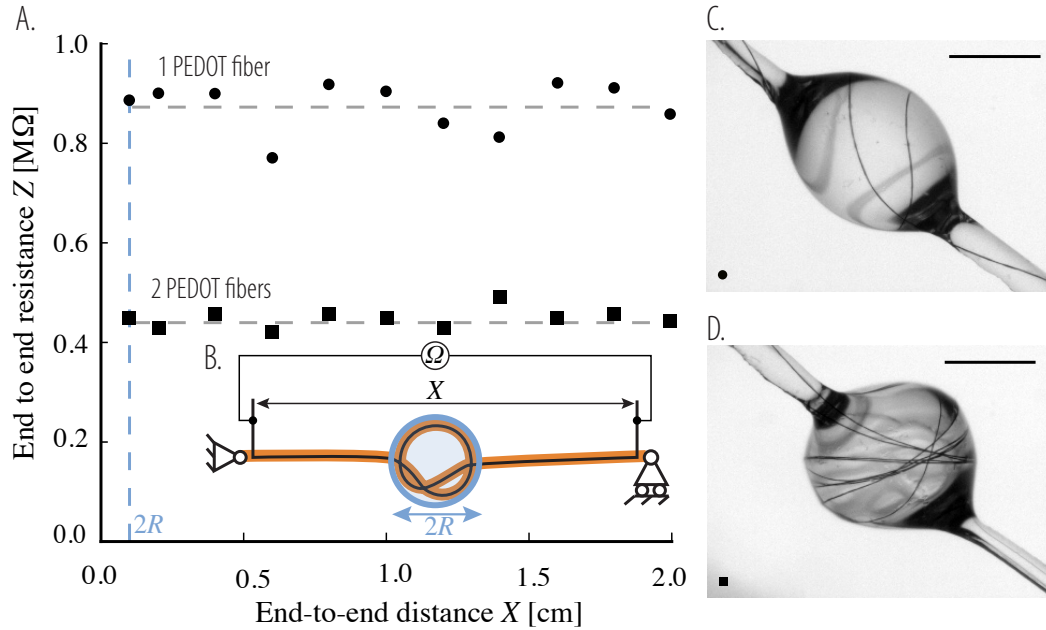
Figure 2.22 – Coiling conductive micronic PEDOT:PSS fibers ($a_{\text{PEDOT}} = 4.2\ \mu$m) inside a silicone oil droplet with the assistance of a soft auxiliary beam. This composite fiber conducts electricity throughout the 1900% stretching test. **A** – Electrical resistance versus of end-to-end distance X of the fiber for 1 and 2 PEDOT:PSS fibers and one soft auxiliary PVS beam. The resistance was measured between two points, further apart than the actual ends of the auxiliary beam (total fiber length: 3.5 cm), see **B**. Pictures **C** and **D** show macroscope snapshots of the droplets for $X = 1.6$ cm and $X = 0.8$ cm for 1 and 2 PEDOT:PSS fibers respectively. The dark PEDOT:PSS can easily be spotted inside and outside the droplet. The PVS beam, however, is only visible outside the droplet due to a refraction index too close to that of the silicone oil. Scale bar on both pictures: 500 μm.

PEDOT:PSS is a conductive GPa-modulus polymer with which micronic fibers can easily be spun. A single 3.5 centimeter long PEDOT:PSS fiber spun with a 50 μm needle has a cross section with radius $a_{\text{PEDOT}} = 4.2\ \mu$m and an end-to-end resistance of about $Z_0 = 0.90$MΩ.

This corresponds to a specific conductivity of $\sigma = 7$ S/cm, which is approximately what is found for the P-grade PEDOT:PSS in (Okuzaki et al. 2009), $\sigma = 11$ S/cm. Figure 2.22 shows the end-to-end electrical resistance $Z(X)$ of this conductive fiber coupled with a PVS auxiliary beam ($w_{\text{soft}} = 190\,\mu$m and $h_{\text{soft}} = 65\,\mu$m), as a function of the end-to-end distance X. Starting with $X = 2R = 1$ mm where the entire fiber and beam are coiled inside the drop, we stretch the system up to a factor 20 where everything is straight. Throughout this 1900% extension the end-to-end resistance of the composite system does not decrease but fluctuates around the nominal resistance Z_0.

Poly(3,4-ethylenedioxythiophene)-poly(styrenesulfonate) (PEDOT:PSS, a conductive polymer) dry re-dispersible pellets from Sigma-Aldrich were used to draw fibers using the wetspinning process described in Okuzaki and Ishihara (2003); Okuzaki et al. (2009). A 2.9% wt. PEDOT:PSS-water solution was first prepared using a Mettler-Toledo MS scale. The solution was then injected through a calibrated needle (Adhesive Dispensing Ltd and Cluzeau Info Labo) out of a Terumo 10mL glass syringe into an acetone bath. As water is more soluble in acetone than in PEDOT:PSS, it flows out of the PEDOT:PSS, which itself is not soluble in acetone, and the injection leads to the contraction and solidification of a continuous flow of PEDOT:PSS. The resulting solid microfiber was then manually extracted from the acetone bath and dried out in ambient air for about one minute. Even though the PEDOT:PSS fibers thereby created are not exactly the same as in Okuzaki et al. (2009), we use their value for the Young's modulus. Our PEDOT:PSS fibers showed a specific electric conductivity of 7 S/cm.

We then design a second system where two PEDOT:PSS fibers are coupled to the PVS auxiliary beam and find a weakly fluctuating resistance around 50% of Z_0. We conclude that no permanent short circuits happen in spite of the multiple possible contacts between the coils in the drop. However, brief spontaneous short-circuits could explain the observed fluctuations in resistance. A one-loop length shortening (i.e. $2\pi R$) would lead to a 9% drop of end-to-end resistance, consistent with the typically observed fluctuations of figure 2.22-A ($2R = 1$ mm and the total probed length is 3.5 cm).

End-to-end electrical resistance of straight and in-drop coiled PEDOT:PSS microfibers were measured using an ohmmeter (Amprobe 5XP-A). The electrical connections between macro-parts and the microfiber were established with a Hi-Bond Conductive Copper Tape.

2.6 Conclusions

In conclusion, we showed that by introducing a soft supporting beam, we induce in-drop coiling on fibers with an *a priori* too large bending stiffness: the beam-fiber composite system coils in situations where the bare fiber would not. We thus have designed a composite system capable of coping with extension ratios larger than twenty while staying functional. The high extensibility is due to the liquid drop that stores and gives back excess length, but liquid forces also enable the system to stay taut.

The conductor property is brought by a fiber that needs an auxiliary supporting beam to coil inside the drop. Like in every successful hybrid system, each component brings its own function while gently combining with the others. The mechanical response of the composite system is inherited from that of its components. A bare conductive fiber, of length L, carrying a drop does not coil and hence exhibits a force-extension curve shown in red in Figure 2.23: if the end-to-end distance X is larger than L, the fiber is stretched and the applied tension T grows linearly with a steep slope, due to the high Young's modulus of the fiber, while if $X < L$ global buckling occurs and the applied tension is negative, see red curve. Now if one considers the soft supporting beam alone, stretching ($X > L$) is achieved
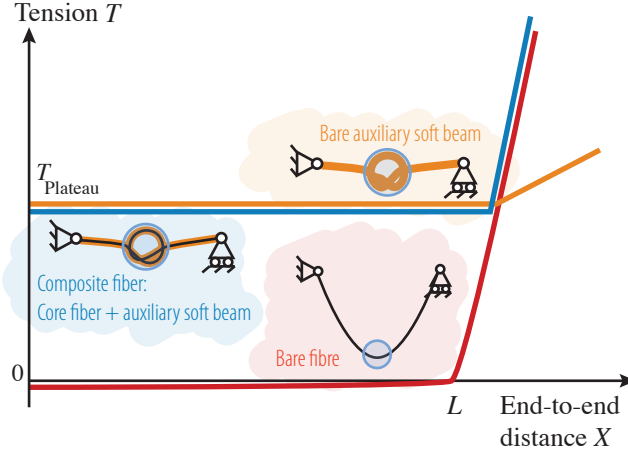
Figure 2.23 – Phenomenological mechanical behaviors for the different systems.

with a gentle slope and compression ($X < L$) leads to in-drop coiling at a constant plateau value T_p, see the orange curve. The composite system inherits from the behavior of the soft supporting beam under compression, with an in-drop coiling at virtually the same plateau value T_p, and from the behavior of the conductive fiber under extension with the same steep slope when $X > L$, see the blue curve.

We further showed that the composite system is conducting electricity with a constant resistance over a large range of end-to-end distances (from $X = L/20$ to $X = L$): in-drop coiling does not affect the conductive character of the fiber. Finally we gave the limiting radius of the fiber for which in-drop coiling could be achieved, as a function of material properties (Young's moduli E and E_{soft}) and liquid properties (density ρg and surface tension γ). Further work involves the study of other geometries for the supporting beam (*e.g.* cylindrical coating) and other physical properties for the functional fiber (*e.g.* light conductivity) with the aim to design super-extensible conductive systems.

To sum up the auxiliary beam strategy presented in this Chapter, Figure 2.24 provides the possible scenarios regarding the spontaneous coiling of a fiber inside a liquid drop sitting on it.
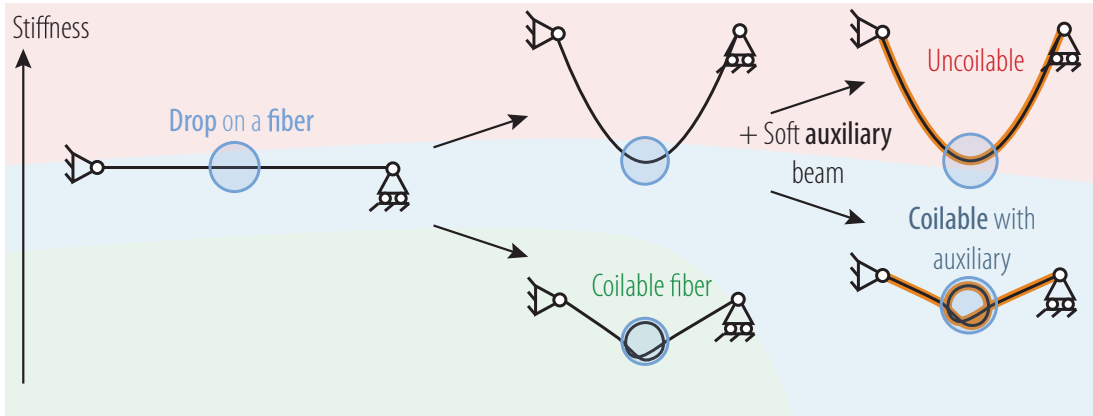
Figure 2.24 – Graphical summary of the auxiliary beam strategy for the onset of elasto-capillary coiling of stiff fibers.

3 Coiling and uncoiling dynamics

Contents

Figure 3.1 – A drop is deposited on a fiber, leading to elasto-capillary coiling. **A** – If the ends of the fiber are kept at a fixed distance or slowly separated, the tension F in the fiber is given by T_p. **B** – If a boundary is now set in rapid motion, the tension F is no longer given by T_p but depends on the displacement velocity.

In the previous Chapter, we have shown that the capillary forces generated by a wetting droplet sitting on a fiber can be sufficient to make the fiber coil within it. Indeed, if the compressive capillary load between the drop's menisci $F_\gamma = 2\pi a\gamma$ overcomes the elastic resisting force $F_e = \pi E a^4/(8R^2)$, it becomes energetically favorable for the system to store fiber loops inside the drop when its ends are brought closer. Moreover, if this condition is satisfied, elasto-capillary coiling sets the fiber under tension, given by its plateau equilibrium

value $T_{\mathrm{p}} = F_\gamma - F_e$ at any extension (as long as fiber slack is available to be coiled inside the drop). This theoretical result is valid for a quasi-static extension experiment, and therefore does not take the extension rate into account. Figure 3.1-A describes this situation; for a slow enough displacement velocity $U \simeq 0$ of an end of the fiber, the tension in the fiber is given by T_{p}.

The uncoiling (coiling) behavior of the fiber out of (into) the drop greatly depends on the velocity at which the coils are extruded out of (ingressed within) the drop. Studying the dependence of the fiber tension on the global extension rate seems natural and may be of interest in the context of the prey trapping ability of the spider web. As an insect flies into the spider web, the capture silk is suddenly largely extended and if preformed elasto-capillary coils are present in the structure, their uncoiling upon impact may significantly contribute to the energy dissipation of the insect. A simplified approach for this scenario is provided Figure 3.1-B where the mobile end of the fiber is now moved at a velocity U. The tension in the fiber is no longer given by T_{p} but is a function of the displacement velocity U.

In order to give theoretical and experimental insight into the elasto-capillary coiling and uncoiling dynamics, we first introduce a simple model to describe viscous dissipation at the triple line in the case of a drop sliding along a straight fiber. We then design four experiments to test this model and extend it to the coiling and uncoiling dynamics of the drop-on-fiber system.

3.1 Triple line advancing along a rod: an introduction

When the ends of the fiber are separated as in Figure 3.1-B, some slack fiber exits the drop and the relative difference in velocity of the drop and the fiber generates viscous dissipation inside the drop. In order to apprehend the forces applied on the fiber as it uncoils out of the drop, we first consider the idealized configuration in Figure 3.2 where a rigid cylindrical fiber of radius a is withdrawn out of a liquid bath of surface tension γ and viscosity η at a velocity $\boldsymbol{U} = U\,\boldsymbol{d}$.
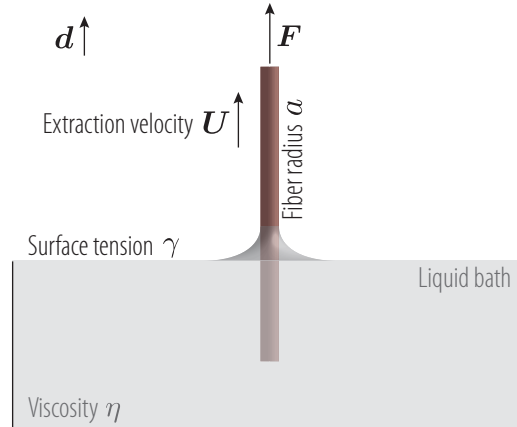
Figure 3.2 – A fiber of radius a is extracted from a liquid bath at velocity $\boldsymbol{U}$. The force $\boldsymbol{F}$ required to achieve steady motion balances opposing capillary and viscous forces: $\boldsymbol{F} = \boldsymbol{F}_\gamma + \boldsymbol{F}_\eta$ where $\boldsymbol{F}_\gamma = 2\pi a \gamma\, \boldsymbol{d}$ and $\boldsymbol{F}_\eta = F_\eta(a, U, \eta)\, \boldsymbol{d}$, the unitary vector $\boldsymbol{d}$ is aligned with the fiber axis.

The fiber axis, described by the unitary vector $\boldsymbol{d}$, is perpendicular to the bath surface, the liquid perfectly wets the fiber and we neglect gravity. We study the influence of the extraction velocity $\boldsymbol{U}$ on the force $\boldsymbol{F} = F\,\boldsymbol{d}$ applied on the fiber at its upper end. First, we notice that even at zero velocity, capillarity imposes a force $\boldsymbol{F}(U = 0) = \boldsymbol{F}_\gamma$, necessary to

keep the system motionless. This capillary force is given by:

$$\boldsymbol{F}_\gamma = F_\gamma \, \boldsymbol{d} = 2\pi a \gamma \, \boldsymbol{d}. \tag{3.1}$$

When the fiber is set in motion at velocity $\boldsymbol{U}$, viscous dissipation acts against motion and we write $\boldsymbol{F}_\eta = F_\eta \, \boldsymbol{d}$ the force the operator has to apply to balance this viscous dissipation. The viscous force only depends a, η and U and dimensional analysis readily gives $F_\eta(a, \eta, U) \sim a\eta U$. The total force applied by the operator to extract the fiber of the bath at velocity $\boldsymbol{U}$ is finally given by:

$$\boldsymbol{F} = \boldsymbol{F}_\gamma + \boldsymbol{F}_\eta \tag{3.2}$$

In the next section, we focus on a liquid drop sliding along a fiber in order to further study the viscous dissipation force $\boldsymbol{F}_\eta$.

3.1.1 Theoretical framework: drop sliding along a fiber

We study a perfectly wetting drop sliding along a straight fiber and focus on friction forces. We consider the drop to be at its rest unduloidal configuration even when set in motion, i.e. we consider that friction forces do not deform the drop. For a drop with surface tension γ, viscosity η and moving at velocity U along the fiber, this assumption is reasonable for low capillary numbers, $Ca = \eta U/\gamma \ll 1$. The capillary number compares the viscous effects to their capillary counterpart and a low capillary number therefore indicates that viscous forces have little effect on the shape of the drop; the latter is dominated by surface tension. Figure 3.3 presents a schematic representation of a drop sliding on a fiber of radius a at velocity $\boldsymbol{U} = U \, \boldsymbol{d}$ with $\boldsymbol{d}$ the unitary vector aligned with the fiber axis. Note that U can take positive or negative values. The drop has an effective radius R and its axially symmetric unduloid profile $Y_{\mathrm{drop}}(X)$ is calculated using the expression introduced by B. J. Carroll (Carroll 1976), described in Equation (1.5). As it advances, the drop is slowed down by viscous friction forces for which we here seek an analytical expression.
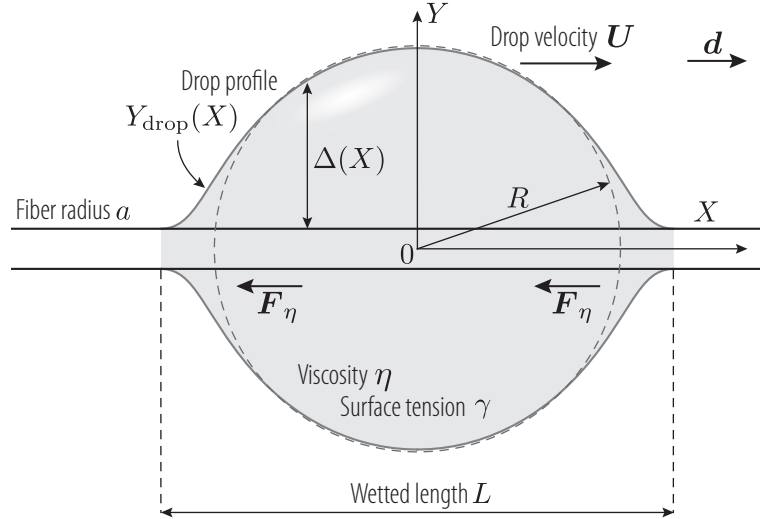
Figure 3.3 – Schematical drop advancing on a fiber. The unitary vector $\boldsymbol{d}$ is aligned with the fiber axis and the drop advances at velocity $\boldsymbol{U} = U \, \boldsymbol{d}$ with respect to the fiber. This motion generates viscous forces $\boldsymbol{F}_\eta$ at each side of the drop. It will be shown that the forces $\boldsymbol{F}_\eta$ are localized near the triple lines. Note that even though the drop is moving, we consider a left-right symmetric drop profile.

Taking advantage of left-right geometrical symmetry; we propose a simple model describing the viscous force $\boldsymbol{F}_\eta$ acting on the left side of the drop against its motion. As a first

approximation, we consider the liquid velocity to be zero at $Y = a$ (adherence at the fiber surface) and equal to the droplet velocity $\boldsymbol{U}$ at $Y = Y_{\mathrm{drop}}(X)$ where $Y_{\mathrm{drop}}(X)$ describes the drop profile along the axial direction X. Considering a linear velocity profile between $Y = a$ and $Y = Y_{\mathrm{drop}}(X)$, the viscous shear stress in the liquid at the fiber surface is approximated as

$$\tau(X) \approx \eta \frac{U}{\Delta(X)} \tag{3.3}$$

where

$$\Delta(X) = Y_{\mathrm{drop}}(X) - a \tag{3.4}$$

corresponds to the liquid thickness covering the fiber at the position X. Note that the linear velocity profile we here consider does not satisfy a zero shear stress condition at the drop surface as in de Gennes et al. (2005), i.e. the velocity profile does not provide $\tau = 0$ at $Y = Y_{\mathrm{drop}}$. In spite of this inaccuracy, the viscous dissipation physics depicted by our model remains valid and only a change in numerical prefactor results from this difference. We write $\boldsymbol{F}_\eta$, the viscous drag force applied by the fiber on the left half of the drop,

$$\boldsymbol{F}_\eta = -\int_{-L/2}^{0} 2\pi a \, \boldsymbol{d} \, \tau(X) \mathrm{d}X = -2\pi a \eta U \, \boldsymbol{d} \int_{-L/2}^{0} \frac{\mathrm{d}X}{\Delta(X)}. \tag{3.5}$$

The integrand in Equation (3.5), $\mathrm{d}X/\Delta X$, diverges at the triple line, where $X = -L/2$ because $\Delta(X = -L/2) = 0$. Although this divergence is physically inconsistent with a moving drop, it suggests that the viscous friction force $\boldsymbol{F}_\eta$ is localized near the triple line, and this assumption will be made throughout this Chapter. In order to bypass this divergence issue, referred to as the Huh-Scriven paradox (Huh and Scriven 1971), Pierre-Gilles de Gennes (de Gennes et al. 2005) introduces a cut-off length of the order of magnitude of the molecular size $m \sim 1$ Å for the liquid thickness Δ. This elegantly allows to regularize the singularity. Here, we do not attempt to solve the singular integral analytically but try to do so experimentally by writing:

$$\boldsymbol{F}_\eta = -2\pi a k \eta \boldsymbol{U} = -2\pi a k \eta \, U \, \boldsymbol{d} = F_\eta \, \boldsymbol{d} \tag{3.6}$$

with $F_\eta = -2\pi a k \eta U$ and the dimensionless friction coefficient k is given by the mathematical term:

$$k = \int_{-L/2}^{0} \frac{\mathrm{d}X}{\Delta(X)}. \tag{3.7}$$

Before carrying on, we verify that in this model, k does not depend on the drop radius R or the fiber radius a. Since the viscous force is localized near the triple line, we can intuitively assume that the drop radius will have little effect on the viscous drag force. However, a thicker fiber (larger a) corresponds to a larger meniscus region and since k strongly depends on the meniscus geometry, it may depend on a. In order to clear up this doubt, we normalize the variables X, Y_{drop}, R, L and Δ by the fiber radius a as follows:

$$x = \frac{X}{a}; \quad y_{\mathrm{drop}} = \frac{Y_{\mathrm{drop}}}{a}; \quad r = \frac{R}{a}; \quad l = \frac{L}{a}; \quad \delta = \frac{\Delta}{a} = \frac{Y_{\mathrm{drop}} - a}{a} = y_{\mathrm{drop}} - 1 \tag{3.8}$$

and rewrite Equation (3.7) with an $L/2$ shift:

$$k = \int_{0}^{L/2} \frac{\mathrm{d}X}{\Delta(X - L/2)} = \int_{0}^{l/2} \frac{a \, \mathrm{d}x}{a \, \delta(x - l/2)} = \int_{0}^{l/2} \frac{\mathrm{d}x}{\delta(x - l/2)}. \tag{3.9}$$

Equation (3.9) shows that even though it is still not rigorously defined, the coefficient k does not depend on the fiber radius a in this simple model. Indeed, a larger fiber radius leads to a longer meniscus region (which increases viscous dissipation), but it also leads to a thicker meniscus (this thickness is described by Δ). These two effects compensate each

other and the viscous dissipation force therefore does not depend on a. In order to evaluate the importance of the drop radius r on the coefficient k, we represent in Figure 3.4-A the normalized analytical solution of a drop at its rest shape (axially symmetric unduloid) on a fiber. A close-up on the meniscus is provided in Figure 3.4-B for different drop radii ($r = R/a$ ranging from 10 to 100). It is to be noted that the drop's dimensionless wetting length $l = L/a$ is adapted for each drop radius so that the triple line is placed at $x + l/2 = 0$. If the dimensionless effective drop radius r is large enough ($r > 10$), the similarity of the drop profiles near the meniscus, i.e. near $x + l/2 = 0$, suggests that the coefficient k, presented in Equation (3.9), does not depend on r.
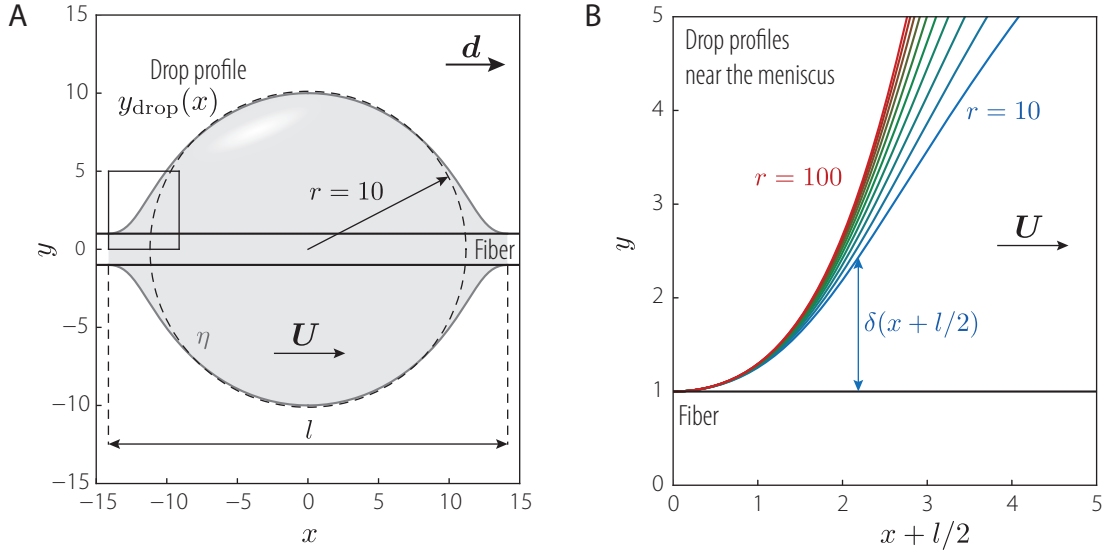
Figure 3.4 – **A** – Theoretical profile of a drop sliding on a fiber for $r = 10$ and $\theta_Y = 0°$ at a constant velocity U. It is here considered that motion is taking place at a low capillary number Ca, and the profile therefore corresponds to that of a drop sitting on a fiber in the axially symmetric unduloidal configuration at rest. **B** – Zoom on the triple line (around $x + l/2 = 0$) for different drop radii for r ranging from 10 to 100. Drops have very similar menisci profiles (near $x + l/2 = 0$) described by the liquid thickness $\delta = y_{\mathrm{drop}}(x) - 1$, regardless of their radius. All the variables (x, y, r, l and δ) are here normalized by the fiber radius a.

Finally, we normalize the viscous friction force at one meniscus by the capillary force $F_\gamma = 2\pi a \gamma$,

$$\boldsymbol{f}_\eta = \frac{\boldsymbol{F}_\eta}{2\pi a \gamma} = -k\, Ca\, \boldsymbol{d} = f_\eta\, \boldsymbol{d} \tag{3.10}$$

with $f_\eta = -k\, Ca$ and $Ca = \eta U/\gamma$.

In this chapter, we seek the friction coefficient k in the light of three experiments for a drop advancing on a straight fiber, as well as for a fiber coiling or uncoiling out of a drop. First, we give a non-exhaustive overview of the drag coefficients k brought forward in literature for different experimental configurations.

3.1.2 Friction coefficient k in literature

As mentioned earlier, P. G. de Gennes introduced a cut-off length of the order of the molecular size m for the liquid thickness covering the solid surface. This allows to give an expression for F_η for a drop exhibiting an equilibrium angle θ_Y with the fiber it slides on as in de Gennes et al. (2005):

$$\boldsymbol{F} = 2\pi a\, \frac{3\ln(L_{\mathrm{macro}}/m)}{\tan\theta_Y}\, \eta \boldsymbol{U} \tag{3.11}$$

where L_{macro} corresponds to a typical macroscopic length of the order of the cm and m is of the order of a few Å. The ln-term is therefore typically of the order of 15. Our friction coefficient k corresponds to the term $3\ln(L_{\mathrm{macro}}/m)/\tan\theta_{\mathrm{Y}}$ and it diverges for perfectly wetting liquids for which $\theta_{\mathrm{Y}} = 0$.

Haefner et al. (Haefner et al. 2015), propose an original experiment to quantify the viscous dissipation at the triple line of a drop advancing along a fiber. Figure 3.5-left, reproduced from this article, presents the setup. A thin hydrophobic glass fiber is first coated with a homogeneous polystyrene layer. The system is then heated above the glass transition temperature of polystyrene which therefore becomes liquid. The generated liquid viscous film quickly undergoes the Rayleigh-Plateau instability, leading to an array of drops sitting on the fiber and connected by thin metastable liquid films. The spontaneous dewetting of this thin film between two drops generates a triple line, set in motion towards the wet side due to the capillary imbalance. In this article, the authors show experimentally that the velocity U of the triple line does not depend on the size of the advancing drop and that it can universally be described by the law $\eta U = A^{-1}$ with $A = 3900 \pm 300$ m/N. In this configuration, the driving force F_{drive} is given by $F_{\mathrm{drive}} = 2\pi a|S|$ with S the spreading coefficient $S = \gamma(\cos\theta_{\mathrm{Y}} - 1)$ and since this driving force is balanced by the friction force $F_\eta = 2\pi ak\eta U = 2\pi akA^{-1}$, Haefner and collaborators predict a friction coefficient $k = A|S| = 106$ ($\theta_{\mathrm{Y}} = 60 \pm 5^{\circ}$ and $\gamma = 30.8$ mN/m).
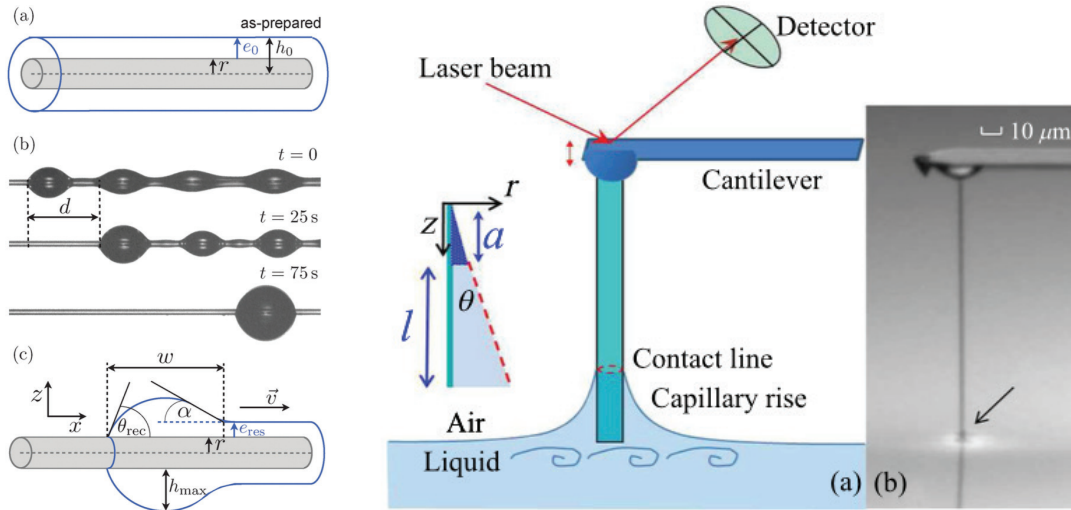
Figure 3.5 – **Left** – A glass fiber is first coated with a solid polystyrene film which is subsequently molten. The Rayleigh Plateau instability that follows leads to the dewetting of the liquid film which is set in motion due to the capillary imbalance. Reproduced from Haefner et al. (2015). **Right** – A glass fiber is glued onto the tip of an AFM cantilever and immersed in a liquid bath. Thermal fluctuations set the fiber in an oscillatory motion due to Brownian forces. This setup allows to directly measure friction forces of the triple line. Reproduced from Guo et al. (2013).

Another experiment, proposed in Guo et al. (2013) is presented in Figure 3.5-right. A vertical glass fiber is attached to an Atomic Force Microscopy (AFM) cantilever beam. The glass fiber is partially immersed in a liquid bath and random Brownian forces due to thermal fluctuations of the surrounding fluid induces a vertical oscillatory motion of the fiber. By analyzing the power spectrum of vertical deflections of the cantilever, the authors measure the friction coefficient $k = 0.8$ experimentally and show that it is independent of the liquid-solid contact angle. Note that in this case, the geometry is not exactly the same since the fiber pierces a planar liquid interface instead of a drop.

Finally, T. Gilet and collaborators (Gilet et al. 2010) study the velocity of perfectly wetting droplets sliding downwards along vertical nylon fibers. Here, the drop weight drives

the motion and once the stationary velocity is attained, viscosity balances gravity. In this article, the authors suggest that the friction coefficient k does depend on the fiber radius a. For viscous drops, they introduce:

$$k = \frac{0.33}{\sqrt{2a\kappa}} \ln(L_{\mathrm{macro}}/m) \tag{3.12}$$

which typically takes the value $k = 30$ for $a = 20\,\mu$m.

Viscous dissipation at the triple line is an ongoing research area among the fluid-dynamics community (Bonn et al. 2009) and the friction coefficient k, as defined here, does likely not capture the entire physics of dewetting. This Chapter introduces a new experiment to further study the contact line dynamics; we quantify the viscous dissipation force of a solid fiber uncoiling out of a liquid drop.

3.2 Experiment 1: Drop sliding along a vertical fiber

3.2.1 Drop sliding along a straight fiber

In order to test the validity of Equation (3.10), we perform the experiment described in Gilet et al. (2010) where drops slide down vertical fibers, Figure 3.9 provides a schematic representation of this first experiment. A perfectly wetting drop of known volume Ω is deposited on a vertical fiber of radius a. The drop starts sliding downwards due to its weight and rapidly attains a stationary velocity $\boldsymbol{U} = U\,\boldsymbol{d}$. The unitary vector $\boldsymbol{d}$ now points downwards and is aligned with the fiber. Note that the velocity $\boldsymbol{U}$ corresponds to the sliding velocity of both menisci with respect to the fiber. We report in Figure 3.7 the experimentally observed velocity U for drops of different volumes sliding along fibers of four different radii.
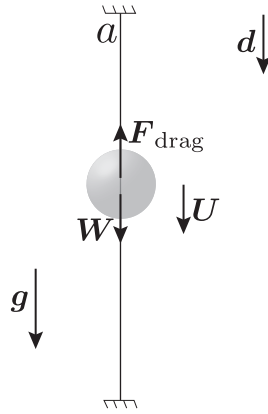
Figure 3.6 – Schematic representation of a drop sliding downwards on a vertical straight fiber. The drop has specific weight ρg, dynamic viscosity η, surface tension γ, volume Ω, and velocity $\boldsymbol{U}$. This sliding velocity is constant after a brief transient phase. The weight $\boldsymbol{W}$ of the drop drives motion and once the stationary regime is reached, the total friction force $\boldsymbol{F}_{\mathrm{drag}}$ applied on the drop balances the weight.

Thermoplastic polyurethane fibers are obtained through a meltspinning process described in Chapter 2 and their radius a is determined optically using a Leica microscope. In order to focus on large dimensionless drop radii $r = R/a$, yet undergoing little gravity influence on their shape ($R\kappa < 1$), we turn to thin fibers. Drops are obtained by brushing the fibers with v1000 silicone oil ($\eta = 1$ Pa.s). The resulting coating rapidly destabilizes through the Rayleigh-Plateau instability and thus forms a bundle of drops on the fiber which instantaneously start sliding downwards and rapidly attain their stationary sliding velocity U. For such small fibers, it is challenging to perform

Figure 3.7 – Sliding velocity of a drop on a vertical fiber versus its volume for different fiber radii $a = 3$, 6.5, 12 and 28 μm. As a reference, a unitary steepness is represented and shows that the velocity seems to scale linearly with the volume of the drop. Parameters: $\eta = 1$ Pa·s and $\gamma = 21$ mN/m.
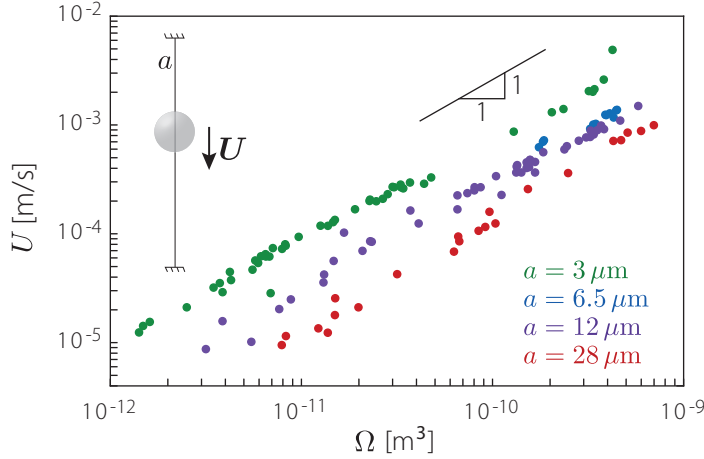
this experiment with less viscous silicone oils ($\eta = 0.1$ Pa.s for example). Indeed, the thickness t of the liquid coating when brushing a fiber of radius a is studied in de Gennes et al. (2005) and is given by Bretherton's law:

$$t \sim a\,Ca_{\mathrm{brush}}^{2/3} \tag{3.13}$$

where Ca_{brush} is given by the capillary brushing number $\eta U_{\mathrm{brush}}/\gamma$. Since the operator has a limited brushing velocity U_{brush}, obtaining thick coatings (leading to large droplets) is difficult for low-viscosity liquids. Moreover, high-viscosity silicone oil is preferred for its motion is slower and thus allows for more precise velocity measurements.

Because the drops are large compared to the fiber ($r \gg 1$), their volume can be measured optically and is considered to be that of the best-fitting sphere. Since the larger drops go faster, they meet and coalesce with little (thus slower) drops and therefore form a new larger drop. This ramification process allows to test a vast range of droplet sizes with few experiments. Moreover, the vertical fiber is mounted on a rotating setup that allows to flip the system upside-down at any moment and therefore reset the drops higher in the gravity field, which allows for repeatability tests.

Little variations in the sliding velocity for a given volume can be explained by potential imperfections on the fiber surface or residual silicone oil left behind by previously sliding drops.

According to Equation (3.6), the drop is slowed down at both its menisci by a viscous force $\boldsymbol{F_\eta}$ and the total viscous drag force $\boldsymbol{F}_{\mathrm{drag}}$ applied to the drop is therefore

$$\boldsymbol{F}_{\mathrm{drag}} = 2\boldsymbol{F_\eta} = -4\pi ak\eta\boldsymbol{U} \tag{3.14}$$

which in its dimensionless form is written:

$$\boldsymbol{f}_{\mathrm{drag}} = -2k\,Ca\,\boldsymbol{d} = f_{\mathrm{drag}}\,\boldsymbol{d} \tag{3.15}$$

with $Ca = \eta U/\gamma$. In this vertical setup, the viscous drag force acting on the drop is balanced by its weight $\boldsymbol{W} = \rho g\Omega\,\boldsymbol{d}$ and we therefore write

$$\boldsymbol{f}_{\mathrm{drag}} = -\boldsymbol{w} \tag{3.16}$$

where $\boldsymbol{w}$ is the normalized drop weight $\boldsymbol{w} = \boldsymbol{W}/(2\pi a\gamma) = w\,\boldsymbol{d}$. Projected on $\boldsymbol{d}$, Equation (3.16) yields:

$$w = 2kCa. \tag{3.17}$$

Figure 3.8 presents the normalized results of Figure 3.7, the dimensionless weight of a drop as a function of its dimensionless velocity, the capillary number Ca. It should be noted that
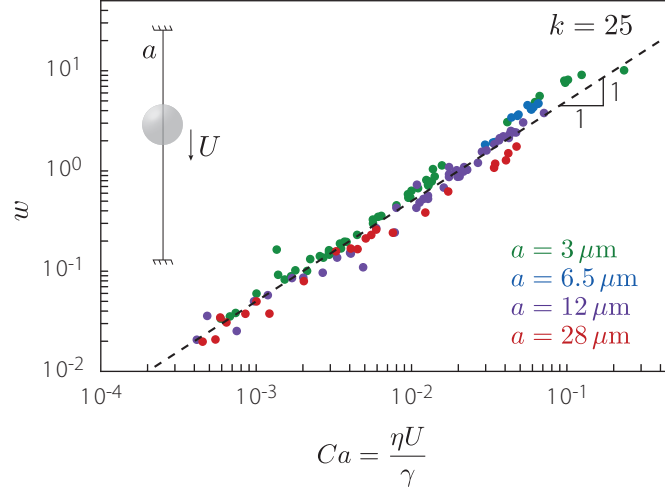
Figure 3.8 – Experimental dimensionless weight of a drop as a function of its dimensionless velocity (represented by the capillary number Ca) for drops sliding along fibers of different radii $a = 3$, 6.5, 12 and 28 μm. The dashed line represents our prediction proposed in Equation (3.16) by $w = 2k\,Ca$. Here, k is fitted and takes the value $k = 25$. Parameters $\eta = 1$ Pa·s and $\gamma = 21$ mN/m.

surface tension γ appears in both the dimensionless force and velocity but γ does not have any importance in the model. Its rather artificial inclusion however allows to assess key parameters of the experiment. Indeed, normalizing the drop weight by $2\pi a \gamma$ gives an idea of the relative weight of the drop compared to the capillary force responsible for securing it on the fiber. The capillary number, on the other hand, also seems to be a natural way to quantify the drop velocity, as it allows us to estimate the relative importance of viscous forces over surface tension forces regarding the drop shape. The assumption of low capillary numbers is necessary to consider the drop shape as if at rest, and this condition is here met experimentally as $Ca < 1$ throughout the experiments.

Figure 3.8 shows a satisfying collapse of the data, which bears witness of a good agreement between our model and the experimental results. In this case (drops sliding along a vertical straight fiber), $w = 2k\,Ca$ is a good prediction with $k = 25$.

3.2.2 Droplet sliding on a coiled fiber

We showed that for a drop sliding along a straight fiber, the drag force acting at one meniscus of the drop is well described by $\boldsymbol{F}_\eta = -2\pi a k \eta \boldsymbol{U}$, where k was experimentally found to be $k = 25$. In order to study the influence of the coiled structure inside the droplet, we now perform the same experiment as before but bring the ends of the fiber closer in order to generate some slack in the fiber. This slack is 'swallowed' by the drop, in the form of fiber loops within it, if the elasto-capillary condition for in-drop coiling is met. This is only possible for thin enough fibers and this experiment was therefore only successfully performed with the thin fibers of radii $a = 3$ and 6.5 μm of TPU (Young's modulus $E = 23$ MPa), the other two fibers (of radii $a = 12$ and 28 μm) did not undergo coiling in any of the drops and therefore do not appear in Figure 3.10.

Although the global geometry of a drop sitting on a coiled fiber is very different than when sitting astride a straight fiber, the assumption is made that the same drag force is applied at both menisci ($\boldsymbol{F}_\eta = -2\pi a k \eta \boldsymbol{U}$) but with another friction coefficient k. Although less obvious because of the results scatter, this theory is approximately verified in Figure 3.10 where the results for the force versus velocity are also represented in the coiled state (star symbols). The experimentally observed friction coefficient is lower in the coiled configuration than for the straight fiber; k is fitted and we find $k = 10$. The introduction of passive tracers in the drops (here: cocoa powder particles) provides a qualitative explanation for this
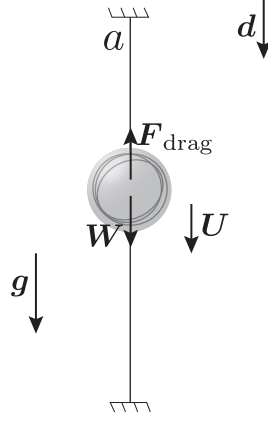
Figure 3.9 – This setup is similar to the one presented in Figure 3.6, but the ends of the fiber are now brought closer to generate slack in the fiber. If the fiber is thin enough (i.e. if its bending resistance is low enough), it coils inside the drop. In this new configuration, the drop still slides downwards, continuously absorbing fiber at the front meniscus while simultaneously releasing fiber length at the rear meniscus.

behavior: when the fiber is straight inside the drop, the fluid motion describes an axially symmetric recirculation of typical scale $R/2$ with R, the drop radius. On the other hand, when the fiber is coiled inside the drop, the fluid adopts a solid body rotation as it slides down the fiber, thus generating less friction, hence the lower k for the coiled configuration.
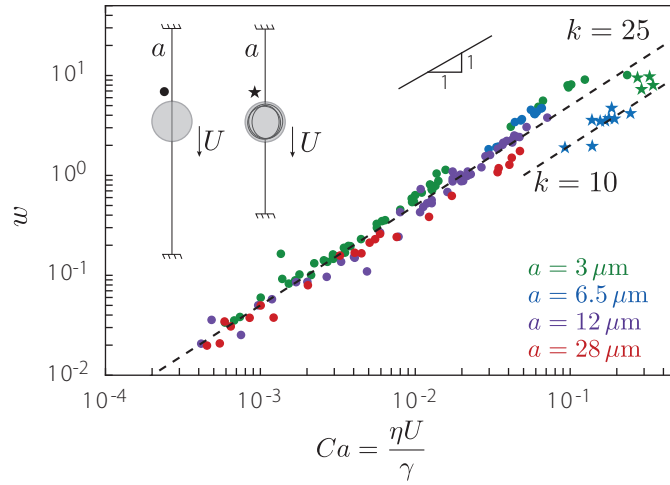
Figure 3.10 – The graph presented in Figure 3.8 is here complemented by force versus velocity experimental observations (represented by a star symbol) of drops sliding down coiled fibers (radius of the fiber $a = 3$ and 6.5 μm). The menisci show to slow the droplet significantly less in the coiled state than in the straight state. As in the straight fiber case, we consider $w = 2k\,Ca$ and in this coiled state, we fit k and find $k \simeq 10$. Parameters $\eta = 1$ Pa·s and $\gamma = 21$ mN/m.

Note that the number of fiber coils inside the drop were not characterized in these experiments, but may have some importance on the sliding velocity. Indeed, when a large quantity of slack is introduced in the system (i.e. large number of loops inside the drop), the drop sometimes suddenly stops sliding along the vertical fiber and remains still indefinitely from this moment on. This can be explained by the formation of an entanglement which does no untie at the rear meniscus, the drop therefore remains 'trapped' on the knotted fiber.

3.3 Experiment 2: Imposed force

In the previous section, we showed that a drop sitting on a vertical fiber slides downwards and quickly attains a stationary velocity which helps us quantify the friction coefficient k, with the drag force opposing the drop's motion at one meniscus given by $\boldsymbol{F}_\eta = -2\pi a k \eta \boldsymbol{U}$ where $\boldsymbol{U}$ corresponds to the relative velocity of the meniscus with respect to the fiber. In this experiment, the drop was set in motion in the gravity field due to its own weight, on a straight or coiled fiber. In order to further investigate the dissipative properties of the uncoiling process, we now turn to an experiment where a constant force is applied at one end of the fiber as it uncoils out of the drop.
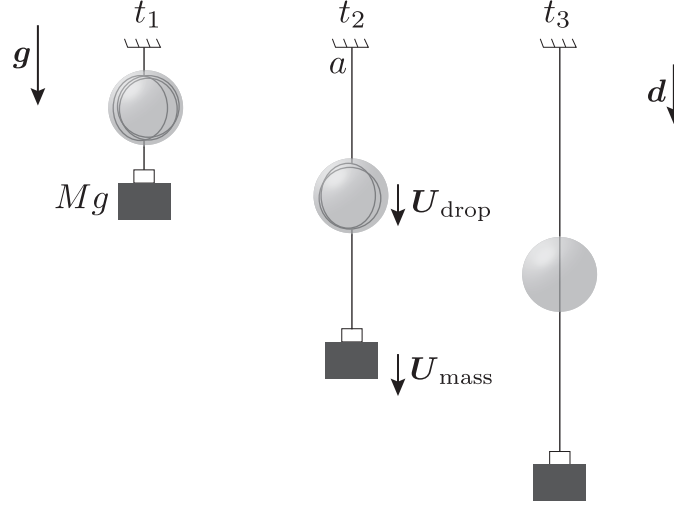

Figure 3.11 – Schematic representation of the setup providing a constant force throughout the uncoiling of a fiber out of a drop. A calibrated mass M hanging from a fiber is lifted in order to coil the fiber inside a deposited drop. The mass is then dropped and moves downwards at mean velocity $\boldsymbol{U}_{\text{mass}}$. This motion also sets the drop in motion at a mean velocity $\boldsymbol{U}_{\text{drop}}$.

The setup of this experiment is presented in Figure 3.11: a calibrated mass is fixed to the lower end of the fiber while the other end is attached to a supporting roof. A drop is then deposited on the fiber and the mass is lifted by the operator. If the fiber and the drop dimensions are well chosen, the fiber is gradually coiled inside the drop as the mass is lifted. Once the mass is at the desired height, it is suddenly dropped with a zero initial velocity and starts falling downwards because of its weight, thus extruding fiber out of the drop. When the whole fiber has been pulled out the drop, the mass stops. Although the falling velocity of the mass is not perfectly constant throughout this downwards motion, the mean mass velocity can be measured $\boldsymbol{U}_{\text{mass}}$, as well the mean drop velocity $\boldsymbol{U}_{\text{drop}}$. Considering the drop has a negligible weight compared to the meniscus drag forces (i.e. $\rho g \Omega \ll F_\eta$), one can show that the velocity of the drop should be equal to half of the mass velocity: $\boldsymbol{U}_{\text{drop}} = \boldsymbol{U}_{\text{mass}}/2$. Figure 3.12 shows the experimental mean drop velocity as a function of the mean mass velocity during the experiments for 3 different fiber radii. Note that in Figure 3.12, we use the notation $\boldsymbol{U}_{\text{mass}} = U_{\text{mass}}\,\boldsymbol{d}$ and $\boldsymbol{U}_{\text{drop}} = U_{\text{drop}}\,\boldsymbol{d}$. The prediction

$$\boldsymbol{U}_{\text{drop}} = \frac{1}{2}\boldsymbol{U}_{\text{mass}} \tag{3.18}$$

is qualitatively verified although the high results scatter impedes a clear-cut validation of the model. The assumption provided in Equation (3.18) is made throughout this Section.

As the mass travels downwards, fiber is extruded out of the lower meniscus of the drop. In order to assess the friction viscous force applied by the fiber on the drop at this meniscus, we write the relative velocity of the liquid meniscus with respect to the fiber in this region $\boldsymbol{U}_{\text{low}}$.
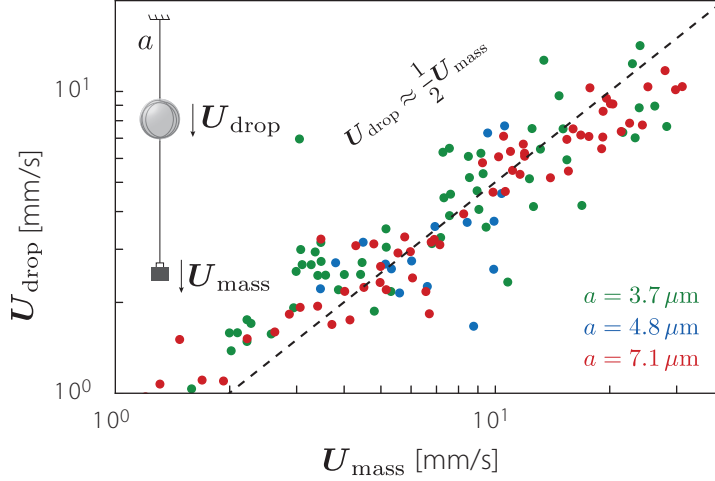
Figure 3.12 – Experimental mean drop velocity as a function of the mean mass velocity. The dashed line corresponds to the prediction $U_{\text{drop}} = U_{\text{mass}}/2$ for 3 different fibers radii $a = 3.7$, 4.8 and 7.1 μm. Although the results are highly scattered, the prediction shows a fair agreement with the experiments. Parameters $\eta = 1$ Pa·s and $\gamma = 21$ mN/m.

Noticing that the fiber has a velocity $\boldsymbol{U}_{\text{mass}}$ at the lowest meniscus, this yields:

$$\boldsymbol{U}_{\text{low}} = \boldsymbol{U}_{\text{drop}} - \boldsymbol{U}_{\text{mass}} = -\frac{1}{2}\boldsymbol{U}_{\text{mass}} \tag{3.19}$$

where we used Equation (3.18). That $\boldsymbol{U}_{\text{low}}$ points upwards, relatively to the fiber, the lower drop meniscus travels upwards. According to our model, the fiber therefore generates a viscous friction force on the drop at its lower meniscus given by

$$\boldsymbol{F}_{\eta,\text{low}} = -2\pi a k \eta\, \boldsymbol{U}_{\text{low}}. \tag{3.20}$$

We now focus on the force applied on the lower part of the fiber. Taking the capillary and fiber elastic bending resisting force into account, the lower meniscus of the drop applies a total force $\boldsymbol{F}$ on the lower part of the fiber:

$$\boldsymbol{F} = -\boldsymbol{F}_{\eta,\text{low}} - (F_\gamma - F_e)\,\boldsymbol{d} \tag{3.21}$$

with $F_\gamma = 2\pi a\gamma$ and $F_e = \pi E a^4/(8R^2)$. The force $\boldsymbol{F}$ points upwards (resisting displacement). For a stationary velocity of the mass, $\boldsymbol{F}$ balances the weight Mg of the mass, which yields:

$$\boldsymbol{F} = -Mg\,\boldsymbol{d}. \tag{3.22}$$

Projecting Equation (3.22) on $\boldsymbol{d}$ provides a theoretical relation between the mass weight and its velocity:

$$\pi a k U_{\text{mass}} = Mg - (F_\gamma - F_e) \tag{3.23}$$

and in its dimensionless form:

$$\frac{Mg}{2\pi a\gamma} = 1 - \epsilon + \frac{1}{2}k\, Ca_{\text{mass}} \tag{3.24}$$

where $Ca_{\text{mass}} = \eta U_{\text{mass}}/\gamma$ and $\epsilon = F_e/F_\gamma$ is usually very small. Figure 3.13 presents the normalized experimental results of this imposed-force experiment. The dimensionless weight of the mass is represented as a function of its downwards velocity. The huge scatter in the data makes it impossible to deduce any quantitative parameters for this configuration. Indeed, the little trustworthy results (significant difference of mass velocity for two experiments involving the same mass) renders this experiment unreliable. As piece of information, the theoretical prediction $Mg/(2\pi a\gamma) = 1 + k\, Ca/2$ is provided in Figure 3.13 with $k = 40$ (we take $\epsilon = 0$). The results are not reliable but we find that the friction

coefficient k is of the same order of magnitude as the ones deduced in the previous Section.
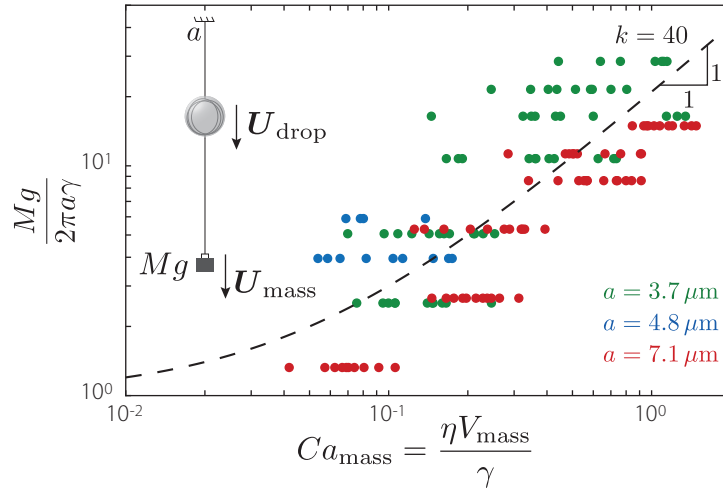

Figure 3.13 – Dimensionless weight of the hanging mass $Mg/(2\pi a\gamma)$ vs. its dimensionless mean velocity $Ca_{\text{mass}} = \eta U_{\text{mass}}/\gamma$ for different fiber radii a. The prediction provided by Equation (3.24) is represented with $k = 40$ and $\epsilon = 0$. Parameters $\eta = 1$ Pa·s and $\gamma = 21$ mN/m.

Unfortunately, the results presented in Figure 3.13 do not provide reliable information on the drag forces induced by the uncoiling of a fiber out of a drop. The large scatter among the data can be understood by the fact that performing this experiment is challenging. Indeed, the drop naturally tends to slide downwards during the coiling process (when lifting the mass) and in order to avoid this, this step has to be performed rapidly thus potentially jeopardizing precision. Moreover, in order to limit the total descent of the drop while fiber is being coiled inside of it, the operator turns to the use of small drops (which display lower descending velocities than larger ones, as studied in the previous Section). The uncoiling dynamics is affected by the small size of the drop as steric confinement hinders the smooth extrusion of fiber out of the drop. This is the most likely reason to explain the scatter in the results, fiber uncoiling is here strongly subjected to the uncoiling's unpredictable statistics and therefore presents little repeatability. Moreover, when releasing the mass, although special care was taken not to introduce any initial velocity, an initial balancing motion of the mass is almost inevitable and may significantly affect the results. Finally, although the applied force Mg is constant, the resulting velocity is not uniform and undergoes sudden changes throughout the mass descent. These jolts, rooted in the uncoiling dynamics of the fiber, go beyond the scope of this work but probably have a significant impact on the mean descent velocity.

3.4 Experiment 3: Imposed displacement velocity

The previous section considers an imposed and constant force at the end of a previously coiled fiber inside a liquid drop. This experiment shows little reliability as the results display a vast scatter. Here, we propose another setup where a constant displacement velocity $\boldsymbol{U} = U\,\boldsymbol{d}$ is imposed at one end of the fiber. A representation of this new setup is presented in Figure 3.14. Imposing a constant velocity helps avoiding bumps and jolts during the uncoiling of the fiber out of the drop. Throughout extension, the force $\boldsymbol{F} = F\,\boldsymbol{d}$ applied to the moving end is monitored and the results (dimensionless force versus displacement velocity) are presented in Figure 3.15 for three different fibers.

The same reasoning as the previous section is performed and provides the theoretical
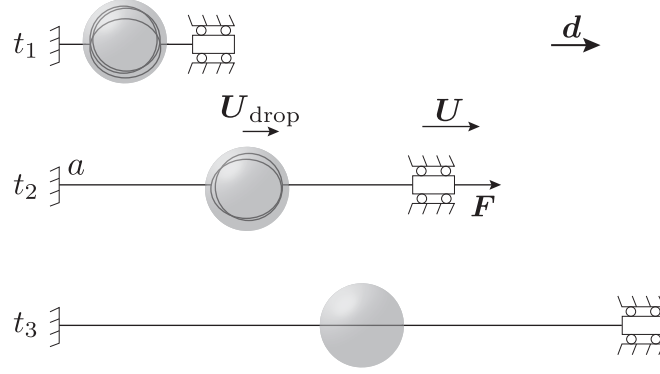
Figure 3.14 – Schematic representation of the setup allowing to impose a known uncoiling velocity U. At the compressed (initial) state, the fiber is coiled inside the drop, extension is then started at a given extension rate. The force F necessary to achieve this uncoiling velocity is monitored throughout the experiment.

prediction:

$$U_{\text{drop}} = \boldsymbol{U}_{\text{drop}} \cdot \boldsymbol{d} = U/2 \quad \text{and} \quad f = \frac{F}{2\pi a \gamma} = 1 - \epsilon + \frac{1}{2} k Ca \tag{3.25}$$

with $Ca = \eta U/\gamma$ and $\epsilon = F_e/F_\gamma$.

This experiment provides results with better repeatability than the one presented in the previous Section. A well defined slope emerges when representing the pulling force f as a function of the pulling dimensionless velocity Ca, directly giving access to the sought friction coefficient k. We here find $k = 10$. Note that for the fiber radius $a = 4.2~\mu$m, the results strongly deviate from the prediction for large displacement velocities.
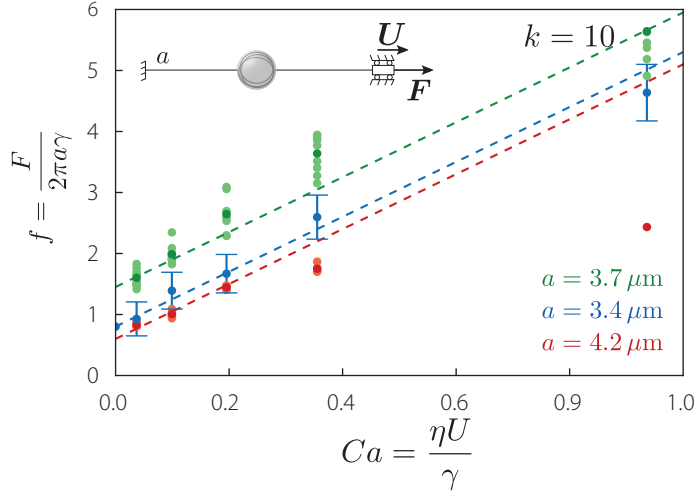
Figure 3.15 – Average force during the uncoiling of a fiber out of a drop versus the dimensionless uncoiling velocity Ca for three different fibers of radii $a = 3.7$, 3.4 and $4.2~\mu$m. The dashed lines correspond to linear fits using $f = 1 - \epsilon + kCa/2$ with $k = 10$. The small term ϵ, adapted to fit the data, should normally be positive and corresponds to the elastic correction $\epsilon = F_e/F_\gamma$, it is responsible for the small deviation around 1 at the intercept. Parameters $\eta = 1$ Pa·s and $\gamma = 21$ mN/m.

These results provide valuable insights into the dissipative forces acting on the fiber at the drop meniscus as it is uncoiled out of the drop. This setup therefore shows to be a good candidate for further analysis and experiments. The main disadvantage undermining this setup lies in the limited drop size that can be used to coil the fiber. Indeed, a large drop weight affects the geometry of the system (the fiber then sags because of the weight of the drop, see Chapter 2) and will therefore jeopardize the analysis: the actuating force F

will not be horizontal anymore. Again, the usage of small drops complicates the uncoiling physics because of the strong steric confinement they generate. Therefore, even though this setup provides promising results, we now turn to a last setup where no size limit applies to the drop (except the gravito-capillary limit discussed in Chapter 2, which cannot be overcome).

In this experiment, the force F is measured using the setup presented in Figure 3.16. The right end of the fiber is attached to a translational motor, imposing a constant spreading speed U while the other end is fixed to an elevated immobile support. A mass M is attached to the fiber between the immobile support and the liquid drop. The equilibrium of forces acting on the mass allows to geometrically measure the tension F of the fiber using the angle α between the vertical axis and the left strand of the fiber:

$$F = Mg \tan \alpha. \tag{3.26}$$

The mass M corresponds to a small square ($\sim 2 \times 2$ mm^2) cut out of an aluminum cooking foil. Its value is precisely determined by weighing a larger sheet of the same aluminum foil and using the area ratios.
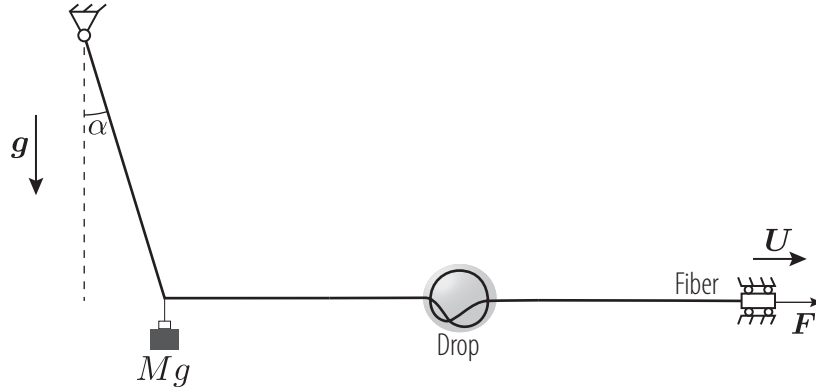

Figure 3.16 – Schematic representation of the setup allowing to measure the tension F of the fiber during uncoiling at velocity U. The weight Mg is known and the measured angle α described by the left strand of the fiber with respect to the vertical axis allows to assess the fiber tension as described in Equation (3.26).

3.5 Experiment 4: Heavy coiling drop

The three experiments presented in the Sections above had as goal the deeper understanding of the dissipative forces at the drop's menisci when a coiled fiber enters or leaves the drop. The three experiments suffered drawbacks which led to only a blurred understanding of the uncoiling physics. This last section proposes a setup taking advantage of the drawbacks hampering the previous experiments. Here, the drop is used an as indirect force sensor but is not directly the motor of motion. Figure 3.17 presents the configuration.

We study the forces applied to the drop. First, the weight of the drop is given by:

$$\boldsymbol{W} = -\rho g \Omega \boldsymbol{e}_y \tag{3.27}$$

with Ω, the volume of the drop. The capillary force, minus the elastic resisting force at the right meniscus is written

$$\boldsymbol{T}_{\mathrm{p}} = \left(F_\gamma - F_e\right) \boldsymbol{d} = T_{\mathrm{p}} \boldsymbol{d} \tag{3.28}$$

with $F_\gamma = 2\pi a \gamma$ and $F_e = \pi E a^4/(8R^2)$. Finally, we write the viscous force at the right
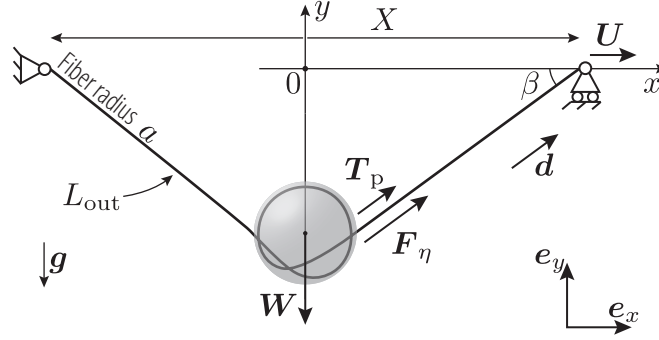
Figure 3.17 – Heavy drop (radius R) sitting on a fiber (radius a and total length $L = L_{\text{out}}+L_{\text{in}}$). The system displays a sagging angle β which will show to strongly depend on the displacement velocity U of an end of the fiber.

meniscus

$$\boldsymbol{F}_\eta = -2k\pi a\eta \boldsymbol{U}_{\text{menisc}} \tag{3.29}$$

where $\boldsymbol{U}_{\text{menisc}}$ corresponds to the relative velocity of the right meniscus with respect to the fiber. Considering left-right symmetry yields

$$\boldsymbol{U}_{\text{menisc}} = -\frac{\mathrm{d}(L_{\text{out}}/2)}{\mathrm{d}t}\,\boldsymbol{d} \tag{3.30}$$

where L_{out} refers to the fiber length outside the drop. Note that the forces $\boldsymbol{T}_{\text{p}}$ and $\boldsymbol{F}_\eta$ posses a symmetric force applied at the left meniscus, in the direction of the left fiber strand. As inertia is neglected, the sum of the forces projected along $\boldsymbol{e}_y$ must satisfy

$$2F_{\eta,y} + 2T_{\text{p},y} - W = 0. \tag{3.31}$$

The capillary forces at the menisci, minus the elastic resisting force is given by:

$$T_{\text{p},y} = T_{\text{p}}\sin\beta = \left(F_\gamma - F_e\right)\sin\beta. \tag{3.32}$$

The viscous forces due to the dissipation at the menisci write:

$$F_{\eta,y} = 2k\pi a\eta\frac{\mathrm{d}(L_{\text{out}}/2)}{\mathrm{d}t}\sin\beta \tag{3.33}$$

where $L_{\text{out}}(t) \approx X(t)/\cos\beta(t)$ for $L_{\text{out}} \gg R$, Equation (3.33) therefore rewrites:

$$F_{\eta,y} = \pi ak\eta\frac{\mathrm{d}(X/\cos\beta)}{\mathrm{d}t}\sin\beta = \pi ak\eta\left(\dot{X}\tan\beta + X\dot{\beta}\tan^2\beta\right). \tag{3.34}$$

We finally write the sum of the vertical components of forces as in Equation (3.31)

$$2T_{\text{p}}\sin\beta + 2\pi ak\eta\left(\dot{X}\tan\beta + X\dot{\beta}\tan^2\beta\right) - W = 0. \tag{3.35}$$

At equilibrium ($\dot{\beta} = 0$ and $\dot{X} = 0$), Equation (3.35) yields:

$$\sin\bar{\beta} = \frac{W}{2T_{\text{p}}} \tag{3.36}$$

which had been brought forward in the previous Chapter. If one end of the fiber moves at a horizontal velocity $\dot{X}(t) = U(t)$, we must solve:

$$\dot{X} = U$$
$$\dot{\beta} = \left[\frac{W/2 - T_{\text{p}}\sin\beta}{k\pi a\eta} - U\tan\beta\right] \Big/ \left[X\tan^2\beta\right] \tag{3.37}$$

3.5.1 Normalization of the variables

We normalize the variables as follows:

$$w = \frac{W}{2\pi a\gamma}; \quad 1 - \epsilon = \frac{T_{\mathrm{p}}}{2\pi a\gamma}; \quad x = \frac{X}{L}; \quad \tau = \frac{\gamma\,t}{\eta L} \quad \text{and} \quad u = \frac{\eta U}{\gamma} \tag{3.38}$$

where $\epsilon = F_e/(2\pi a\gamma)$.

In its dimensionless form, Equation (3.37) is therefore re-written:

$$\dot{x} = u$$
$$\dot{\beta} = \frac{w - 2(1 - \epsilon)\sin\beta - ku\tan\beta}{kx\tan^2\beta} \tag{3.39}$$

where the notation $\dot{[\,]}$ now refers to the derivative with respect to the dimensionless time $\mathrm{d}/\mathrm{d}\tau$.

3.5.2 Fixed end-to-end distance x

When the ends of the fiber are fixed, $u = 0$ and the system presented in Equation (3.39) is re-written:

$$\dot{\beta} = \frac{w - 2(1 - \epsilon)\sin\beta}{kx\tan^2\beta} \tag{3.40}$$

The equilibrium angle $\bar{\beta}$ is given by $\dot{\beta} = 0$ in Equation (3.39) and satisfies:

$$\sin\bar{\beta} = \frac{w}{2(1 - \epsilon)} \tag{3.41}$$

which could also have been deduced from Equation (3.36).

Figure 3.18 shows the numerical integration of Equation (3.40) for different initial angles β_0 ranging from $0.5\,\bar{\beta}$ to $1.5\,\bar{\beta}$. Starting from this initial angle, the system converges to its equilibrium angle $\bar{\beta}$. The normalized end-to-end distance is $kx = 7$ and ϵ is here arbitrarily chosen with $\epsilon = 0.05$. Two drop weights are considered, $w = 0.5$ and 1. Experimentally, this approach should allow to determine the friction coefficient k corresponding to the coiling and uncoiling of the fiber in or out of a liquid drop. Moreover, if k experimentally shows to depend on whether the fiber *enters* or *exits* the drop, the theoretical model can easily be adjusted to capture the difference.

For β small, Equation (3.40) equation is re-written:

$$\frac{\mathrm{d}\left(\beta^3\right)}{\mathrm{d}\tau} = 3(A - B\,\beta) \tag{3.42}$$

and presents the implicit solution

$$\tau = C - \frac{A^2\ln(A - B\beta(t))}{B^3} - \frac{A\beta(t)}{B^2} - \frac{\beta^2(t)}{2B} \tag{3.43}$$

with

$$A = \frac{w}{kx}; \quad B = \frac{2(1 - \epsilon)}{kx} \quad \text{and} \quad C = \frac{A^2\ln(A - B\,\beta_0)}{B^3} + \frac{A\,\beta_0}{B^2} + \frac{\beta_0^2}{2B}. \tag{3.44}$$

Note that C takes complex values for $\beta_0 = \beta(\tau = 0) < \frac{w}{2(1-\epsilon)}$. The solution proposed in Equation (3.43) is represented in Figure 3.19 for the smallest drop weight $w = 0.5$, which generates relatively small angles β.
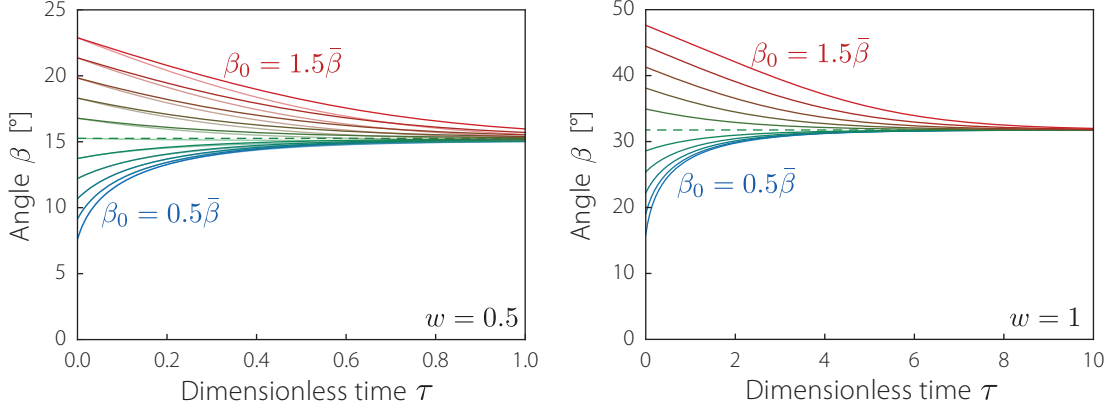
Figure 3.18 – **Angle β versus dimensionless time. Left** – the main continuous lines represent the exact solution of Equation (3.39) for different initial angles β_0 with $kx = 7$, $w = 0.5$ and $\epsilon = 0.05$. The light continuous lines represent the approximate solution for small angles β proposed in Equation (3.43). Here, $\bar{\beta} = 15.26º$. **Right** – Same results for a larger drop weight $w = 1$, the continuous lines represent the exact solution of Equation (3.39). Here, $\bar{\beta} = 31.76º$. Note that in this model (Equation (3.39)), the friction coefficient k does not depend on whether the fiber is being coiled *in* or *out* of the droplet, the asymmetric behavior is only due to the fact that gravity helps increasing β (droplet going downwards), whereas it hinders its decreasing (droplet going upwards).

3.5.3 Constant spreading velocity u

Equation (3.39) reveals that a stationary angle β_s (corresponding to $\dot{\beta} = 0$) can be obtained even for a non-zero displacement velocity u of an end of the fiber. For a constant velocity u, the stationary angle β_s is given by the relation:

$$2(1 - \epsilon) \sin \beta_s + ku \tan \beta_s = w. \tag{3.45}$$

Note that

$$\beta_s(u = 0) = \bar{\beta}. \tag{3.46}$$

For small angles, Equation (3.45) provides an explicit expression for β_s:

$$\beta_s = \frac{w}{2(1 - \epsilon) + ku} \tag{3.47}$$

In Figure 3.19, we show the dependence of the stationary angle β_s on the normalized displacement velocity of the right end of the fiber for different drop weights between $w = 0$ and $w = 2(1-\epsilon)$. Note that the upper limit $w = 2(1-\epsilon)$ corresponds to the gravito-capillary limit discussed in the previous Chapter. If the weight of the drop is larger than twice the force applied by the fiber on the drop at one meniscus, the drop cannot lift itself up the fiber and Equation (3.45) admits no solution. The numerical solution of Equation (3.45) and the approximate solution provided in Equation (3.47) are both represented in Figure 3.19. If the velocity u is negative and too large (i.e. $u < u^\star$), Equation (3.45) admits no solution. This happens when the right and the left terms are equal and their derivatives respective to β_s as well. This condition is written:

$$2(1 - \epsilon) \sin \beta^\star + ku^\star \tan \beta^\star = w \tag{3.48}$$

$$2(1 - \epsilon) \cos \beta^\star + ku^\star (1 + \tan^2 \beta^\star) = 0 \tag{3.49}$$

which is solved for $u^\star$ and $\beta^\star$:

$$ku^\star = -2(1 - \epsilon) \left(1 - \left(\frac{w}{2(1 - \epsilon)} \right)^{2/3} \right)^{3/2} \tag{3.50}$$
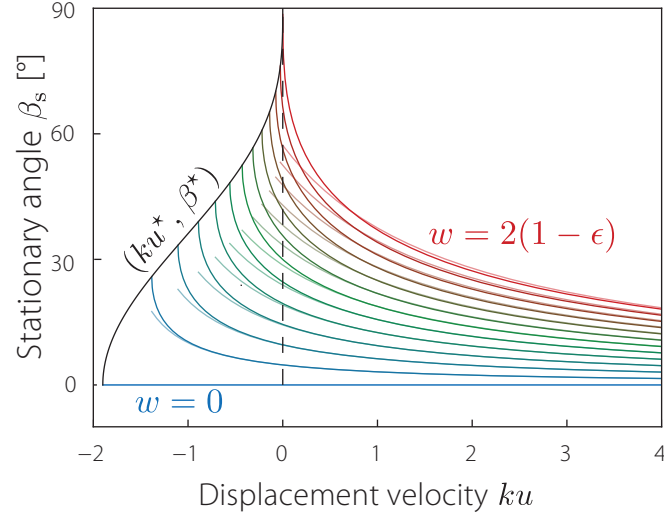
Figure 3.19 – Stationary angle β_{s} versus the normalized horizontal displacement velocity of an end of the fiber ku (with $u = U\eta/\gamma$) for different drop weights w between 0 and $2(1 - \epsilon)$. We arbitrarily choose $\epsilon = F_e/F_\gamma = 0.05$. The curve $(\beta^\star, ku^\star)$ represents the limit at which Equation (3.45) admits no solution anymore. The light continuous lines correspond to the approximate solution for β_{s} small, described in Equation (3.47). The intersection of the black dashed line $(ku = 0)$ and the main continuous lines shows the equilibrium angles $\bar{\beta}$ for the corresponding weight w.

and

$$\cos \beta^\star = \left(1 - \left(\frac{w}{2(1 - \epsilon)} \right)^{2/3} \right)^{1/2}. \tag{3.51}$$

The limit $(ku^\star, \beta^\star)$ above which Equation (3.45) admits no solution is represented in Figure 3.19. This limit is easily understood for $w = 0$. In this case, $ku^\star = -2(1 - \epsilon)$ which corresponds to a velocity at which the viscous force and the capillary one compensate exactly. A larger (negative) velocity cannot take place, the viscous drag force would then be larger than the driving capillary force.

This theory, although not confronted to experimental data yet, should also allow for the precise determination of the friction coefficient k of the fiber coiling and uncoiling out of the drop. Note that in this experiment, the weight of the drop is known and acts as an indirect force sensor. The drops can therefore be large. This will likely limit the steric confinement of the fiber inside the drop and therefore allow for more precise measurement than the ones provided by the first three experiments.

Part II

Wicked membrane

4 | Elasto-capillarity with fibrous membranes

Contents

The spontaneous coiling of fiber inside a drop previously deposited on it provides self-organized fiber reserves, inspired by spider capture silk, which provide apparent extreme extensibility. This extensibility is all the more appealing that it does not demand the fine engineering of complex geometries and it can be applied to virtually any material, as long as a thin enough fiber can be manufactured.

This extreme one-dimensional extensibility naturally raises the question: can we design membranes which will spontaneously generate membrane reserves and therefore provide **two-dimensional** extensibility? Surprisingly enough, the answer to our question again lies in Nature. Two-dimensional membrane reserves are found inside our own body. Indeed, some cells display a particular ability to cope with stretch. Macrophages extending their surface area by a factor 5 to engulf large microbes or cellular debris (Lam et al. 2009) (see Figure 4.1), patrolling T-lymphocytes stretching by 40% to squeeze into the microvasculature (Guillou et al. 2016), hundreds of μm sized neuronal projections extruded from 10 μm wide neurons (Raucher and Sheetz 1999; Dai and Sheetz 1995) or osmotic swelling of fibroblast leading to 70% increase in area (Groulx et al. 2006) are a few out of many examples of the extreme mechanical solicitations encountered by living animal cells on a routine basis. This resistance is all the more spectacular that the lytic stretching level at which the plasma membrane ruptures is about 4% (Raucher and Sheetz 1999; Nichol and Hutter 1996). Why do these cells then just not burst under stress? Actually cells have evolved a strategy

consisting in storing excess membrane in the form of folds and microvilli (Erickson and Trinkaus 1976; Majstoravich et al. 2004) which can be recruited and deployed on demand. Interestingly, these geometrical corrugations enabling stretching do not fluff the membrane. Cellular tension is indeed preserved thanks to the pulling action of the underlying cortical actin layer (Salbreux et al. 2012).
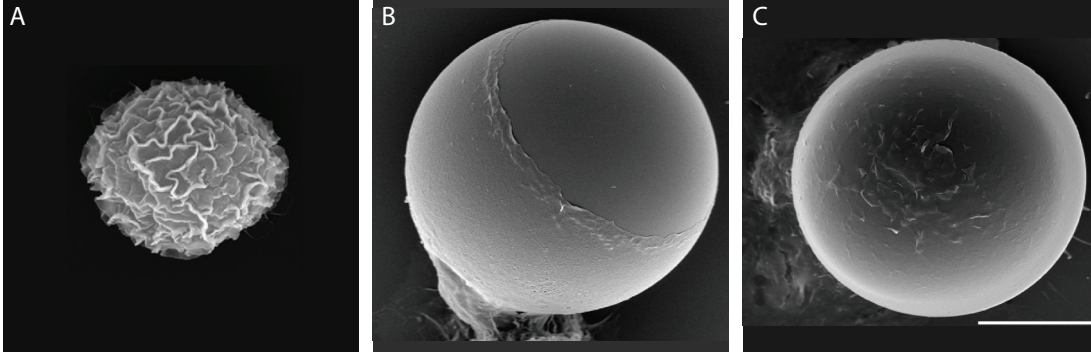
Figure 4.1 – **Scanning Electron Microsopy micrographs of a J774 macrophage**. The first snapshot (**A**) presents the macrophage at rest (cell size is not representative due to shrinkage during fixation). The two following pictures (**B** and **C**) show the macrophage engulfing an antibody-coated (FCγ-opsonized) 30 μm diameter bead. Throughout this engulfment, the initially corrugated cell membrane smooths out, thus recruiting membrane surface, necessary for its up to 5-fold surface area expansion. Reproduced from Lam et al. (2009). Scale bar: 10 μm.

Again, Nature provides blueprints for our need for stretchable materials; the ingredients for the self-organization of surface reserves are the following:

○ A membrane presenting a low bending stiffness in order to fold easily under the action of a surface force,
○ A surface force which naturally tends to compress the membrane.

In this chapter, we propose a method to fabricate synthetic membranes displaying these bio-inspired mechanical properties (self-organization of membrane reserves). Therefore, we will first produce a very flexible membrane and the necessary surface forces will be generated by the surface tension of a liquid wicking the membrane.

Liquid drops on flexible membranes have been studied before, and the next Section provides a quick (non-exhaustive) overview of the work performed up to date on the subject.

4.1 Elasto-capillarity with thin membranes: an introduction

Elasto-capillarity with thin and soft membranes has led to beautiful experiments throughout the last decades. For example, capillary-origami, the science (art?) of folding a pre-formed 2D thin sheet into a 3D object by wrapping it around a liquid drop allows to easily design small yet complex structures. The final 3D shape adopted depends on the initial 2D pattern and three illustrations of this concept are presented in Figure 4.2. Moreover, it was experimentally shown in Antkowiak et al. (2011) that the final 'wrapped' structure can even be tuned depending on the impact velocity of the liquid drop on the 2D sheet (see Figure 4.2-C). Other illustrations of elasto-capillarity with thin membranes are presented in the recent elasto-capillarity review article Bico et al. (2017).
But depositing a drop on a thin membrane does not necessarily result in its complete folding. Indeed, if the border of the membrane is attached to a support, the drop only deforms the membrane locally, resulting in a configuration similar to the Neumann construction. This case, studied in Hui and Jagota (2015) and Fortais et al. (2017) is presented in Figure 4.3. If
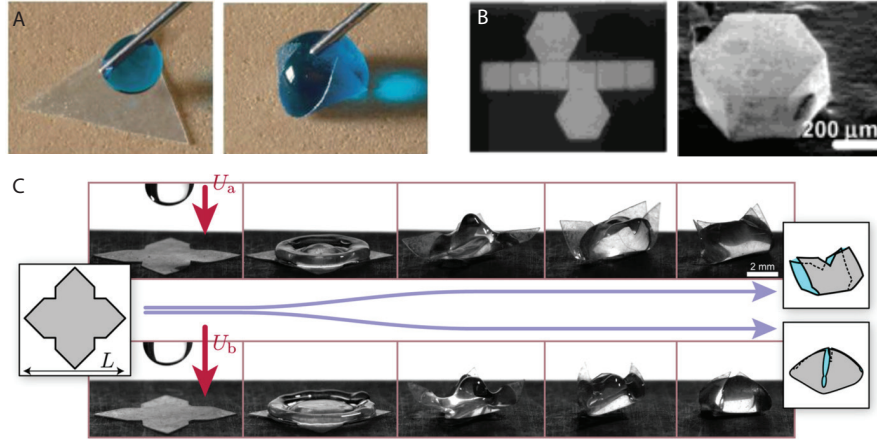
Figure 4.2 – **A** – Wrapping a drop of dyed water with a thin PDMS triangular sheet. Reproduced from Py et al. (2007). **B** – Folding micrometric metallic 2D structures into 3D polyhedra with a solder drop. Reproduced from Gracias et al. (2002). **C** – The final shape adopted by the elasto-capillary fold can be selected with the impact velocity of the water drop upon the PDMS sheet. Reproduced from Antkowiak et al. (2011).

the membrane is previously deformed, say stretched or sheared, the liquid drops footprints, usually circular, become elliptic and thus provide information on the stress state of the membrane, acting as stress 'compass needles' (Schulman et al. 2017).
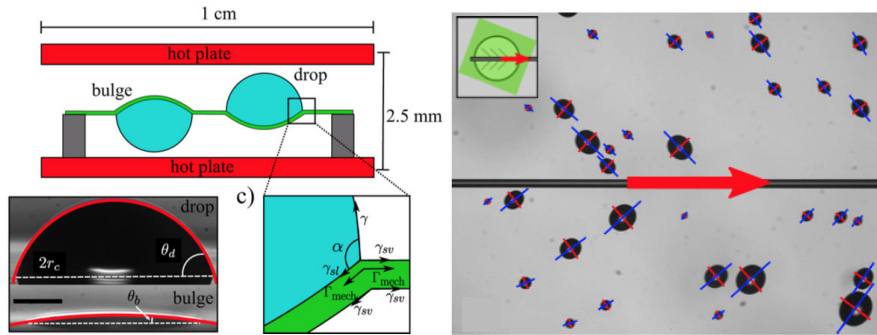
Figure 4.3 – **Left** – The capillary action of glycerol drops sitting on a thin polystyrene sheet deforms the sheet. Reproduced from Fortais et al. (2017). **Right** – Drops on a sheet reveal its stress state. Here, the membrane is sheared along the center line and the elliptic footprint of the drops acts as 'compass needle' for the stresses in the membrane. Reproduced from Schulman et al. (2017).

A last example of elasto-capillarity with thin membranes is found in Nature, and is presented in Figure 4.4. Here, water dew drops sit on a mosquito wing and through their capillary action make the wing buckle and shrink.

Note that in these introductory examples, the liquid drop always sits on **one** side of the membrane, because the latter is not porous. But how would the system behave if the drop could **wick** (i.e. infuse) a porous membrane and therefore present **two** interfaces with the surrounding air (one above and one under the membrane)?

4.2 Elasto-capillary folding and unfolding of membrane surface reserves

As discussed earlier, the design of a membrane which spontaneously generates self-organized surface reserves requires *i)* a flexible membrane and *ii)* a surface force to ensure tension of the membrane. In this Chapter, we introduce a method to manufacture synthetic

Figure 4.4 – A mosquito wing collapses under the capillary action of a droplets sitting on it. Between the third and the fourth snapshot, a large water drop drips out, capillary forces then crush the wing. Reproduced from Dickerson et al. (2015).
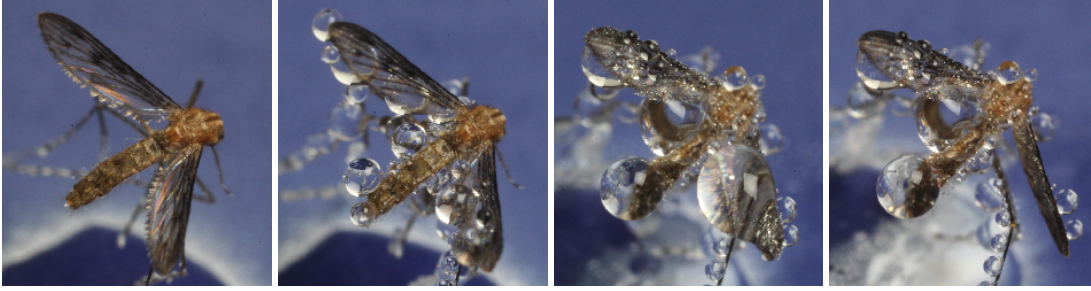
membranes spontaneously generating surface reserves.

4.2.1   A fibrous flexible membrane

For the fabrication of a flexible membrane, we turn to the electrospinning technology (Greiner and Wendorff 2007) which allows to create mats composed of thin fibers with diameters of a few hundred nanometers. Although usually used to produce thick fibrous membranes, this manufacturing technique also allows to create very thin membranes (a few microns thickness). Moreover, as the membranes are porous, any wetting liquid wicks it entirely and effortlessly, and the system then presents two liquid-vapor interfaces.

The fibrous membranes are obtained using an electrospinning apparatus ES-1A (Electrospinz Ltd.) following these key steps:

○ A polymer is dissolved in a solvent (the polymers and corresponding solvents that are used in this work are presented in Table 4.1).

○ The solution is injected through an electrically charged blunt needle (diameter of the needle 1 mm at an injection rate of 0.02 ml/min, electric field between 10 and 15kV), see Figure 4.5-A. The outgoing droplet is instantaneously destabilized through the formation of a Taylor cone (Figure 4.5-B) which is ejected as a liquid rod towards an electrically earthed fixed planar target (distance between the tip of the needle and the target: 17 cm), see Figure 4.5-C. As it travels towards the target, the solvent evaporates from the liquid rod which therefore quickly undergoes a swirling instability. A nanometric fiber is continuously spun towards the earthed target and after a few minutes, the target is covered by a thin mat. Tuning the spinning time (i.e. the duration of the fiber ejection) provides a fine control over the thickness of the membrane.

○ The resulting fibrous mat (made of the addition of solid fibers continuously generated) is removed from the target, which was previously covered with anti-adhesive cooking paper to avoid sticking.

Polymer	Solvent	Wicking liquid
PAN	DMF	water - glycerol - ethanol - silicone oil
PVDF-HFP	DMF	ethanol - silicone oil
PCL	DMF	ethanol - silicone oil
PVP	ethanol	silicone oil

Table 4.1 – Polymers used to fabricate fibrous membranes with their respective solvents and wicking liquids.

The polymers used to fabricate the fibrous membranes are Poly(vinylidene fluoride-co- hexafluoropropylene) (PVDF-HFP, Solvay), Polyacrylonitrile (PAN, M.W. 150,000, Sigma Aldrich), Polycaprolactone (PCL, M.W. 80,000, Sigma Aldrich) and Polyvinylpyrrolidone (PVP, M.W. 1,300,000, Acros Organic). The solvents are n,n-dimethylformamide (DMF, Carlo Erba Reagents) and ethanol (absolute, Sigma Aldrich). The liquids used to wick the fibrous membranes are deionized water, glycerol (Sigma Aldrich), ethanol (absolute, Sigma Aldrich) and v10 silicone oil (Sigma Aldrich). The concentration of polymer of each polymer-solvent solution is 10% weight. A summary of the
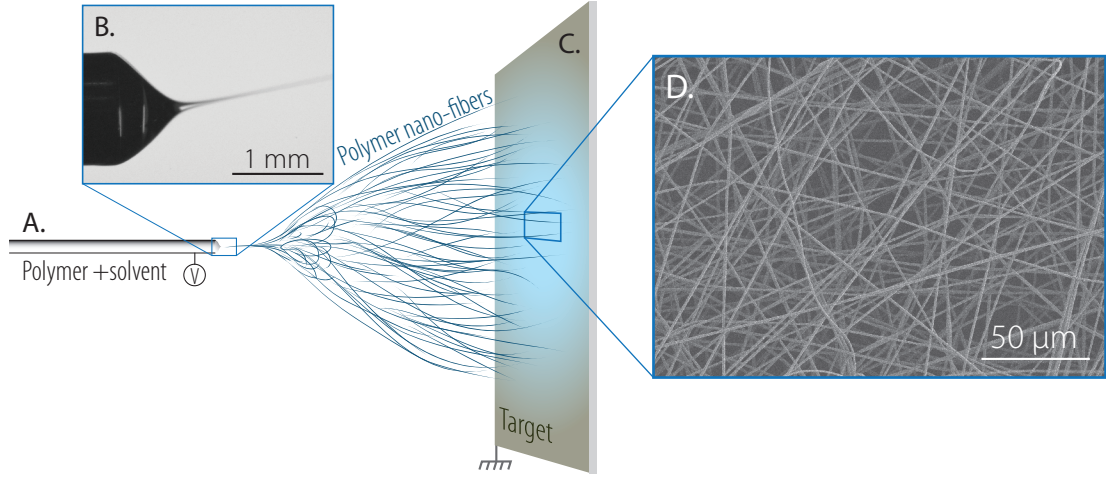
Figure 4.5 – **Fabrication of the fibrous membrane. A** – The polymer-solvent solution is injected through an electrically charged needle. **B** – The electrical field generated between the needle and the earthed target destabilizes the drop through a Taylor cone which is ejected as a continuous liquid rod towards the neutral target. Throughout this flight, the liquid rod dries out and lands as a solid nanofiber on the target. **C** – The target is covered with a non-sticking (cooking) paper to facilitate subsequent membrane recovery. **D** – A scanning electron microscopy shot of a PAN membrane spun for 2 minutes is presented. The typical radius of the fibers composing the membrane is $a = 250$ nm.

After electrospinning, the membrane is removed from the target thanks to the anti-adhesive cooking paper. The membrane is extremely light and can be colored by adding a few drops of food coloring agent in the polymer-solvent solution. Figure 4.6-left shows a membrane dyed blue recovered from the cooking paper. The characteristic size of the membrane is 10×10 cm^2. The use of a zero-stat gun allows to avoid electrostatic effects which would otherwise render the manipulation of the membrane uneasy. It should also be mentioned that although the membrane is extremely thin (around a few microns thick), it is rather opaque because of the fibrous structure which greatly scatters light as it travels through the membrane. The precise thickness of the fibrous membrane is difficult to characterize as the precision of a micrometer is of the order of magnitude of the membrane thickness (a few microns). However, weighing the membrane provides insightful information about its composition. A fibrous membrane spun for one minute weighs about 30 μg/cm^2 which corresponds to an effective thickness of about 250 nm if the membrane was bulky (i.e. zero porosity). The membranes in this work are spun for 2 to 4 minutes and therefore have effective thicknesses under one micron. Moreover, the visualization of the membrane using a Scanning Electron Microscope, see Figure 4.5-D, suggests that the membrane has a thickness of few fibers diameter. The fibers have diameters around 500 μm, so the membrane has an actual thickness t_0 of a few microns, which is in agreement with the order of magnitude we just calculated. The difference between the bulk effective thickness (hundreds of nanometers) and the actual thickness (few microns) is explained by membrane porosity.

Once the membrane is recovered, it is fixed to supports with double faced tape. The fibrous network presents a great sticking surface with the tape and even when the membrane is later wicked with a liquid, this fixing strategy is durable. Figure 4.6-right shows a PVDF-HFP
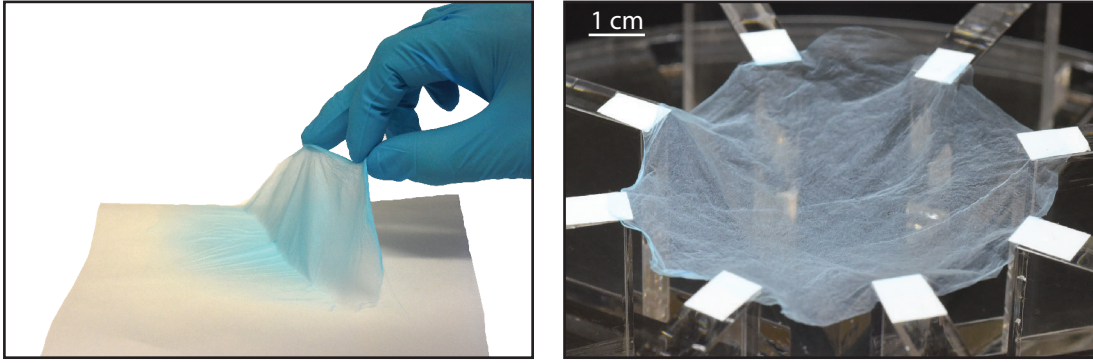
Figure 4.6 – **Manipulation of the membrane. Left** – The membrane is recovered from the non-adhesive cooking paper by hand. **Right** – The membrane is fixed to any kind of support using double face tape. Here, it is attached to eight translational supports which can be brought closer or pulled apart.

membrane fixed to eight translational PMMA supports which can slide in carved rails. This system allows to test the membrane in extension and in compression.

Before deepening into the properties that the membrane displays once it is wicked with a wetting liquid, we demonstrate that its native (dry) state has no remarkable mechanical properties. To do so, the membrane is attached to the eight translational supports previously set in a narrow position (Figure 4.7-A). The supports are then pulled apart, thus stretching the membrane which rapidly undergoes irreversible damage (at around 30% area extension - Figure 4.7-B). It finally completely ruptures at a larger extension (Figure 4.7-C), showing only moderate stretchability. This intrinsic lack of stretchability is reminiscent of plasma membrane's low lytic extension; plasma membrane ruptures at around 4% (Raucher and Sheetz 1999; Nichol and Hutter 1996). It should be mentioned that even though the synthetic membrane ruptures at low extension, it is robust and can withstand significant loads before tearing off.
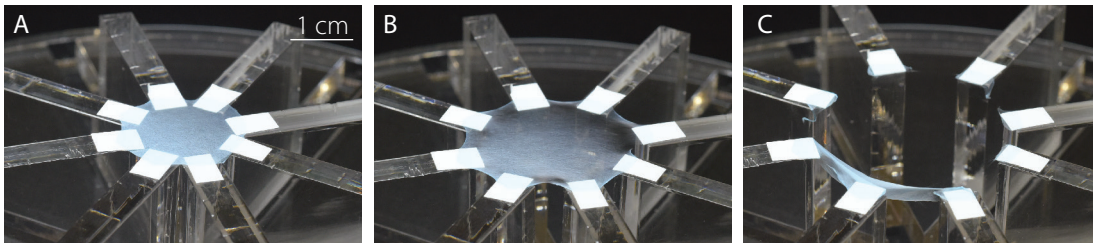
Figure 4.7 – In its native (dry) state, the membrane is attached to eight translational supports slowly separated from each other. As the membrane is not intrinsically stretchable, it rapidly and irreversibly tears off.

4.2.2   Surface forces: Wicking the fibrous membrane with a wetting liquid

Our aim is to generate self-organized surface reserves similar to the ones displayed by the J774 macrophage (see Figure 4.1) which will be subsequently recruited upon stretching of the membrane. In order to develop such surface reserves, the membrane requires a surface force pulling on it. We obtain this surface force by wicking the membrane with a wetting liquid. Because the membrane is fibrous, the liquid can easily percolate through it. First, Figure 4.8 presents a dry fibrous membrane attached to the eight translational supports. In Figure 4.8-A, the supports are slightly brought closer to generate some slack in the membrane. A few liquid drops of v10 silicone oil are deposited on the membrane

in Figure 4.8-B. These wetting liquid drops make the membrane immediately fold within them; the drops generate a capillary pulling force at the triple line. As the supports are further brought closer, the membrane remains globally straight by continuously storing excess membrane surface in the liquid veins (see Figure 4.8-C).

Figure 4.8 – Based on the biological observation of self-organized membrane reserves in the J774 macrophage, our membrane is now attached to the eight translational supports (set in a wide position) and wicked with a wetting liquid (v10 silicone oil). When the supports are brought in, the membrane does not sag as one would expect; it spontaneously folds inside the liquid veins due to surface tension. Note that the PVDF-HFP membrane is colored blue for visualization purposes.
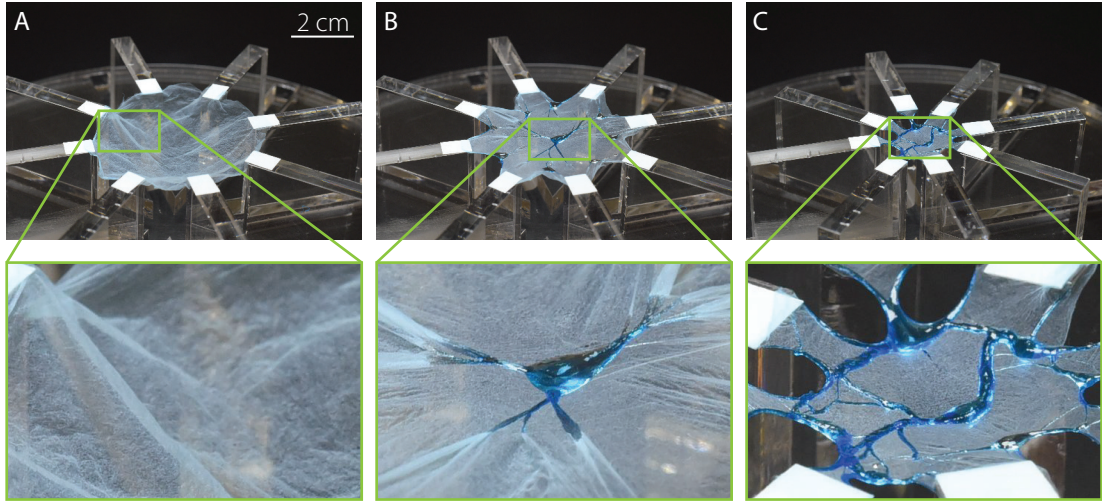
Throughout this work, we mainly use PAN and PVDF-HFP to electrospin the membranes (see the list of polymers in Table 4.1). The main advantage of PAN is that it is hydrophilic and therefore allows to perform experiments with water as wicking liquid, which is not the case for the three other tested polymers. PVDF-HFP, on the other hand, is slightly hydrophobic, but it is commonly used in electrospinning applications and provides good mechanical resistance. To show the universality of membrane reserves in the wicked membrane, PCL and PVP membranes were also tested once and behaved similarly to the PAN and PVDF-HFP membranes.

4.2.3 A synthetic membrane coping with extreme deformations

Even once the liquid has wicked the entire membrane (either by letting it infuse slowly or by spreading the liquid by hand), the membrane remains straight when its borders are brought closer. The excess membrane is no longer stored in the liquid veins, but as folds inside the liquid film. Figure 4.9-A shows the fully wicked membrane at a compressed state (i.e. with the 8 supports close to each other). From this compressed state, it can be stretched as shown in Figure 4.9-B&C. The previously self-organized folds of the membrane act as surface reserves which are recruited upon stretching; the membrane smooths out to fuel deformation. When the membrane is totally smoothed out, i.e. straight at the liquid film level, it cannot be stretched more without suffering irreversible damage. The effective extensibility of this wicked membrane is virtually unlimited as long as surface reserves can be stored inside the liquid film when the membrane is compressed. Moreover, the membrane can also adapt to any imposed shape while always remaining straight, provided the fibers are never put in extension. Indeed, it should be emphasized that the fibers composing the membrane can easily fold inside the liquid film during compression, but cannot withstand
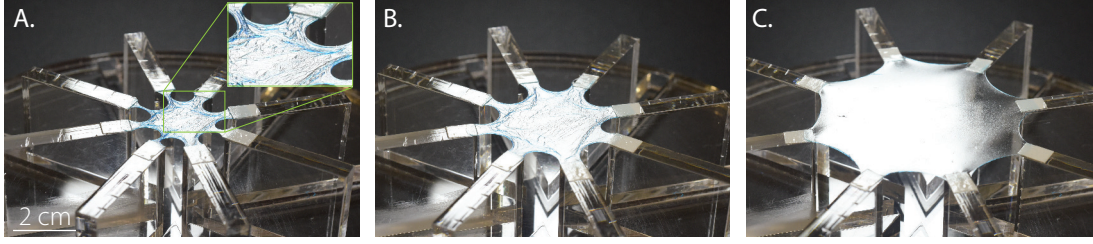
Figure 4.9 – Once the whole membrane is wicked with the liquid, its compressed state spontaneously adopts a wrinkled and folded surface, similar to that of the resting J774 membrane. Just like for the J774 macrophage, our self-corrugated wicked membrane smooths out when stretched; wrinkles and folds act as membrane reserves that can fuel up to a 50-fold surface area expansion. Moreover, as the process relies only on elasticity and capillarity, it is reversible and repeatable (wrinkles and folds continue self-organizing upon subsequent compression-extension cycles).

extension. Different configurations are presented in Figure 4.10 where the membrane seems to stretch as if elastic, though here, the forces responsible for keeping the membrane straight are not rooted in elasticity, but in capillarity.
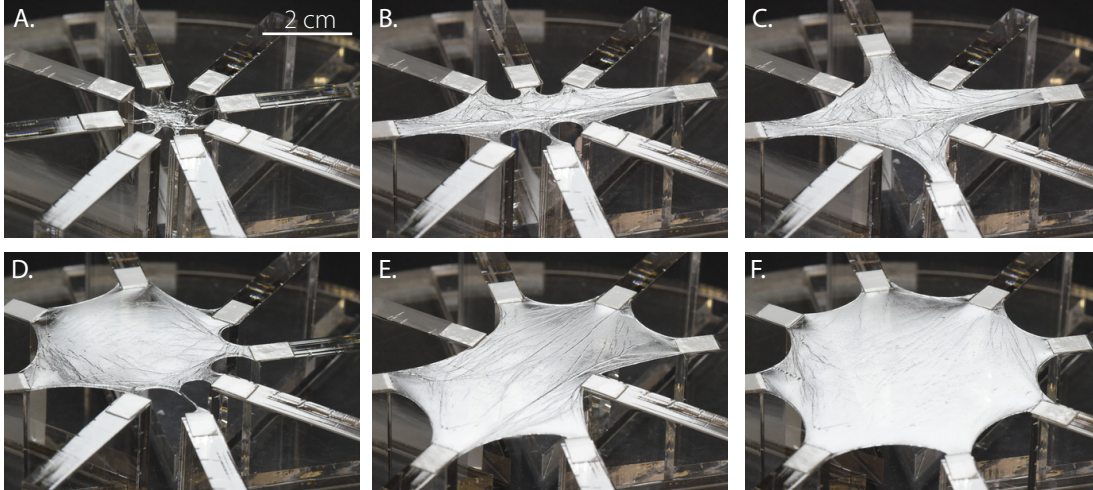
Figure 4.10 – When the membrane is entirely wicked with the wetting liquid, it can adapt to any imposed shape, while always remaining straight, as long as a distance between two points does not exceed the corresponding distance in its native shape.

4.3 Planar wicked membrane

As discussed previously, the wicked membrane presents the property of adapting its shape to any imposed boundary conditions while always remaining under tension. This tension is reminiscent of the capillary surface tension found in liquid soap films. And indeed, when wicked, the membrane inherits surface tension and while usual wetted objects are too stiff to be deformed by these capillary surface stresses, this membrane is thin enough to fold inside the liquid film under surface-tension stresses. In this section, we experimentally and theoretically study a rectangular wicked membrane, attached to two straight parallel mobile supports in a planar configuration. The membrane has a width W and a rest length L. The two free edges therefore have an initial length L. In the presented experiments, $L < W$. Once the membrane is fixed on the mobile supports and wicked with a wetting liquid, the supports are brought closer, starting from a distance $X = L$. The force pulling

on one of the supports is monitored throughout a compression-extension cycle. In order to avoid capillary sticking of the supports, the minimal distance X at which they are brought together is slightly larger than 0.
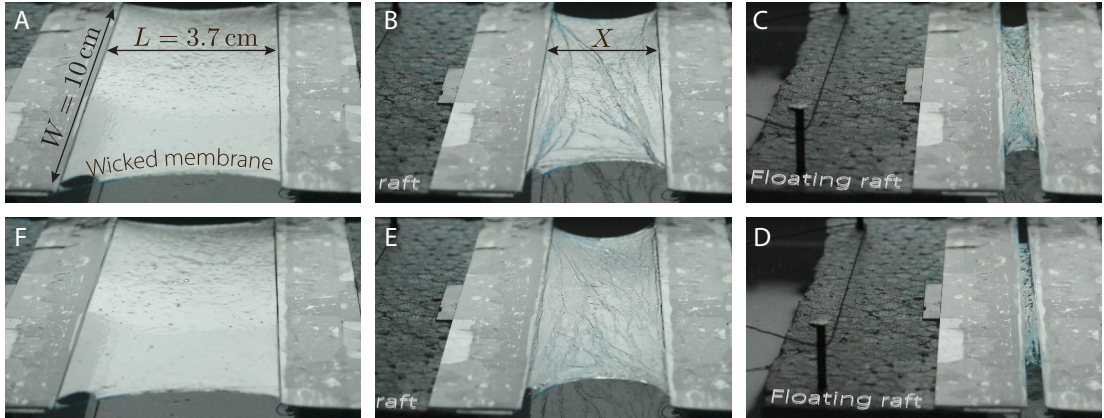
Figure 4.11 – PVDF-HFP membrane wicked with ethanol, mounted on mobile supports floating on a water bath to avoid friction. The left support is slowly released and the membrane, because it undergoes a surface tension, pulls on it throughout a compression-extension cycle. The right support is fixed and the force it undergoes is monitored at any displacement X.

A compression-extension cycle is presented in Figure 4.11 where a rectangular PVDF-HFP membrane wicked with ethanol is compressed and extended. The membrane is attached to two supports floating on a water bath in order to avoid friction. Remarkably, the membrane remains straight when compressed and this sequence makes it clear that the constant planarity of the membrane is mediated by the wrinkles and folds which develop inside the liquid film throughout the compression. The origin and the physics of these wrinkles and folds will be studied more deeply in the next Chapter.

The force versus displacement curve of the planar wicked membrane is performed using a cantilever beam method (see Figure 4.12). The cantilever beam mechanical response was calibrated using selected weights (weighed with a Mettler-Toledo MS 0.01 mg precision scale). The membrane is supported by two floating rafts on a water bath to ensure frictionless translational supports. The presented extension-compression force measurement cycles are performed at around 1mm/s but show little sensitivity to displacement velocity (the same force vs. displacement curve was obtained for a twice as large displacement velocity).

Figure 4.12 – Schematic representation of the setup allowing to measure the force F developed by the planar wicked membrane. The cantilever beam has a bending stiffness EI and length L, its tip displacement Δ is previously calibrated for a horizontal beam with calibrated weights and allows to precisely measure the force F.

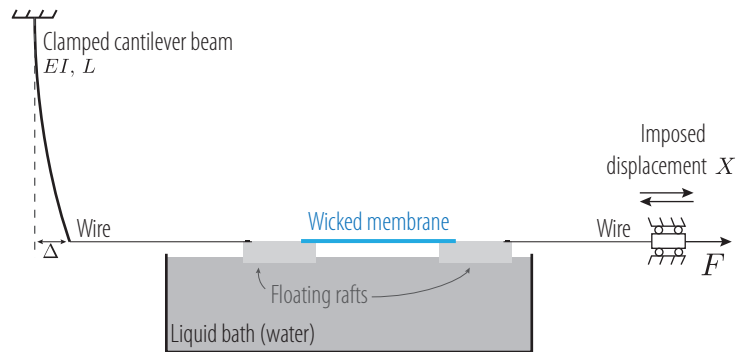The force versus displacement curve for a PVDF-HFP membrane wicked with v10 silicone oil is presented in Figure 4.13 and compared to a first simple approach described by equation Equation (4.1) which corresponds to a soap-film-on-a-frame calculation.

$$F = \frac{\partial \mathcal{V}}{\partial X} = \frac{\partial (2\gamma S)}{\partial X} = \frac{\partial (2\gamma W X)}{\partial X} = 2\gamma W \tag{4.1}$$

where S is the surface area of one side of the soap film, γ its interface energy, and $\mathcal{V}$ the total surface energy.
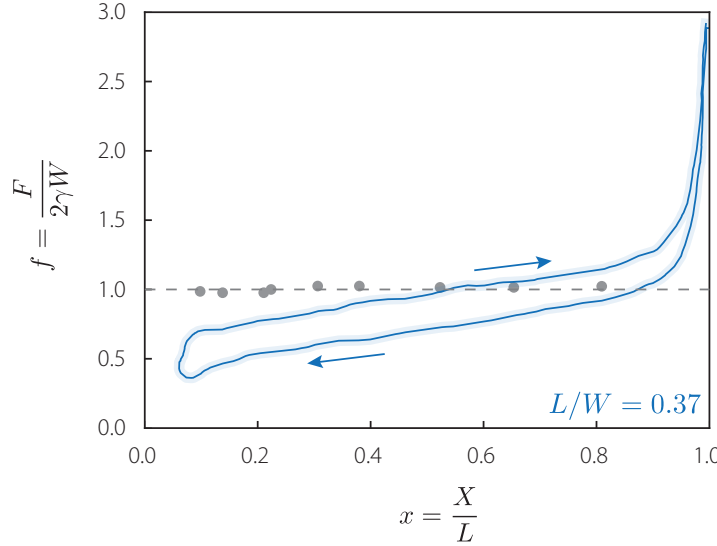

Figure 4.13 – Experimental force vs. displacement curve for a PVDF-HFP membrane wicked with v10 silicone oil ($\gamma = 21$mN/m). The membrane has a width $W = 10$ cm and a length $L = 3.7$ cm. The dashed line corresponds to the first and simple approach, where $F = 2\gamma W$, just as for a soap film on a frame and the gray dots correspond to the experimental data of the restoring force of a liquid soap film on frame of width $W = 12$ cm and surface tension $\gamma = 30$ mN/m.

The experimental results presented in Figure 4.13 only show a rough quantitative agreement with the first model to which it is compared (a soap film on a frame of width W) but the measured forces have the same order of magnitude. Moreover, the force versus displacement curve comprises two distinct regions:

○ a plateau force region for normalized displacements x smaller than 1 where $f \simeq 1$: the surface tension force dominates.
○ a diverging force for $x \simeq 1$ where the solid (inextensible) behavior of the membrane is expressed.

Although this qualitative interpretation provides a first glance into the mixed nature of the wicked membrane, the difference between the model ($F = 2\gamma W$) and the experimental curve calls for further comprehension. To understand this discrepancy, it should first be noted that unlike a soap film on a rigid frame, our rectangular membrane is only attached at two edges and therefore has two free edges. A soap film would shrink immediately if it was only "attached" at two of its edges.

In order to minimize its interface energy with air, the wicked membrane minimizes its surface area and this may put some regions of the membrane in an extension state up to a point where the surface reserves are fully exhausted. Pure stretching deformations represent a far higher energetical cost as compared to interfacial ones and as a first approximation, this sharp energetical penalty can be modeled as an inextensibility constraint. This surface minimization with inextensibility constraint is reminiscent of a problem described in Bérest

where an inextensible closed fiber is deposited on a planar soap film. The soap film is then popped open inside the closed fiber which immediately adopts a circular configuration. This surface minimization with **isoperimetric** constraint indeed naturally leads to a circular shape.

In order to better theoretically predict the force vs. displacement curve of the wicked membrane, we consider that the free edges adopt a circular shape and conserve their initial length L throughout the deformation process.

4.3.1 Early compression: $\frac{2}{\pi}L < X < L$

At early compression, assuming that the free edges describe circular arcs of length L and that the two supports are at a distance X, we include two new variables R and β, respectively the radius and angle span of the circular arc, which are presented in figure 4.14.
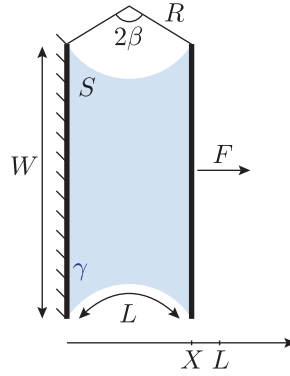
Figure 4.14 – Schematic representation of a planar wicked membrane during early compression. The surface minimization with isoperimetic constraint on the free edges is responsible for the circular shape they adopt.

R and β are related to L and X through two equations:

$$L = 2R\beta \qquad \text{and} \qquad X = 2R\sin\beta. \tag{4.2}$$

The surface area of the liquid wicked membrane then writes:

$$S = WX - 2R^2\beta + 2RX\cos\beta \tag{4.3}$$

and the normalized force ($f = F/2\gamma W$) that an operator has to apply on the mobile edges to ensure a distance X is given by the derivative of the energy with respect to X:

$$f = \frac{1}{2\gamma W}\frac{\partial(2\gamma S)}{\partial X} \tag{4.4}$$

which can be solved numerically. Another way to access the force in this slightly compressed state is to consider the tension in the free edges, which can be considered as inextensible wires. This tension T_{wire} is given by

$$T_{\text{wire}} = 2R\gamma \tag{4.5}$$

where the factor 2 corresponds to the fact that the membrane has two sides exhibiting a liquid-vapor interface. The horizontal force applied by the wires on the mobile supports is therefore equal to

$$F_{\text{wire}} = 2T_{\text{wire}}\cos\beta = 4R\gamma\cos\beta \tag{4.6}$$

Using the equations in (4.2), the total force applied on the mobile supports is finally written:

$$F = 2L\gamma\frac{\cos\beta}{\beta} + 2\gamma W \tag{4.7}$$

which in its dimensionless form reads:

$$f = 1 + \frac{L}{W}\frac{\cos\beta}{\beta} \quad \text{with} \quad x = \frac{\sin\beta}{\beta}. \tag{4.8}$$

4.3.2 Advanced compression: $0 < X < \frac{2}{\pi}L$

At a more advanced compression, when β reaches $\pi/2$ (i.e. when X becomes smaller than $2L/\pi$), the geometry adopted by the liquid infused membrane changes and a schematic representation of it is provided in figure 4.15. In addition of the radius R, a new variable Δ is considered, it represents the length on which the membrane sticks to the mobile support. R and Δ are given by the 2 relations:

$$L = 2\Delta + \pi R \quad \text{and} \quad X = 2R \tag{4.9}$$

and again, the surface area is calculated:

$$S = WX - 2X\Delta - \pi R^2 \tag{4.10}$$

Finally, injecting the three previous relations in the force equation (4.4) leads to an explicit expression for the force:

$$f = 1 - \frac{L}{W}\left(1 - \frac{\pi x}{2}\right) \tag{4.11}$$

where $x = X/L$. Note that now, the tension in the equivalent inextensible wire representing the free edges is still given by $T_{\text{wire}} = 2R\gamma$ as in Equation (4.5). However, since the free edges meet the straight supports tangentially, this tension does not generate a horizontal force on the supports ($\beta = \pi/2$ in Equation (4.6)).
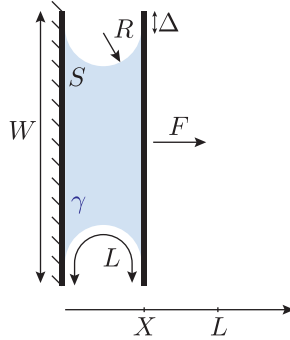
Figure 4.15 – Schematic representation of planar liquid wicked membrane at a strong compression. Note that in this advanced compression state ($X < 2L/\pi$), the free edge radius R is dictated by the distance between the two rigid mobile supports X ($2R = X$). The length Δ corresponds to the length on which the free edge 'sticks' to the mobile edges.

4.3.3 Discussion about the planar wicked membrane force response

Theoretical normalized force vs. displacement curves are given in Figure 4.16 for different initial length to width ratios L/W. Note that as mentioned above, there are two regions of compression with different force vs. displacement behaviors.

For strong compressions, $0 < x < 2/\pi$, the force increases linearly with the distance of the mobile straight edges (see Equation (4.11)) with a slope $0.5\pi L/W$ and a force at zero spreading (i.e. the intercept, when the two mobile edges touch) $f = 1 - L/W$. This
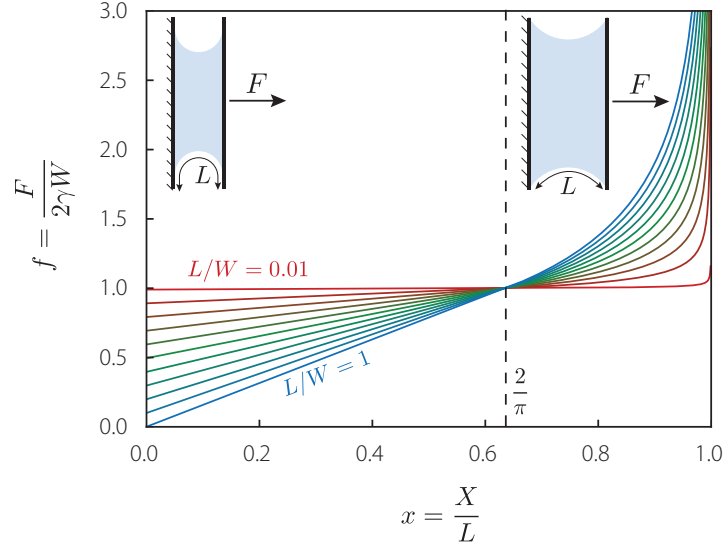
Figure 4.16 – Theoretical normalized force versus displacement curve of the planar wicked membrane for different initial length to width ratios L/W ranging from 0.01 to 1. Note that when L/W approaches 0 (i.e. the length of the free edges is very small compared to the width of the membrane), the force vs. displacement curve approaches that of liquid film on a frame ($f = 1$) up until $x = 1$ where the inextensibilty of the membrane makes the force diverge.

corresponds to a force $F = 2\gamma(W - 2\Delta)$ and in other words, in this first region, the force is dictated by the length on which the surface tension pulls on the straight edges of the membrane $W - 2\Delta$.

The second region $(x > 2/\pi)$ does not have an explicit force expression. In this region, the tension in the free edge starts adding up to the global force necessary to maintain the membrane at a distance x.

Interestingly, the first simple model ($F = 2\gamma W$) considers that the membrane acts as liquid film for $x < 1$ and that it expresses its solid component for $x = 1$ where the force should diverge. The second and more complete model reveals slightly more complex physics; the 'liquid' component (liquid film wicking the membrane), by means of the surface energy it carries, is responsible for the force throughout the compression. However, the 'solid' component (inextensible fibrous membrane) also expresses its presence through the inextensibility constraint on the free edges. This constraint is in turn responsible for the shape adopted by the membrane and therefore gives rise to the particular force vs. displacement behavior of the planar wicked membrane.

The results provided by this second model are compared to the experimental results in Figure 4.17 where they show excellent agreement. Indeed, although the experimental curve presents a hysteresis, i.e. the force path is not the same in compression as in extension, the ascending tendency of the force f with respect to the displacement x is very well captured.

4.3.4   Hysteretic behavior of the planar membrane

The hysteretic behavior, i.e. the difference between the force while increasing X (extension) and the force while decreasing X (compression) is studied in this section. Interestingly, this hysteretic behavior shows little dependence on the compression-extension velocity.

The key parameter influencing the force difference between extension and compression lies in the quantity of liquid wicking the membrane. When a PVDF-HFP membrane is generously wicked with ethanol (the membrane is very wet), the force cycle shows little hysteresis (see Figure 4.18-A). We then let the ethanol partially evaporate for a few minutes and perform the same mechanical test, the resulting force displacement curve is presented
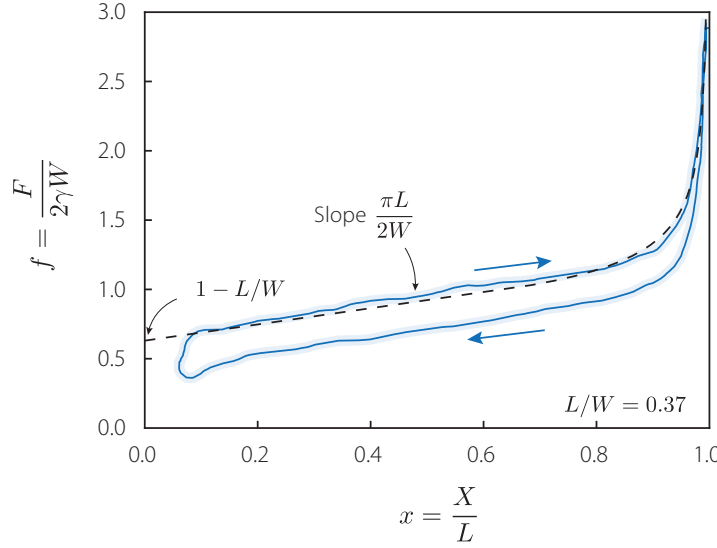
Figure 4.17 – Experimental force vs. displacement curve for a PVDF-HFP membrane wicked with v10 silicone oil ($\gamma = 21\text{mN/m}$). The membrane has a width of $W = 10$ cm and a length $L = 3.7$ cm. The dashed line corresponds to the prediction presented in Equations (4.4 and 4.11). The theory seems to correctly predict the initial slope but does not provide any insight into the hysteretic behavior of the wicked membrane.

Figure 4.18-B. It should be noted that during this second experiment, the membrane is still wicked but with a smaller amount of liquid. The cycle now displays a larger hysteresis; the pulling force developed by the membrane is significantly higher during extension than during compression. Both curves in Figure 4.18 represent growing cycles in amplitude to provide insight on the memory effect. This memory is not negligible for the partially dried membrane (Figure 4.18-B); a stronger previous compression leads to a higher pulling force during the subsequent extension.
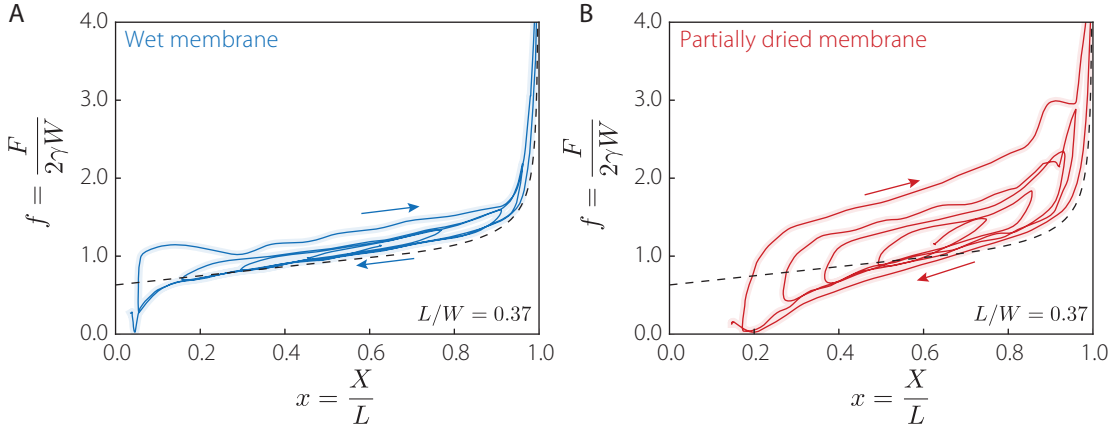
Figure 4.18 – **Force vs. displacement curves for a planar PVDF-HFP membrane wicked with ethanol**. **A** – A big amount of ethanol wicks the membrane. **B** – After letting ethanol evaporate for a few minutes, the membrane is still wicked but with a small quantity of liquid. The main difference between these two experiments lies in the hysteresis which is amplified when the membrane is only wicked with a small amount of liquid.

The dissipative property of the wicked membrane could be of interest for *e.g.* shock absorption. The energy dissipated E throughout an entire compression-extension cycle can be written as follows:

$$E = \oint F \mathrm{d}X \simeq \Delta X \Delta F = 2\gamma LW \, \Delta x \Delta f \tag{4.12}$$

where ΔX and ΔF respectively represent the displacement span experienced by an edge of the membrane during one cycle and the difference in force at a given displacement between the extension and the compression phase, Δx and Δf refer to the normalized corresponding quantities. The specific energy dissipation per unit volume of the membrane is then given by e with:

$$e = \Delta x \, \Delta f \, \frac{2\gamma}{t} \tag{4.13}$$

where t refers to the thickness of the membrane. Since Δx and Δf are both of the order of 1 (for the partially dried ethanol wicked membrane), we find that the characteristic energy dissipation per unit volume of the membrane throughout a compression-extension cycle is of the order of 400 J/m^3 or 0.4 J/kg where we considered a typical wicked membrane thickness $t = 100\,\mu$m and an effective density $\rho = 1000\,$kg/m^3. Note that the thickness t we consider is significantly larger than the thickness of the native dry membrane t_0 because the liquid film significantly increases the total thickness. A typical human muscle develops about 40 J/kg (100 times more than our wicked membrane) during contraction but tensile actuation (i.e. displacement span) of biological or artificial muscles are usually much lower (Haines et al. 2014) than the wicked membrane which can here deform up to more than 500% between its compressed and its extended state.

These preliminary tests regarding the hysteretic loading cycle of the wicked membrane provide an axis for further investigation. A deeper understanding of the dissipating mechanisms and how they depend on the wetting conditions would require additional experimental and theoretical analysis.

4.3.5 Fatigue resistance of the membrane

The wicked membrane can undergo large shape deformations due to its spontaneous geometric reorganization. Since stretchability is here not achieved by stretching the material itself (i.e. at the molecular level) but through the local wrinkling and folding of the membrane, the wicked membrane, along with its extreme stretchability, provides appealing prospects in terms of durability throughout imposed compression-extension cycles it might undergo. Two membranes were tested to assess their resistance to fatigue, a PVDF-HFP
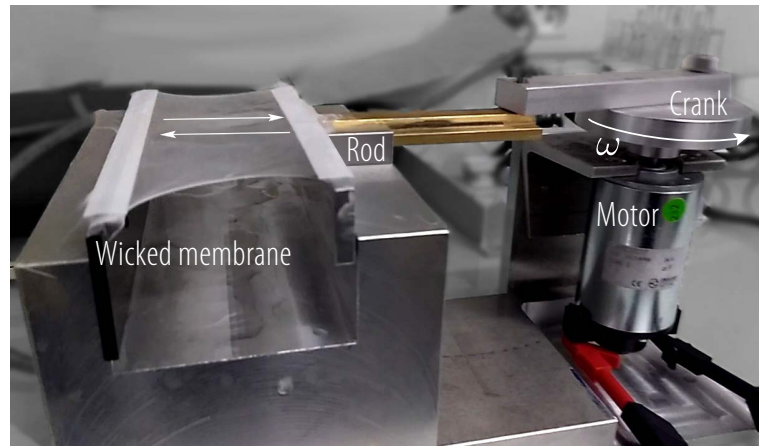
Figure 4.19 – **Fatigue test setup.** In order to test their resistance to fatigue, the membranes are mounted on this motor-crank-rod setup, allowing to impose end displacement of one of the membrane edges from $X_{\min} = 2$ mm to $X_{\max} = 3.7$ cm (effective elongation of factor 18). The high cycling rate (here 3 cycles per second) allowed to test a membrane in only a few days.

membrane wicked with v10 silicone oil and a PAN membrane wicked with deionized water. For this, the tested membranes are mounted on the setup presented in Figure 4.19.

Fatigue test on the PVDF-HFP membrane

The first fatigue test was performed on a silicone oil infused PVDF-HFP fibrous membrane mounted on a crank rod system and the wicked membrane underwent 3 extension-compression cycles per second, see Figure 4.19 . The compression-extension cycle corresponds to an end to end distance X varying from $X_{\min} = 2$ mm to $X_{\max} = 3.7$ cm. The membrane was re-wicked with silicone-oil every 20,000 cycles to avoid drying. Small circular holes (hundreds of microns in diameter) appear at around 60,000 cycles, slowly growing up to 150,000 cycles. At this last point, the holes have a significant impact on the mechanical behavior of the wicked membrane. The force-displacement measurement performed after N cycles presented in Figure 4.20 shows that the holes restrain the x-displacement range above $x = 0.2$ for $N =$150,000 cycles. Holes kept growing and the membrane tore off shortly after 150,000 cycles.
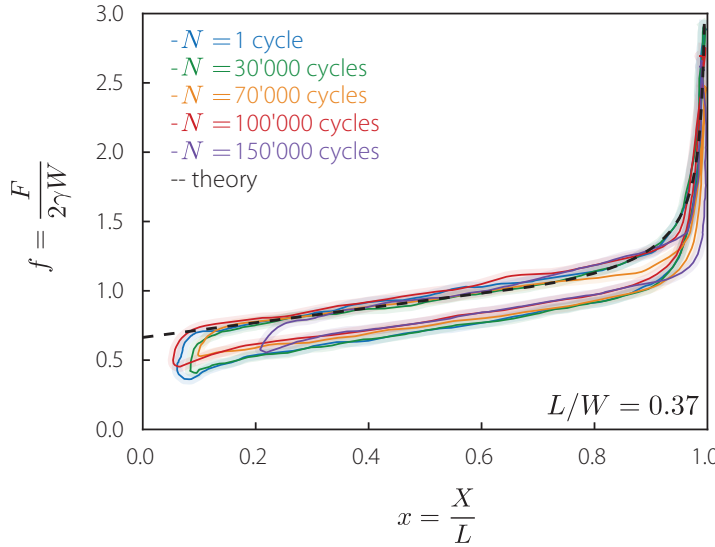
Figure 4.20 – Force vs. displacement of the planar PVDF-HFP membrane during one compression-extension cycle after imposing N cycles to it. PVDF-HFP membrane wicked with v10 silicone oil ($\gamma = 21$ mN/m), $L/W = 0.37$.

Fatigue test on the PAN membrane

A PAN membrane wicked with deionized water was also mounted on the fatigue test setup presented in Figure 4.19. It showed significantly less longevity as holes began to appear at around 5,000 cycles and the membrane tore off before reaching 10,000 cycles. To understand this significant difference between the PAN and the PVDF-HFP membrane, we focus on the microscopic structure of the fiber organization of these membranes.

Difference between the PAN and the PVDF-HFP membrane

Figure 4.21 presents two Scanning Electron Microscopy snapshots of a PAN and PVDF-HFP membrane. The PAN membrane (Figure 4.21-A) displays rather thick fibers (between 500 and 800 nm) which are not linked to each other through bonds at the nodes. The PAN membrane can therefore be seen as an unorganized stack of fibers which only interact through local van der Waals and friction forces but with no solid bonds between them. As a matter of fact, when a tension is applied by hand on the PAN membrane (either in its native dry state or after wicking it with a water), it shows to creep significantly (and irreversibly) before rupturing.

With these key elements in mind, it comes as no surprise that the PAN membrane (as manufactured in this work) suffers fatigue since the forces generated on the membrane at each cycle are likely to slowly make it creep up until a point where holes start to be generated.

Figure 4.21 – **Scanning Electron Microscopy snapshot of a two different dry membranes.** **A** – PAN membrane, the fibers have typical diameters between 500 and 800 nm and do not show bonds between them. **B** – PVDF-HFP membrane, the fibers have lower diameters (between 200 and 300 nm) and present bonds at some fiber nodes. These bonds are likely present due to liquid dr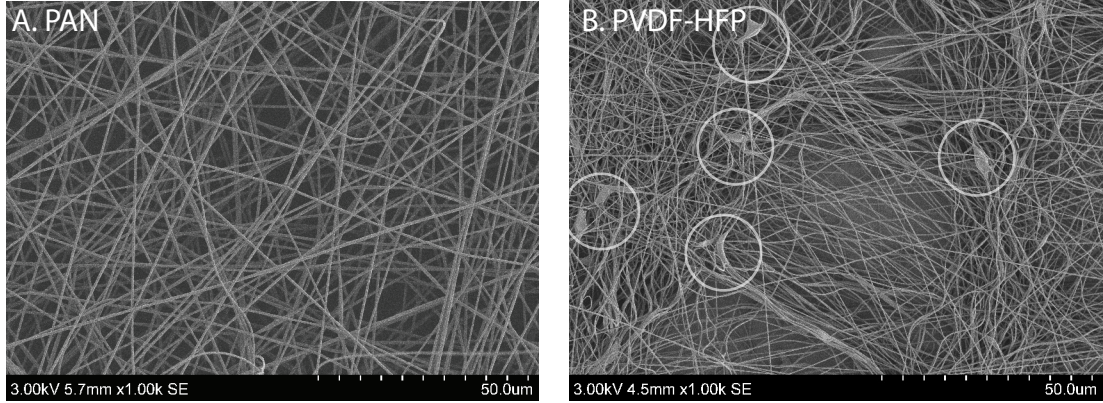ops of polymer ejected during the electrospinning process which dried afterwards. These bonds probably are responsible for the significant resistance of the PVDF-HFP membrane by warrantying robust structural integrity.

The PVDF-HFP membrane (Figure 4.21-B), on the other hand, is composed of thinner fibers (between 200 and 300 nm) and above all, displays solid bonds between the fibers at some nodes. These soldering-looking bonds are probably rooted in the ejection of liquid droplets during the electrospinning process. These 'bridges' between fibers are likely responsible for the good mechanical resistance of the PVDF-HFP membrane. It should indeed be noted that in its dry state a PVDF-HFP membrane is significantly more resistant to stretching than a PAN membrane. It withstands stronger loads and does not creep before rupture. This resistance is revealed in the membrane's strong capacity to endure numerous compression-extension cycles (up to more than 100,000 cycles) before undergoing failure.

The promising results concerning the resistance to fatigue of the PVDF-HFP membrane, when repeatedly subjected to a factor 18 elongation could undoubtedly be improved by follow-up research and optimization.

First of all, it should be emphasized that the presented fatigue test imposes 3 compression-extension cycles per second to the membrane, which corresponds to important elongation rates. The main reason for this rather high cadence is to perform the fatigue test during a short period (under these conditions, performing 150,000 cycles took 2 working days). This high tempo may have rushed the failure of the membrane due to higher membrane-on-membrane friction forces. Moreover, the membrane was here re-wicked with silicone oil every 20'000 cycles in order to avoid drying. The re-wetting frequency could also influence the durability of the membrane since a dryer membrane suffers higher tension stresses as discussed in section 4.3.4 (see Figure 4.18).

Another key parameter determining the fatigue resistance of the membrane could be its thickness. Here, a delicate compromise will probably have to be found, as the membrane should be thin enough to undergo the spontaneous wrinkling and folding inside the liquid film, but should also be thick enough to present good mechanical robustness. For similar forces applied on it, a thicker membrane will probably show higher resistance.

Finally, the difference between the PAN and the PVDF-HFP membranes in microscopic fiber organization and in mechanical resistance to fatigue highlights the importance of structural robustness. A promising optimizing path for membrane resistance is therefore the bonding of fibers to each other at the fibrous mat scale through soldering bridges. Even the PAN membrane, or any membrane which performs poorly to the fatigue test could

be upgraded with this fiber-bonding technique. A potential way to ensure this bonding could be through the pressing of a membrane in a solvent-saturated environment to make the fibers partially dissolve and therefore fuse to each other at nodes, while conserving membrane porosity.

4.4   Cylindrical wicked membrane

The previous section focused on the mechanical behavior of a wicked membrane in a planar configuration and pointed out that capillarity, carried by the liquid constituent of this hybrid system, is responsible for the forms and forces adopted by the membrane. The main difference between this wicked membrane and the analogous liquid film was shown to be the intrinsic inextensibility of the fibrous membrane which influences the shape and the mechanical response of the system through the application of a length constraint on the free edges of the membrane. In order to further investigate the similarities and differences between the wicked membrane and classical soap films, we turn to another archetypical capillary structure: the catenoid.

4.4.1   The pure liquid catenoid

The catenoid refers to a pure liquid film in a cylindrical configuration, attached to two parallel open rings which do not necessarily have the same diameter. Here, for simplicity, we consider only the case of rings with equal diameters. Due to the liquid surface tension, the resulting shape adopted is not a straight cylinder between the two ring, but a more complex (and harmonious) silhouette which we characterize in this Section.
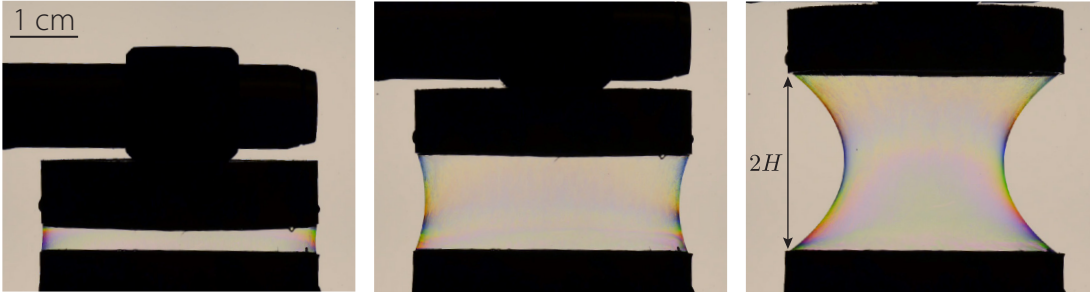
Figure 4.22 – Liquid soap film between two parallel rings adopting a catenoid shape for different ring distances $2H$. It should be noted that the rings are open, therefore the pressure inside the catenoid is therefore equal to atmospheric pressure.

We study the profile $R(Y)$ adopted by a liquid soap film between two parallel rings of equal radii R_H for which an experimental photographic sequence is provided in Figure 4.22. To perform this experiment, two rings are attached facing each other on a Thorlabs 25 mm translational stage in order to precisely control their distance. To fabricate the soap film, the two parallel rings are first put in contact and a soap-water-glycerol mixture is applied by touching the rings with a solution-soaked brush. As the rings are subsequently pulled apart, the soap film grows and adopts the catenoid shape. A schematic representation of such a soap catenoid is presented in Figure 4.23.

Because the liquid surface carries an interface energy, the equilibrium shape adopted by the liquid film between the two parallel rings seeks to minimize this interface energy $2\gamma S$ where γ is the surface tension of the liquid film and S its total surface. Since surface tension is constant, the equilibrium shape minimizes the total surface S which is written:

$$S = \int_{-H}^{H} 2\pi R \sqrt{1 + R'^2} \, \mathrm{d}Y \tag{4.14}$$

Figure 4.23 – Schematic representation of a liquid film between two parallel rings at a distance $2H$. Due to the cylindrical configuration, the equilibrium shape adopted by the liquid film (the one which minimizes the global energy) corresponds to a **catenoid**. A common measure of the catenoid is the neck radius $R_{neck} = R(Y = 0)$.

and the energy of the system is written as:

$$V = 2\gamma \int_{-H}^{H} 2\pi R \sqrt{1 + R'^2}\, \mathrm{d}Y = 4\pi\gamma \int_{-H}^{H} \mathcal{L}(R, R')\, \mathrm{d}Y. \tag{4.15}$$
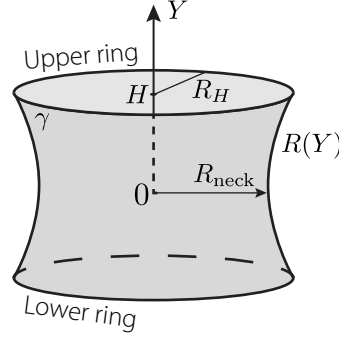
Minimizing V is done by solving Euler-Lagrange equation:

$$\frac{\partial \mathcal{L}}{\partial R} = \frac{\partial}{\partial Y}\left(\frac{\partial \mathcal{L}}{\partial R'}\right) \quad \Rightarrow \quad RR'' = 1 + R'^2 \tag{4.16}$$

Equation (4.16) admits the solution:

$$R(Y) = a \cosh\left(\frac{Y - b}{a}\right) \tag{4.17}$$

where a is an unknown constant which is found using the boundary condition $R(Y = H) = R_H$,

$$a \cosh\left(\frac{H}{a}\right) = R_H \tag{4.18}$$

and as we search a symmetric profile, $R'(0) = 0$ yields $b = 0$.
Equation (4.18) has no explicit solution but can be solved numerically. In order to sum up the catenoid shape with only one variable, we turn to its neck radius defined by $R_{neck} = R(Y = 0)$. For the classic liquid catenoid, the neck radius is given as:

$$R_{neck} = a. \tag{4.19}$$

Moreover, it should be noted that Equation (4.18) admits 2 solutions a_1 and a_2 for $0 < H < 0.66\, R_H$ and no solution for $H > 0.66\, R_H$. And experimentally, the catenoid indeed shows to follow the solution $a_1 > a_2$ which minimizes the total surface of the catenoid and it pops open at $H = 0.66\, R_H$ (or $h = 1.51 H/R_H = 1$), leading to the formation of two separate liquid films discs attached to the parallel rings. The analytical result depicted in Equation (4.19) and the experimental measurements of the neck radius as a function of the two parallel rings' distance is provided in Figure 4.24.

4.4.2 Wicked membrane catenoid

We now study the equilibrium forms adopted by a wicked membrane in a cylindrical configuration.

To do so, a PAN membrane is attached on the edge of two laser-cut PMMA rings (diameter $2R_H = 4\,\mathrm{cm}$) with 3M double face tape. The membrane is wicked with deionized water and the distance between the two discs is controlled using a Thorlabs 25 mm manual translation stage.
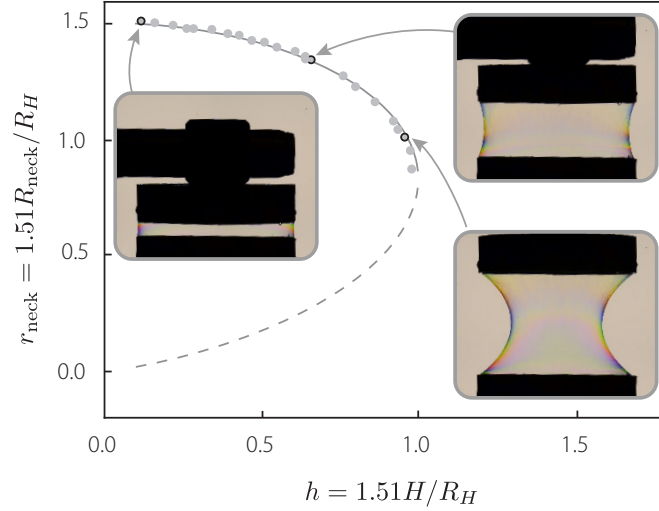
Figure 4.24 – **The pure liquid catenoid bifurcation diagram.** The normalized neck radius r_{neck} is represented as a function of the half-distance h between the two rings. The solid and dashed gray lines respectively correspond to the stable and unstable liquid catenoid, solutions of Equation (4.18). The gray dots show the experimental results corresponding to the sequence provided in Figure 4.22, where the ring diameter is $2R_H = 4$ cm.

Throughout the compression-extension cycle, the shape adopted by the wicked membrane is filmed with a Nikon D810 camera and image post-processing (Python) allows to gather the neck radii of the resulting catenoid for the visited ring distances.

Figure 4.25 presents a sequence of the compression-extension cycle and clearly shows that the shape adjustments of the wicked membrane are mediated by the self-organized folds that act as surface reserves. Figure 4.26 shows the experimental neck radius of the cylindrical wicked membrane as a function of the ring half-distance H throughout a compression-extension cycle. The theoretical prediction of the pure liquid soap catenoid is also represented. Interestingly, at the beginning of the experiment, when the two rings are at their initial half-distance $h = l > 1$, the system adopts a stable configuration although the purely liquid catenoid would not exist in this region. The normalized length $2l = 1.51 \cdot 2L/R_H$ describes the initial length of the wicked membrane, it corresponds to the distance between the two rings for which the membrane is perfectly cylindrical. As the rings are brought closer, the neck slims down to a point (near $h = 0.5$) where it suddenly jumps to a wider configuration (see transition between Figure 4.25-C and D). When the rings are subsequently pulled apart, the wicked membrane catenoid qualitatively follows the stable path of the purely liquid catenoid up to a region where the latter stops existing (at $h = 1$) and the wicked membrane profile then converges back to its initial configuration.

In order to explain the experimental results displayed in Figure 4.26, we develop a model taking advantage of the comprehension that the planar-wicked-membrane experiment provided (Section 4.3).

A catenoid with an inextensibility constraint
The liquid constituent of the wicked membrane provides surface tension and as the membrane is thin enough to wrinkle and fold inside the liquid film, it can adapt to extreme deformations. However, this wicked membrane also displays an intrinsic inextensibility because of the solid fibrous membrane carrying the liquid. Here, we develop a model for the catenoid-like shape adopted by the wicked membrane which takes into account the global surface energy minimization, but also the fact that the membrane cannot be stretched.

To fulfill this intrinsic inextensibility condition, we impose the peripheral arc length of the profile to remain lower or equal to its initial value (i.e. the ring distance for which
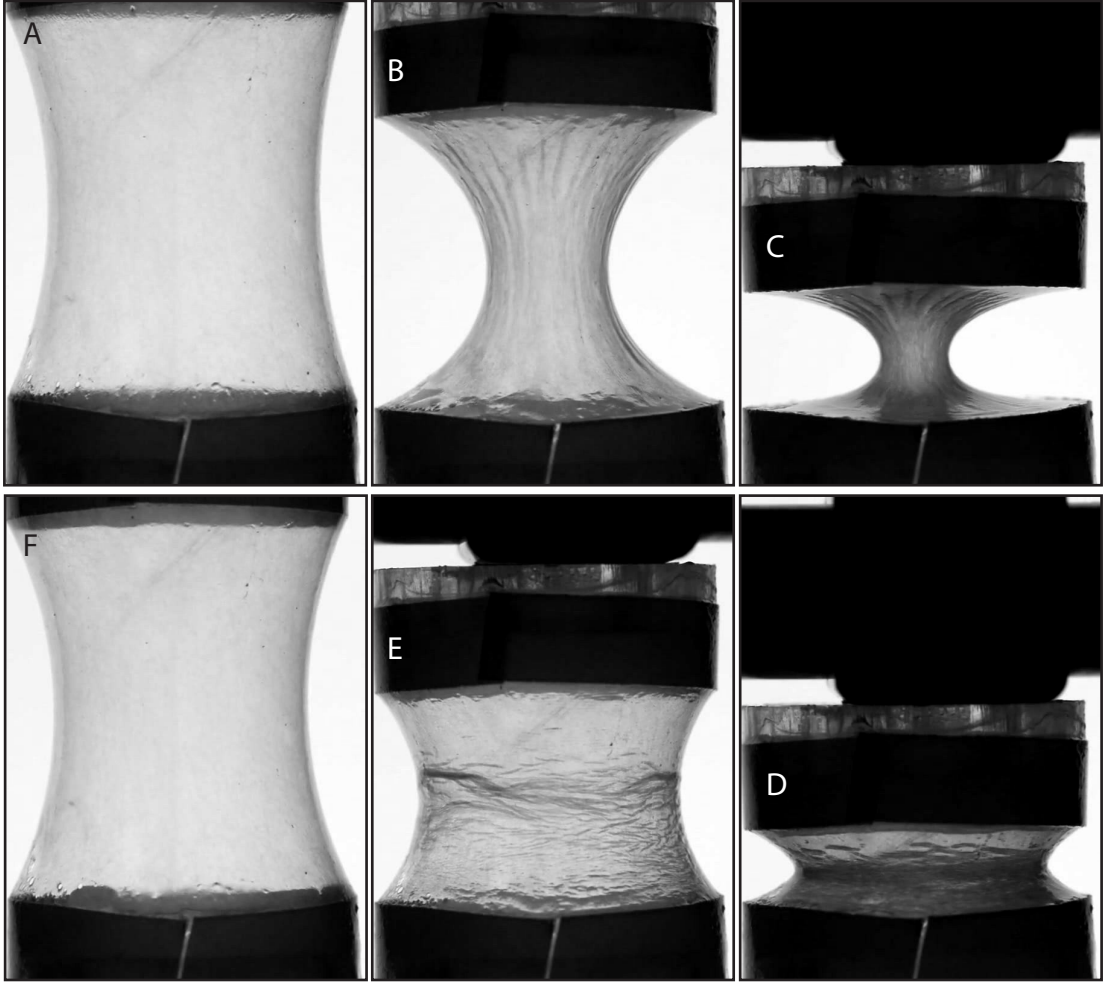
Figure 4.25 – Catenoid-like shape adopted by a wicked membrane attached to the edge of two rings (diameter of the ring: $2R_H = 4$ cm) throughout a compression-extension cycle. Note that the this catenoid jumps from a thin to wide state between image **C** and **D**. This sudden change in shape is due to the inextensibility constraint, responsible for a strong path dependence of the equilibrium state.

the membrane is perfectly cylindrical). This fixed membrane length is given by the initial length $2L$ and is shown, along with the other key parameters of the system, in Figure 4.27. Since the membrane is infused with a liquid, the shape minimizes the total interfacial energy of the system, $2\gamma S$ where γ is the liquid-vapor surface energy of the liquid, and S the surface area of the catenoid-like shape. As for the purely liquid catenoid, the surface area of the wicked membrane is written

$$S = \int_{-H}^{H} 2\pi R\sqrt{1 + R'^2}\, dY. \tag{4.20}$$

Moreover, since the fibers of the membrane cannot be stretched, an inextensibility constraint is applied in the Y-direction:

$$\int_{-H}^{H} \sqrt{1 + R'^2}\, dY \leq 2L. \tag{4.21}$$

The energy of the system is then re-written

$$\mathcal{V} = \int_{-H}^{H} 2\pi(R + \mu)\sqrt{1 + R'^2}\, dY \tag{4.22}$$
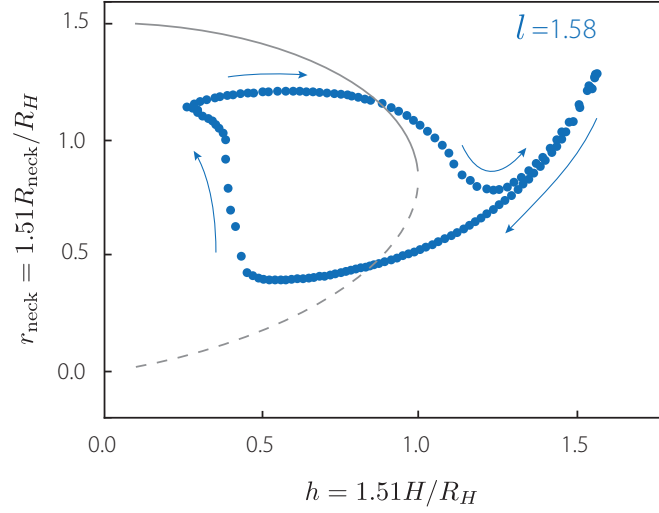
Figure 4.26 – **Wicked membrane catenoid's experimental bifurcation curve.** Experimental neck radii r_{neck} as a function of the distance between the rings h (blue dots) for a wicked membrane of initial length $l = 1.51L/R_H = 1.58$. These results correspond to the sequence provided in Figure 4.25. The theoretical purely liquid catenoid prediction is also represented as in Figure 4.27 and again, lengths are normalized by $R_H/1.51$. Surprisingly, the wicked membrane's catenoid exists in regions where the purely liquid catenoid does not (i.e. where $h > 1$).
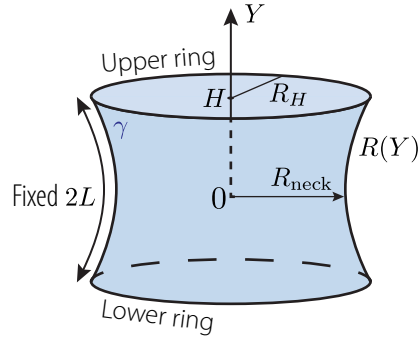
Figure 4.27 – Schematic representation of the catenoid-like shape adopted by the wicked membrane attached in a cylindrical configuration to two parallel rings. Due to the intrinsic inextensibility of the fibrous membrane, the side arc length of the profile cannot exceed $2L$.

where $2\pi\mu \geq 0$ is the Lagrange multiplier corresponding to the constraint given in Equation (4.21)). The inextensibibilty constraint is not active when $\mu < 0$. Equation (4.22) has the same structure as the purely liquid catenoid energy given in Equation (4.15) and in this case, we express the profile that minimizes interface energy as:

$$R(Y) = c\cosh\left(\frac{Y}{c}\right) - \mu \tag{4.23}$$

with two implicit equations for c and μ. The first one corresponds to the inextensibility constraint and is obtained by injecting Equation (4.23) in Equation (4.21):

$$c\sinh\left(\frac{H}{c}\right) \leq L \tag{4.24}$$

The second one accounts for the boundary condition $R(Y = H) = R_H$:

$$c\cosh\left(\frac{H}{c}\right) - \mu = R_H \tag{4.25}$$

These two last expressions have no explicit solutions but are solved numerically for c and μ.

The neck radius of this catenoid-like shape reads

$$R_{\text{neck}} = c - \mu. \tag{4.26}$$

Graphical interpretation of the inextensibility constrained catenoid
A set of paths for different peripheral lengths $l = 1.51L/R_H$ (between $l = 0.8$ and 1.7) is provided in Figure 4.28 where the solid lines correspond to the regions where $\mu > 0$ and the dashed lines correspond to $\mu < 0$. This figure also represents the bifurcation path of the purely liquid catenoid. When $\mu > 0$, the inextensibility constraint is active and the peripheral arc length of the catenoid-like shape is equal to $2l$. On the other hand, when $\mu < 0$ the inextensibility constraint becomes inactive and as for the usual liquid catenoid, only the surface area given in Equation (4.20)) has to be minimized, the corresponding configuration is therefore the same as the purely liquid catenoid discussed previously in Section 4.4.1.
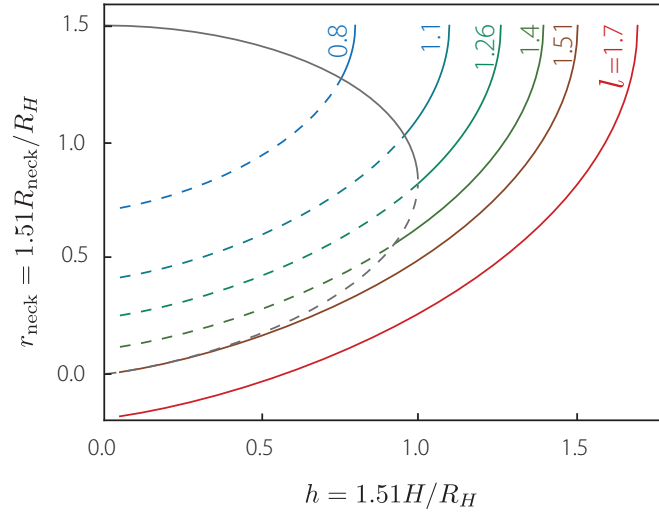

Figure 4.28 – **Dimensionless neck radius r versus dimensionless distance between the two rings h** for different length constraints l. The length $R_h/1.5090$ is commonly used to normalize lengths in catenoid-related problems as it allows to the set the tip of this saddle node bifurcation at $h = 1$. It is to be noted that the inextensibibilty constraint allows for catenoid geometries to exist in a region where purely liquid catenoids do not exist (*i.e.* where $h > 1$).

Note that the limit case $\mu = 0$ corresponds exactly to the case where no inextensibility constraint is to be considered at all and therefore, the transition between active constraint ($\mu > 0$) and inactive constraint ($\mu < 0$) always occurs on the stable or unstable branch of the purely liquid catenoid bifurcation curve.

It can be shown that the crossing of the inextensibility constrained catenoid and the purely liquid one occurs on the stable branch for $l < 1.26$ and on the unstable branch for $1.26 < l < 1.51$. The constraint is always active for $l > 1.51$ and in this case, the model predicts a negative neck radius r_{neck} which does not make any physical sense and really corresponds to pinching of the catenoid-like shape at the middle.

It is to be mentioned that a wicked membrane can display two stable equilibrium shapes for the same h. For example, in Figure 4.28 the curve corresponding to $l = 1.4$ shows that for a given height h slightly below 1.0, the neck radius can be that of a pure liquid catenoid (gray curve), or that of a catenoid with inextensibility constraint ($l = 1.4$) corresponding to the green curve. This bistability results in a strong path-dependence for the adopted shape of the system. Indeed, it will allow us to give a qualitative interpretation of the experimental results displayed in Figure 4.26 for a wicked membrane with $l = 1.58$. In Figure 4.29, we reproduce these results along with the theoretical inextensibility constrained catenoid (solid blue curve) for this experimentally-observed peripheral length $l = 1.58$. The

region where $h > 1.5$ seems to be well captured by the model and as the rings are brought closer (h decreases), the experimental results slightly deviate from the theoretical curve but the tendency is respected. At a point near $h = 0.5$, the catenoid-like shape jumps to a configuration much closer to the purely liquid catenoid.
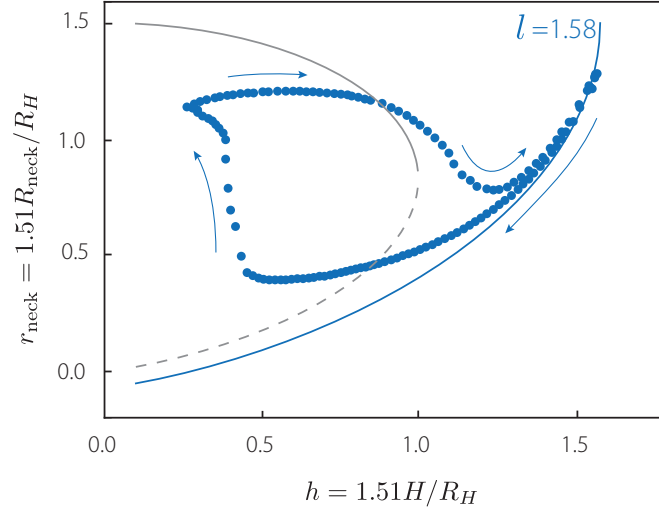
Figure 4.29 – Comparison between theory and experiments for the wicked membrane in a cylindrical configuration. The blue dots correspond to the experimental dimensionless neck radius of the wicked membrane. In this case, the initial rest half length between the rings (the native length of the membrane) is $l = 1.51L/R_H = 1.58$. For large h, the neck radius measurements is in good agreement with the theoretical behavior described by the blue solid curve (Equation (4.26)). As h is lowered (rings are brought closer), the experimental results of the wicked membranes deviate from theory up to a point where the shape suddenly jumps to a state with a wider neck (closer to the stable liquid catenoid). When the rings are subsequently pulled apart, the shape seems to qualitatively follow the stable liquid catenoid configuration until it does not exist anymore (at $h = 1$), where it converges back to the inextensibility solution.

This sudden configurational change is more deeply understood in Figure 4.30, where we follow the path taken by a inextensibility constrained catenoid with peripheral arc length $l = 1.50$.

The experimental wicked membrane path (for $l = 1.58$) should theoretically not have crossed the purely liquid catenoid path (because $l = 1.58 > 1.51$), however a small deviation from the theoretical model makes it cross the unstable catenoid branch anyway and makes it jump towards the stable liquid catenoid. This small deviation probably finds its explanation in the fact that the wicked membrane does not behave as a perfect liquid film with an inextensibility constraint. Indeed, as discussed in Section 4.3.4 (hysteresis of the planar wicked membrane), the wicked membrane likely deviates from its theoretical path due to membrane-membrane friction upon local reorganization through wrinkling and folding.
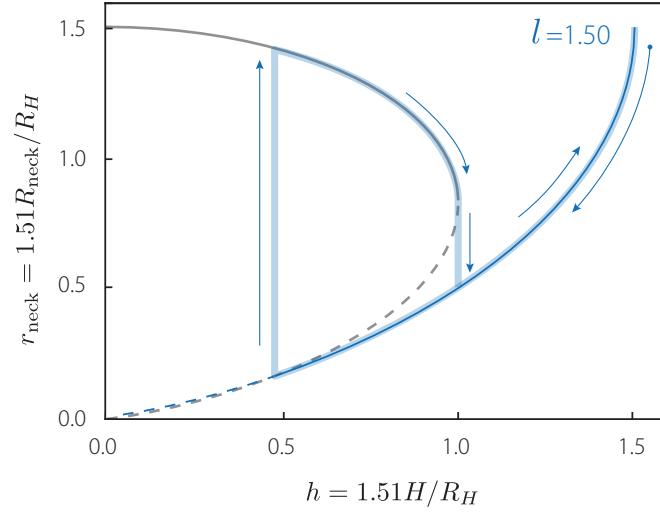
Figure 4.30 – Theoretical bifurcation curve of the neck radius of a catenoid with inextensibility constraint as a function of the distance between the parallel rings for a peripheral length of the membrane $l = 1.50$. At the beginning of this experiment, for $h = l$, the membrane is perfectly cylindrical. As the rings are brought closer, the neck radius shrinks due to the surface minimization with inextensibility constraint. The curve follows Equation (4.23) for $Y = 0$ until it crosses the unstable liquid catenoid solution for $\mu = 0$. At this point, because μ becomes negative, the inextensibility constraint is no longer active and the configuration jumps to the stable liquid catenoid branch of the bifurcation diagram. When the rings are subsequently pulled apart, the shape follows the stable liquid catenoid branch until the latter does not exist anymore (at $h = 1$), it then jumps back to the branch of the inextensibility constrained catenoid. This scenario explains the sudden jump and strong hysteresis that was experimentally observed for a wicked membrane.

4.5 Spherical wicked membrane

The two previous sections (planar membrane in 4.3 and cylindrical membrane in 4.4) demonstrated that the wicked membrane displays mixed liquid (surface tension) and solid (inextensibility) properties which are sometimes expressed simultaneously in a given configuration. In this section, we will briefly consider a third archetypical capillary structure: the spherical bubble. In order to study the wicked membrane in this configuration, we fix a PAN membrane to the tip of a tube in a carefully prepared bubble conformation which will allow us to blow it up using a syringe pump, after wicking it with water. A sequence of the resulting blowing up of this 'bubble' is provided in Figure 4.31.

> To measure the pressure inside an inflated spherical wicked membrane, the visualization of an adjacent ethanol filled tube is used. The bubble is inflated with air using a PHD Ultra Syringe Pumps (Harvard Apparatus) at a rate of 6 ml/min. The air-entrance tube is connected to a U-shaped tube partially filled with dyed ethanol with a T-junction. One end of the U-shaped tube is therefore pneumatically linked to the bubble, while the other end is open (at atmospheric pressure). The difference in height Δh of the two ethanol interfaces inside the U-shaped tube indicates the pressure P inside the bubble, knowing its density $\rho = 789$ kg/m^3 and earth acceleration $g = 9.81$ m/s^2 ($P = \rho g \Delta h$). The pressure P is normalized by $P_{\max} = 4\gamma/R_{\text{tube}}$, which is the theoretical maximum pressure for a spherical bubble of surface tension γ, inflated out of cylindrical tube of radius R_{tube} ($R_{\text{tube}} = 4.5$ mm in our experiment). In contact with the PAN membrane, the surface tension of deionized water drops from 72 to 53 mN/m.
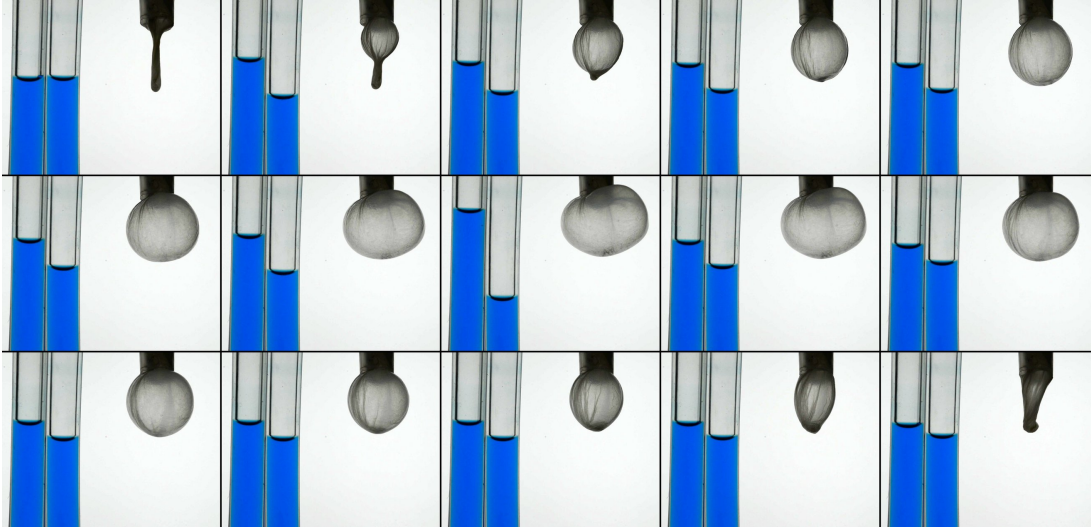
Figure 4.31 – Side view of the bubble-like PAN wicked membrane inflated with air. The tubes filled with blue dyed ethanol allow to characterize pressure inside the wicked membrane bubble throughout its inflating. The external diameter of the tube supporting the bubble is 9 mm.

The experimental bubble pressure throughout the inflating and deflating of the wicked membrane bubble is exposed in Figure 4.32 (blue dots) and compared to the analogous liquid bubble theoretical results (solid gray line). This theoretical curve is obtained by considering that the pressure inside the bubble is given by:

$$P = \frac{4\gamma}{R_{\text{curve}}} \tag{4.27}$$

where R_{curve} corresponds to the curvature radius of the bubble (the two main curvature radii of this bubble are equal due to the axial symmetry of the system).

Note that the first ascending part of the pressure curve corresponds to the first inflating stage where pressure builds up because the curvature radius of the bubble first decreases down to a value R_{tube} (it theoretically starts at $R_{\text{curve}} = \infty$ since the initial configuration

is a flat liquid disc at the tip of the inflating tube).

As shown in Figure 4.32, the pressure inside the wicked membrane bubble is well characterized by the theoretical Laplace law when the membrane is inflated. However, near $r = R/R_{\max} = 1$, the experimental values deviate strongly from theory as the bubble pressure diverges. This is due to the intrinsic inextensibility of the membrane; when all the membrane reserves are exhausted, the bubble can no longer grow, this leads to the pressure build-up.

Surprisingly, the pressure path taken upon deflation of the bubble is very different to that of the inflation phase. This strong hysteresis may find its root in friction of the membrane with itself when it wrinkles and folds inside the liquid layer to form membrane reserves. Despite the hysteresis, the inflation-deflation cycle is reversible.
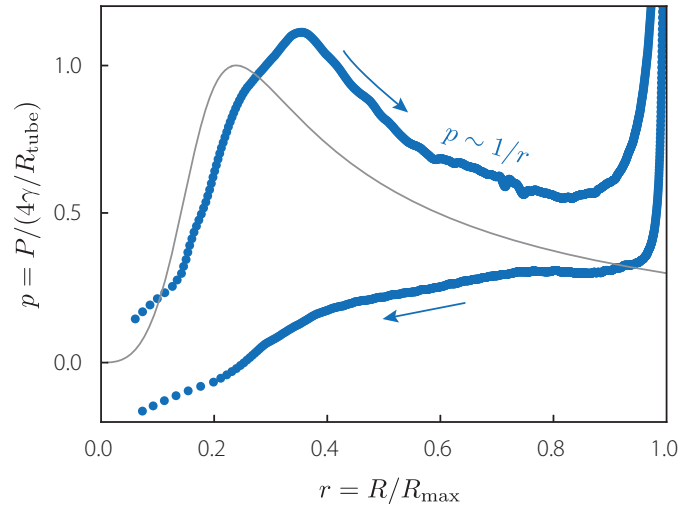
Figure 4.32 – Normalized pressure p versus normalized effective radius of the bubble $r = R/R_{\max}$ where $R = (3\Omega/(4\pi))^{1/3}$, Ω is the air volume injected in the bubble. The blue dots correspond to the pressure measurements carried out on the wicked membrane in a bubble configuration whereas the solid gray line shows the theoretical pressure of liquid bubble. The first increasing behavior and the subsequent decreasing (characteristic of the Laplace pressure decrease with $p \sim 1/r$) are well captured by the theoretical liquid theory. Near $r = 1$, inextensibility of membrane is expressed; the volume of the bubble can no longer increase and pressure diverges. When the spherical membrane is deflated, the path taken by the pressure is significantly lower that during the inflation. This is probably due to the intrinsic friction of the membrane with itself when wrinkling and folding inside the liquid layer.

This wicked-membrane bubble experiment is similar to cortical tension measurements of passive J774 cells studied in Lam et al. (2009). In this article, the authors propose a dual law to describe the tension T of the cell membrane which reads:

$$T = \gamma \quad \text{for} \quad S \leq S_0 \tag{4.28}$$

$$T = \gamma + k\frac{S}{S_0} \quad \text{for} \quad S > S_0 \tag{4.29}$$

where γ corresponds to the constant tension they measure for a cell surface area S smaller than the smoothed-out-membrane surface area S_0. The factor k is an elastic expansion modulus. This biologically-inspired model is also valid for our wicked membrane and explains the pressure divergence for $R = R_{\max}$ presented in Figure 4.32.

4.6   Conclusions

Two dimensional membrane reserves are found in Nature as wrinkles and corrugations at the surface of animal cells such as the J774 macrophage. This organism can effortlessly increase its outer membrane surface area by up to a factor 5 to engulf large intruders. The necessary ingredients for the spontaneous formation of such membrane reserves are flexibility of the membrane and a surface force which puts the membrane under tension. In stretchable animal cells, this surface force is ensured by the underlying cortical actin layer and in order to reproduce this mechanism, we have turned to the fabrication of ultra thin fibrous membranes using an electrospinning technique. The fabricated membranes provide the desired flexibility, and surface forces are obtained by wicking the membrane with a wetting liquid. Indeed, the surface tension carried by the liquid allows to ensure tension even when the boundaries of the membrane are brought closer, excess membrane is then spontaneously stored as wrinkles and folds inside the liquid film. Starting from a previously compressed state, the wicked membrane therefore displays a high effective extensibility; membrane reserves fuel any shape change. Three different geometries of the wicked membrane also allowed to show that the wicked membrane inherits the properties of both its constituents. The solid underlying fibrous membrane ensures inextensibility whereas the wicking liquid, through the surface energy it carries, provides tension. The forms and forces developed by the wicked membrane in a planar, cylindrical and spherical configuration were compared the pure liquid analogous ones displayed by soap films.

5 | Buckling pattern of the wicked membrane

Contents

The previous Chapter studied the macroscopic behavior of the wicked membrane. We showed that capillary forces developed by the liquid film were sufficient to keep the wicked membrane straight even when its boundaries are brought closer in the planar configuration and that it adopts catenoid and bubble shapes in a cylindrical and spherical configuration respectively. The theoretical framework predicting the forms and forces of the wicked membrane relies on three assumptions:

○ The wicked membrane minimizes its global surface area because it carries a surface energy (inherited from the wicking liquid).
○ Any segment of the wicked membrane cannot be elongated with respect to its reference (native) length because the fibers composing the membrane are inextensible.
○ Any segment of the wicked membrane can shrink with respect to its reference state, yet remaining straight (the membrane then spontaneously folds inside the liquid film).

This Chapter focuses on the last point. In experiments, the membrane spontaneously folds inside the liquid film and therefore accommodates for the global shape changes it undergoes. We study the wicked membrane buckling mechanics. For example, Figure 5.1 presents a PAN membrane wicked with water. Starting from a straight and smooth state (Figure 5.1-A), the planar wicked membrane is compressed. The visualization technique described in appendix B, taking advantage of the reflectiveness of the wicked membrane, allows to highlight irregularities at its surface when slightly compressed, as in Figure 5.1-B. The wicked membrane surface then displays a well-defined wavy pattern of characteristic wavelength around 100 microns. Upon further compression (Figure 5.1-C&D), a collapsed

phase of closely-packed wrinkles appears and grows while the wavy regions diminish. This first observation leads to three questions:

○ How is the wavy pattern orientation selected?
○ What is the wrinkling wavelength of the wavy pattern?
○ Why do wavy regions of the membrane convert into collapsed regions as compression is carried out?
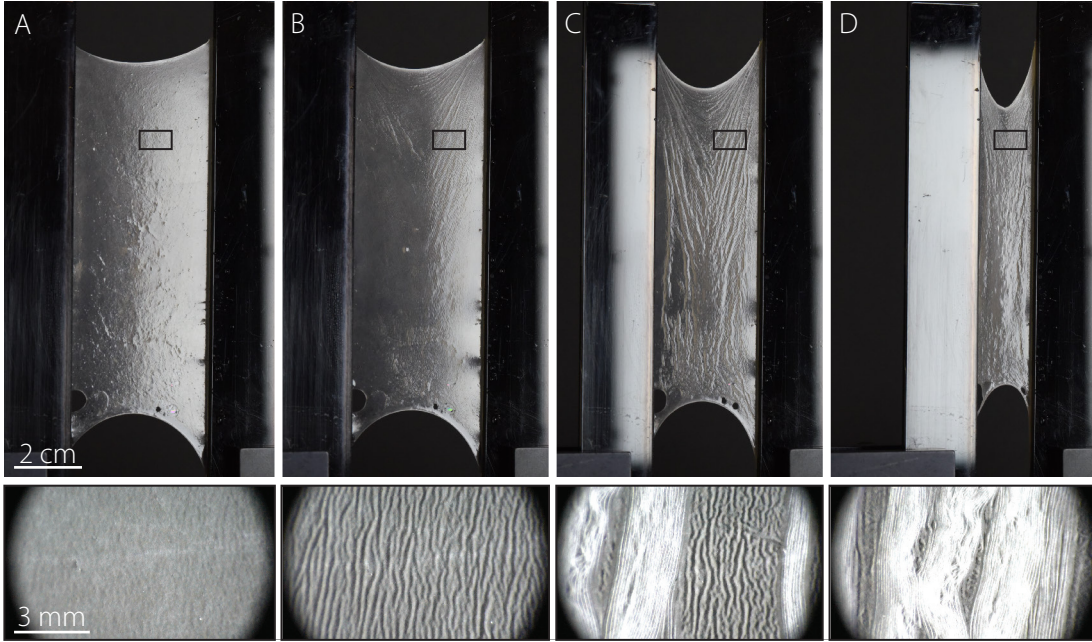
Figure 5.1 – Planar PAN membrane wicked with water and compressed. At its extended state (see **A**), the membrane displays a relatively smooth surface and as compression is initiated, it rapidly (compression $\epsilon < 5\%$) exhibits a wavy pattern which follows a well-defined pattern (see **B**). As compression is pursued, some wavy regions convert into more dense, collapsed regions, while other conserve their wavy texture (see **C**). The collapsed regions correspond to the membrane reserves and then the wicked membrane is completely compressed, the whole membrane displays the collapsed texture (see **D**).

It should be mentioned that this study is performed exclusively with PAN membranes. This material choice may seem counterintuitive since the PVDF-HFP membranes generally provide appealing features such as better mechanical robustness and therefore the possibility of working with thinner membranes which can host extreme compressions. However, since the fibers composing the PAN membrane are not bridged (see Section 4.3.4), they can move freely with respect to one and other. The membranes therefore have an intrinsically lower bending stiffness and the study can therefore be performed on thicker membranes, which generate clearer buckling patterns. Moreover, fixing the membrane on the straight mobile edges can induce internal stresses. Such stresses can affect the buckling pattern of the membrane but they are automatically released in the wicked PAN membrane. As the fibers can locally slide with respect to one and other, this local creep 'anneals' the membrane.

Wrinkling appears in a variety of contexts and before studying the wicked membrane mechanics, a few examples are provided in the next section.

5.1 Wrinkling: an introduction

Wrinkling is a trademark of thin elastic sheets, and develops spontaneously in a many contexts: pinched skin, shriveling fruits (Cerda and Mahadevan 2003), brain sulci (Tallinen

et al. 2016), hanging curtains (Vandeparre et al. 2011) or more generally thin sheets under tension (Davidovitch et al. 2011). This elastic instability occurs whenever a compressed slender structure is bound to a substrate resisting deformation. The emerging wavelength λ of this particular form of buckling therefore results from a trade-off between the deformation of the membrane and that of the substrate in order to minimize global energy. Bo Li and collaborators propose a complete review on surface wrinkling in Li et al. (2012).

To illustrate a classical wrinkling phenomenon, we focus on the elasto-gravitational buckling of an elastic plate on liquid bath. Figure 5.2 presents the experiment, an elastic plate of thickness t, width W and length L is deposited on a liquid bath of specific weight ρg.
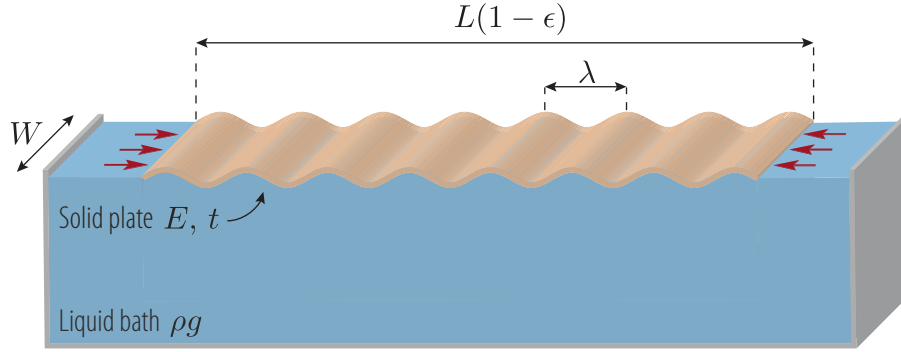

Figure 5.2 – **Elastic buckling on a liquid foundation**. An elastic plate is compressed on a liquid bath. As it buckles, the plate entrains liquid, carrying gravitational hydrostatic energy. The system therefore adopts an equilibrium wrinkling wavelength λ which minimizes global energy.

The elastic plate is compressed uni-axially by bringing its ends closer, to a distance $L(1-\epsilon)$. Upon compression, the plate buckles and displays a wrinkling pattern of wavelength λ. We study the dependence of λ on the physical parameters. For this, we write the elastic energy of the plate:

$$\mathcal{V}_e \sim \epsilon L W \frac{EI}{\lambda^2} \tag{5.1}$$

where E is the Young's modulus of the plate and I the quadratic moment of area of its cross section given by $I = Wt^3/12$. As the plate buckles, it draws liquid, which introduces a hydrostatic energy written:

$$\mathcal{V}_g \sim \epsilon L W \rho g \lambda^2. \tag{5.2}$$

To minimize energy, the elastic plate favors a large wavelengths λ whereas the liquid benefits from small wavelengths. Global energy minimization therefore leads to a trade-off wavelength λ given by:

$$\frac{\partial(\mathcal{V}_e + \mathcal{V}_g)}{\partial \lambda} = 0 \quad \Rightarrow \quad \lambda_{eg} \sim \left(\frac{EI}{\rho g}\right)^{1/4} \tag{5.3}$$

This elasto-gravitational wavelength λ_{eg} was first introduced by Hertz and Föppl (Hertz 1884; Föppl 1897) as they were studying the buckling of fluid supported slender structures.

A similar wavelength is exhibited when a thin stiff film is bound to a soft foundation. When this system is compressed, it adopts a wavelength $\lambda \sim t \left(E_{\text{stiff}}/E_{\text{soft}}\right)^{1/3}$ where t is the thickness of the stiff film and E_{stiff} and E_{soft} respectively correspond to the Young's modulus of the stiff film and the soft foundation. Bowden et al. (Bowden et al. 1998) take advantage of this 'self-assembling' mechanism to design controlled wrinkled surface by tuning both the buckling pattern and its wavelength exhibited by a thin metallic layer on a polymer (PDMS) substrate (see Figure 5.3). Another ingenious application of wrinkling is presented in Figure 5.3-right, reproduced from Terwagne et al. (2014), where a soft hollow

sphere is covered with a stiff thin film. When a negative pressure is imposed inside the sphere, its surface spontaneously wrinkles, displaying a dimpled texture. This wrinkled geometry is reminiscent of the golf ball and depending on the imposed depression, the aerodynamic performances of the sphere are tuned. A review of the physics of buckling on elastic and hydrostatic foundations is presented in Brau et al. (2013).
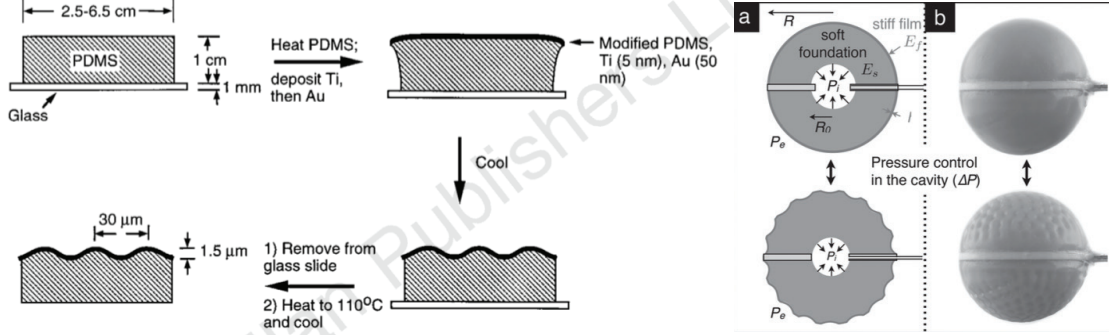
Figure 5.3 – **Left** – A thin metallic layer (titanium + gold) is deposited on a pre-heated Polydimethylsiloxane (PDMS) substrate. Upon cooling, the PDMS shrinks, leading to the wrinkling of the metallic film. Reproduced from Bowden et al. (1998). **Right** – A soft hollow sphere is covered by a thin stiff film. A well-defined buckling pattern appears upon depressurizing its cavity. Reproduced from Terwagne et al. (2014).

Tension can also generate wrinkling in thin elastic sheets and Figure 5.4 illustrates this phenomenon in four different configurations. For example, when an elastic sheet is sheared as in Figure 5.4-A, diagonal wrinkles are generated and a method to predict their orientation is provided in Mansfield (1970). Capillary forces can also generate tension-induced wrinkles. Huang et al. (2007) presents this scenario (see Figure 5.4-C): a drop sits on thin polystyrene sheet deposited on a liquid bath. The capillary forces developed by this drop set the sheet under tension, leading to an array of radial wrinkles.
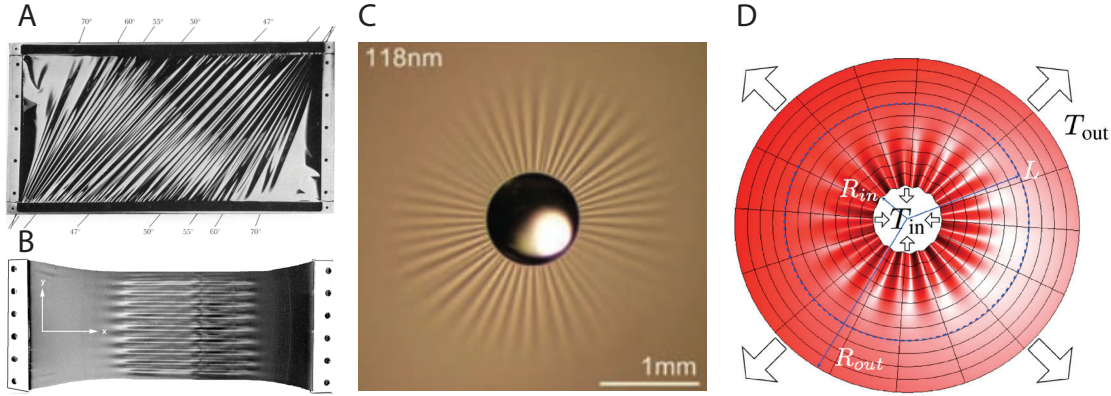
Figure 5.4 – **A** – Tension ray lines in rectangular membrane under shear. Reproduced from Mansfield (1970). **B** – Wrinkles in a polyethylene sheet of length $L \simeq 25$ cm, width $W \simeq 10$ cm and thickness $t \simeq 100\,\mu$m under a uni-axial elongation $\epsilon = 0.1$. Reproduced from Cerda and Mahadevan (2003). **C** – A water drop of radius $R = 0.5$ mm is deposited on a 118 nm-thick polystyrene sheet floating on the surface of water. The developed capillary forces set the sheet under tension, leading to an array of wrinkles. Reproduced from Huang et al. (2007). **D** – The Lamé configuration: A mismatch between the inner and outer stresses yields a compression, which is relieved by wrinkling. Reproduced from Davidovitch et al. (2011).

5.2   Orientation of the wavy pattern of the wicked membrane

In this Section, we experimentally observe the orientation of the wavy pattern patterns (i.e. the directions followed by the wrinkles all over the membrane) of a wicked membrane in three different configurations. In order to gain a deeper physical understanding of these patterns, we turn to an analogous elastic plate problem under compression and solve it using a Finite Element Method. Determining the inner stress state of this plate for a similar geometry and under similar boundary conditions provides a glance into the wrinkling directionality of the wicked membrane.

5.2.1   Experimental observation

We focus on the wrinkling pattern displayed by a compressed planar wicked membrane and therefore study three cases. The first one corresponds to a wicked membrane in the absence of gravity. The second one is influenced by gravity and is set in a vertical position, its compression axis is perpendicular to the gravity field's direction. The third one corresponds to a rotated version (90°) of the previous one and has a compression axis parallel to gravity.

Absence of gravity

In the first case, since the visualization setup constrains a vertical position of the membrane, we turn to a thin PAN membrane (electrospun for 2 minutes) wicked with a little amount of water in order to limit the influence of gravity to a minimum. The precise quantity of wicking water is not defined in the experiment. However, by letting the infused water drain downwards for a few minutes, and then sponge it with a cloth, it is reduced to a small quantity. A typical visualization of this experiment is provided in Figure 5.5. The wrinkling pattern displays a satisfying top-down symmetry. The wrinkles show an angle at the top and bottom part of the membrane (see respective close-ups on these areas), and follow the direction of the circular arcs described by the top and bottom free edges. The wrinkles direction is vertical in the middle of the membrane.
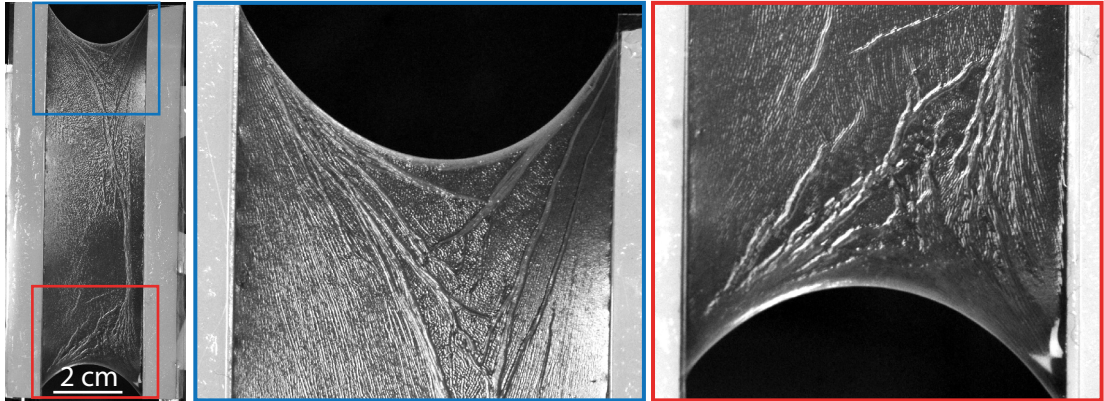
Figure 5.5 – Thin PAN membrane wicked with a small quantity of water. The resulting wrinkling pattern follows a well defined structure and has a satisfying top-down symmetry. A previous compression may have concentrated the liquid at the right side, therefore generating the left-right asymmetry that is observed.

Gravity perpendicular to compression axis

Now, a thicker membrane (electrospun for 4 minutes) is wicked with a larger amount of water and is again slightly compressed (about 5% compression). The observations are provided in Figure 5.6 where we clearly see that gravity plays an important role in the wrinkling pattern as it now displays a top-down asymmetry. The wrinkles show an angle (they exhibit a 'V' shape) over the whole membrane except at the bottom where they

describe a Λ shape. In both the bottom and top area, the wrinkle pattern adjusts to follow the circular arc described by the free edges.
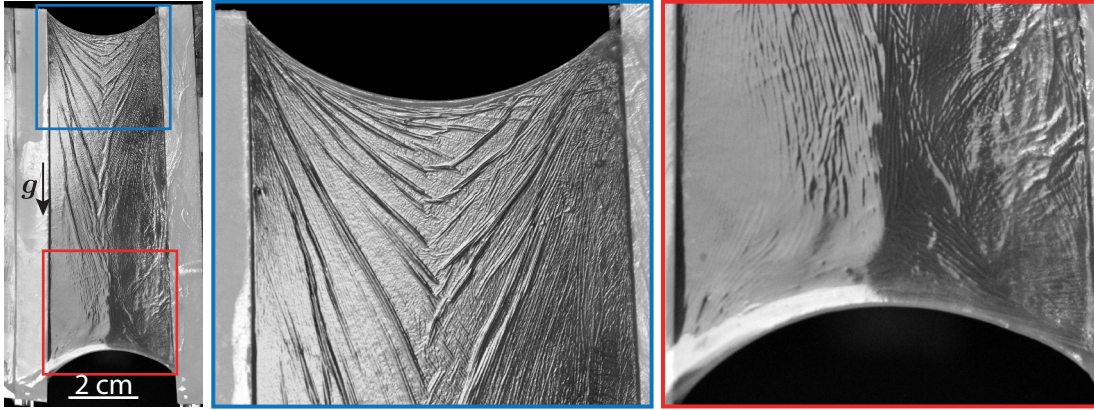
Figure 5.6 – Thick PAN membrane wicked with a large amount of water. Here, gravity plays an important role in the pattern adopted by the wrinkles. It displays a 'V' structure on the whole membrane, except at the bottom of it, where the 'V' is inverted and the wrinkles direction follow the circular arc described by the free edge.

Gravity parallel to global compression axis

The last experiment is performed on a thick membrane (electrospun for 4 minutes) wicked with a large amount of water. Unlike the previous experiment, the compression axis of the membrane is now parallel to the gravity field and the resulting wrinkling pattern again exhibits an obvious top-down asymmetry. Once again, the wrinkling pattern seems to adjust near the free edges to follow their circular shape.

Figure 5.7 – Thick PAN membrane wicked with a large amount of water. Unlike the case presented in Figure 5.6, gravity now is oriented in the same direction as the compression axis of the membrane. This results in a wrinkling pattern where again, the preferred directions follow the circular arcs of the free edges. It should be noted that the inhomogeneities in the membrane's color density correspond differences in thickness, but they do not affect the wrinkling pattern significantly.

5.2.2 Major compression axis criterion: Comparison with an elastic plate under compression

The orientation of the wavy pattern is likely dictated by the early stress state of the membrane just before wrinkling occurs. It is reasonable to assume that, being flexible, the membrane can not withstand compression and that it buckles instantaneously when compression occurs. When a wrinkle appears, it therefore likely takes the perpendicular direction to local compression axis in the membrane. In order to the approximate the stress state of the membrane at early compression, we turn to an elastic Finite Element Method (FEM) and compute the stress state of an analogous rectangular planar plate of width W

and length L. As for the planar wicked membrane, the right and left edges of the plate are straight and brought closer by a length ΔL. In order to reproduce the geometry adopted the planar wicked membrane, a displacement is imposed at the top and bottom edges of the plate in order to reproduce circular arcs of fixed length L. The key ingredients of the numerical simulations are presented in the next sections.

Plate equations: plane stress condition

The deformation field ε of the plate is related to its displacement field u and is given by:

$$\varepsilon = \frac{1}{2}\left(\boldsymbol{\nabla} u + \boldsymbol{\nabla}^T u\right) \tag{5.4}$$

or:

$$\varepsilon_{xx} = \frac{\partial u_x}{\partial x} \quad \text{and} \quad \varepsilon_{yy} = \frac{\partial u_y}{\partial y}; \quad \varepsilon_{xy} = \varepsilon_{yx} = \frac{1}{2}\left(\frac{\partial u_x}{\partial y} + \frac{\partial u_y}{\partial x}\right) \tag{5.5}$$

where no out of plane deformation is taken into account. Moreover, for a thin plate, the internal stress state shows no components on the z-axis (i.e. $\sigma_{zz} = \sigma_{xz} = \sigma_{yz} = 0$) and the stresses are therefore written (Bazant and Cedolin 2010):

$$\sigma_{xx} = \frac{E}{1-\nu^2}\left(\varepsilon_{xx} - \nu\varepsilon_{yy}\right); \quad \sigma_{yy} = \frac{E}{1-\nu^2}\left(\varepsilon_{yy} - \nu\varepsilon_{xx}\right) \quad \text{and} \quad \sigma_{xy} = \frac{E}{1+\nu}\varepsilon_{xy}. \tag{5.6}$$

The total elastic energy of the system writes:

$$\mathcal{V}_{\mathrm{el}} = \iint \frac{1}{2}T\,\boldsymbol{\sigma} : \boldsymbol{\varepsilon}\,\mathrm{d}S \tag{5.7}$$

where T refers to the thickness of the plate. The gravitational energy of the system, is

$$\mathcal{V}_{\mathrm{grav}} = -\iint \rho T\,\boldsymbol{g}\cdot u\,\mathrm{d}S. \tag{5.8}$$

Boundary conditions

The straight edges (right and left) are brought closer in a linear way along the x-axis at a relative compression $\Delta L/L$.

$$u_{\mathrm{right}} = \left[-(L-\Delta L)/2,\,0\right] \tag{5.9}$$
$$u_{\mathrm{left}} = \left[(L-\Delta L)/2,\,0\right] \tag{5.10}$$

whereas the top and down free edges adopt circular shapes, while conserving their arc length L as described in Section 4.3.1 (the variables R and β are found in that section).

$$u_{\mathrm{top}} = \left[R\sin\left(\frac{X_{\mathrm{top}}}{R}\right) - X_{\mathrm{top}},\, R\left(\cos\beta - \cos\left(\frac{X_{\mathrm{top}}}{R}\right)\right)\right] \tag{5.11}$$

$$u_{\mathrm{bot}} = \left[R\sin\left(\frac{X_{\mathrm{bot}}}{R}\right) - X_{\mathrm{bot}},\, -R\left(\cos\beta - \cos\left(\frac{X_{\mathrm{bot}}}{R}\right)\right)\right] \tag{5.12}$$

where X_{top} and X_{bot} respectively correspond to the X-coordinates of the nodes of the top and bottom free edges.

Numerical solution with FEniCS

FEniCS is an open-source computing platform for solving partial differential equations using a Finite Element Method and we will here use it to numerically solve the problem exposed above by minimizing the total energy $\mathcal{V} = \mathcal{V}_{\mathrm{el}} + \mathcal{V}_{\mathrm{grav}}$ of the system. The calculations are performed for $L = 2$, $W = 6$, $\Delta L/L = 0.05$, $T = 0.001$, $E = 1$, $\rho g = 0$ (or 0.2 for the study of the influence of gravity) and the number of nodes meshing the plate is $N = 20 \times 20$.

Major compression criterion

Once the problem is solved numerically, we study the planar stress tensor $\boldsymbol{\sigma}$ at each node of the elastic plate. We compute its eigenvalues $\sigma_{1,2}$ and eigenvectors $(\boldsymbol{V}_{1,2})$ which reveal the principal stress directions throughout the plate. A positive eigenvalue σ_i $(i = 1, 2)$ corresponds to tension state in the $\boldsymbol{V}_i$ direction whereas a negative one denotes compression. Therefore, finding the lowest eigenvalue σ_i and ensuring it is negative gives access to the major compression axis, i.e the axis along which compression is the strongest. Transposed to the wicked membrane, this information is valuable. Indeed, since the membrane has a low bending rigidity, it cannot withstand any compression and it locally buckles inside the liquid film as soon as compression is present. If the membrane is subjected to two orthogonal compressions, it seems reasonable to assume that it will buckle first along the highest compression axis. The wrinkling lines would therefore appear perpendicularly to the major compression axis. A set of results for the three different cases discussed in the previous section is presented in Figure 5.8, where the elastic plate's stress field was computed using the parameters provided in Section 5.2.2. The lines correspond to the perpendicular directions of the eigenvector $\boldsymbol{V}_i$ $(i = 1, 2)$ where σ_i is the lowest of the eigenvalues of $\boldsymbol{\sigma}$, and is negative.
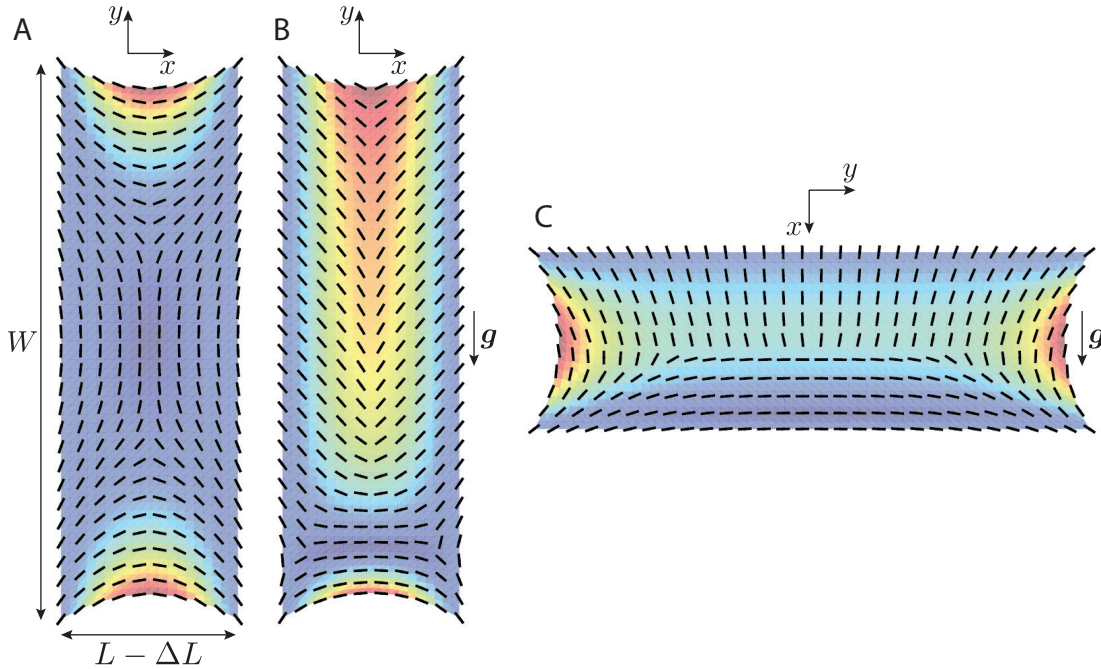
Figure 5.8 – **An elastic planar plate under compression to read the major local compression axes.** Calculations performed with FEniCS. There is no gravity in **A** while **B** and **C** respectively correspond to calculations with gravity pointing perpendicular and parallel to the plate's global compression axis. The straight black lines show the orthogonal directions to the local major compression axes and thus show the direction along which wrinkles are generated in the wicked membrane case. Qualitatively, we find a good match between the patterns predicted by the elastic planar plate model and the experimental wicked membrane wrinkling patterns (resp. presented in Figures 5.5, 5.6 and 5.7). All the calculations are performed with $L = 2$, $W = 6$, $T = 0.001$, $E = 1$, $\nu = 0$, $N = 20 \times 20$, $\Delta L/L = 0.05$ and $\rho g = 0.2$ (ρg was arbitrarily chosen) for **B** and **C**. The color scale refers to the displacement field.

5.2.3 Discussion

The numerical calculation of the orientation of the major compression axis in an elastic plate, presented in Figure 5.8, is in good qualitative agreement agreement with the experimental observations of Figures 5.5, 5.6 and 5.7. The stress state of the wicked membrane just

before it starts wrinkling gives rise to the well defined wrinkling pattern; any local small compression will result in wrinkling of the membrane. Since the compressive stresses inside the membrane remain relatively low, a small exterior perturbation can significantly modify the wrinkling orientation. For example, Figure 5.9 shows a planar wicked PAN membrane in a slightly compressed state. Bubbles are present at its surface and the capillary forces they exert on the membrane are sufficient to locally distort the orientation of the wrinkling pattern. Indeed, the tension applied by the liquid meniscus seems to rotate the major compression axis of the membrane which therefore displays wrinkles perpendicular to the bubble periphery.
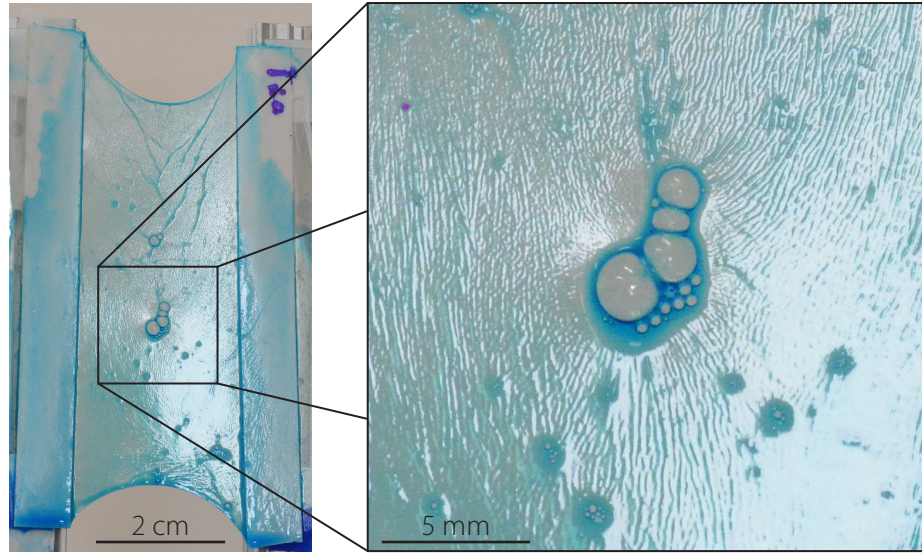
Figure 5.9 – PAN membrane wicked with a water-surfactant solution. A bubble is present at the surface and the capillary forces it applies are sufficient to significantly distort the wrinkling orientation which locally points perpendicularly to the bubbles' periphery.

Further experiments could be performed in other membrane configurations to test the validity of the assumption that the early stress state of the membrane is responsible for the orientation of the wavy pattern. To further understand the interactions between the solid membrane and the liquid film, we study in the next section the wavelength of the wrinkling pattern.

5.3 Wavelength of the wavy pattern

5.3.1 Experimental observation

We study the wavelength of the wavy pattern that naturally arises when a planar wicked membrane is uni-axially slightly compressed. Note that the wavelength is not sensitive to the intensity of the compression state. We first focus on the experimental method used to explore the wrinkling wavelength depending on the thickness of the liquid film wicking the fibrous membrane.

Thickness characterization of the wicking liquid film

In order to study the wrinkling wavelength λ as a function of the liquid thickness h, a colorimetry tool is used to characterize the liquid film thickness. The membrane is wicked with a dyed liquid (water, dyed blue) and a photograph of the infused membrane is taken next to a calibration wedge containing the same dyed liquid with a D810 Nikon camera. Comparing the photograph's local gray value on the membrane and the thickness versus

the gray value curve (see figure 5.10), we can locally estimate the thickness of the liquid film. Image analysis is performed using the image processing package Fiji.
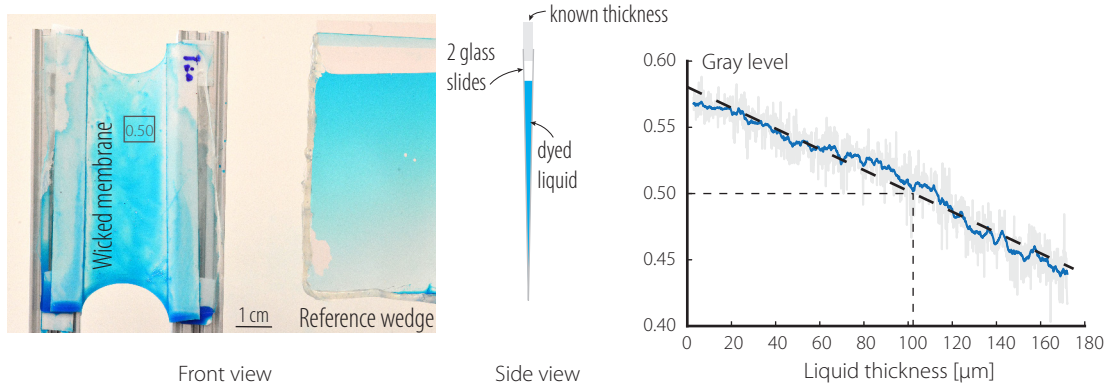
Figure 5.10 – Measurement of the liquid film thickness of the infused membrane with a colorimetry method. A scale wedge (two slightly non parallel glass slides) is used to calibrate the gray level as a function of thickness of the dyed liquid film on a photograph. In this case, we show an area on the membrane where the gray level is 0.50, corresponding to a liquid film thickness of around 100 μm.

Wavelength measurement

The wrinkling wavelength λ is measured when the wicked membrane is slightly compressed. The membrane is illuminated from the side in order to enhance the wrinkles' contrast and a photograph is taken with a D810 Nikon Camera. For each liquid film thickness (different amount of wicked liquid), a set of 4 wavelength measurements is performed. The coloring agent (erioglaucine disodium salt) did not show to change the liquid surface tension significantly. A typical wavelength measurement image is presented in figure 5.11.
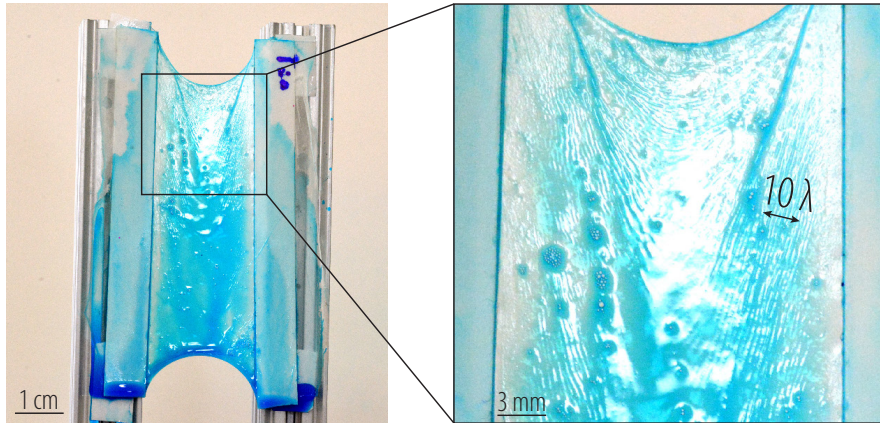
Figure 5.11 – Visualization of the wrinkles on a slightly compressed wicked membrane.

In Figure 5.12, we report the experimental wrinkling wavelength as a function of the liquid thickness for four different PAN membranes wicked with different liquids. Three PAN membranes of different native thicknesses (i.e. the thickness of the dry fibrous membrane) were tested. The wrinkling wavelength shows to increase with the liquid thickness independently of the native thickness of the membrane and adding surfactant to the wicking water does not notably alter the results. Note that in contact with the PAN membrane, the surface tension of water shows to drop from $\gamma = 72$ to 53 mN/m. Adding surfactant (here, soap) decreases water surface tension to 30 mN/m.
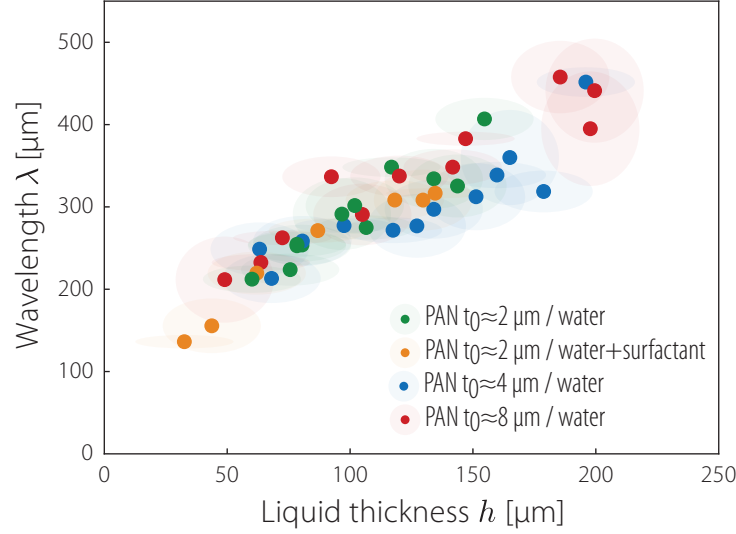
Figure 5.12 – Experimental wavelength λ of the wavy pattern versus the thickness of the liquid wicking a PAN membrane for different native membrane thicknesses t_0 and different wicking liquids.

In order to further understand the wrinkling of the wicked membrane, we propose a model in the following section describing the buckling of a 1-dimensional beam between two liquid interfaces.

5.3.2 Analytical calculation of the wrinkling wavelength λ

Here, we study the buckling of an elastic beam of total length L confined inside a liquid film of thickness h. The potential energy of the system comprises two terms: the deformation energy of the beam and the surface energy of the liquid-air interface. We impose an end-shortening ΔL on the end-to-end distance of the system. The beam tries to accommodate this imposed constraint by developing a shape with a long axial wavelength, the end-shortening generating a transverse deflection of the beam. This deflection then induces an important deformation of the liquid-air interface and hence raises the surface energy of the interface, compared to the surface energy of a flat interface. A trade-off has to be found between elastic and surface energies, where the total potential energy is minimum.
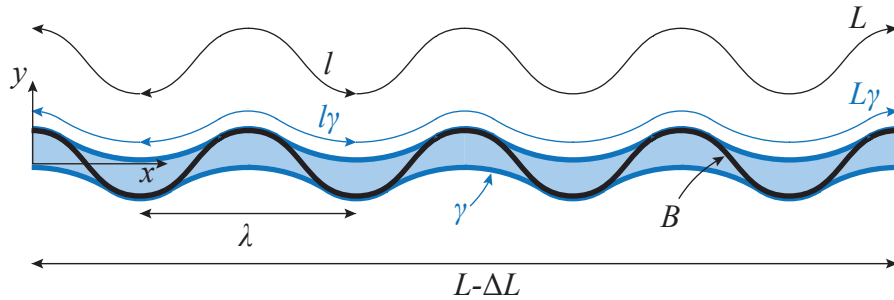
Figure 5.13 – Wrinkling of a beam of length L under compression (ΔL) in a liquid film of volume $V = hL$. The liquid-air and solid-air interfaces have the same interface energy γ and the liquid-solid interface is considered to have a constant interface energy. The beam has a bending resistance B and the texture wavelength is λ.

The present analysis is one dimensional and the energies presented here are considered per unit of depth (in the z direction). As the thickness of the liquid film h is very small

compared to the total contour length L of the beam, boundary conditions at the ends of the beam are not considered. The elastic deformation energy of the beam is written as

$$E_\mathrm{e} = \frac{1}{2} B \int_0^{L-\Delta L} \kappa^2(x)\, dx \quad \text{with} \quad \kappa(x) = \frac{y''(x)}{[1 + y'^2(x)]^{3/2}} \tag{5.13}$$

where B is the bending stiffness of the beam, $y(x)$ is the elastic beam shape, and $\kappa(x)$ is the curvature of the beam, see figure 5.13. The surface energy of the liquid-air interface is given by

$$E_\gamma = 2\gamma \int_0^{L-\Delta L} \sqrt{1 + y_\gamma'^2(x)}\, dx \tag{5.14}$$

where $y_\gamma(x)$ represents the lower liquid-air interface. The factor 2 in Eq. (5.14) arises from the top/down symmetry, the upper and lower interfaces having the same lengths. The total energy $E_\mathrm{e} + E_\gamma$ of the system has to be minimized under the two following constraints. First the total liquid volume V is conserved. Per unit depth we have $V = hL$, with

$$2 \int_0^{L-\Delta L} \left[y_\gamma(x) - y(x)\right]\, dx = V \tag{5.15}$$

where we only consider the liquid confined between the lower interface and the beam, the factor 2 accounting for the upper half of the liquid. Second, as the beam is considered inextensible, its total contour-length remains unchanged in the deformed configuration:

$$\int_0^{L-\Delta L} \sqrt{1 + y'^2(x)}\, dx = L \tag{5.16}$$

Finally the beam has to stay between the upper and lower liquid-air interfaces. As the upper and lower interfaces are symmetric, we focus on the lower interface $y_\gamma(x)$ and write the inequality constraint

$$y(x) \geq y_\gamma(x) \quad \text{for all } x \in (0; L - \Delta L) \tag{5.17}$$

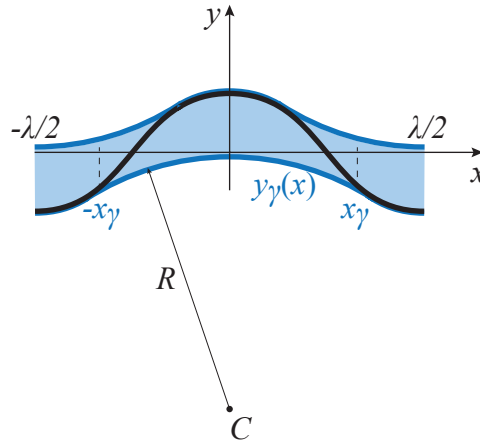**Figure 5.14** – Local problem on one wavelength λ with new unknowns x_γ and $y_\gamma(x)$.

The periodic wave ansatz

The present problem resembles a buckling-on-elastic-foundation problem. In such problems the buckling shape is x-periodic. Here the 'foundation' is the liquid-air interface and we conjecture that the shapes of the beam and of the interface are periodic also; we call λ its

period. The integrals in Eqs. (5.13)-(5.16) are then rewritten as

$$\int_0^{L-\Delta L} \cdots \, dx = N \int_0^{\lambda} \cdots \, dx \tag{5.18}$$

where the number of waves is $N = (L - \Delta L)/\lambda$. We therefore focus on one wave length and position the origin in x at a maximum in $y(x)$, see Fig. 5.14.

Non-dimensionalization

Using $L_{\text{ec}} = \sqrt{B/\gamma}$ as unit length and B/L_{ec} as unit energy, we introduce the following dimensionless quantities:

$$x_{\text{new}} = \frac{x_{\text{old}}}{L_{\text{ec}}} \; ; \quad y_{\text{new}} = \frac{y_{\text{old}}}{L_{\text{ec}}} \; ; \quad y_{\gamma\text{new}} = \frac{y_{\gamma\text{old}}}{L_{\text{ec}}} \; ; \quad L_{\text{new}} = \frac{L_{\text{old}}}{L_{\text{ec}}} \; ; \quad \lambda_{\text{new}} = \frac{\lambda_{\text{old}}}{L_{\text{ec}}} \; ; \tag{5.19a}$$

$$h_{\text{new}} = \frac{h_{\text{old}}}{L_{\text{ec}}} \; ; \quad \kappa_{\text{new}} = \kappa_{\text{old}} L_{\text{ec}} \; ; \quad E_{e\text{new}} = \frac{E_{e\text{old}} L_{\text{ec}}}{B} \; ; \quad E_{\gamma\text{new}} = \frac{E_{\gamma\text{old}} L_{\text{ec}}}{B} \; ; \tag{5.19b}$$

and work from now on with the new variables without using the 'new' subscript.

Interface $y_\gamma(x)$

We focus on the lower liquid-air interface. As shown in figure 5.14, along one wave-length $x \in (-\lambda/2; \lambda/2)$ the interface and the beam merge for $|x| > x_\gamma$ and are separated otherwise. The inequality constraint (5.17) is then replaced by

$$y(x) \;\; = \;\; y_\gamma(x) \text{ for } |x| \geq x_\gamma \tag{5.20}$$

$$y(x) \;\; > \;\; y_\gamma(x) \text{ for } |x| < x_\gamma \tag{5.21}$$

The liquid is therefore confined in $|x| < x_\gamma$ and volume conservation (5.15) reads

$$h - 2\frac{1-\epsilon}{\lambda} \int_{-x_\gamma}^{x_\gamma} \left[y(x) - y_\gamma(x)\right] \, dx = 0 \tag{5.22}$$

where $\epsilon = \Delta L/L$. As h is small compared to the gravito-capillary length $\sqrt{\gamma/(\rho g)}$, the pressure is nearly uniform inside the liquid film. The interface $y_\gamma(x)$ is then a circular arc of radius R and center C $(0; y_c)$, yielding the implicit equation $x^2 + (y_\gamma - y_c)^2 = R^2$. The two unknowns R and y_c are found with the following two conditions. First, the arc touches the beam at $x = \pm x_\gamma$

$$y_\gamma(x_\gamma) = y(x_\gamma) \tag{5.23}$$

Second, as the liquid wets the beam perfectly, the beam and interface tangents have to coincide at $x = \pm x_\gamma$

$$y_\gamma'(x_\gamma) = y'(x_\gamma) \tag{5.24}$$

These two conditions are used to express R and y_c as

$$y_c = y(x_\gamma) + \frac{x_\gamma}{y'(x_\gamma)} \quad \text{and} \quad R = x_\gamma\sqrt{1 + \frac{1}{y'^2(x_\gamma)}} \tag{5.25}$$

and we finally write the liquid-air interface equation as

$$y_\gamma(x) = \sqrt{x_\gamma^2 + \frac{x_\gamma^2}{y'^2(x_\gamma)} - x^2} + y(x_\gamma) + \frac{x_\gamma}{y'(x_\gamma)} \qquad \text{for} \quad |x| < x_\gamma \tag{5.26}$$

$$y_\gamma(x) = y(x) \qquad \text{for} \quad |x| \geq x_\gamma \tag{5.27}$$

Summary
In conclusion, the minimization of the potential energy under the constraints of conserved volume and conserved contour length is treated by introducing the Lagrangian

$$
\begin{aligned}
\mathcal{L} &= \mathcal{L}(y(x), y'(s), y_\gamma(x), y'_\gamma(x), \lambda, x_\gamma) \\
&= \frac{1-\epsilon}{\lambda} \int_0^{\lambda/2} \kappa^2(x)\, dx + 4\frac{1-\epsilon}{\lambda} \int_0^{x_\gamma} \sqrt{1 + y'^2_\gamma(x)}\, dx + \\
&\quad 4\frac{1-\epsilon}{\lambda} \int_{x_\gamma}^{\lambda/2} \sqrt{1 + y'^2(x)}\, dx + \mu_1 \left(h - 4\frac{1-\epsilon}{\lambda} \int_0^{x_\gamma} \left[y(x) - y_\gamma(x) \right] dx \right) - \\
&\quad \mu_2 \left(1 - 2\frac{1-\epsilon}{\lambda} \int_0^{\lambda/2} \sqrt{1 + y'^2(x)}\, dx \right)
\end{aligned}
\tag{5.28}
$$

where we have used $N = (L - \Delta L)/\lambda$ and divided by the constant L. We also have used the $x \to -x$ symmetry and focused on the positive x part of the system. Equilibrium of the system is found by considering the conditions for which the first variation of this Lagrangian vanishes. The Lagrange multiplier μ_1 associated with volume constraint is interpreted as the pressure inside the liquid (per unit depth, per unit length). The Lagrange multiplier μ_2 associated with inextensibility constraint is related to the tension inside the beam.
The unknowns of the problem are:

○ f the elastic beam geometry with $y(x) = f\left(\frac{2\pi}{\lambda} x \right)$
○ λ the wavelength adopted by the beam
○ x_γ the x-coordinate where the liquid film meets with the beam

The parameters of the problem, on the other hand, are:

○ ϵ the compression
○ h the initial liquid film thickness

Energy minimization for a sinusoidal buckling pattern
In order to simplify the problem, we restrict ourselves to sinusoidal buckling patterns of wavelength λ for the elastic beam, *i.e.* $y(x) = A\cos\left(\frac{2\pi}{\lambda} x \right)$. The liquid-air interface (5.27) then writes

$$
y_\gamma(x) = \sqrt{x_\gamma^2 + \left(\frac{\lambda x_\gamma}{2\pi A \sin\left(\frac{2\pi}{\lambda} x_\gamma \right)} \right)^2 - x^2} + A\cos\left(\frac{2\pi}{\lambda} x_\gamma \right) - \frac{\lambda x_\gamma}{2\pi A \sin\left(\frac{2\pi}{\lambda} x_\gamma \right)}
\tag{5.29}
$$

and the Lagrangian (5.28) is now a simple function $\mathcal{L} = \mathcal{L}(A, \lambda, x_\gamma)$. Minimization is performed numerically and results are presented in figure (5.15).

Considering a non-zero thickness of a porous beam
Experimentally, the membrane has a non-zero thickness. In the model, the thickness of the beam is taken into account by considering a vertical shift of the liquid interface. The vertical position (5.25) of the center of the circular arc described by the liquid-air interface is then shifted and we now have

$$
y_c = A\cos\left(kx_\gamma \right) - \frac{x_\gamma}{Ak\sin(kx_\gamma)} - \frac{t}{2}
\tag{5.30}
$$

where t is the thickness of the beam. Additionally the membrane is porous and entirely wicked with the liquid. Volume conservation is then rewritten as

$$
h = 4\frac{1-\epsilon}{\lambda} \int_0^{x_\gamma} \left[y(x) - \frac{t}{2} - y_\gamma(x) \right] dx + (1 - \epsilon)t
\tag{5.31}
$$

Please note that (5.30) and (5.31) are only valid for small deflections $|y'(x)| \ll 1$, *i.e.* small compression ϵ.

5.3.3 Graphical results

The wavelength λ which minimizes the total energy under the liquid volume and beam length conservation is function of the compression ϵ, the liquid thickness h and the membrane thickness t.

$$\lambda = \lambda(\epsilon, h, t) \tag{5.32}$$

Figure 5.15 presents λ as a function of compression ϵ for different liquid thicknesses h and for a beam thickness $t = 0$. It should be reminded that λ and h are normalized by the elasto-capillary length $L_{\text{ec}} = \sqrt{B/\gamma}$.
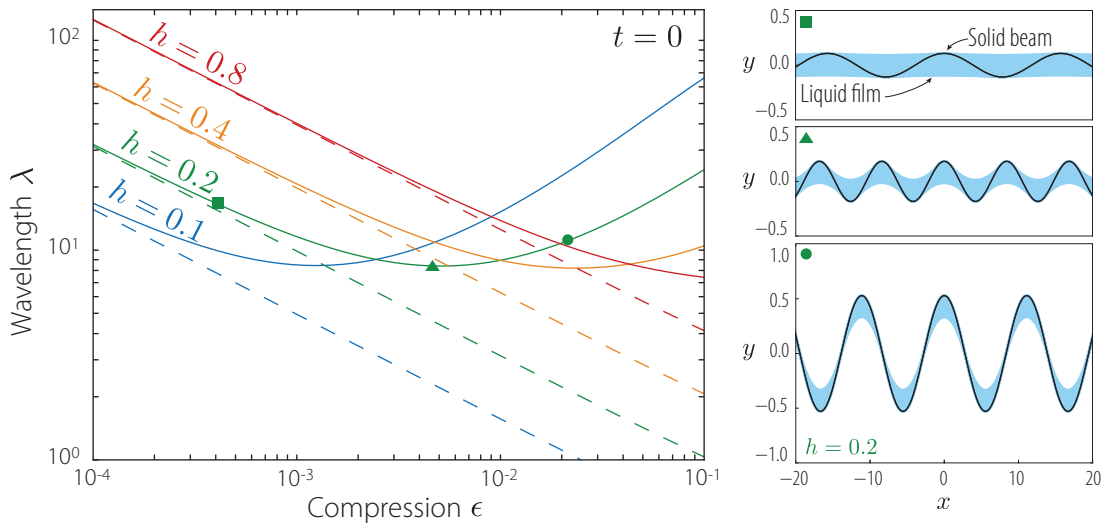

Figure 5.15 – **Left** – Theoretical wavelength λ versus compression ϵ for four different liquid dimensionless thicknesses h and beam thickness $t = 0$. The dashed lines represent the hard wall prediction depicted in Equation (5.34) which corresponds to $A = h/(2(1 - \epsilon))$ in Equation (5.33). **Right** – Representation of the beam and liquid film for $h = 0.2$ at different compressions ϵ. The visualization frame is fixed as compression is carried out.

For $\epsilon \ll 1$, the amplitude A of the sinusoidal pattern is defined analytically by the length constraint in Equation (5.28):

$$A = \frac{1}{\pi} \lambda \sqrt{\epsilon} \tag{5.33}$$

and for small enough compressions, the liquid interfaces act as rigid walls confining the beam. The buckling pattern then adopts a wavelength given by $A = h/(2(1 - \epsilon))$ in Equation (5.33), which yields:

$$\lambda = \frac{\pi h}{2(1 - \epsilon)\sqrt{\epsilon}} \simeq \frac{\pi h}{2\sqrt{\epsilon}}. \tag{5.34}$$

A similar configuration is studied in Roman and Pocheau (1999) where a plate is compressed between two rigid walls separated by an adjustable distance h. In this study, the plate is first compressed at a given compression ϵ and the distance h between the two rigid walls is then gradually decreased. Since the plate studied in this article has a finite length, the observed wavelength does not vary continuously but undergoes sudden configurational changes throughout the experiment. However, the general law $\lambda \sim h$ for a given compression ϵ is brought forward in their experiments.

As our beam between two liquid interfaces is further compressed (i.e. increasing ϵ), the buckling wavelength deviates from the rigid wall prediction as the beam starts to push the liquid interface. Independently of the liquid thickness h, this event (beam pushing the liquid liquid interface) always arises around $\lambda = 8$ where the wavelength goes through a minimum and subsequently increases with ϵ.

In Figure 5.16, we take the thickness t of the membrane into account in the calculations using Equation (5.31) and again report the wavelength minimizing global energy as a function of compression. Here, we fix the liquid film thickness $h = 0.8$ and vary the membrane thickness t. At small compressions ϵ, $\lambda(\epsilon, h, t)$ behaves similarly as $\lambda(\epsilon, h - t, 0)$ and the dashed lines represent the prediction, similar to Equation (5.34):

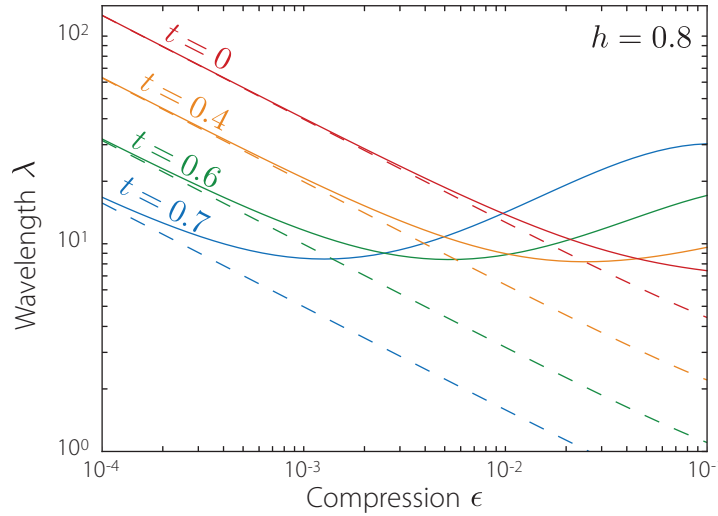$$\lambda = \frac{\pi(h-t)}{2(1-\epsilon)\sqrt{\epsilon}} \simeq \frac{\pi(h-t)}{2\sqrt{\epsilon}}. \qquad (5.35)$$

Figure 5.16 – Wavelength versus compression of for a fixed liquid thickness h. The calculation is performed for four different membrane thicknesses corresponding to $t = 0$, 0.4, 0.6 and 0.7 and fixed $h = 0.8$. For small compression ϵ, these curves resemble the curves presented in Figure 5.15.

Even when the beam thickness is taken into account, the wavelength goes through a minimum around $\lambda = 8$ and subsequently increases as for the case with $t = 0$.
Further modelisation is currently underway to better understand the non-linear behavior of the wavelength λ as a function of the problem parameters ϵ, h and t in this theoretical model.

5.3.4   Discussion

In the experiments, upon compression of the membrane, a clear wavelength λ is exhibited by the wavy pattern. This wavelength remains constant for a large range of compression. This behavior is not captured by our model, where the wavelength does depend on ϵ. For a given set of parameters, we compare the model with the experimental observations presented in Figure 5.12.

Figure 5.17 presents the dimensionless wavelength λ versus the dimensionless liquid thickness h for PAN fibrous membranes of different thicknesses wicked with different liquids. Both λ and h are normalized by the elasto-capillary length $L_{\text{ec}} = \sqrt{B/\gamma}$. The surface tension γ was measured with the Krüss K6 manual tensiometer (deionized water showed a drop in surface tension when previously put in contact with a PAN membrane, from 72 mN/m to 53 mN/m). To test the dependence of the wavelength on surface tension, the

experience was performed with deionized water and a water/soap solution (of measured surface tension $\gamma = 30$ mN/m). The membrane bending rigidity per unit depth B being low, it could not be measured experimentally. Therefore, it was roughly estimated as $B = \alpha \frac{t_0}{a} E a^3$ where t_0 is the membrane dry thickness, a the typical radius of the fiber composing the membrane ($a = 500$ nm) and E is the PAN Young's modulus ($E \simeq 30$ GPa). Finally, α is a dimensionless parameter to account for the membrane porosity (here adjusted to the experiments using $\alpha = 2 \cdot 10^{-4}$).
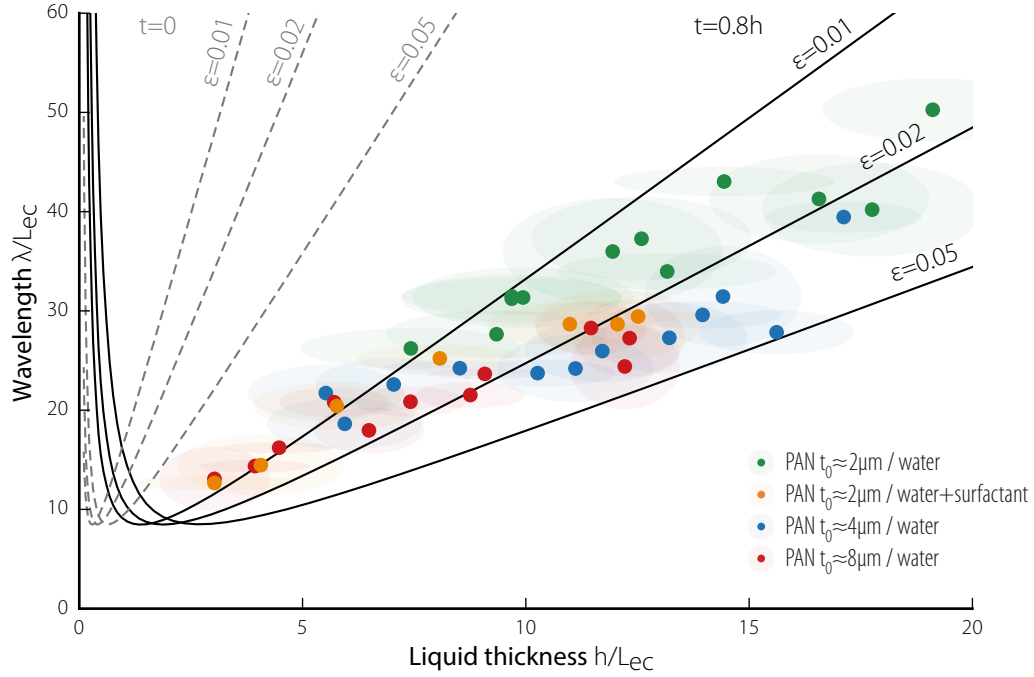
Figure 5.17 – Dimensionless wavelength λ versus liquid thickness h. The points refer to experimental data for different PAN membrane dry ticknesses and different wicking liquids. The gray solid lines are results of the presented model for $\epsilon = 1\%$, 2% and 5%. It is considered that the membrane grows as it is infused with liquid. To capture this growth, we choose the membrane thickness t to be proportional to the liquid thickness h ($t = 0.8h$). The gray dotted lines represent the same results for a zero-thickness beam $t = 0$.

The comparison between experiments and theory presented in Figure 5.17 displays a quantitative agreement. However, some experimental parameters of the problem are unknown and are adjusted to ensure this experiment-theory agreement. The fact that the model predicts a wavelength-dependence on the compression ϵ attests that it misses a key ingredient. The next section presents a perspective to improve the theoretical model.

5.4   Phase transition: from wavy to collapsed

Figure 5.18 presents a close-up on a wicked PAN membrane as it is compressed. The wavy pattern presented in Figure 5.1-B is rapidly complemented by a 'collapsed' phase where the wrinkles display a closely packed structure. This collapsed phase grows as compression is increased, while the wavy phase declines; the wavy phase is continuously transferred to the collapsed phase throughout compression.
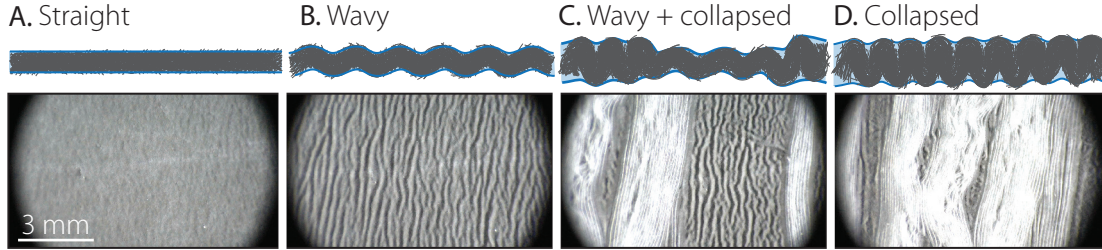

A. Straight   **B.** Wavy   **C.** Wavy + collapsed   **D.** Collapsed

Figure 5.18 – Close-up snapshots of a PAN membrane wicked with water throughout compression.

Mechanical phase transitions are commonly observed in chains of elements displaying softening (Bigoni 2012). Here, when the wicked membrane is compressed, the elasto-capillary interaction between the fibrous membrane and the liquid film is likely responsible for such a softening. The geometry of the wavy phase, in equilibrium with the collapsed phase, is therefore probably dictated by the phase transition. Experimental and theoretical investigation is underway and may allow to predict the equilibrium wavelength of the wavy pattern.

The phase transition is reversible as presented in Figure 5.19; membrane is transfered from the wavy phase to the collapsed phase throughout compression and then restored upon subsequent extension. Note that in this figure, the PAN membrane is thick ($t_0 \simeq 8\,\mu$m) and the collapsed phase is therefore only twice as dense as the wavy phase.
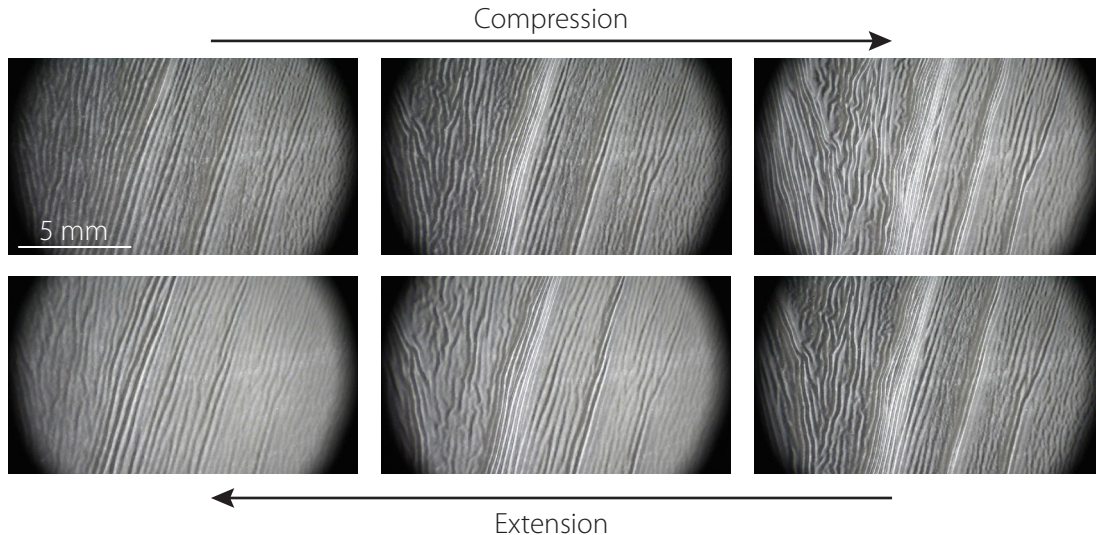

Compression

Extension

Figure 5.19 – Close-up on thick wicked PAN membrane as it is compressed and then extended again. At small compression, the membrane is entirely in a **wavy phase** and as compression is carried on, a **collapsed phase** appears and grows. Upon subsequent extension, the collapsed phase reduces as the wavy phase grows again.

Conclusions and perspectives

Throughout this PhD work, we have studied how elasticity and capillarity interact in the drop-on-fiber and wicked-membrane systems. In both cases, the liquid constituent carries capillarity, responsible for surface forces strong enough to make the thin solid object buckle and spontaneously undergo geometrical re-organization.

The drop-on-fiber system was first studied without considering deformation of the fiber. We showed how capillarity and gravity shape the liquid drop and this theoretical comprehension, along with numerical and experimental validation, led to the design of a novel tool for precise fiber radius measurement. This potential metrology application motivates further development, as for example the design of an image-processing routine to identify the radius of the drops as well as their eccentricity with respect to the fiber. This would provide a rapid and precise tool for the radius measurement of submicronic fibers.

Figure 5 – **Elasto-capillary buckling.** Silicone oil drop sitting on a polyvinyl-siloxane fiber. When slack is given to the system, i.e. the fiber ends are brought closer, the capillary forces developed by the drop are sufficient to make the fiber buckle and coil within it.

If now the fiber is flexible, it can spontaneously buckle and coil inside a wetting liquid drop sitting on it as presented in Figure 5. This elasto-capillary mechanism was extensively studied in Elettro (2015) where it was shown that it allows to 'pack' fiber reserves inside drops when the fiber ends are brought closer, while providing tension to the system. This geometrical re-arrangement of the fiber can be interpreted as 'fiber reserves' which are recruited when the fiber ends are separated. Further research was here led to make stiff functional fibers eligible for this in-drop coiling, and therefore endow them with an apparent extreme stretchability. The strategy consists in adding an auxiliary soft beam to the stiff

functional fiber. This increases the capillary compressive force applied by the drop without significantly increasing the bending stiffness of the new composite fiber. This method could be used for the design of stretchable electronic connectors, as fibers made of the conductive polymer PEDOT:PSS were successfully coiled inside silicon oil droplets and therefore displayed a 20-fold extension while continuously conducting electricity.

The spontaneous coiling a fiber inside a drop sets the system under tension. This tension strongly depends on the extension rate of the fiber ends and we therefore proposed four experiments to quantify the viscous dissipation during the fiber uncoiling out of the drop. Further experimental work is necessary and a comparison with the presented model may give new information concerning the delicate physics of viscous dissipation at a liquid contact line.

The concept of fiber reserves, ensuring apparent stretchability to fibers, was extended to 'membrane reserves'. By wicking a thin fibrous membrane with a wetting liquid, capillary forces provide tension to the membrane even when its boundaries are brought closer as presented in Figure 6. The membrane excess is then stored in the form of wrinkles and folds confined within the liquid film. This surface-tension induced buckling, again, provides stretchability as it allows for the membrane to macroscopically undergo large deformations while always remaining under tension.
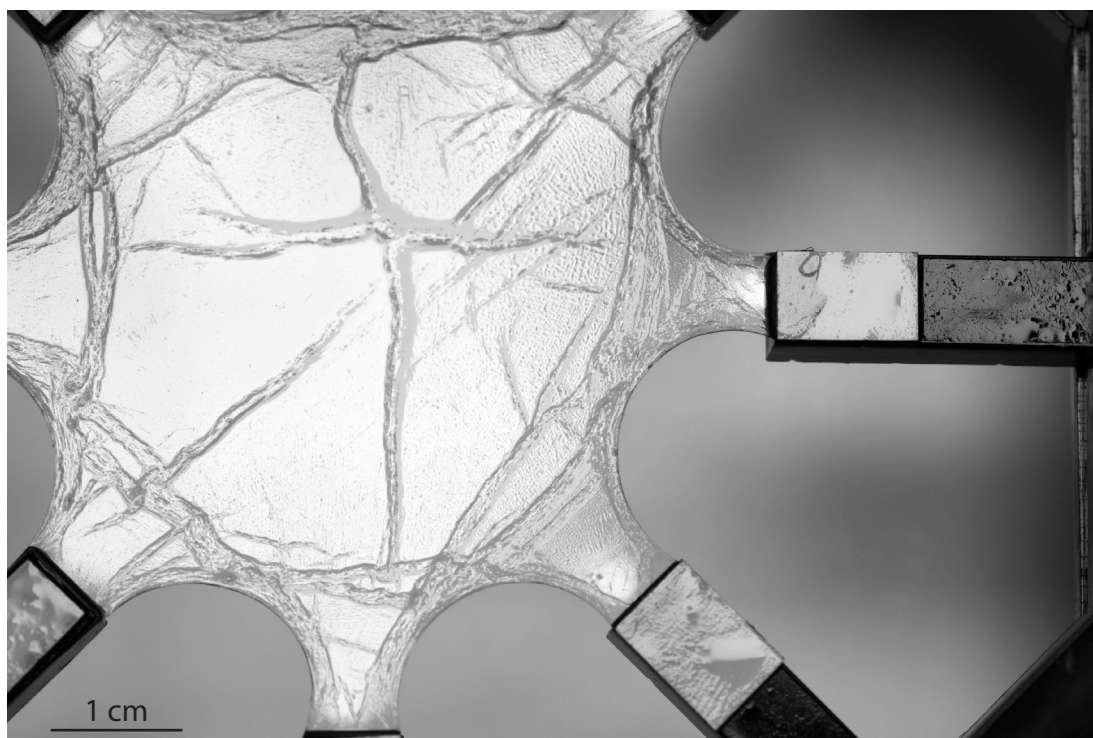

Figure 6 – **PVDF-HFP membrane wicked with silicone oil**. The capillarity-inextensibility interaction is expressed at two scales. Macroscopically, the wicked membrane always remains under tension and its free edges adopt circular shapes due to the surface minimization with isoperimetric constraint. Microscopically, on the other hand, the solid membrane interacts with the liquid film, which generates elasto-capillary wrinkling patterns.

There is still a lot to learn about the elasto-capillary interactions between the solid fibrous membrane and the wicking liquid film. A theory regarding wrinkling orientation and wavelength was proposed and ongoing experiments and modelisation will probably allow to further understand the two wrinkling phases observed during compression of the wicked membrane. These two phases can be spotted in Figure 6. The pronounced 'veins', which we call the collapsed phase, host the membrane reserves while a coexisting wavy pattern is observed in other parts of the membrane.
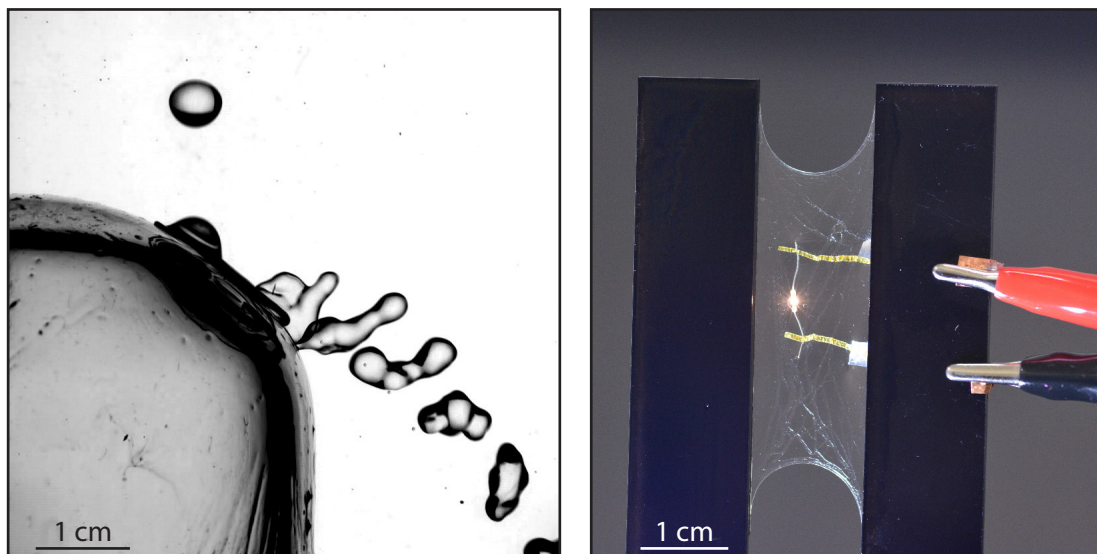
Figure 7 – **Potential applications of the wicked membrane. Left** – A PVDF-HFP fibrous membrane is apposed to a spherical glass surface and is wicked with silicone oil. The wicked membrane then adapts its shape and acts as a slippery surface treatment with water repellent properties. The chrono-photography (10 ms intervals) shows a water droplet bouncing off the surface. **Right** – A thin gold strip (1 mm wide, 100 nm thick) is apposed to the wicked membrane (here: planar PVDF-HFP membrane wicked with silicone oil). Electricity runs through the gold strips even when membrane reserves are spontaneously generated upon compression which allows to light a 1.5V LED throughout an 8-fold compression-extension cycle of this basic circuit.

Hybrid materials, by combining the respective strengths of their constituents, can provide unprecedented material properties (Ashby and Bréchet 2003). As our wicked membrane inherits the deformability of a liquid and the mechanical robustness of a solid, the resulting extensibility and longevity may give rise to new functions. For example, Figure 7 presents two potential applications of the wicked membrane. As it presents important geometrical adaptability, a PVDF-HFP fibrous membrane, once wicked with silicone oil, provides a water repellent coating which can be applied to any warped surface. The silicone oil layer is stabilized on a glass surface by the PVDF-HFP membrane, which impedes water droplets to stick on the surface. The wicked membrane could also be of use in the stretchable electronics area. Since stretchability is here not obtained by stretching the material at a microscopic level but by spontaneous local re-arrangement, flexible electronic paths can be implanted to it, thus creating stretchable electronic circuits.

A | Drop on a fiber with Surface Evolver

Surface Evolver is a powerful free tool for the numerical calculation of liquid surfaces by energy minimization under user specified constraints. It was developed by Kenneth A. Brakke and first presented in Brakke (1992). The program, complete instructions and tutorials can be downloaded freely at http://facstaff.susqu.edu/brakke/evolver/evolver.html.

Among other features, Surface Evolver allows to predict the shape that a liquid body (*e.g.* a drop) adopts in contact with solid elements (*e.g.* a fiber) and subject to forces such as gravitational ones. In order to quickly present Surface Evolver, the key ingredients for the simulation of a liquid drop on a fiber and its principal outputs are presented here. The code was adapted from the 'Toroidal liquid ring on a rotating rod in weightlessness' tutorial (`ringblob.fe`).

A.1   Geometry of the drop

The geometry of the liquid drop is fed to Surface Evolver by the user who manually introduces the (x, y, z) coordinates of a set of vertices corresponding to a rough estimate of the drop's surface. These vertices are then connected 2 by 2 to form edges which are in turn connected 4 by 4 to form the object's faces. The faces are finally connected to form the liquid body: our drop. The left-right symmetry of a drop on a fiber (see Figure 1.3) allows to simulate only one half of it. Here, we simulate the right half (Surface Evolver provides a practical function to visualize the other half of the drop by a mirror effect). For simplicity, the right drop half is initiated as a cube presented in Figure A.1. Its left face, as it corresponds to symmetry plane, is simply not declared (the liquid body is not necessarily closed). The right face, on the other hand, possesses a hole (corresponding to the passage of the fiber through the drop). The line describing the border of this hole corresponds to the **triple line**, the line in contact with the solid, the liquid, and the vapor phases, it is colored red in Figure A.1.

Starting from the user input, Surface Evolver automatically splits the faces into triangular facets. Before remodeling the rudimentary surface generated in seeking its equilibrium shape, some constraints are applied.

Figure A.1 provides two views of the generated half drop on the fiber. The fiber's axis is aligned with the x-axis, while gravity points downwards and is aligned with the y-axis.

A.2 Constraints

The most straightforward constraint applied to the drop is its volume. It is ensured at each energy minimization step and an error message is generated if the constraint is not respected. In our case, the imposed volume of course corresponds to only half of the true drop's volume.

The other key constraint corresponds to the fact that the vertices describing the triple line must stay on at the fiber's surface. This constraint is initially imposed to the vertices initiated at the triple line (corresponding to the hole on the right face mentioned above) and it reads:

$$y^2 + z^2 = a^2. \tag{A.1}$$

with a the radius of the fiber. This constraint is also applied to the edges connecting these vertices (red edges in Figure A.1).
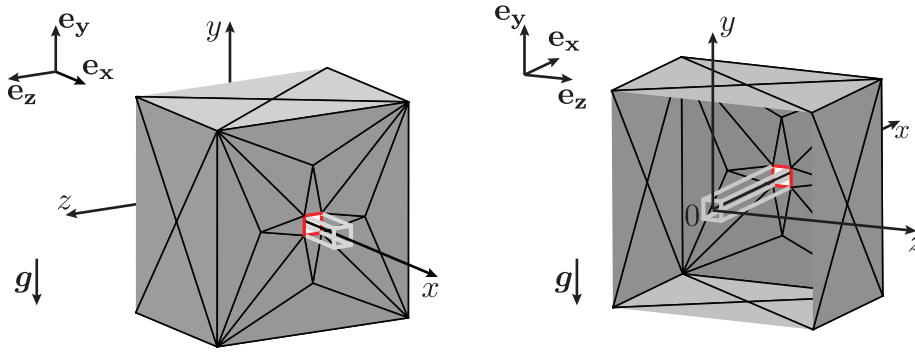

Figure A.1 – Two views of the half droplet generated by the user. The red edges are the ones constrained to remain on the fiber. The fiber is here represented for visualization purposes and is oriented following the x-axis. Gravity points downwards and is aligned with the y-axis. Note that the triangular mesh is generated automatically by Surface Evolver and that it can be refined by the user (see the 'Mesh refinement' section

.

A.3 Mesh refinement

Upon user command, the mesh describing the drop's surface is refined by splitting every existing facet into 3 new facets. This tool can be adapted in order to refine the mesh of specific regions of the drop's surface. Here, a method was developed to refine the mesh near the triple line, where the drop's surface is highly curved and therefore needs numerous facets to account for the surface's complexity. Special care was taken to generate new facets with a satisfying aspect ratios (the long edges of an excessively elongated facet are split in half). Note than when an edge is refined, the newly generated vertices inherit the constraints of the two vertices composing the original edge.

Throughout this work, drop-on-fiber simulations are performed with around 2000 facets.

A.4 Energy

Surface Evolver seeks the equilibrium shape of a discretized drop's surface, i.e. the shape which minimizes the total energy (usually under a set of constraints). Therefore, Surface

Evolver needs to be able to calculated the energy contributions to the global energy of the drop: the interfacial and the gravitational energies. Here, we describe how Surface Evolver calculates these energies.

A.4.1 Interfacial energy

The surface energy of free faces of the drop (i.e. the faces in contact with surrounding vapor) is directly handled by Surface Evolver and requires no special care. Indeed, the interfacial energy of a numerical facet of surface S_{facet} is directly given by γS_{facet} and the total interfacial energy of the free surface is numerically calculated by summing the contributions of all the facets.

The energy contributions coming from the solid-vapor (i.e. fiber-air) and solid-liquid (i.e. fiber-drop) interfaces require special attention as they are not as straightforward to handle. With S_{SV} and S_{SL} the surface areas respectively corresponding to the solid-vapor and solid-liquid interface, the sum of their corresponding surface energies writes:

$$E_{\text{SV}} + E_{\text{SL}} = S_{\text{SL}}\,\gamma_{\text{SL}} + S_{\text{SV}}\,\gamma_{\text{SV}}. \tag{A.2}$$

Moreover, since the fiber has a total surface $S_{\text{fiber}} = S_{\text{SL}} + S_{\text{SV}}$, we rewrite Equation (A.2):

$$E_{\text{SV}} + E_{\text{SL}} = S_{\text{SL}}(\gamma_{\text{SL}} - \gamma_{\text{SV}}) + S_{\text{fiber}}\gamma_{\text{SV}}. \tag{A.3}$$

The constant term $S_{\text{fiber}}\gamma_{\text{SV}}$ can be discarded because it does not depend on the drop's shape. Finally, using Young-Dupré's relation (described in Equation (1.3)), we write the sum of the solid-liquid and solid-vapor energy contributions as a function of the liquid's surface tension γ, its contact angle with the fiber θ_{Y} and the wetted surface S_{SL},

$$E_{\text{SV}} + E_{\text{SL}} = -\gamma S_{\text{SL}} \cos\theta_{\text{Y}} = -\gamma \cos\theta_{\text{Y}} \iint_{S_{\text{SL}}} \boldsymbol{n} \cdot \boldsymbol{n}\, \text{d}S \tag{A.4}$$

with $\boldsymbol{n}$, the unitary vector normal to the fiber's surface. We use Stokes' theorem,

$$E_{\text{SV}} + E_{\text{SL}} = -\gamma \cos\theta_{\text{Y}} \iint_{S_{\text{SL}}} (\boldsymbol{\nabla} \times \boldsymbol{G}) \cdot \boldsymbol{n}\, \text{d}S = -\gamma \cos\theta_{\text{Y}} \oint_{\ell} \boldsymbol{G} \cdot \text{d}\boldsymbol{\ell} \tag{A.5}$$

where $\boldsymbol{G}$ is an unknown function verifying $(\boldsymbol{\nabla} \times \boldsymbol{G}) \cdot \boldsymbol{n} = \boldsymbol{n} \cdot \boldsymbol{n}$ and ℓ corresponds to the path described by the triple line. For a cylindrical surface (fiber of radius a), the unitary normal vector $\boldsymbol{n}$ to the cylinder surface is known and we find a solution for $\boldsymbol{G}$:

$$\boldsymbol{n} = \frac{1}{a}\begin{pmatrix} 0 \\ y \\ z \end{pmatrix}; \quad \boldsymbol{G} = \frac{1}{a}\begin{pmatrix} 0 \\ xy \\ -xz \end{pmatrix}. \tag{A.6}$$

The energy $E_{\text{SV}} + E_{\text{SL}}$ is then calculated numerically with Equation (A.5) where the path ℓ corresponds to the path defined by the edges describing triple line.

Note that the solid-liquid interface could also directly have been defined as an actual face and bestowed with a surface tension $-\gamma \cos\theta_{\text{Y}}$. However, this method is not robust and will therefore not be used in this work.

A.4.2 Gravitational energy

The gravitational energy E_{grav} of the drop can be taken into account with Surface Evolver. It is given by:

$$E_{\text{grav}} = \iiint_{\Omega} \rho g y\, \text{d}\Omega \tag{A.7}$$

where Ω denotes the drop's volume. Because Surface Evolver does not handle volume elements, but surface elements, we use the divergence theorem:

$$E_{\text{grav}} = \rho g \iiint_{\Omega} (\boldsymbol{\nabla} \cdot \boldsymbol{F}) \, \mathrm{d}\Omega = \rho g \iint_{\partial\Omega} \boldsymbol{F} \cdot \boldsymbol{n} \, \mathrm{d}S \tag{A.8}$$

where $\boldsymbol{F}$ is a function which verifies $\boldsymbol{\nabla} \cdot \boldsymbol{F} = y$. The notations $\partial\Omega$ and $\boldsymbol{n} = (n_x, n_y, n_z)^T$ respectively refer to the outer surface of the drop and the unitary vector normal to it. $\boldsymbol{F}$ is easily found,

$$\boldsymbol{F} = \frac{1}{2} y^2 \begin{pmatrix} 0 \\ 1 \\ 0 \end{pmatrix}, \tag{A.9}$$

and the gravitational energy of the drop is numericaly calculated by Surface Evolver using

$$E_{\text{grav}} = \frac{1}{2} \rho g \iint_{\partial\Omega} n_y y^2 \, \mathrm{d}S. \tag{A.10}$$

where the integral, for the discretized surface handled by Surface Evolver, is replaced by a sum on all the facets of the drop.

A.5   Equilibrium shape

Once the geometry, the constraints and the energy are declared, Surface evolver can compute the total energy of the drop $E_{\text{tot}}(\boldsymbol{x_1}, \boldsymbol{x_2}, \dots, \boldsymbol{x_N})$ where $\boldsymbol{x_i}$ corresponds to the (x, y, z) coordinates of the i'th vertex. The energy gradient with respect to the vertices' coordinates is also calculated and energy minimization is then achieved by conventional gradient descent method. Note that the drop shape obtained by this technique will corresponds to a **stable** equilibrium shape as it will correspond to an energy minimum.

Surface Evolver provides another powerful method to compute the equilibrium (stable and unstable) shapes of a liquid object. The **Hessian** method calculates the Hessian matrix corresponding to the total energy and seeks the nearest state which makes the energy gradient vanish (corresponding to a local energy minimum **or** maximum). This method is efficient for systems which are already close to an equilibrium state and moreover, it allows to access **unstable** states. When Surface Evolver finds an equilibrium shape using the Hessian method, it can also calculate the number of negative eigenvalues of the Hessian matrix. One or more strictly negative eigenvalues attest the instability of the computed shape.

A.6   Forces

Beyond computing the equilibrium shapes adopted by our drop on a fiber, Surface Evolver is also able to numerically calculate the forces at stake. For example, knowing the detailed geometry of the triple line and its adjacent facets allows to precisely determine the capillary force developed by the drop on fiber (or by the action-reaction principle, of the fiber on the drop). Surface Evolver also has access to the pressure inside the drop and therefore allows to calculate pressure forces generated by the fiber on the drop. Throughout this work, the subscript SE will refer to values computed numerically with Surface Evolver.

A.7 Conclusion

This section gives a far-from-complete overview of the features provided by the liquid surface modeling software Surface Evolver. Its principal objective is to give an idea of its approach and the interesting computational possibilities it opens. In this work, the drop's volume and its weight are handled separately and the reader should therefore be aware that even though it is not intuitive, a larger drop is not necessarily heavier.

B | Visualization of the buckling pattern in the wicked membrane

Since the optic indexes of the wicking liquids and of the fibers composing the fibrous membrane are relatively close, the membrane becomes almost transparent when wicked. Classical lighting techniques such as placing a uniform back light behind the wicked membrane or lighten it from the side provide poor information regarding the in-film configuration of the membrane. Consequently, we turn to two alternative observation methods which we present here.

B.1 Textured back light behind the wicked membrane

A planar PVDF-HFP membrane wicked with v100 silicone oil is presented in Figure B.1 where it stands in front of a check patterned back light. At its extended state, the membrane's surface appears smooth and a small compression leads to the apparition of vein-like structures (which we here refer to as the membrane reserves) which will grow in width and in number as compression is further carried out.

   Throughout the compression, the membrane remains relatively transparent and apart from the appearance of these vein-like membrane reserves, we cannot tell how the membrane reorganizes inside the liquid film. The membrane's transparency, once wicked, may be of use for some applications, but it hinders the deeper understanding of the local reorganization events of the membrane.

B.2 Reflected image of a semi-infinite back light

Apart from transparent, the membrane is also reflective thanks to the presence of somewhat smooth water-air interfaces. Here, we take advantage of this reflectiveness and develop a simple setup to highlight the small irregularities that appear at the wicked membrane's surface when compressed.

   A schematic representation of this visualization setup is presented in Figure B.2 where the pattern of a generic wavy reflective surface is brought out by illuminating it with a semi-infinite planar back light. Due to the waviness of the hypothetical surface, only some areas will reflect the bright light rays back into the observing eye (or camera) and will therefore appear bright. Some other areas, on the other hand, will send back light rays
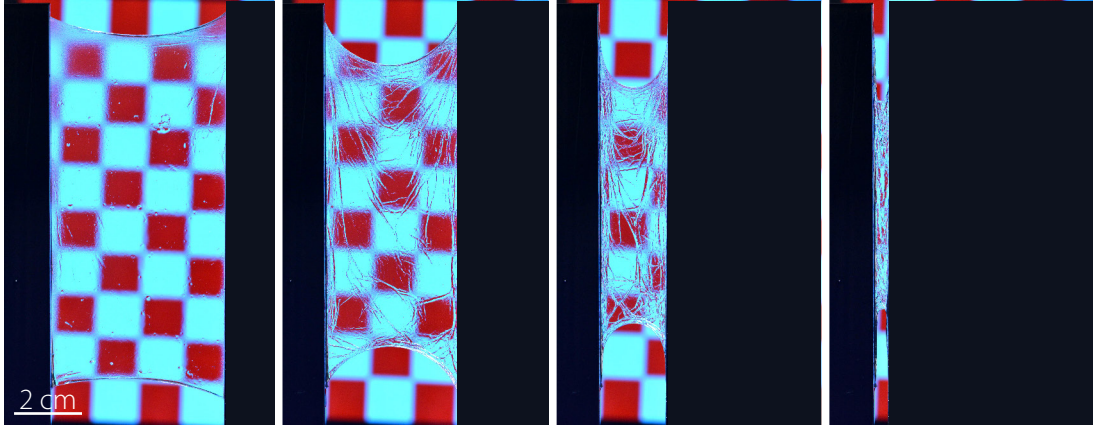
Figure B.1 – The first visualization method consists in placing a textured back light behind the membrane in order to highlight imperfections at its surface. Here, a blue and red check pattern is placed behind a wicked PVDF-HFP membrane. When it is compressed, the vein-like structures, or membrane reserves are brought out. Note that these structures only emerge optically thanks to the inhomogeneity of the back light, a homogeneous white back light provides very little detail concerning the membrane reserves (an example is given in Figure B.3).

that do not come from the back light and will therefore appear dark if no other light sources are present on this setup. In this case, the resulting image displays a zebra-like structure; a succession of bright and dark stripes which reveals the global structure of the wavy pattern as well as a characteristic wavelength. Note that this setup allows to reveal surface imperfections or wavy patterns of very low amplitude since small angle variations at the surface are sufficient to deviate the light rays significantly and therefore reflect light rays coming from radically different sources.

A typical example of the use of this method is proposed in Figure B.3 where a slightly compressed PAN membrane, wicked with dyed (blue) water is first put in front of a homogeneous back light. The same back light is then used following the second visualization method order to reveal the "imperfections" on the surface. This technique reveals an unexpected wrinkling pattern all over the membrane.
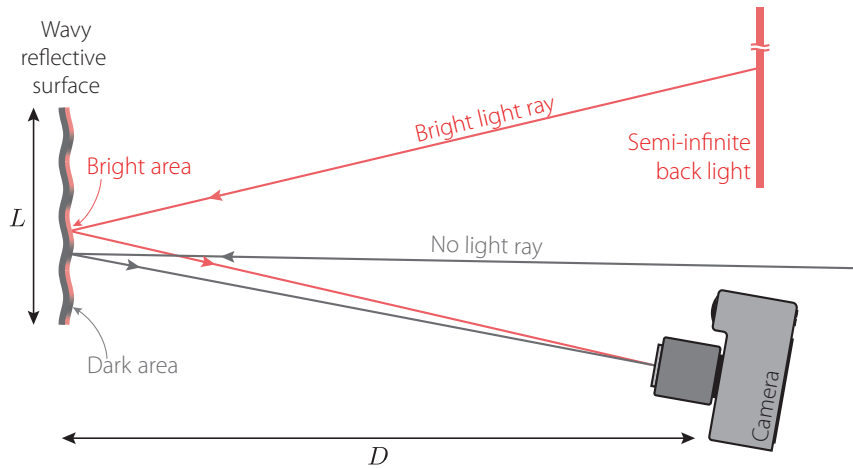

Figure B.2 – The second visualization method makes use of the reflective property of the wicked membrane. Here, by placing a semi-infinite homogeneous light source far away from a generic reflective surface ($D \gg L$), even small irregularities on this surface will deflect the incoming light rays significantly and the image taken by the camera (placed in the axis of the reflected light rays) will therefore provide information regarding the surface's texture. A wavy reflective surface such as the one presented here will indeed generate a striped image, reporting the wavy pattern of the surface and the associated wavelength.
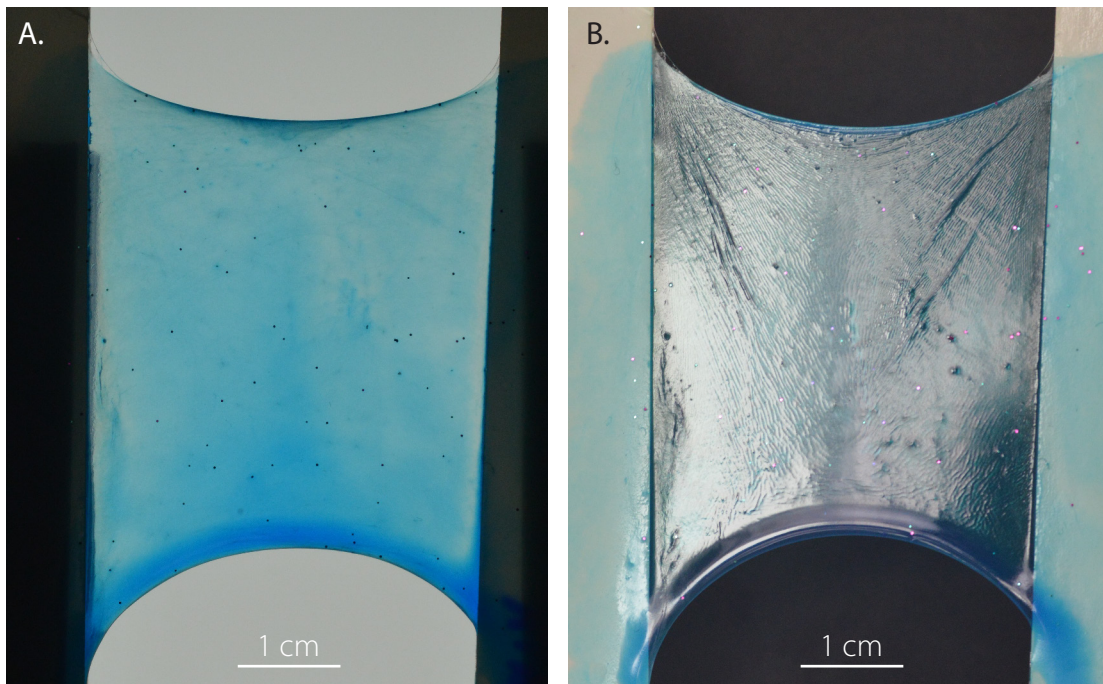
Figure B.3 – The second visualization method is applied on a planar PAN membrane. **A** – The slightly compressed membrane is illuminated homogeneously from behind and as it was mentioned earlier, this illuminating technique provides no information on the in-film configuration of the membrane. **B** – The setup presented in Figure B.2 is used to reveal an unexpected wrinkling pattern all over the membrane for the same compression. Note that the membrane is wicked with dyed water (blue).

Bibliography

N. K. Adam. Detergent action and its relation to wetting and emulsification. *Journal of the Society of Dyers and Colourists*, 53(4):121–129, 1937.
⌗ . Cited on page 13.

A. Antkowiak, B. Audoly, C. Josserand, S. Neukirch, and M. Rivetti. Instant fabrication and selection of folded structures using drop impact. *Proceedings of the National Academy of Sciences*, 108(26):10400–10404, 2011.
⌗ . Cited on pages 76 and 77.

M. F. Ashby and Y. J. M. Bréchet. Designing hybrid materials. *Acta Materialia*, 51(19): 5801 – 5821, 2003.
⌗ . Cited on pages 37 and 123.

M. F. Ashby and K. Johnson. *Materials and design: the art and science of material selection in product design.* Butterworth-Heinemann, 2013. Cited on page 1.

Z. P. Bazant and L. Cedolin. *Stability of Structures: Elastic, Inelastic, Fracture, and Damage Theories.* World Science Publishing, 2010. Cited on page 109.

J. Bico, B. Roman, L. Moulin, and A. Boudaoud. Adhesion: Elastocapillary coalescence in wet hair. *Nature*, 432(7018):690–690, 2004.
⌗ . Cited on page 36.

J. Bico, E. Reyssat, and B. Roman. Elastocapillarity: When surface tension deforms elastic solids. *Annual Review of Fluid Mechanics*, 50(1), 2017.
⌗ . Cited on page 76.

D. Bigoni. *Nonlinear solid mechanics : bifurcation theory and material instability.* Cambridge University Press, 1 edition, 2012. Cited on page 120.

P.-B. Bintein. *Dynamics of drops on fibers: applications to glass wool manufacturing.* PhD thesis, Université Pierre et Marie Curie - Paris VI, 2015. Cited on page 8.

D. Bonn, J. Eggers, J. Indekeu, J. Meunier, and E. Rolley. Wetting and spreading. *Reviews of Modern Physics*, 81(2):739–805, May 2009.
⌗ . Cited on page 59.

N. Bowden, S. Brittain, A. G. Evans, J. W. Hutchinson, and G. M. Whitesides. Spontaneous formation of ordered structures in thin films of metals supported on an elastomeric polymer. *Nature*, 393(6681):146–149, 1998.
⌗ . Cited on pages 105 and 106.

K. A. Brakke. The Surface Evolver. *Experimental Mathematics*, 1(2):141–165, 1992.
⌗ . Cited on page 125.

F. Brau, P. Damman, H. Diamant, and T. A. Witten. Wrinkle to fold transition: influence of the substrate response. *Soft Matter*, 9:8177–8186, 2013. ⬀ . Cited on page 106.

P. Bérest. *Calcul des variations : application a la mecanique et a la physique.* ellipses, 1998. Cited on page 84.

B. J. Carroll. The accurate measurement of contact angle, phase contact areas, drop volume, and Laplace excess pressure in drop-on-fiber systems. *Journal of Colloid and Interface Science*, 57(3):488–495, 1976. ⬀ . Cited on pages 11, 12, 13, 15, 39, and 55.

B. J. Carroll. Equilibrium conformations of liquid drops on thin cylinders under forces of capillarity. A theory for the roll-up process. *Langmuir*, 2(2):248–250, 1986. ⬀ . Cited on pages 13 and 14.

E. Cerda and L. Mahadevan. Geometry and physics of wrinkling. *Physical Review Letters*, 90(7), 2003. ⬀ . Cited on pages 104 and 106.

T.-H. Chou, S.-J. Hong, Y.-E. Liang, H.-K. Tsao, and Y.-J. Sheng. Equilibrium phase diagram of drop-on-fiber: Coexistent states and gravity effect. *Langmuir*, 27(7):3685–3692, 2011. ⬀ . Cited on pages 14, 15, 25, and 26.

J. Dai and M. Sheetz. Mechanical properties of neuronal growth cone membranes studied by tether formation with laser optical tweezers. *Biophysical Journal*, 68(3):988–996, 1995. ⬀ . Cited on page 75.

B. Davidovitch, R. D. Schroll, D. Vella, M. Adda-Bedia, and E. A. Cerda. Prototypical model for tensional wrinkling in thin sheets. *Proceedings of the National Academy of Sciences*, 108(45):18227–18232, 2011. ⬀ . Cited on pages 105 and 106.

P.-G. de Gennes, F. Brochard-Wyart, and D. Quéré. *Gouttes, bulles, perles et ondes.* Belin, Paris, 2005. Cited on pages 56, 57, and 60.

A. K. Dickerson, X. Liu, T. Zhu, and D. L. Hu. Fog spontaneously folds mosquito wings. *Physics of Fluids*, 27(2):021901, 2015. ⬀ . Cited on page 78.

L. du Peloux, O. Baverel, J.-F. Caron, and F. Tayeb. From shape to shell: a design tool to materialize freeform shapes using gridshell structures. In *Design Modelling Symposium Berlin*, Rethinking Prototyping: Proceedings of the Design Modelling Symposium Berlin 2013, Berlin, Germany, 2013. Cited on page 1.

H. Elettro. *Elasto-capillary windlass: from spider silk to smart actuators.* PhD thesis, Université Pierre et Marie Curie-Paris VI, 2015. Cited on pages 3, 33, 34, 40, and 121.

H. Elettro, F. Vollrath, A. Antkowiak, and S. Neukirch. Coiling of an elastic beam inside a disk: A model for spider-capture silk. *International Journal of Non-Linear Mechanics*, 75:59 – 66, 2015. ⬀ . Cited on page 33.

H. Elettro, S. Neukirch, F. Vollrath, and A. Antkowiak. In-drop capillary spooling of spider capture thread inspires hybrid fibers with mixed solid–liquid mechanical properties. *Proceedings of the National Academy of Sciences*, 113(22):6143–6147, 2016. . Cited on pages 3, 7, 33, 37, and 45.

H. B. Eral, J. de Ruiter, R. de Ruiter, J. M. Oh, C. Semprebon, M. Brinkmann, and F. Mugele. Drops on functional fibers: from barrels to clamshells and back. *Soft Matter*, 7(11):5138, 2011. . Cited on page 8.

C. Erickson and J. Trinkaus. Microvilli and blebs as sources of reserve surface membrane during cell spreading. *Experimental Cell Research*, 99(2):375–384, 1976. . Cited on page 76.

A. Föppl. *Vorlesungen über technische Mechanik*. B. G. Teubner, Leipzig, 1897. Cited on page 105.

A. Fortais, R. D. Schulman, and K. Dalnoki-Veress. Liquid droplets on a free-standing glassy membrane: Deformation through the glass transition. *The European Physical Journal E*, 40(7), 2017. . Cited on pages 76 and 77.

T. Gilet, D. Terwagne, and N. Vandewalle. Droplets sliding on fibres. *The European Physical Journal E: Soft Matter and Biological Physics*, 31(3):253–262, 2010. . Cited on pages 58 and 59.

J. E. Gordon. *The new science of strong materials: or why you don't fall through the floor*. Penguin UK, 1991. Cited on page 1.

D. Gracias, V. Kavthekar, J. Love, K. Paul, and G. Whitesides. Fabrication of micrometer-scale, patterned polyhedra by self-assembly. *Advanced Materials*, 14(3):235–238, 2002. . Cited on page 77.

A. Greiner and J. H. Wendorff. Electrospinning: A fascinating method for the preparation of ultrathin fibers. *Angewandte Chemie International Edition*, 46(30):5670–5703, 2007. . Cited on pages 38 and 78.

N. Groulx, F. Boudreault, S. N. Orlov, and R. Grygorczyk. Membrane reserves and hypotonic cell swelling. *Journal of Membrane Biology*, 214(1-2):43–56, 2006. . Cited on page 75.

L. Guillou, A. Babataheri, M. Saitakis, A. Bohineust, S. Dogniaux, C. Hivroz, A. I. Barakat, and J. Husson. T-lymphocyte passive deformation is controlled by unfolding of membrane surface reservoirs. *Molecular Biology of the Cell*, 27(22):3574–3582, 2016. . Cited on page 75.

S. Guo, M. Gao, X. Xiong, Y. J. Wang, X. Wang, P. Sheng, and P. Tong. Direct measurement of friction of a fluctuating contact line. *Phys. Rev. Lett.*, 111:026101, 2013. . Cited on page 58.

S. Haefner, O. Baumchen, and K. Jacobs. Capillary droplet propulsion on a fibre. *Soft Matter*, 11(35):6921–6926, 2015. . Cited on page 58.

C. S. Haines, M. D. Lima, N. Li, G. M. Spinks, J. Foroughi, J. D. Madden, S. H. Kim, S. Fang, M. J. de Andrade, F. Goktepe, et al. Artificial muscles from fishing line and sewing thread. *Science*, 343(6173):868–872, 2014. ☑ . Cited on page 89.

T. S. Hansen, K. West, O. Hassager, and N. B. Larsen. Highly stretchable and conductive polymer material made from poly(3, 4-ethylenedioxythiophene) and polyurethane elastomers. *Advanced functional materials*, 17(16):3069–3073, 2007. ☑ . Cited on page 38.

H. Hertz. über das gleichgewicht schwimmender elastischer platten. *Annalen der Physik*, 258(7):449–455, 1884. Cited on page 105.

J. Huang, M. Juszkiewicz, W. H. de Jeu, E. Cerda, T. Emrick, N. Menon, and T. P. Russell. Capillary wrinkling of floating thin polymer films. *Science*, 317(5838):650–653, 2007. ☑ . Cited on page 106.

C. Huh and L. Scriven. Hydrodynamic model of steady movement of a solid/liquid/fluid contact line. *Journal of Colloid and Interface Science*, 35(1):85–101, 1971. ☑ . Cited on page 56.

C.-Y. Hui and A. Jagota. Planar equilibrium shapes of a liquid drop on a membrane. *Soft Matter*, 11:8960–8967, 2015. ☑ . Cited on page 76.

J. A. Kluge, O. Rabotyagova, G. G. Leisk, and D. L. Kaplan. Spider silks and their applications. *Trends in Biotechnology*, 26(5):244 – 251, 2008. ☑ . Cited on page 38.

J. Lam, M. Herant, M. Dembo, and V. Heinrich. Baseline mechanical characterization of J774 macrophages. *Biophysical Journal*, 96(1):248–254, 2009. ☑ . Cited on pages 75, 76, and 101.

B. Li, Y.-P. Cao, X.-Q. Feng, and H. Gao. Mechanics of morphological instabilities and surface wrinkling in soft materials: a review. *Soft Matter*, 8(21):5728, 2012. ☑ . Cited on page 105.

R. J. Linderman, P. E. Kladitis, and V. M. Bright. Development of the micro rotary fan. *Sensors and Actuators A: Physical*, 95(2–3):135 – 142, 2002. ☑ . Cited on page 37.

E. Lorenceau, C. Clanet, and D. Quéré. Capturing drops with a thin fiber. *Journal of Colloid and Interface Science*, 279(1):192 – 197, 2004. ☑ . Cited on pages 9, 10, 17, 28, and 29.

S. Majstoravich, J. Zhang, S. Nicholson-Dykstra, S. Linder, W. Friedrich, K. A. Siminovitch, and H. N. Higgs. Lymphocyte microvilli are dynamic, actin-dependent structures that do not require wiskott-aldrich syndrome protein (wasp) for their morphology. *Blood*, 104 (5):1396–1403, 2004. ☑ . Cited on page 76.

E. H. Mansfield. Load transfer via a wrinkled membrane. *Proceedings of the Royal Society of London. Series A, Mathematical and Physical Sciences*, 316(1525):269–289, 1970. ☑ . Cited on page 106.

G. McHale and M. I. Newton. Global geometry and the equilibrium shapes of liquid drops on fibers. *Colloids and Surfaces A: Physicochemical and Engineering Aspects*, 206(1–3): 79–86, 2002. ⬀ . Cited on pages 14, 15, and 25.

G. McHale, N. A. Käb, M. I. Newton, and S. M. Rowan. Wetting of a high-energy fiber surface. *Journal of Colloid and Interface Science*, 186(2):453–461, 1997. ⬀ . Cited on pages 14 and 15.

S. Mora and Y. Pomeau. Souple et solide : comment la matière élastique se déforme-t-elle ? *Reflets de la physique*, (55):18–23, 2017. ⬀ . Cited on page 2.

S. Neukirch, B. Roman, B. de Gaudemaris, and J. Bico. Piercing a liquid surface with an elastic rod: Buckling under capillary forces. *Journal of the Mechanics and Physics of Solids*, 55(6):1212–1235, 2007. ⬀ . Cited on page 35.

J. A. Nichol and O. F. Hutter. Tensile strength and dilatational elasticity of giant sarcolem-mal vesicles shed from rabbit muscle. *The Journal of Physiology*, 493(1):187–198, 1996. ⬀ . Cited on pages 75 and 80.

H. Okuzaki and M. Ishihara. Spinning and characterization of conducting microfibers. *Macromolecular rapid communications*, 24(3):261–264, 2003. ⬀ . Cited on page 51.

H. Okuzaki, Y. Harashina, and H. Yan. Highly conductive PEDOT/PSS microfibers fabricated by wet-spinning and dip-treatment in ethylene glycol. *European Polymer Journal*, 45(1):256 – 261, 2009. ⬀ . Cited on page 51.

F. Onofri, A. Lenoble, H. Bultynck, and P.-H. Guéring. High-resolution laser diffractometry for the on-line sizing of small transparent fibres. *Optics Communications*, 234(1–6): 183–191, 2004. ⬀ . Cited on page 24.

H. Poincaré. *Capillarité*. Jacques Gabay, 1895. Cited on page 39.

C. Py, P. Reverdy, L. Doppler, J. Bico, B. Roman, and C. N. Baroud. Capillary origami: Spontaneous wrapping of a droplet with an elastic sheet. *Phys. Rev. Lett.*, 98(15):156103, 2007. ⬀ . Cited on pages 36 and 77.

A. Rafsanjani and K. Bertoldi. Buckling-induced kirigami. *Physical Review Letters*, 118(8): 084301, 2017. ⬀ . Cited on page 1.

D. Raucher and M. P. Sheetz. Characteristics of a membrane reservoir buffering membrane tension. *Biophysical Journal*, 77(4):1992–2002, 1999. ⬀ . Cited on pages 75 and 80.

M. Rivetti and A. Antkowiak. Elasto-capillary meniscus: pulling out a soft strip sticking to a liquid surface. *Soft Matter*, 9(27):6226, 2013. ⬀ . Cited on page 36.

J. A. Rogers, T. Someya, and Y. Huang. Materials and mechanics for stretchable electronics. *Science*, 327(5973):1603–1607, 2010.
⬀ . Cited on pages 1 and 38.

B. Roman and J. Bico. Elasto-capillarity: deforming an elastic structure with a liquid droplet. *Journal of Physics: Condensed Matter*, 22(49):493101, 2010.
⬀ . Cited on page 36.

B. Roman and A. Pocheau. Buckling cascade of thin plates: Forms, constraints and similarity. *Europhysics Letters (EPL)*, 46(5):602–608, 1999.
⬀ . Cited on page 117.

G. Salbreux, G. Charras, and E. Paluch. Actin cortex mechanics and cellular morphogenesis. *Trends in Cell Biology*, 22(10):536–545, 2012.
⬀ . Cited on page 76.

R. D. Schulman, R. Ledesma-Alonso, T. Salez, E. Raphaël, and K. Dalnoki-Veress. Liquid droplets act as "compass needles" for the stresses in a deformable membrane. *Physical Review Letters*, 118(19), 2017.
⬀ . Cited on page 77.

K. Singh, J. R. Lister, and D. Vella. A fluid-mechanical model of elastocapillary coalescence. *Journal of Fluid Mechanics*, 745:621–646, 2014.
⬀ . Cited on page 36.

J.-Y. Sun, X. Zhao, W. R. Illeperuma, O. Chaudhuri, K. H. Oh, D. J. Mooney, J. J. Vlassak, and Z. Suo. Highly stretchable and tough hydrogels. *Nature*, 489(7414):133–136, 2012.
⬀ . Cited on page 2.

R. R. A. Syms, E. M. Yeatman, V. M. Bright, and G. M. Whitesides. Surface tension-powered self-assembly of microstructures - the state-of-the-art. *Microelectromechanical Systems, Journal of*, 12(4):387 – 417, 2003.
⬀ . Cited on page 37.

T. Tallinen, J. Y. Chung, F. Rousseau, N. Girard, J. Lefevre, and L. Mahadevan. On the growth and form of cortical convolutions. *Nat Phys*, 12(6):588–593, 2016.
⬀ . Cited on page 104.

T. Tanaka, M. Morigami, and N. Atoda. Mechanism of resist pattern collapse during development process. *Japanese Journal of Applied Physics*, 32(12S):6059, 1993. Cited on page 36.

M. Taroni and D. Vella. Multiple equilibria in a simple elastocapillary system. *Journal of Fluid Mechanics*, 712:273–294, 2012.
⬀ . Cited on page 36.

D. Terwagne, M. Brojan, and P. M. Reis. Smart morphable surfaces for aerodynamic drag control. *Advanced Materials*, 26(38):6608–6611, 2014.
⬀ . Cited on pages 105 and 106.

H. Vandeparre, M. Piñeirua, F. Brau, B. Roman, J. Bico, C. Gay, W. Bao, C. N. Lau, P. M. Reis, and P. Damman. Wrinkling hierarchy in constrained thin sheets from suspended graphene to curtains. *Physical Review Letters*, 106(22), 2011.
⬀ . Cited on page 105.

F. Vollrath and D. T. Edmonds. Modulation of the mechanical properties of spider silk by coating with water. *Nature*, 340(6231):305–307, 1989. ⬈ . Cited on pages 3, 7, and 33.

S. Xu, Z. Yan, K.-I. Jang, W. Huang, H. Fu, J. Kim, Z. Wei, M. Flavin, J. McCracken, R. Wang, and et al. Assembly of micro/nanomaterials into complex, three-dimensional architectures by compressive buckling. *Science*, 347(6218):154–159, 2015. ⬈ . Cited on page 1.